

# **ADVANCED MATERIALS FOR ENERGY STORAGE IN SUPERCAPACITORS AND CAPACITIVE WATER PURIFICATION**

By Kaiyuan Shi, B.S., M.Eng.

A Thesis Submitted to the School of Graduate Studies in Partial Fulfillment of the  
Requirements for the Degree Doctor of Philosophy

DOCTOR OF PHILOSOPHY (2016)

McMaster University

Department of Materials Science & Engineering

Hamilton, Ontario

TITLE: Advanced Materials for Energy Storage in Supercapacitors and Capacitive  
Water Purification

AUTHOR: Kaiyuan Shi, M.Eng., (Huazhong University of Science and Technology),  
B.S., (Huazhong University of Science and Technology, Wuhan, China)

SUPERVISOR: Prof. Igor Zhitomirsky, Distinguished Engineering Professor, Ph.D.,  
P.Eng.

NUMBER OF PAGES: XLII, 288

## Abstract

In this study, polypyrrole (PPy) prepared by chemical and electrochemical polymerization was investigated as the electrode of electrochemical supercapacitor (ES). New strategies were developed for the fabrication of nano-structured PPy and PPy based nano-composites, which included discovery of advanced anionic dopants and multi-functional nano-crystals, and development of co-dispersing agents. These methods improved the capacitive performance and cycle stability of PPy electrodes.

The results indicated that high material loading and good capacitance retention of PPy was achieved using an electrochemical polymerization method and Ni plaque as the current collectors. Nano-crystalline  $(\text{CTA})_2\text{S}_2\text{O}_8$  formed by a chemical precipitation method from solutions, containing anionic oxidant ( $\text{S}_2\text{O}_8^{2-}$ ) and cationic surfactant ( $\text{CTA}^+$ ), could be used as the oxidant to synthesize PPy nano-fibers. We demonstrated that multi-wall carbon nanotubes (MWCNT) can be efficiently dispersed using such nano-crystals. Application of multi-functional nano-crystals is a conceptually new approach for the fabrication PPy coated MWCNT. Moreover, safranin and malachite green were found as universal dispersing and charging agents for cataphoretic deposition of graphene, MWCNT and PPy nano-fibers. It opens new strategies in colloidal and electrochemical processing of PPy nano-composites for ES electrodes.

PPy coated MWCNT, prepared by the multi-functional nano-crystals  $(\text{CTA})_2\text{S}_2\text{O}_8$ , was employed for the fabrication of N-doped activated carbon-coated MWCNT (N-AC-MWCNT). The obtained N-AC-MWCNT was uniformly coated and possessed with high surface area. The use of N-AC-MWCNT enabled the fabrication of ES electrodes with high mass loading and high active material to current collector mass ratio. Symmetric and asymmetric ES cells, fabricated by N-AC-MWCNT and aqueous  $\text{Na}_2\text{SO}_4$  electrolyte, showed high specific capacitance, good capacitance retention and large voltage window. The positive electrode of asymmetric ES,  $\text{MnO}_2$  coated MWCNT, was successfully prepared by the chemical reaction between  $\text{KMnO}_4$  and N-AC-MWCNT. The problem of degradation of MWCNT was avoided by the use of N-AC as the sacrificial carbon.

Significant progress on ES technology has allowed for the development of capacitive dyes removal (CDR) methods using ES devices. In our study, porous carbon materials, N-doped activated carbon coated MWCNT (N-AC-MWCNT) and N-doped activated carbon nano-fibers (N-AC-NF), were developed as the electrodes for CDR applications. The experimental results indicated that capacitive performance of ES cells was influenced by the chemical structure, size, charge-to mass ratio, concentration and redox-active ligands of the dyes. CDR is a promising method for removal of various cationic and anionic dyes, which offers advantages of energy saving and simple electrode regeneration.

Key words: polypyrrole, carbon nanotubes, activated carbon, electrophoretic deposition, symmetric supercapacitors, asymmetric supercapacitors, water purification

## **Acknowledgements**

First of all, I would like to express my deepest gratitude to my supervisor Professor Igor Zhitomirsky for constant support, kind guidance, patient discussion and valuable suggestions in carrying out the research project. Thank you so much for your great patience and tolerance during the entire course of my Ph.D. study! I have been really very fortunate to work with you. Your hardworking, enthusiasm, and endless quest to perform high quality research influenced me deeply and set a great example for my career.

I would also like to thank all my committee members, Professor Gianluigi Botton and Professor Anthony Petric, for their valuable time in evaluating my research work and provide useful suggestions and comments. The assistance and suggestions for my dissertation from Prof. Michael Pope at the University of Waterloo were greatly appreciated. Additionally, I am very appreciating Dr. Xin Pang for all her kind support in experimental setup and laboratory issues at CanmetMATERIALS. Her patience in reviewing the documents line by line helped me a lot, and her suggestions provided a great support toward refining my research.

I would like to express my profound thanks to all the collaborators for their contribution and efforts in these excellent works. I am really grateful to Professor Emily Cranston, for her inspiring discussion, constructive advices and great support in my research study. I am very thankful to Dr. Babak Shalchi Amirkhiz for fruitful

discussions and kind help with TEM characterization. Assistance and support from technicians and staff members, Xiaogang Li, Megan Fair, Victoria Jarvis, Chris Butcher, Steve Koprach and Frank Gibbs, were also greatly acknowledged.

It was trully my pleasure to work at Department of Materials Science and Engineering, McMaster Unverity. I enjoy the time with my wonderful groupmates and friends. I would like to express my appreciation to Xuan Yang, Yisong Su, Yangshuai Liu, Yeling Zhu, Mustafa Ata, Cameron Wallar, Parick Wojtal, Dan Luo, Tianshi Zhang, Shilei Chen, Yanchao Sun, Jieming Li, Meng Ren, Hanshuo Liu, Siwei Ma, Sheikh Jamil Ahmed and Xavier Michaud, for their generous help in course work, research projects and daily life.

Last, but the most important, I wish to express my appriciation to my family. I would like to thank my dear parents for their love and endless support. I also would like to thank all the other family members for their continuous support for my decisions. In particularly, I would like to express my gratitude to my wife Juan Wu for her patience, encouragement and unconditional support both in my Ph.D. study and life.

## Declaration of Academic Achievements

This dissertation was used to fulfill the requirements of Ph.D. degree. The major research project was undertaken from May 2012 to January 2016. Over the course of this thesis study, I carried out experimental and theoretical research on developing advanced materials for supercapacitors and capacitive water purification applications, which included improving cyclic stability of polypyrrole, development of new methods of fabrication of composite electrodes and development of a new activated carbon, etc. The major contribution of this study came from myself and my supervisor.

The results of this dissertation were published in 18 papers in peer-reviewed journals, in which I was the first author on 11 of these papers. The papers were listed below.

- 1 **Kaiyuan Shi** and Igor Zhitomirsky, Influence of chemical structure of dyes on supercapacitive dye removal from solutions, *Electrochimica Acta*, 2015, 17, 588-595
- 2 **Kaiyuan Shi**, Xin Pang and Igor Zhitomirsky, Fabrication of Tiron-doped polypyrrole/MWCNT composite electrodes with high mass loading and enhanced performance for supercapacitors, *Journal of Applied Polymer Science*, 2015, 132(32), 42376-42384
- 3 **Kaiyuan Shi** and Igor Zhitomirsky, Electrodeposition of Carbon Nanotubes Triggered by Cathodic and Anodic Reactions of Dispersants, *Materials and Manufacturing Processes*, 2015, 30(6), 771-777
- 4 **Kaiyuan Shi** and Igor Zhitomirsky, Asymmetric supercapacitors based on

- activated carbon coated carbon nanotubes, *ChemElectroChem*, 2015, 2(3), 396-403
- 5 **Kaiyuan Shi** and Igor Zhitomirsky, Supercapacitor devices for energy storage and capacitive dye removal from aqueous solutions, *RSC Advances*, 2014, 5 (1), 320-327
  - 6 **Kaiyuan Shi**, Meng Ren and Igor Zhitomirsky, Activated carbon coated carbon nanotubes for energy storage in supercapacitors and capacitive water purification, *ACS Sustainable Chemistry & Engineering*, 2014, 2(5), 1289-1298
  - 7 **Kaiyuan Shi** and Igor Zhitomirsky, Fabrication of polypyrrole coated carbon nanotubes using oxidant-surfactant nanocrystals for supercapacitor electrodes with high mass loading and enhanced performance, *ACS Applied Materials & Interfaces*, 2013, 5, 13161-13170
  - 8 **Kaiyuan Shi** and Igor Zhitomirsky, Polypyrrole nanofiber-carbon nanotube electrodes for supercapacitors with high mass loading obtained using organic dye as a co-dispersant, *Journal of Materials Chemistry A*, 2013, 1(38):11614-1162
  - 9 **Kaiyuan Shi** and Igor Zhitomirsky, Influence of current collector on capacitive behavior and cycling stability of tiron doped polypyrrole electrodes, *Journal of Power Sources*, 2013, 240,42-49
  - 10 **Kaiyuan Shi** and Igor Zhitomirsky, Cataphoretic nanotechnology of graphene-carbon nanotube composites using safranin dye as universal dispersant and film forming agent, *Journal of Colloid and Interface Science*, 2013, 407, 474-481
  - 11 **K. Shi**, Y. Su and I. Zhitomirsky, Characterization of Ni plaque based polypyrrole electrodes prepared by pulse electropolymerization, *Materials Letters*, 2013, 96,135-138

In addition to the work presented at here, I was the co-first author or co-author of 6

papers relevant to my thesis study.

- 12 Xuan Yang (Co-first author), **Kaiyuan Shi (Co-first author)**, Igor Zhitomirsky and Emily Cranston, Cellulose Nanocrystal Aerogels as Universal 3D Lightweight Substrates for Supercapacitor Materials, *Advanced Materials*, 2015, 27, 6104–6109
- 13 Y. Liu, **K. Shi** and I. Zhitomirsky, Azopolymer triggered electrophoretic deposition of MnO<sub>2</sub>-carbon nanotube composites and polypyrrole coated carbon nanotubes for supercapacitors, *Journal of Materials Chemistry A*, 2015, 3(33), 16486–16494
- 14 Y. Liu, **K. Shi** and I. Zhitomirsky, Film deposition mechanisms and properties of optically active chelating polymer and composites, *Colloids and Surfaces A Physicochemical and Engineering Aspects*, 2015, 487, 17-25
- 15 P. Wojtal, S. Chen, **K. Shi**, R. Mathews and I. Zhitomirsky, Electrophoretic deposition of a memory-type flame retardant material, *Materials Letters*, 153, 106-109
- 16 Y. Liu, M.S. Ata, **K. Shi**, G.-z. Zhu, G.A. Botton and I. Zhitomirsky, Surface modification and cathodic electrophoretic deposition of ceramic materials and composites using Celestine blue dye, *RSC advances*, 2014, 4(56), 29652-29659
- 17 Yeling Zhu, **Kaiyuan Shi** and Igor Zhitomirsky, Polypyrrole coated carbon nanotubes for supercapacitor devices with enhanced electrochemical performance, *Journal of Power Sources*, 2014, 268(15), 233-239
- 18 Yeling Zhu, **Kaiyuan Shi** and Igor Zhitomirsky, Anionic dopants-dispersants for synthesis of polypyrrole coated carbon nanotubes and fabrication of supercapacitor electrodes with high active mass loading, *Journal of Materials Chemistry A*, 2014, 2(35), 14666-14673

## Tables of Contents

|  |     |
|--|-----|
| Abstract.....  | III |
| Acknowledgements.....  | VI  |
| 1. Introduction.....   | 1   |
| 2. Literature review.....  | 5   |
| 2.1 The development of capacitors and electrochemical supercapacitors (ESs)..... | 5   |
| 2.2 Comparison of energy and power of ESs, batteries and fuel cells.....         | 8   |
| 2.3 Two types of capacitive materials and energy storage mechanism.....          | 12  |
| 2.3.1 Electrochemical double-layer capacitors (EDLCs).....                       | 12  |
| 2.3.2 Pseudocapacitors.....  | 14  |
| 2.4 The double-layer at the electrode interfaces.....                            | 18  |
| 2.4.1 Electric potential profiles and electrostatic principles.....              | 18  |
| 2.4.2 Models and structures.....   | 20  |
| 2.4.3 Equivalent circuit representation.....                                     | 22  |
| 2.5 Materials for electrode of ES.....   | 24  |
| 2.5.1 Porous Carbon materials for EDLCs.....                                     | 24  |
| 2.5.2 Conducting polymers.....   | 26  |
| 2.5.3 Metal oxides.....  | 33  |
| 2.5.4 Composite electrodes and hybrid configurations.....                        | 35  |

|  |    |
|--|----|
| 2.6 Electrolyte for ESs .....                                      | 39 |
| 2.6.1 Aqueous electrolytes .....                                   | 40 |
| 2.6.2 Organic electrolytes .....                                   | 41 |
| 2.6.3 Ionic liquids .....  | 42 |
| 2.6.4 Solid-state ES.....  | 43 |
| 2.7 New application of ESs technique--Capacitive deionization..... | 44 |
| 2.8 References.....  | 47 |
| 3. Problem statements and proposed approaches.....                 | 59 |
| 3.1 Dispersion of carbon nanotube (CNT) and graphene .....         | 59 |
| 3.1.1 Challenges.....  | 59 |
| 3.1.2 Proposed approaches.....                                     | 61 |
| 3.2 Energy density of ESs.....                                     | 62 |
| 3.2.1 Challenges.....  | 62 |
| 3.2.2 Proposed approaches.....                                     | 64 |
| 3.3 Real performance of ESs .....                                  | 68 |
| 3.3.1 Challenges.....  | 68 |
| 3.3.2 Proposed approaches.....                                     | 70 |
| 3.4 Rate capability of ESs.....                                    | 71 |
| 3.4.1 Challenges.....  | 71 |
| 3.4.2 Proposed approaches.....                                     | 73 |

|   |     |
|---|-----|
| 3.5 Cycle stability of PPy-based electrode .....                            | 76  |
| 3.5.1 Challenges.....   | 76  |
| 3.5.2 Proposed approaches.....  | 76  |
| 3.6 Electrode materials for capacitive deionization.....                    | 77  |
| 3.6.1 Challenges.....   | 77  |
| 3.6.2 Proposed aspects .....  | 79  |
| 3.7 Overall objectives .....  | 81  |
| 3.7 References.....   | 82  |
| 4. Experimental methods and materials characterization .....                | 88  |
| 4.1 Starting materials .....  | 88  |
| 4.2 Capacitive materials preparation.....                                   | 90  |
| 4.2.1 Synthesis of PPy .....  | 90  |
| 4.2.2 Preparation of PPy based composites .....                             | 93  |
| 4.2.3 Preparation of activated carbon by carbonization of PPy.....          | 97  |
| 4.2.3.1 Activated carbon coated MWCNTs obtained from PPy coated MWCNTs .... | 97  |
| 4.3 Materials characterization.....   | 99  |
| 4.3.1 Adhesion study of deposited films.....                                | 99  |
| 4.3.2 Morphology study.....   | 99  |
| 4.3.3 Crystallinity study.....  | 100 |
| 4.3.4 Composition study .....   | 100 |

|   |     |
|---|-----|
| 4.4 Fabrication of electrodes and cells for ESs.....  | 100 |
| 4.4.1 Fabrication of electrodes from electro-polymerized and electrophoretically deposited films.....                       | 100 |
| 4.4.2 Fabrication of electrodes using the slurry impregnation method.....   | 101 |
| 4.4.3 Fabrication of ES cells.....  | 101 |
| 4.5 Characterization of capacitive performance .....  | 102 |
| 4.5.1 Cyclic voltammetry.....   | 102 |
| 4.5.2 Impedance spectroscopy .....  | 103 |
| 4.5.3 Galvanostatic charge-discharge .....  | 104 |
| 4.6 Characterization of capacitive water purification.....  | 105 |
| 4.7 References.....   | 106 |
| 5. PPy electrodes for energy storage in supercapacitors.....  | 108 |
| 5.1 Influence of current collector on the capacitive performance of PPy prepared by the electrochemical polymerization..... | 108 |
| 5.1.1 Electrochemical polymerization of PPy on different current collectors.....  | 108 |
| 5.1.2 Capacitive performance of PPy deposits .....  | 110 |
| 5.1.3 Cycling stability of PPy deposits on Ni foils and Ni plaques based electrodes   | 117 |
| 5.1.4 Morphology of PPy deposits before and after cycling tests .....   | 119 |
| 5.1.5 Discussion.....   | 122 |
| 5.1.6 Conclusions.....  | 124 |

|   |     |
|---|-----|
| 5.2 Pulse electrochemical polymerization of PPy using Ni plaque as the current collector..... | 124 |
| 5.2.1 Morphology characterization.....  | 125 |
| 5.2.2 Specific capacitance and capacitance retention.....                                     | 126 |
| 5.2.3 Cycling stability.....  | 127 |
| 5.2.4 Conclusions.....  | 129 |
| 5.3 References.....   | 130 |
| 6. PPy based composite electrodes for energy storage in supercapacitors .....                 | 133 |
| 6.1 Tiron doped PPy/MWCNTs composite prepared using SAF as the co-dispersant .....            | 133 |
| 6.1.1 Morphology of PPy, prepared by chemical polymerization.....                             | 134 |
| 6.1.2 Fabrication of PPy/MWCNT composites.....  | 135 |
| 6.1.3 Capacitive performance of single electrode.....   | 138 |
| 6.1.4 Capacitive performance of symmetric supercapacitor.....                                 | 147 |
| 6.1.5 Conclusions.....  | 149 |
| 6.2 PPy nano-fiber/MWCNTs composite prepared using MG as the co-dispersant .                  | 150 |
| 6.2.1 Morphology of PPy nano-fiber .....  | 151 |
| 6.2.2 Investigation of MG adsorption.....   | 152 |
| 6.2.3 Morphology of PPy nano-fiber/MWCNT composites.....                                      | 158 |
| 6.2.4 Capacitive performance of PPy nano-fiber based electrodes .....                         | 159 |

|   |     |
|---|-----|
| 6.2.5 Influence of mass loading on the capacitive performance.....  | 164 |
| 6.2.6 Cycling stability of the PPy nano-fiber/MWCNT electrode.....  | 165 |
| 6.2.7 Conclusions.....  | 167 |
| 6.3 Graphene/MWCNTs and Graphene/PPy nano-fibers composite films prepared by electrophoretic deposition.....                        | 167 |
| 6.3.1 Dispersion of MWCNT, graphene and PPy nano-fiber .....  | 169 |
| 6.3.2 Electrophoretic deposition of MWCNT, graphene and PPy nano-fiber .....  | 170 |
| 6.3.3 Composite films fabricated by electrophoretic deposition .....  | 175 |
| 6.3.4 Capacitive performance of deposited films .....   | 177 |
| 6.3.5 Conclusions.....  | 180 |
| 6.4 PPy coated MWCNTs synthesized by multi-functional nano-crystals.....  | 181 |
| 6.4.1 PPy synthesized by $(\text{NH}_4)_2\text{S}_2\text{O}_8$ and $(\text{CTA})_2\text{S}_2\text{O}_8$ .....                       | 182 |
| 6.4.2 Capacitive performance of PPy .....   | 186 |
| 6.4.3 Dispersion of MWCNT using $(\text{CTA})_2\text{S}_2\text{O}_8$ .....  | 187 |
| 6.4.4 PPy/MWCNT nano-composites synthesized by $(\text{NH}_4)_2\text{S}_2\text{O}_8$ and $(\text{CTA})_2\text{S}_2\text{O}_8$ ..... | 192 |
| 6.4.5 Capacitive performance of PPy/MWCNT nano-composites.....  | 196 |
| 6.4.6 Conclusions.....  | 200 |
| 6.5 References.....   | 201 |
| 7. Activated carbon electrodes for energy storage in supercapacitors.....   | 212 |

|   |     |
|---|-----|
| 7.1 Symmetric supercapacitors fabricated based on activated carbon coated MWCNT .....   | 212 |
| 7.1.1 Characterization of N-AC-MWCNT .....  | 213 |
| 7.1.2 Capacitive performance of the N-AC-MWCNT electrodes .....                         | 218 |
| 7.1.3 Capacitive performance of the symmetric ES cell.....                              | 222 |
| 7.1.4 Conclusions.....  | 226 |
| 7.2 Asymmetric supercapacitor fabricated by activated carbon coated MWCNT ....          | 226 |
| 7.2.1 Fabrication of MnO <sub>2</sub> coated N-AC-MWCNT and asymmetric ES cells.....    | 228 |
| 7.2.2 Materials characterization.....   | 229 |
| 7.2.3 Capacitive performance of the MnO <sub>2</sub> coated N-AC-MWCNT electrodes ..... | 232 |
| 7.2.4 Capacitive performance of the asymmetric ES cell .....                            | 239 |
| 7.2.5 Conclusion .....  | 242 |
| 7.3 References.....   | 243 |
| 8. Activated carbon based electrodes for capacitive dye removal .....                   | 250 |
| 8.1 Activated carbon coated MWCNTs for capacitive dye removal .....                     | 250 |
| 8.1.1 Chemical structure of different dyes.....   | 251 |
| 8.1.2 Investigation of capacitive behavior in solution of Safranin and Calcon dyes.     | 252 |
| 8.1.3 Investigation of capacitive behavior in Amaranth solutions.....                   | 261 |
| 8.1.4 Conclusions.....  | 264 |
| 8.2 Activated carbon nano-fibers for capacitive dye removal .....                       | 265 |

|   |     |
|---|-----|
| 8.2.1 Chemical structure of different dyes.....                                   | 266 |
| 8.2.2 Characterization of N-doped activated carbon nano-fibers .....              | 269 |
| 8.2.3 Optimization of the voltage window for capacitive removal of different dyes | 270 |
| 8.2.4 Capacitive performance of ES cells in triphenylmethane dyes .....           | 274 |
| 8.2.5 Capacitive performance of ES cells in chromotropic dyes.....                | 277 |
| 8.2.6 Conclusions.....  | 280 |
| 8.3 References.....   | 281 |
| 9. Conclusions.....   | 286 |

## List of Figures

|   |    |
|---|----|
| Figure 2.1 Schematic illustration of the electrostatic capacitor with a plate area of $A$ , distance between two plates of $d$ . .....  | 6  |
| Figure 2.2 Power density versus energy density, also called the Ragone plot, for various electrochemical energy storage systems compared to combustion engine, gas turbines and electrostatic capacitors. ....  | 8  |
| Figure 2.3 (A) Charge-discharge curve and (B) energy storage of ideal battery and ideal ES. ....  | 9  |
| Figure 2.4 Scheme of electrochemical double-layer capacitors (EDLCs) and illustration of the potential profile at the electrode/electrolyte interface after charging. ....  | 13 |
| Figure 2.5 Different types of pseudocapacitive behaviour from B.E. Conway: (a) underpotential deposition, (b) redox pseudocapacitance, and (c) intercalation pseudocapacitance. ....  | 16 |
| Figure 2.6 Diagrams of electric potential profiles in an ES cell comprising a double-layer at each of two electrodes: (a) charged capacitor in an open circuit, (b) capacitor passing current on discharge with IR drops. ....  | 19 |
| Figure 2.7 Models of the electrical double-layer at a positively charged surface: (a) the Helmholtz model, (b) the Gouy–Chapman model, and (c) the Stern model showing the inner Helmholtz plane (IHP) and outer Helmholtz plane (OHP). $\psi_0$ and $\psi$ are the potentials at the electrode surface and the electrode/electrolyte interface, respectively. .... | 21 |
| Figure 2.8 Simple equivalent circuit representation of the Stern model of the electrical double-layer. ....   | 22 |

Figure 2.9 Simple equivalent circuit representation of the basic operation of a single-cell ES. ....23

Figure 2.10 Schematic diagram of the pore size network of an activated carbon. ....25

Figure 2.11 Various conducting polymer structures: A) polypyrrole (PPy), B) polyaniline (PAni), C) polythiophene (PTh) and D) poly(3,4-ethylenedioxythiophene) (PEDOT). ....27

Figure 2.12 Charge and discharge mechanism for a) p-doping and b) n-doping conductive polymer. ....28

Figure 2.13 Schematic representation of mechanism for the formation of PPy chain proposed by Shubhra. ....30

Figure 2.14 Charge storage mechanism for PPy. .... 32

Figure 2.15 Schematic illustration of cyclic voltammetry for a MnO<sub>2</sub>-electrode cell in neutral aqueous electrolyte (0.1 M K<sub>2</sub>SO<sub>4</sub>) shows the successive multiple surface redox reactions leading to the pseudocapacitive charge storage mechanism. ....34

Figure 2.16 Possible strategies to improve both energy and power densities for ESs. a) carbon activation and b) decorating with pseudocapacitive materials on porous carbon; c) highly ordered high surface area carbon nanotubes and d) deposit of pseudocapacitive materials on carbon nanotubes. ....35

Figure 2.17 Scheme of MnO<sub>2</sub>/active carbon (AC) hybrid ES. ....38

Figure 2.18 Types of ion pairs in an electrolyte solution: (a) solvated-ion pairs, (b) solvent shared ion pairs, and (c) contact ion pairs. ....40

Figure 2.19 Schematic of all-solid-state ES in flexible sandwiched cell configuration (left), interdigitated finger cell configuration (middle), and coaxial fiber cell configuration (right). .....44

Figure 2.20 Schematic design of a cell for (a) capacitive deionization (CDI) and (b) membrane capacitive deionization (MCDI), where in front of the cathode a cation-exchange membrane is placed, while an anion-exchange membrane is placed in front of the anode. ....45

Figure 3.1 Schematic illustration of various surfactant assembly structures on a CNT, including (a) cylindrical micelles, side and cross-section views, (b) hemimicelle, and (c) random adsorption. ....60

Figure 3.2 Chemical structure of (A) safranin and (B) malachite green oxalate salt. ....61

Figure 3.3 Possible adsorption of safranin on MWCNT and graphene. ....62

Figure 3.4 Chemical structure of aromatic dopants proposed to improve the capacitive behaviour of PPy. A) Tiron and B) Ponceau S. ....64

Figure 3.5 SEM images of (A) granular polypyrrole without additive. (scale bar: 200 nm); (B) polypyrrole nano-fibers prepared by  $(\text{CTA})_2\text{S}_2\text{O}_8$  (scale bar 1  $\mu\text{m}$ ). ....66

Figure 3.6 Fabrication of (A)  $\text{MnO}_2@\text{N-AC-MWCNT}$  and (B) coin cells, containing  $\text{MnO}_2@\text{N-AC-MWCNT}$  positive electrode and N-AC-MWCNT negative electrode. ....67

Figure 3.7 The plots for the same electrochemical capacitors are (A) on a gravimetric (per weight) basis and (B) on a volumetric basis. ....69

Figure 3.8 SEM picture of as-received Ni plaque. ....70

Figure 3.9 Specific capacitance (SC) versus scan rate, demonstrated that SC decrease sharply with decrease of the scan rate. The electrode was made by sodium salicylate doped PPy. The PPy was deposited on a stainless steel foil with the film mass of (a) 165, (b) 373 and (c) 658  $\mu\text{ cm}^{-2}$ . ....71

Figure 3.10 Schematic illustration of EPD process. (a) Cathodic EPD and (b) anodic EPD. ....73

Figure 3.11 Fabrication of suspension and EPD of graphene-MWCNT composite films. ....74

Figure 3.12 Schematic illustration of pulse current electrodeposition PPy. ....75

Figure 3.13 SEM images of precipitation of (A-C) cationic basic fuchsin dye at cathode and (D-F) anionic fluorescein dye at anode from 500  $\text{mg L}^{-1}$  aqueous solutions, at voltage of (A,D) 2, (B,E) 5 and (C,F) 10 V after 10 min. ....81

Figure 4.1 Scheme of fabrication of Tiron doped PPy films using electro-polymerization method. ....91

Figure 4.2 Scheme of fabrication of PPy-NF/ MWCNTs composite. ....94

Figure 4.3 Scheme of fabrication of graphene–MWCNT and graphene–PPy composite films by cathodic EPD. ....95

Figure 4.4 Scheme of fabrication of PPy coated MWCNT using  $(\text{CTA})_2\text{S}_2\text{O}_8$  as the dispersants for MWCNT and oxidants for Py. ....96

|  |     |
|--|-----|
| Figure 4.5 Scheme of fabrication of activated carbon coated MWCNTs. ....   | 97  |
| Figure 4.6 Scheme of fabrication electrodes using slurry impregnation. ....  | 101 |
| Figure 4.7 (A) Princeton PARSTAT 2273 potentiostat and (B) scheme of three-electrode setup. ....   | 102 |
| Figure 4.8 Scheme of QCM analysis system for capacitive water purification. ....   | 105 |
| Figure 5.1 (A, B) Deposit mass versus charge passed for deposition on (A) Ni foil (inset shows a chemical structure of Tiron dopant) and on (B) Ni plaque substrates and (C, D) SEM images of Ni plaques at different magnifications. ....   | 109 |
| Figure 5.2 (A) CVs at a scan rate of $5 \text{ mV s}^{-1}$ , (B) $C_m$ and (C) $C_s$ obtained from the CV data versus scan rate and (D) Nyquist plot of $Z^*$ for PPy deposits on Ni foil with PPy mass of (a) 0.10, (b) 0.20 and (c) $0.42 \text{ mg cm}^{-2}$ , the inset shows high frequency range. .... | 111 |
| Figure 5.3 (A) CVs at a scan rate of $5 \text{ mV s}^{-1}$ , (B) $C_m$ and (C) $C_s$ obtained from the CV data versus scan rate and (D) Nyquist plot of $Z^*$ (inset shows high frequency range) for PPy deposits on Ni plaque with PPy mass of (a) 0.84, (b) 1.54 and (c) $2.80 \text{ mg cm}^{-2}$ . ....  | 112 |
| Figure 5.4 (A) Capacitance retention versus mass of PPy deposits on (a) Ni foil and (b) Ni plaque substrates and (B) $C_m$ at the scan rates from 2 to $100 \text{ mV s}^{-1}$ versus mass of PPy deposits for Ni foil and Ni plaque based electrodes. ....  | 114 |

Figure 5.5  $C_s^*$  obtained from impedance data versus frequency for PPy deposits on (A, B) Ni foil with PPy mass of (a) 0.10, (b) 0.13, (c) 0.20, (e) 0.29 and (f)  $0.42 \text{ mg cm}^{-2}$  and (C, D) Ni plaque with PPy mass of (a) 0.84, (b) 1.16, (c) 1.54, (e) 2.09 and (f)  $2.80 \text{ mg cm}^{-2}$ . .....115

Figure 5.6 (A, B) Capacitance retention versus cycle number (insets show CVs for (a)  $10^{\text{th}}$  (b)  $250^{\text{th}}$  and (c)  $500^{\text{th}}$  cycle) and (C, D) Nyquist plots of  $Z^*$  obtained after the corresponding cycles (insets show high frequency range) for (A, C)  $0.15$  and (B, D)  $0.31 \text{ mg cm}^{-2}$  deposits on Ni foil. ....117

Figure 5.7 (A) capacitance retention versus cycle number (inset shows CVs for (a)  $10^{\text{th}}$  (b)  $150^{\text{th}}$ , (c)  $500^{\text{th}}$ , (d)  $750^{\text{th}}$  and (e)  $1000^{\text{th}}$  cycle) and (B) Nyquist plots of  $Z^*$  obtained after the corresponding cycles (inset shows high frequency range) for  $1.10 \text{ mg cm}^{-2}$  PPy deposit on a Ni plaque. ....118

Figure 5.8 SEM images of  $0.15 \text{ mg cm}^{-2}$  PPy deposit on a Ni foil: (A) as prepared and (B) after 500 cycles, arrows show areas of deposit swelling. ....120

Figure 5.9 (A-D) SEM images of impregnated Ni plaques at different magnifications: (A, C) before cycling and (B, D) after 1000 cycles. ....121

Figure 5.10 Scheme of electron transportation within the porous Ni plaque electrodes. ....122

Figure 5.11 SEM images of Ni plaque: (A) as-received and (B) after impregnation with PPy mass loading of  $2.54 \text{ mg cm}^{-2}$ . .....125

Figure 5.12 Capacitance retention versus cycle number for  $1.94 \text{ mg cm}^{-2}$  PPy electrode. Inset shows CVs at a scan rate of  $50 \text{ mV s}^{-1}$ . .....126

Figure. 5.13 Capacitance retention versus cycle number for  $1.94 \text{ mg cm}^{-2}$  PPy electrode. Inset shows CVs at a scan rate of  $50 \text{ mV s}^{-1}$ . .....128

Figure 5.14 (A) Nyquist plots of complex impedance (inset shows high frequency range) and corresponding Bode plots of (B)  $C'$  and (C)  $C''$  (insets show low frequency range) for the PPy electrode with a mass loading of  $1.94 \text{ mg cm}^{-2}$  after (a) 1<sup>st</sup>, (b) 250<sup>th</sup>, (c) 500<sup>th</sup>, (d) 750<sup>th</sup> and (e) 1,000<sup>th</sup> cycles. ....129

Figure 6.1 SEM images at different magnifications of (A, B) PPy prepared without Tiron, arrows show agglomerates of particles; and (C, D) Tiron doped PPy. ....134

Figure 6.2 (A) Chemical structure of SAF, (B) Scheme of Tiron doped PPy/MWCNT suspension fabrication and (C) SEM image of Tiron doped PPy/MWCNT composite obtained from a mixed Tiron doped PPy/MWCNT suspension. ....135

Figure 6.3 FTIR for (a) SAF, (b) pristine MWCNT, (c) SAF dispersed MWCNT (d) Tiron doped PPy, (e) SAF dispersed Tiron doped PPy. ....137

Figure 6.4 (A) CV data at a scan rate of  $2 \text{ mV s}^{-1}$ , (B)  $C_m$  and (C)  $C_s$  obtained from the CV data versus scan rate and (D) Nyquist plot of  $Z^*$  (inset shows high frequency

range) for (a) PPy without Tiron with a mass of  $14 \text{ mg cm}^{-2}$ ; (b) Tiron doped PPy with a mass of  $14 \text{ mg cm}^{-2}$ ; (c) Tiron doped PPy with a mass of  $27 \text{ mg cm}^{-2}$ ; (d) Tiron doped PPy/MWCNT composite with a mass of  $27 \text{ mg cm}^{-2}$ . .....139

Figure 6.5 (A,B) Tiron doping of PPy: (A) in the same chain and (B) in different polymer chains, and (C) the charge-discharge mechanism of Tiron doped PPy. ....141

Figure 6.6 (A)  $C_s'$  and (B)  $C_s''$  obtained from the impedance data versus frequency for (a) undoped PPy with a mass of  $14 \text{ mg cm}^{-2}$ ; (b) Tiron doped PPy with a mass of  $14 \text{ mg cm}^{-2}$ ; (c) Tiron doped PPy with a mass of  $27 \text{ mg cm}^{-2}$ ; and (d) Tiron doped PPy/MWCNT composite with a mass of  $27 \text{ mg cm}^{-2}$ . .....142

Figure 6.7 Capacitance retention as a function of cycle number, inset shows corresponding CVs after 1,000 cycles at a scan rate of  $50 \text{ mV s}^{-1}$  for (a) Tiron doped PPy and (b) Tiron doped PPy/MWCNT composite with a mass of  $27 \text{ mg cm}^{-2}$ . .....144

Figure 6.8 SEM images of Tiron doped PPy after 1,000 CV cycles at different magnifications. ....145

Figure 6.9 (A)  $C_s'$  and (B)  $C_s''$  for Tiron doped PPy and (C)  $C_s'$  and (D)  $C_s''$  for Tiron doped PPy/MWCNT composite with a mass of  $27 \text{ mg cm}^{-2}$  after (a) 1<sup>st</sup>, (b) 250<sup>th</sup>, (c) 500<sup>th</sup>, (d) 750<sup>th</sup> and (e) 1,000<sup>th</sup> cycle, insets show low frequency range. ....146

Figure 6.10 Galvanostatic charge-discharge curves of ES fabricated from (A) PPy without Tiron, (B) Tiron doped PPy and (C) Tiron doped PPy/MWCNT composite at

current densities: (a) 0.5, (b) 0.75, (c) 1, (d) 2, (e) 3, (f) 4 and (g) 5 mA cm<sup>-2</sup>. (D) C<sub>c</sub> versus current density obtained from the galvanostatic discharge data and (E) Ragone plot of the ES devices for (a) PPy without Tiron, (b) Tiron doped PPy and (c) Tiron doped PPy/MWCNT composite (inset shows LED powered by a ES module). (F) Capacitance retention as a function of cycle number for Tiron doped PPy/MWCNT composite ES, inset shows the charge/discharge curves at a constant current density of 5 mA cm<sup>-2</sup> for the initial cycles and after 1,000<sup>th</sup> cycle. ....147

Figure 6.11 (A) SEM and (B) TEM images of PPy nano-fiber. ....151

Figure 6.12 (A) Chemical structure of MG, (B) electrophoretic deposition mass for the films, prepared at a deposition voltage of 10 V and deposition time of 5 min versus MG concentration in (a) 1 g L<sup>-1</sup> MWCNT and (b) 1 g L<sup>-1</sup> PPy nano-fiber suspensions. ....152

Figure 6.13 SEM images of the films prepared from suspensions, containing (A,B) 0.2, (C,D) 0.5, (E,F) 0.8 g L<sup>-1</sup> MG and (A), (C), (E) 1 g L<sup>-1</sup> MWCNT or (B), (D), (F) 1 g L<sup>-1</sup> PPy nano-fibers, arrows in Fig. 6.13C and D show co-deposited MG. ....155

Figure 6.14 (A) FTIR and (B) UV-Vis spectra for (a) MG, (b) pristine MWCNT, (c) deposited MWCNT (d) pristine PPy nano-fiber, (e) deposited PPy nano-fiber. ....156

Figure 6.15 (A-D) SEM images of composites obtained from mixed PPy nano-fiber/MWCNT suspension containing (A) 10, (B) 20 and (C) 30 wt.% MWCNT, (D) high

magnification image of composite (A) and (E,F) TEM images of composite (A) at different magnifications. ....159

Figure 6.16 (A,B,C) CVs for different electrodes with mass loading of  $15 \text{ mg cm}^{-2}$ : (A) PPy nano-fiber, (B) PPy nano-fiber/MWCNT (10 wt.%) composite, prepared without dispersant and (C) PPy nano-fiber/MWCNT (10 wt.%) composite dispersed using MG at scan rates of (a) 2, (b) 5, (c) 10, (d) 20, (e) 50 and (f)  $100 \text{ mV s}^{-1}$  and (D) corresponding  $C_s$  and  $C_m$  values obtained from the CV data versus scan rate. (E)  $C_s$  at scan rate of  $2 \text{ mV s}^{-1}$  ( $C_s(2)$ ) and (F)  $C_s$  at scan rate of  $100 \text{ mV s}^{-1}$  ( $C_s(100)$ ) versus mass for different electrodes: (a) PPy nano-fiber, (b) PPy nano-fiber/MWCNT (10 wt.%) composite, prepared without dispersant and (c) PPy nano-fiber/MWCNT (10 wt.%) composite, prepared using MG. ....159

Figure 6.17(A) Nyquist plot of complex impedance  $Z^*=Z'-iZ''$  and (B) high frequency range of  $Z^*$ , (C)  $C_s'$  and (D)  $C_s''$  calculated from the impedance data versus frequency for different electrodes: (a) PPy nano-fiber, (b) PPy nano-fiber/MWCNT composite, prepared without dispersant and (c,d,e) PPy nano-fiber/MWCNT composite, prepared using MG dispersant and containing (c) 10, (d) 20 and (e) 30 wt.% MWCNT. All electrodes have mass loading of  $15 \text{ mg cm}^{-2}$ . ....162

Figure 6.18 (A) CVs at a scan rate of  $2 \text{ mV s}^{-1}$ , (B)  $C_s$  and  $C_m$  obtained from the CV data versus scan rate, (C)  $C_s'$  and (D)  $C_s''$  calculated from impedance data versus

frequency for PPy nano-fiber/MWCNT (10 wt.%) composite electrodes, prepared using MG, with mass loading of (a) 20, (b) 25 and (c) 30 mg cm<sup>-2</sup>. .....164

Figure 6.19 (A) Capacitance retention versus cycle number N (inset shows CVs at a scan rate of 50 mV s<sup>-1</sup>), (B) Nyquist plots of complex impedance, (C) C<sub>s</sub>' and (D) C<sub>s</sub>" (insets show low frequency range) calculated from impedance data versus frequency for PPy nano-fiber/MWCNT (10 wt.%) composite electrodes, prepared using MG, with a mass loading of 27 mg cm<sup>-2</sup> after (a) 1<sup>st</sup>, (b) 250<sup>th</sup>, (c) 500<sup>th</sup>, (d) 750<sup>th</sup> and (e) 1,000<sup>th</sup> cycles. ....166

Figure 6.20 (A) Chemical structure of SAF, and (B) SAF (C) MWCNT, (D) MWCNT and SAF, (E) graphene, (F) graphene and SAF, (G) graphene, MWCNT and SAF, (H) PPy nano-fiber, (I) PPy nano-fiber and SAF, (J) graphene, PPy nano-fiber and SAF in water. Suspensions D, F, G, I and J were stable for more than two months. ....170

Figure 6.21 Deposit mass for (A,B) 1g L<sup>-1</sup> MWCNT, (C,D) 1g L<sup>-1</sup> graphene, (E,F) 1g L<sup>-1</sup> PPy nano-fiber suspensions versus (A,C,E) SAF concentration in the suspensions at a deposition time of 5 min and versus (B,D,F) deposition time at SAF concentration of 0.5 g L<sup>-1</sup>. ....171

Figure 6.22 (A) FTIR and (B) UV-Vis spectra for (a) SAF, (b) pristine MWCNT, (c) deposited MWCNT, (d) pristine graphene, (e) deposited graphene. ....172

Figure 6.23 (A) FTIR and (B) UV-Vis spectra for (a) as-prepared and (b) deposited PPy nano-fiber. ....174

Figure 6.24 SEM images of (A) MWCNT, (B) graphene and (C) PPy films prepared by EPD. ....175

Figure 6.25 SEM images of (A,B) surfaces and (C,D) cross sections (fractures) of composite (A,C) graphene/MWCNT and (B,D) graphene/PPy nano-fiber films. Arrows in (C,D) show graphene. ....176

Figure 6.26 (A) CVs at a scan rate of  $10 \text{ mV s}^{-1}$ , (B) capacitance calculated from CV data versus scan rate, (C) EIS data presented in a Nyquist plot and (D) capacitance calculated from EIS data versus frequency for  $0.15 \text{ mg cm}^{-2}$  films of MWCNT, graphene and graphene/MWCNT composite. ....177

Figure. 6.27 (A) CVs at a scan rate of  $10 \text{ mV s}^{-1}$ , (B) capacitance calculated from CV data versus scan rate, (C) EIS data presented in a Nyquist plot and (D) capacitance calculated from EIS data versus frequency for  $0.15 \text{ mg cm}^{-2}$  films of PPy nano-fiber and graphene/PPy nano-fiber composite. ....179

Figure 6.28 Chemical structure of (A)  $(\text{CTA})_2\text{S}_2\text{O}_8$  and (B) Ponceau S. ....182

Figure 6.29 (A, B) HRTEM of  $(\text{CTA})_2\text{S}_2\text{O}_8$  nano-crystals formed by mixing CTAB and  $(\text{NH}_4)_2\text{S}_2\text{O}_8$  solutions and (C) Low-angle XRD pattern of  $(\text{CTA})_2\text{S}_2\text{O}_8$ . ....182

Figure 6.30 SEM images of PPy powders, prepared from 0.05 mol L<sup>-1</sup> Py solutions, using (A,B) 0.06 mol L<sup>-1</sup> (NH<sub>4</sub>)<sub>2</sub>S<sub>2</sub>O<sub>8</sub> or (C,D) 0.06 mol L<sup>-1</sup> (CTA)<sub>2</sub>S<sub>2</sub>O<sub>8</sub> oxidants; (A,C) without PS and (B,D) with 0.015 mol L<sup>-1</sup> PS. ....184

Figure 6.31 (A) CVs at 2 mV s<sup>-1</sup>, (B) C<sub>s</sub> and C<sub>m</sub> versus scan rate, (C) C<sub>s</sub>' and (D) C<sub>s</sub>" versus frequency for 20 mg cm<sup>-2</sup> PPy electrodes; (a),(b),(c),(d) present data for powders, shown in (A), (B), (C), (D) of Fig. 6.30, respectively. ....186

Figure 6.32. (A,B) Deposit mass for 1 g L<sup>-1</sup> MWCNT suspension versus (A) (CTA)<sub>2</sub>S<sub>2</sub>O<sub>8</sub> concentration at a deposition time of 5 min (inset shows a MWCNT film on stainless steel) and (B) deposition time at (CTA)<sub>2</sub>S<sub>2</sub>O<sub>8</sub> concentration of 0.5 g L<sup>-1</sup>; (C) deposition current versus deposition time for (a) 1 g L<sup>-1</sup> MWCNT, (b) 0.5 g L<sup>-1</sup> (CTA)<sub>2</sub>S<sub>2</sub>O<sub>8</sub>, (c) 1 g L<sup>-1</sup> (CTA)<sub>2</sub>S<sub>2</sub>O<sub>8</sub>, (d) 1 g L<sup>-1</sup> MWCNT and 0.5 g L<sup>-1</sup> (CTA)<sub>2</sub>S<sub>2</sub>O<sub>8</sub> and (e) 1 g L<sup>-1</sup> MWCNT and 1 g L<sup>-1</sup> (CTA)<sub>2</sub>S<sub>2</sub>O<sub>8</sub> suspensions; (D) SEM image of the MWCNT film obtained by cathodic EPD. ....188

Figure 6.33 Sedimentation tests for aqueous suspensions of (A) 1 g L<sup>-1</sup> PPy nano-fibers, prepared using (CTA)<sub>2</sub>S<sub>2</sub>O<sub>8</sub>, (B) 1 g L<sup>-1</sup> PPy, prepared using PS and (CTA)<sub>2</sub>S<sub>2</sub>O<sub>8</sub>, (C) 1 g L<sup>-1</sup> PPy-MWCNT composite, prepared using PS and (NH<sub>4</sub>)<sub>2</sub>S<sub>2</sub>O<sub>8</sub> and (D) 1 g L<sup>-1</sup> PPy coated MWCNT, prepared using PS and (CTA)<sub>2</sub>S<sub>2</sub>O<sub>8</sub>, mass ratio MWCNT:Py 3:7. ....191

Figure 6.34. SEM images of PPy-MWCNT powders prepared using (A)  $(\text{CTA})_2\text{S}_2\text{O}_8$  (arrows show PPy nano-fibers), (B) PS and  $(\text{NH}_4)_2\text{S}_2\text{O}_8$ , (C,D) PS and  $(\text{CTA})_2\text{S}_2\text{O}_8$  at different magnifications, mass ratio MWCNT:Py =3:7. ....192

Figure. 6.35 TEM images of PPy-MWCNT powders prepared using (A)  $(\text{CTA})_2\text{S}_2\text{O}_8$  (arrows show PPy fibers), (B) PS and  $(\text{NH}_4)_2\text{S}_2\text{O}_8$ , (C,D) PS and  $(\text{CTA})_2\text{S}_2\text{O}_8$  at different magnifications, arrow in (D) inset shows HRTEM image of PPy-MWCNT interface; (E) set of resolved EELS spectra measured along a line across PPy coated MWCNT (F) Element distribution obtained from the EELS data, inset shows HAADF image of a region for analysis, concentrations of Py, PS,  $(\text{NH}_4)_2\text{S}_2\text{O}_8$  and  $(\text{CTA})_2\text{S}_2\text{O}_8$  were the same as in Fig. 6.30, mass ratio MWCNT:Py =3:7. ....194

Figure 6.36. TEM images of PPy coated MWCNT, prepared from  $0.05 \text{ mol L}^{-1}$  Py solutions, using  $0.06 \text{ mol L}^{-1}$   $(\text{CTA})_2\text{S}_2\text{O}_8$  and  $0.015 \text{ mol L}^{-1}$  PS, mass ratio MWCNT:Py (A) 1:9, (B) 2:8, (C) 3:7. ....195

Figure 6.37 (A,B,C) CVs at scan rates of (a)2, (b)10, (c)50, (d)100 and (e)200  $\text{mV s}^{-1}$ , (D)  $C_s$  and  $C_m$  versus scan rate (E)  $C_s'$  and (F)  $C_s''$  versus AC frequency, (A,B,C) in Fig. 6.37 and (a),(b),(c) in Fig. 6.37(D-F) present data for powders shown in A,B,C of Fig. 6.35, respectively, for electrode mass of  $20 \text{ mg cm}^{-2}$ . ....197

Figure 6.38  $C_s$  versus electrode mass obtained at scan rates of (A) 2 and (B) 100  $\text{mV s}^{-1}$ , (a),(b),(c) present data for powders, shown in (A), (B), (C) of Fig. 6.35, respectively. ....198

Figure 6.39 (A) Capacitance retention versus cycle number, inset shows corresponding CVs at  $50 \text{ mV s}^{-1}$ , (B) Nyquist plot of complex impedance, inset shows high frequency range, (C)  $C_s'$  and (D)  $C_s''$  versus frequency, insets in (C,D) show low frequency range, after (a)1<sup>st</sup>, (b)250<sup>th</sup>, (c) 500<sup>th</sup>, (d)750<sup>th</sup>, (e)1000<sup>th</sup> cycles, prepared from powder shown in Fig. 6.35C. ....199

Figure 7.1 (A,B) TEM and (C) HRTEM images for (A) PPy-MWCNT and (B,C) N-AC-MWCNT. ....213

Figure 7.2. (A) Nitrogen adsorption-desorption isotherms at  $-196 \text{ }^\circ\text{C}$  and (B) corresponding pore-size distributions calculated with the Barrett-Joyner-Halenda (BJH) method for (a) pristine MWCNT, (b) N-C-MWCNT and (c) N-AC-MWCNT. ....214

Figure 7.3 (A) Survey XPS spectra for (a) pristine MWCNT and (b) N-AC-MWCNT, (B) High-resolution XPS spectra for N1s of N-AC-MWCNT, showing contributions of nitrogen containing functional groups: N5 (pyrrole), N6 (pyridine) and N-Q (quaternary). ....217

Figure 7.4 Raman spectrum of (a) pristine MWCNT and (b) N-AC-MWCNT. ....218

Figure 7.5 (A) CVs at a scan rate of  $5 \text{ mV s}^{-1}$  for (a) pristine MWCNT, (b) N-C-MWCNT and (c) N-AC-MWCNT. (B) CVs for N-AC-MWCNT in voltage windows of (a)  $-1 - 0 \text{ V}$ , (b)  $-0.5 - +0.4 \text{ V}$ , (c)  $-0.1 - +0.8 \text{ V}$  and (d)  $-1 - +0.8$  at a scan rate of  $5 \text{ mV s}^{-1}$ . (C) CVs for N-AC-MWCNT at scan rates of (a) 2, (b) 10, (c) 20, (d)

50, (e) 100, (f) 200  $\text{mV s}^{-1}$ . (D)  $C_m$  and  $C_s$  versus scan rate for (a) pristine MWCNT, (b) N-C-MWCNT and (c) N-AC-MWCNT. All electrodes have mass loading of 15  $\text{mg cm}^{-2}$ . .....219

Figure 7.6 (A) Nyquist plot of complex impedance, inset shows high frequency range, (B)  $C_s'$  and  $C_m'$  and (C)  $C_s''$  and  $C_m''$  calculated from the impedance data versus frequency for (a) pristine MWCNT, (b) N-C-MWCNT and c) N-AC-MWCNT. All electrodes have mass loading of 15  $\text{mg cm}^{-2}$ . .....220

Figure 7.7 (A) Capacitance retention versus cycle number, inset shows corresponding CVs at 100  $\text{mV s}^{-1}$ , (B) Nyquist plot of complex impedance, inset shows high frequency range, (C)  $C_s'$  and  $C_m'$  and (D)  $C_s''$  and  $C_m''$  versus frequency after (a)1<sup>st</sup>, (b)250<sup>th</sup>, (c) 500<sup>th</sup>, (d)750<sup>th</sup>, (e)1000<sup>th</sup> cycles for 20  $\text{mg cm}^{-2}$  electrodes, prepared from N-AC-MWCNT. ....222

Figure 7.8 Capacitive behavior for a symmetric ES cell, containing two N-AC-MWCNT electrodes: (A) CVs at scan rate of 5  $\text{mV s}^{-1}$  for different potential windows, (B) charge-discharge curves at a current of 4  $\text{mA cm}^{-2}$  for different potential windows, C)  $C_{cm}$  calculated from charge-discharge curves and Coulombic efficiency versus width of the potential window. The mass loading of individual electrodes is 15  $\text{mg cm}^{-2}$ . .....223

Figure 7.9 Capacitive behaviour of a symmetric ES cell, containing two N-AC-MWCNT electrodes: (A) CVs at scan rates of (a) 2, (b) 5, (c) 10, (d) 20, (e) 50

and (f)  $100 \text{ mV s}^{-1}$ . (B)  $C_{\text{cm}}$  and  $C_{\text{cs}}$  calculated from CVs versus scan rate. (C) charge-discharge curves at currents of (a) 0.5, (b) 0.75, (c) 1, (d) 2, (e) 4, (f) 6 and (g)  $10 \text{ mA cm}^{-2}$ . (D)  $C_{\text{cm}}$  and  $C_{\text{cs}}$  calculated from the charge-discharge curves versus current. The mass loading of individual electrodes is  $15 \text{ mg cm}^{-2}$ . .....223

Figure 7.10 (A) Ragone plot for a coin cell, containing two activated carbon coated MWCNT electrodes, insets show the coin cells and the light emitting diodes powered by coin cells. (B) Capacitance retention of a coin cell versus cycle number, inset shows the initial and final charge-discharge curves in the cycle performance test. ...225

Figure 7.11 Fabrication of (A)  $\text{MnO}_2$  coated N-AC-MWCNT: dispersion of CNT, fabrication of PPy coating, formation of N-AC coated CNT and synthesis of  $\text{MnO}_2$  coating and (B) coin-cell ES, containing  $\text{MnO}_2$  coated N-AC-MWCNT positive electrode and N-AC-MWCNT negative electrode. ....228

Figure 7.12 (A) SEM, (B) TEM and (C) HRTEM images of N-AC-MWCNT. Arrows in C show thickness of N-AC layer on MWCNT. ....229

Figure 7.13 Electron microscopy images for  $\text{MnO}_2$  coated N-AC-MWCNT, prepared using (A,B,C) solution 1, (D,E,F) solution 2 and (G,H,I) solution 3 (experiments were described in section 4.2.3.2); (A, D, G) SEM and (B, C, E, F, H, I) TEM images at different magnifications. ....330

Figure 7.14 (a) TGA and (b) DTA data of MnO<sub>2</sub> coated N-AC-MWCNT, prepared using solution 2. ....231

Figure 7.15 (A) CVs at a scan rate of 2 mV s<sup>-1</sup> for (a) pristine MWCNT, (b) N-AC-MWCNT and (c) MnO<sub>2</sub> coated N-AC-MWCNT, prepared using solution 1; (B) CVs at 2 mV s<sup>-1</sup> for MnO<sub>2</sub> coated N-AC-MWCNT, prepared using (a) solution 1, (b) solution 2 and (c) solution 3; (C) CVs for MnO<sub>2</sub> coated N-AC-MWCNT, prepared from solution 1 at scan rates of (a) 5, (b) 10, (c) 20, (d) 50 and (e) 100 mV s<sup>-1</sup>; (D) C<sub>m</sub> and C<sub>s</sub> versus scan rate for (a) pristine MWCNT, (b) N-AC-MWCNT and (c-e) MnO<sub>2</sub> coated N-AC-MWCNT, prepared using (c) solution 1, (d) solution 2 and (e) solution 3. All electrodes have mass loading of 20 mg cm<sup>-2</sup>. ....232

Figure 7.16 (A,B) Nyquist plot of complex impedance, (B) shows high frequency range for (A), inset in (A) shows equivalent circuit, (C) C<sub>s</sub>' and C<sub>m</sub>' and (D) C<sub>s</sub>" and C<sub>m</sub>", calculated from the impedance data, versus frequency for (a) pristine MWCNT, (b) N-AC-MWCNT and (c-e) MnO<sub>2</sub> coated N-AC-MWCNT, prepared using (c) solution 1, (d) solution 2 and (e) solution 3. All electrodes have mass loading of 20 mg cm<sup>-2</sup>. ....235

Figure 7.17 (A) Capacitance retention versus cycle number, inset shows corresponding CVs at 50 mV s<sup>-1</sup>, (B) Nyquist plot of complex impedance, inset shows high frequency range, (C) C<sub>s</sub>' and C<sub>m</sub>' and (D) C<sub>s</sub>" and C<sub>m</sub>" versus frequency after (a)1<sup>st</sup>, (b)250<sup>th</sup>, (c) 500<sup>th</sup>, (d)750<sup>th</sup>, (e)1000<sup>th</sup> cycles for MnO<sub>2</sub> coated

N-AC-MWCNT electrodes with mass loading of  $20 \text{ mg cm}^{-2}$ , prepared using solution 2. ....238

Figure 7.18. (A) CVs at a scan rate of  $5 \text{ mV s}^{-1}$  for (a) N-AC-MWCNT electrode and (b)  $\text{MnO}_2$  coated N-AC-MWCNT electrode, prepared using solution 2. (B) CVs for asymmetric cell in different potential windows at a scan rate of  $5 \text{ mV s}^{-1}$ . (C) CVs for asymmetric cell at scan rates of (a) 2, (b) 10, (c) 20, (d) 50, (e) 100 and (f)  $200 \text{ mV s}^{-1}$ . (D)  $C_{\text{cm}}$  and  $C_{\text{cs}}$  calculated from CVs for asymmetric cell versus scan rate in a voltage window of 1.9 V. ....239

Figure 7.19. (A) Charge-discharge curves in a voltage window of 1.9 V for coin cells at currents of (a) 2, (b) 4, (c) 8, (d) 10, (e) 15 and (f)  $20 \text{ mA cm}^{-2}$ . (B)  $C_{\text{cm}}$  and  $C_{\text{cs}}$  calculated from the discharge curves versus current. (C) Ragone plot for a coin cell, insets show the fabricated coin cells and 20 mA LED bulbs, powered by the coin cells. (D) Capacitance retention of a coin cell versus cycle number, inset shows the initial and final charge-discharge curves in the cycling performance test. ....241

Figure. 8.1 (A) Aqueous solutions of (a) Safranin (SAF), (b) Calcon (CAL), (c) Amaranth (AMA) and chemical structures of (B) SAF, (C) CAL and (D) AMA. ...251

Figure 8.2 (A,B) CVs at a scan rate of  $0.5 \text{ mV s}^{-1}$  for N-AC-MWCNT electrodes in the dye solutions of (A) SAF and (B) CAL with concentrations of (a) 100, (b) 200 and (c)  $400 \text{ mg L}^{-1}$ , (C) specific capacitances, calculated from the CV data, (D) Nyquist plot of

complex impedance  $Z^*=Z'-Z''$  for different solutions: (a) 100, (b) 200 and (c) 400 mg L<sup>-1</sup> SAF and (d) 100, (e) 200 and (f) 400 mg L<sup>-1</sup> CAL. ....252

Figure 8.3. QCM data for N-AC-MWCNT coated resonators in 50 mg L<sup>-1</sup> solutions of (A, B) SAF and (C, D) CAL, tested using (A) negative and (C) positive pulses with a constant voltage of 1 V or by applying a series of (B) negative or (D) positive pulses of increasing amplitude in the range of 0.6-1.4 V. ....253

Figure 8.4 Charge and discharge mechanism of symmetric ES fabricated using (A) SAF and (B) CAL dye electrolyte. ....257

Figure 8.5 Capacitive behavior in different voltage windows (from 0.5 to 1.3 V) for ES cells, containing two N-AC-MWCNT electrodes in 400 mg L<sup>-1</sup> (A, B, C) SAF and (D, E, F) CAL solutions as electrolytes. (A, D) CVs at a scan rate of 2 mV s<sup>-1</sup>, (B, E) charge-discharge behavior at a current density of 3 mA cm<sup>-2</sup>, (C, F) C<sub>cm</sub> calculated from discharge curves and Columbic efficiency versus the width of the voltage window. The mass loadings of individual electrodes was 15 mg cm<sup>-2</sup>. ....258

Figure 8.6 CVs in a voltage window of 0.9 V for ES cells prepared using 400 mg L<sup>-1</sup> (A) SAF and (B) CAL electrolytes at scan rates of (a) 0.5, (b) 1, (c) 2, (d) 5, (e) 10 and (f) 20 mV s<sup>-1</sup>. (C) C<sub>cm</sub> and C<sub>cs</sub> calculated from CVs versus scan rate for (a) SAF and (b) CAL electrolytes. The mass loadings of individual electrodes of ES cells is 15 mg cm<sup>-2</sup>. ...259

Figure 8.7 (A,B) Charge-discharge behavior of ES cells in (A) SAF and (B) CAL electrolytes at current densities of (a) 2, (b) 3, (c) 4, (d) 6 and (e) 8 mA cm<sup>-2</sup>; (C) C<sub>cm</sub>

and  $C_{cs}$  calculated from the discharge data versus current density and (D) Ragone plot for ES cells (insets) containing  $400 \text{ mg L}^{-1}$  (a) SAF and (b) CAL solutions as electrolytes. The N-AC-MWCNT mass loadings of individual electrodes of ES cells is  $15 \text{ mg cm}^{-2}$ . .....260

Figure 8.8 (A) CVs at scan rates of (a) 0.5 , (b) 1, (c) 2, (d) 5, (e) 10 and (f)  $20 \text{ mV s}^{-1}$  and (B) charge-discharge curves at current densities of (a) 2 , (b) 3, (c) 4, (d) 6 and (e)  $8 \text{ mA cm}^{-2}$  in a voltage window of 0.9V, (C)  $C_{cm}$  and  $C_{cs}$ , calculated from the CV data versus scan rate, (D)  $C_{cm}$  and  $C_{cs}$ , calculated from the discharge data versus current density, (E) Coulombic efficiency and capacitance, calculated from the discharge data versus the width of the voltage window and (F) Ragone plot for ES cells, containing two N-AC-MWCNT electrodes in  $400 \text{ mg L}^{-1}$  AMA electrolyte. ....261

Figure 8.9 Capacitance retention of ES cells, containing two N-AC-MWCNT electrodes in  $400 \text{ mg L}^{-1}$  AMA electrolyte, versus cycle number, inset shows the initial and final charge-discharge curves in the cycling performance test. ....263

Figure 8.10 Chemical structures of (A) Pyrocatechol Violet (PV), (B) Eriochrome Cyanine R (ECR), (C) Chromotropic Acid Disodium Salt (CHR), (D) 2-(phenylazo) Chromotropic Acid Disodium Salt (CHRP), (E) 2-(1-naphthyldiazenyl)chromotropic acid disodium salt (CHRN) and (F) 7-Bis(2-sulfophenylazo)chromotropic acid tetrasodium salt (CHRB). ....267

Figure 8.11 TEM images of (A) PPy-NF and (B) N-AC-NF. ....269

Figure 8.12. (A) Nitrogen adsorption-desorption isotherms at  $-196\text{ }^{\circ}\text{C}$  and (B) corresponding pore-size distributions calculated with the Barrett-Joyner-Halenda (BJH) method for (a) PPy-NF and (b) N-AC-NF. ....270

Figure 8.13 Capacitive behavior of cells, containing  $500\text{ mg L}^{-1}$  (A-C) ECR and (D-F) CHR electrolytes, (A,D) CVs at scan rate of  $2\text{ mV s}^{-1}$ , (B,E)  $C_m$  calculated from CV data (C,F) constant current charge-discharge data at current densities of (C) 1 and (F)  $2\text{ mA cm}^{-2}$ . ....272

Figure 8.14 (A) Scheme of QCM analysis system for capacitive dye removal, (B,C) mass gain measured by QCM versus time for N-AC-NF coated electrodes in  $0.3\text{ mL}$  of  $50\text{ mg L}^{-1}$  solutions of (B) ECR at applied voltage of  $0.6\text{ V}$  and (C) CHR at applied voltage of  $0.9\text{ V}$ . Arrows show the starting points for applying voltage. ....273

Figure 8.15 (A,B) CVs at scan rates of (a)  $0.5$ , (b)  $1$ , (c)  $2$ , (d)  $5$  and (e)  $10\text{ mV s}^{-1}$  and (C,D) charge-discharge data at current densities of (a)  $0.75$ , (b)  $1$ , (c)  $1.5$ , (d)  $2$  and (e)  $3\text{ mA cm}^{-2}$  for cells containing  $500\text{ mg L}^{-1}$  (A,C) PV and (B,D) ECR electrolytes, (E) capacitance calculated from CVs versus scan rate and (F) capacitance calculated from discharge data versus current density . ....274

Figure 8.16 Capacitive behavior of cells, containing (a)  $100$ , (b)  $300$ , (c)  $500$  and (d)  $700\text{ mg L}^{-1}$  ECR electrolyte: (A) CVs at a scan rate of  $2\text{ mV s}^{-1}$ , (B) Nyquist plots of complex impedance, (C)  $C_s'$  calculated from impedance data, (D) charge-discharge curves at a current density of  $1.5\text{ mA cm}^{-2}$  and (E) Ragone plots. (F) Capacitance

retention and Coulombic efficiency of cells containing 500 mg L<sup>-1</sup> ECR versus cycle number. ....276

Figure 8.17 (A-D) CVs for cells prepared using 500 mg L<sup>-1</sup> (A) CHR, (B) CHRP, (C) CHRN and (D) CHRB electrolytes at scan rates of (a) 0.5, (b) 1, (c) 2, (d) 5 and (e) 10 mV s<sup>-1</sup>, (E) capacitance calculated from CVs versus scan rate and (F) Nyquist plots of complex impedance. ....277

Figure 8.18 (A-D) Charge-discharge curves for cells containing 500 mg L<sup>-1</sup> (A) CHR, (B) CHRP, (C) CHRN and (D) CHRB electrolytes at current densities of (a) 0.75, (b) 1, (c) 1.5, (d) 2 and (e) 3 mA cm<sup>-2</sup>, (E) capacitance calculated from the discharge data versus current density and (F) capacitance retention and Coulombic efficiency for cells containing 500 mg L<sup>-1</sup> CHR versus cycle number. ....279

Figure 8.19 Ragone plots for cells, containing different dyes as electrolytes with concentrations of 500 mg L<sup>-1</sup>. ....281

## List of Tables

|  |     |
|--|-----|
| Table 2.1 Comparison of EDLCs and pseudocapacitor. ....  | 17  |
| Table 1.2 Different carbon structures used in EDLCs with onion-like carbon, carbon nanotubes, graphene, activated carbons, carbide-derived carbons and templated carbons. ....   | 24  |
| Table 2.3 Specific capacitance, conductivity and doping type of conductive polymer. ....   | 29  |
| Table 2.4 Summary of the different types of hybrid ES. ....  | 37  |
| Table 4.1 Chemicals used for materials synthesis and device fabrication. ....  | 88  |
| Table 7.1 BET surface area, total porosity volume ( $V_{\text{total}}$ ), microporosity (diameter<2nm) volume ( $V_{\text{micro}}$ ), average pore diameter and density of activated carbon coated carbon nanotube. .... | 215 |
| Table 8.1 Capacitive adsorption of SAF and CAL dye solution, measured from Figure 8.3, in the voltage range of 0.6-1.4 V. ....   | 256 |
| Table 8.2 3D Chemical structure and physical-chemical properties of CHR family dyes. ....  | 268 |

## **1. Introduction**

In the context of the depletion of fossil fuels and increasing environment pollution, there is an urgent need to develop clean, efficient and renewable energy sources, as well as the new methods to store and convert energy. Although various renewable energy sources, like solar and wind energy, have an increasing energy production in recent years, sun does not shine all days and nights, and wind does not flow on our demands. Electrochemical energy production and storage has attracted more and more attention. Batteries, fuel cells and electrochemical supercapacitors are in the front line of electrochemical energy storage systems.

Electrochemical supercapacitors (ES), also called supercapacitors or ultracapacitors, have been investigated as advanced energy storage devices for decades. The energy storage in ES arises from an electrochemical double-layer or reversible redox reaction at the electrode/electrolyte interface. ES could achieve high power density with combination of porous electrodes and active electrolyte. Compared to batteries, the electrode of ES remains relatively unchanged during charge/discharge cycles, which gives ES excellent cycle stability. The capacitive performance of an ES device is determined by the electrode, electrolyte and cell configuration.

ESs could be classified into two types based on their storage mechanism, the electrochemical double-layer capacitors (EDLCs) and pseudocapacitors. EDLCs

physically store charges through reversible ion adsorption at the electrode–electrolyte interface, while pseudocapacitors chemically store their charges through redox reaction at the vicinity of a few nanometers from the surface. The electrodes for EDLCs are generally made of carbon-based materials, while that for pseudocapacitors are transition metal oxides and conductive polymers. ES could be built using conventional liquid as electrolytes, such as aqueous electrolyte, organic electrolyte and ionic liquid. However, the use of liquid electrolyte has a drawback for fabrication flexible electronic devices. Solid-state electrolytes were developed to avoid sealing and housing of liquid electrolyte in ES device.

Among many efforts of building efficient ES, development of advanced electrodes using nano-structured composite materials has offered major improvements in performance. Since carbon materials have advantages of high surface area as well as conductivity and pseudocapacitive materials offer high specific capacitance, it is expected to achieve improved capacitive performance with the combination of double layer capacitive and pseudocapacitive materials. Specific capacitance of the electrode is increased with the surface area of the active materials. Nanostructuring of capacitive materials is a feasible method to considerably increase the surface area of the electrodes. Different morphologies such as nano-particles, nano-fibers and core-shell nano-composites, could be obtained from the synthesis. However, nano-structured materials are prone to agglomerate during the materials fabrication process. In order to maximize the benefits of the individual components, rational

design and controllable assembly of the composite materials have undergone extensive study [1].

For practical applications of ESs, it is important to develop efficient electrodes with high active mass loading and high active material to current collector mass ratio. However, the increase in material loading usually results in increased resistance, limited electrolyte access to the bulk of active materials. As a result, the specific capacitance and capacitance retention significantly decrease with increasing mass loading of the electrode, especially at high charge-discharge rates[2]. In comparison with a dense capacitive film, impregnation of capacitive nano-materials into a porous current collector offers the advantage of improved electrolyte access to the electrode material, which enhanced the capacitive performance of the ES.

Lastly, the increasing human population combined with exploitation of water resources has resulted in a shortage of fresh water supply in many regions of the world [3]. A growing number of contaminants including organic dyes, heavy metal ions and light metal salts, etc. are entering water supplies due to human activity. A new wave of interest in the development of capacitive technology is related to the application of ES devices for water purifications study, namely, capacitive deionization (CDI). CDI is regarded as a sustainable and economic desalination technology[3], which involves the use of electric double-layer capacitors. The progress in the CDI generates interest of application of ES devices for capacitive dye

removal (CDR). However, the performance of CDR is largely dependent on the structure of organic dyes and the properties of electrode materials, such as specific capacitance, pore structure, pore volume and electrical conductivity. New methods of CDR for different organic dyes will benefit from sustainable management of energy and environment.

### **References**

- [1] G. Wang, L. Zhang, J. Zhang, A review of electrode materials for electrochemical supercapacitors, *Chemical Society Reviews*, 41(2012) 797-828.
- [2] Y. Gogots. Patrice Simon, Materials for electrochemical capacitors, *Nature Materials*, 7(2008) 845-854.
- [3] M.A. Anderson, A.L. Cudero, J. Palma, Capacitive deionization as an electrochemical means of saving energy and delivering clean water. Comparison to present desalination practices: Will it compete? *Electrochimica Acta*, 55(2010) 3845-3856.

## **2. Literature review**

### **2.1 The development of capacitors and electrochemical supercapacitors (ESs)**

The storage of an electrical charge on a surface was discovered in ancient Greece from the phenomena of rubbing amber with fur which attracts dust. Capacitor technology was started by the invention of the Leiden jar in 1754. Benjamin Franklin improved the design of the Leyden jar to a flat capacitor, resulted in reducing the volume of the capacitor and increased its convenience and reliability. In the late 19<sup>th</sup> century, Faraday's laws was applied for solving the electrical charge in the capacitor by Helmholtz. He envisaged two parallel sheets of charges of opposite sign located on the surface of the metal and the solution side. The model of ion distribution near the metal surface was proposed. It paved way for the development of fundamental aspects in capacitive technology and a quantitative science of describing the nature of electrostatic behaviour.

The proposal of electrostatic attraction for energy storage in capacitor was demonstrated and patented by H.I. Becker from General Electric in 1957 (U.S. Patent 2,800,616). The developed capacitor is based on utilization of two porous carbon electrodes and aqueous electrolyte, which lately known as electrochemical double-layer capacitors (EDLCs). In 1966, Standard Oil of Ohio's (SOHIO) researchers developed the modern versions of electrochemical supercapacitor (ES) by

utilizing the double-layer capacitance of high area carbon, but in a non-aqueous electrolyte. The advantage of the SOHIO's non-aqueous electrolyte is larger voltage window, which allows to improve the charge storage capacity of ES. Today several companies such as Maxwell Technologies, NEC/TOKIN, ELNA, Panasonic, and several others invest in electrochemical capacitor development. The market for ES was estimated to about 100 million US dollars in 2004, while in 2010 the worldwide sales of ES reached 400 million US dollars and continues to grow in the recently years.

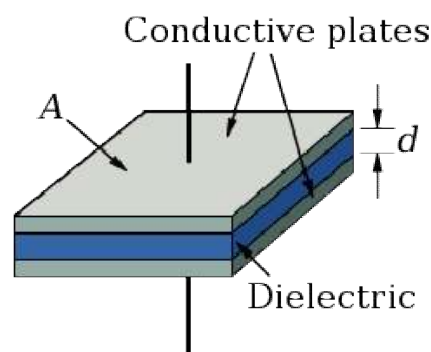


Figure 2.1 Schematic illustration of the electrostatic capacitor with a plate area of  $A$ , distance between two plates of  $d$ .

The capacitive performance of ES is determined by the properties of the electrode material and electrolyte. The development of advanced electrode materials for capacitive technologies requires understanding of the physical theory of the operation of electrostatic capacitor. An electrostatic capacitor stores energy in the form of electrical charge. A typical device consists of two parallel conductive metallic plates,

called electrodes. The dielectric is an insulator inserted between two electrodes as shown in Figure 2.1. When a voltage is applied to the electrostatic capacitor, the electric charge is stored in a static electric field that permeates the dielectric between the electrodes. The total energy increases with the amount of stored charge, which in turn correlates linearly with the voltage between the plates. The maximum potential difference between the plates is limited by the dielectric's breakdown field strength. The increase of dielectric strength improves the operating voltage window of a capacitor and hence more charges can be stored in two metal plates.

An ideal electrostatic capacitor is characterized by a constant capacitance  $C$ . It is the capability of charge storage which defined in relation of the amount of accumulated charge ( $Q$ ) and the strength of applied potential ( $V$ ).

$$C = \frac{Q}{V} \quad (2.1)$$

The capacitance of a parallel-plate electrostatic capacitor with a vacuum in the region between the plates could be estimated from the relationship

$$C = \epsilon \frac{A}{d} \quad (2.2)$$

where  $A$  represents the area of the plates and  $d$  is the distance between them. The parameter  $\epsilon$  called the permittivity of a vacuum, with a constant value of  $8.85 \times 10^{-12}$  F/m. The capacitance estimation for the double-layer at the interface of ES is generally assumed to follow that of a parallel-plate electrostatic capacitor.

Capacitors have two main applications; namely, block of the flow of direct current (DC) and provide energy storage. Performance of energy storage in a capacitor is characterized by their energy and power. The energy could be calculated with the combination of eq. 2.1.

$$W = \int_0^Q Vdq = \int_0^Q \frac{q}{C} dq = \frac{1}{2} \frac{Q^2}{C} = \frac{1}{2} UQ = \frac{1}{2} CU^2 \quad (2.3)$$

C is the specific capacitance and U is the operating potential. The maximum power is determined by the equation

$$P = \frac{W}{t} = \frac{1}{2} UI = \frac{1}{4} \frac{U^2}{R}. \quad (2.4)$$

Here, R is the series resistance. The obtained energy and power values are usually normalized by the weight or volume of the electrode or device.

## 2.2 Comparison of energy and power of ESs, batteries and fuel cells

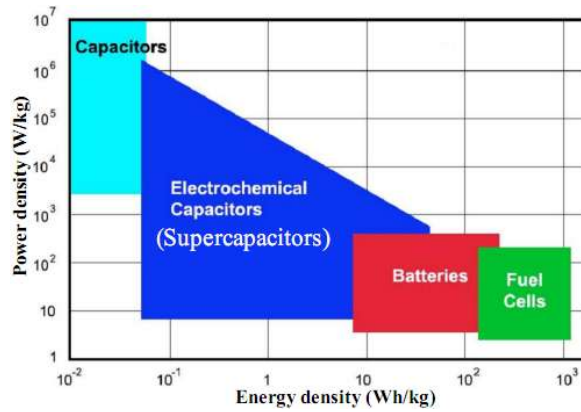


Figure 2.2 Power density versus energy density, also called the Ragone plot, for various electrochemical energy storage systems compared to combustion engine, gas turbines and electrostatic capacitors[1, 2].

Energy and power densities are two main parameters of an energy storage system. Specific energy, expressed in watt-hours per kilogram ( $\text{Wh kg}^{-1}$ ), determines how much energy could be stored in the system. Specific power in watt per kilogram ( $\text{W kg}^{-1}$ ) indicates how fast the stored energy could be converted. To compare the energy and power of the electrochemical energy storage system, a representation known as a Ragone plot has been developed as shown in Figure 2.2. It indicates that the specific energy usually decreases with increase of the specific power. Conventional capacitors are considered to be high-power systems; whereas fuel cells, owing a comparable energy density with the combustion engine, are considered as high-energy systems. Compared with the conventional capacitors, ES has the ability to store greater amounts of energy due to high surface area. Additionally, ES is able to deliver more power than batteries.

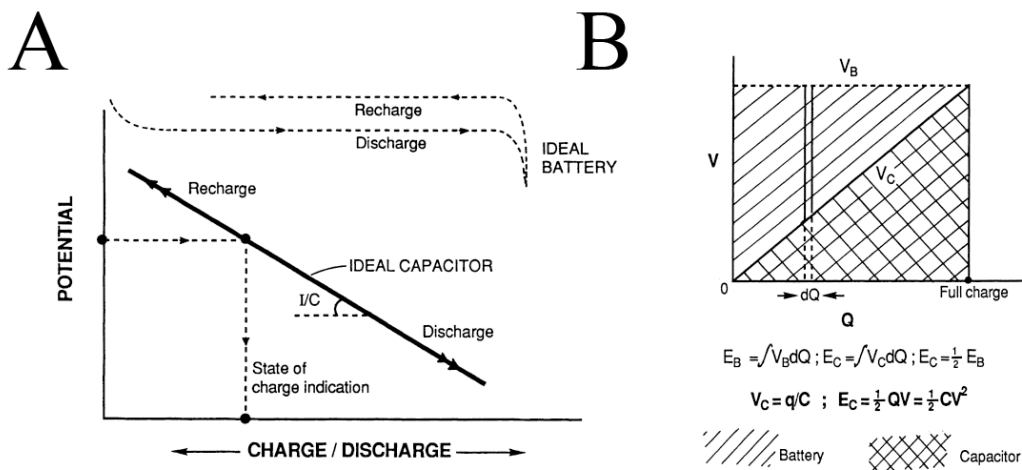


Figure 2.3 (A) Charge-discharge curve and (B) energy storage of ideal battery and ideal ES[3].

The energy storage mechanism of ES and batteries are fundamentally different. The charge storage of ES is only across the surface of capacitive materials, whereas batteries utilize the entire bulk electrodes. In the EDLCs, positive and negative electrical charges are residing on the interface between the electrodes and the electrolyte. Ideally, no electron transfer takes place across the electrode interface and the storage of electric charge and energy is electrostatic. For the battery type-process, the charge transfer is carried out through Faradic reactions on the anode and cathode. The characteristic feature of ESs and batteries could be demonstrated by potential ( $U$ ) versus charge ( $Q$ ) relationship, namely, the charge and discharge curve. As shown in Figure 2.3A, the potential difference of batteries is ideally constant throughout the whole charge and discharge processes; while in a ES device being charged, every addition of charge has to do electrical work against the charges that have already stored in the ES. The accumulated charge has a linear relationship with the potential difference between two electrodes. The potential difference of charging a battery is ideally constant with increase of the accumulated charges because the free energy ( $\Delta G$ ) of redox reactions is independent on electrode potential. The difference of energy storage between capacitors and batteries can be illustrated by Figure 2.3B. The integrals of voltage ( $V$ ) and charge ( $Q$ ) under the two lines of the working diagram correspond to the total energy storage of batteries ( $E_b$ ) and ESs ( $E_s$ ). Therefore, it could be seen that the energy storage of an ES at a voltage ( $V_c$ ) is only half of the energy of charging the battery to the same voltage ( $V_b$ ) by the charge of  $Q$ .

ESs, batteries and fuel cells do not always compete with each other. Complementary strategies for high power and high energy resources have already been proposed by combining electrochemical systems. Besides bridging the gap between capacitors and batteries, ESs also possess a number of desirable properties that make them an attractive energy storage option. For example, charge and discharge of EDLCs are completely reversible, so they are extremely efficient and can withstand a large number of charge/discharge cycles. Moreover, ESs can store or release energy very quickly, and can operate over a wide range of temperatures. They also have a high charge and discharge efficiency. The energy loss to heat during each cycle is relatively small. In addition, ESs generally do not contain toxic materials and are much safer than batteries and fuel cells.

With the aforementioned advantages, ESs have become a very competitive choice for applications in electric vehicles, elevators, digital cameras, mobile phones, pulse laser techniques and uninterruptible power supplies [4-6]. For instances, it is very expensive to make frequent replacement of the batteries in the memory back-up system due to their poor cycle life. In a fuel cell or battery electric vehicles, it is difficult to meet peak load requirements of high power, like accelerating or climbing. With advantages of long life-time and high power density, ESs can solve these problems. In the coming decades, the main market targeted by ESs manufacturers may be transportation, including hybrid electric vehicles and metro trains[6].

## **2.3 Two types of capacitive materials and energy storage mechanism**

Due to the mechanism of charge and discharge process, ESs can be generally classified into two different types, electrochemical double-layer capacitors (EDLCs, non-Faradic) and pseudocapacitors (or redox-based electrochemical capacitors, Faradic). In addition, hybrid systems were developed, which combined Faradaic and non-Faradaic process for the charge storage. In this chapter, the charging mechanism, materials for electrode and electrolyte and cell configuration of different ESs will be discussed.

### **2.3.1 Electrochemical double-layer capacitors (EDLCs)**

Electrochemical double-layer capacitors (EDLCs) have a structure similar to that of conventional electrostatic capacitors, which store charge by a non-Faradic process. Due to the non-Faradic character, there is no limitation caused by electrochemical kinetics. Therefore, EDLCs have a higher power density than pseudocapacitors, and higher energy density than electrostatic capacitors. In EDLCs, the dielectric is replaced by electrolyte and the charge does not accumulate on two conductors. Instead, the charge accumulates at the interface between the surface of conductor and electrolyte as shown in Figure 2.4. The accumulated charge hence forms an electric double-layer, the separation of each layer being of the order of a few Angstroms[7].

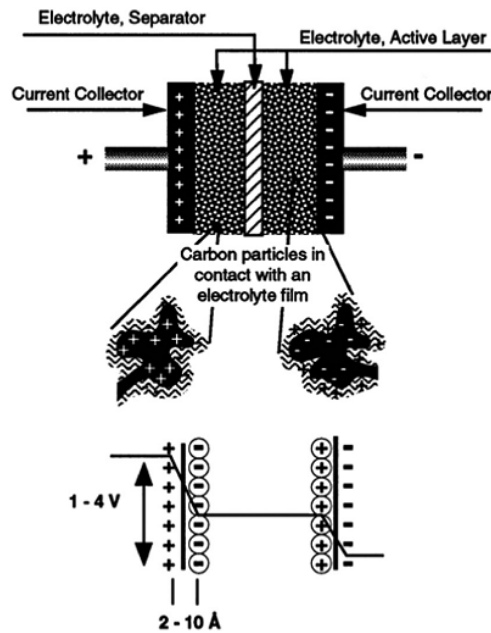
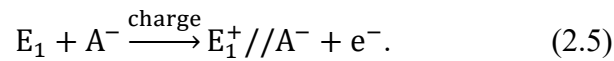


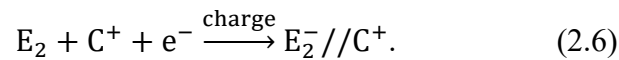
Figure 2.4 Scheme of electrochemical double-layer capacitors (EDLCs) and illustration of the potential profile at the electrode/electrolyte interface after charging[8].

Capacitance can be obtained from the double-layer model proposed by Helmholtz, in which the double-layer consisted of charged electrode and ions in the electrolyte. According to eq. 2.2, the specific capacitance of Helmholtz model was determined by the surface area, dielectric constant and thickness of the double-layer.

During the charging process, the electrons travel from the negative electrode to the positive electrode through an external load. Within the electrolyte, cations move towards the negative electrode while anions move towards the positive electrode. The electrochemical processes for charging can be expressed as the followings. At the positive electrode:



$E_1$  is the positive electrode,  $A^-$  is the anion and // represents the interface of electrode and electrolyte. At the negative electrode:



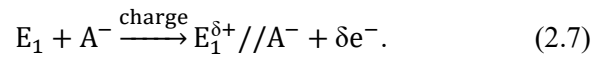
$E_2$  is the negative electrode,  $C^+$  is the cation. The discharge process could be represented by reverse of the above equations.

The electrodes of the EDLC are made of high surface-area materials, such as porous carbon or carbon aerogels, in order to maximize the surface area of the double-layer. The reason is that porous electrodes provide a very short distance between electrode and electrolyte. The surface-area of the porous carbon electrodes has been reported to be as large as 1000–2000 m<sup>2</sup>/g in recent studies[9-11].

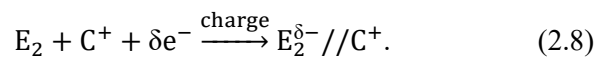
### 2.3.2 Pseudocapacitors

A redox-based electrochemical capacitor is called pseudocapacitor. Redox-based capacitance arises at electrode surfaces where a completely different charge storage mechanism applies. It is not just an accumulation (or deficiency) of electrostatic charge at the interfaces of two electrodes, as the double-layer type of capacitor. When an external potential is applied to a pseudocapacitor, a fast and reversible redox reaction take place on the electrode. It involves the passage of charge between electrode and electrolyte. The mechanisms of charge and discharge of a

pseudocapacitor is similar to what occurs in batteries. During the charge process, the reaction at the positive electrode could be expressed as



The reaction at the negative electrode is represented by



$E_1$  and  $E_2$  are positive and negative electrodes, and the anion and cation are expressed as  $A^-$  and  $C^+$ , respectively.  $//$  describes the interface of electrode and electrolyte. The parameter  $\delta e^-$  is electrosorption valence, related to the oxidation-reduction reaction at the electrode.

In 1970s, B.E. Conway indicated that several faradic mechanisms can result in pseudocapacitive electrochemical features: (1) underpotential deposition, (2) redox pseudocapacitance and (3) intercalation pseudocapacitance[12]. These processes are illustrated in Figure 2.5. Underpotential deposition occurs when metal ions form an adsorbed monolayer at a different metal's surface well above their redox potential. The typical examples of underpotential deposition is the Langmuir-type electrosorption of H on the noble metal substrate such as Pt, Rh, Ru. Redox pseudocapacitive behaviour occurs when ions are electrochemically adsorbed onto the surface or near surface of a material with a concomitant faradaic charge-transfer. Metal oxides, such as  $\text{RuO}_2$ [13-15],  $\text{NiO}$ [16],  $\text{Co}_3\text{O}_4$ [17, 18] and  $\text{MnO}_2$ [19-21], as

well as conducting polymers (polypyrrole[22-24] and polyaniline[25, 26]), are classic examples of redox pseudocapacitive materials, which are currently under extensive research. Intercalation pseudocapacitance is a result of ion intercalation into tunnels or layers of a redox-active material, accompanied with faradaic charge transfer process but with no crystallographic phase change.

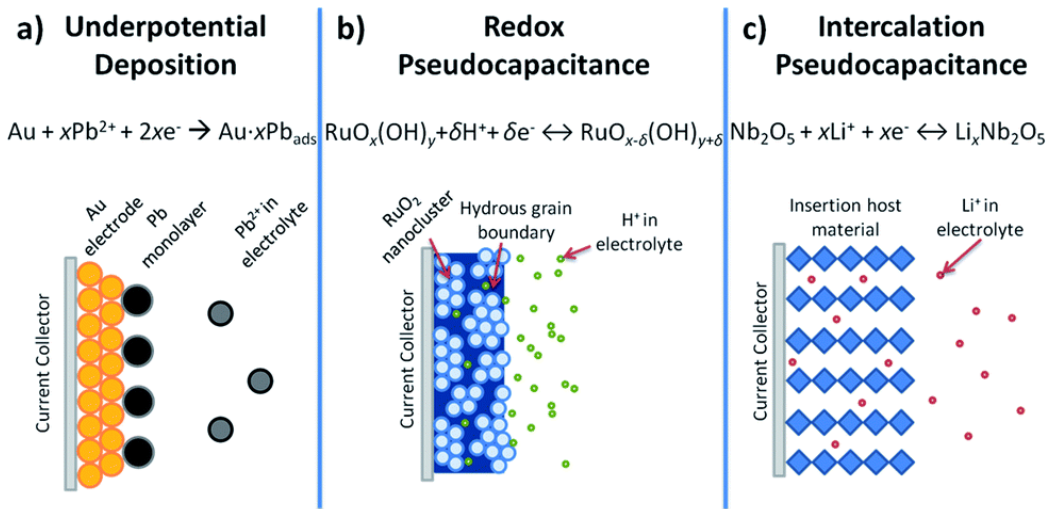


Figure 2.5 Different types of pseudocapacitive behaviour from B.E. Conway: (a) underpotential deposition, (b) redox pseudocapacitance, and (c) intercalation pseudocapacitance[3, 12].

For all three types of pseudocapacitive behaviour, the pseudocapacitance is proportional to differentiated Y with respect to potential (V) ( $C \propto dY/dV$ ), in which Y is the property of capacitive materials. In case of underpotential deposition, Y is the extent of fractional coverage of an electrode surface. Y could be the extent of conversion of an oxidized species to a reduced species and fractional absorption for

redox pseudocapacitance and intercalation pseudocapacitance, respectively. From a thermodynamic point of view, Y is related to potential by an equation:

$$\frac{Y}{1-Y} = K \exp\left(\frac{VF}{RT}\right) \quad (2.9)$$

Therefore, the capacitance of the electrode is dependent on redox potential. The redox potential is expressed as

$$E = E_0 - \frac{RT}{nF} \ln\left(\frac{Y}{1-Y}\right) \quad (2.10)$$

Where  $E_0$  is the electrostatic potential and Y is the capacitive property of electrode.

Table 2.1 Comparison of EDLCs and pseudocapacitor.

| <b><u>Double-layer capacitors (EDLCs)</u></b>  | <b><u>Pseudocapacitor</u></b>   |
|--|---|
| Non-Faradaic process   | Faradaic process  |
| 20–50 $\mu\text{F cm}^{-2}$  | 2000 $\mu\text{F cm}^{-2}$ for single-electron transferred process; 200–500 $\text{mF cm}^{-2}$ for multi-electrons transferred process |
| Capacitance is fairly constant with potential, except for point of zero charge (PZC) | Some single-state materials exhibit marked maximum capacitance  |

|  |  |
|--|--|
| Highly reversible charging/discharging | Quite reversible but has intrinsic electrode kinetic rate limitation |
| High power compared to pseudocapacitor | High energy compared to EDLCs  |

In summary, the high values of specific capacitance attainable through ESs technology are arised from double-layer capacitance, and often pseudocapacitance. Double-layer capacitance could offer good charge storage capabilities due to high active area of electrodes and charge separation at atomic dimension. Pseudocapacitance that arises from redox or ion sorption reactions further improves the achievable capacitance. Comparison of EDLCs and pseudocapacitor is shown in Table 2.1.

## 2.4 The double-layer at the electrode interfaces

### 2.4.1 Electric potential profiles and electrostatic principles

ESs can store much more energy compared with conventional capacitor because of the large interfacial area and the atomic range of charge separation distances. A practical ES can be constructed with two electrode/electrolyte interfaces, which attracted ions with opposite charge from the electrolyte solution. The capacitive behaviour of double-layer at the interfaces between electrode and electrolyte is very important for both EDLCs and pseudocapacitors. The two interfaces in an ES cell are

illustrated in Figure 2.6. In the charged condition, there are two interphasial drops in potential across the ES cell, each of them across one double-layer (Figure 2.6a). During the discharge process, there is also a current-dependent, ohmic IR potential drop within the solution, and the reverse case on recharge (Figure 2.6b).

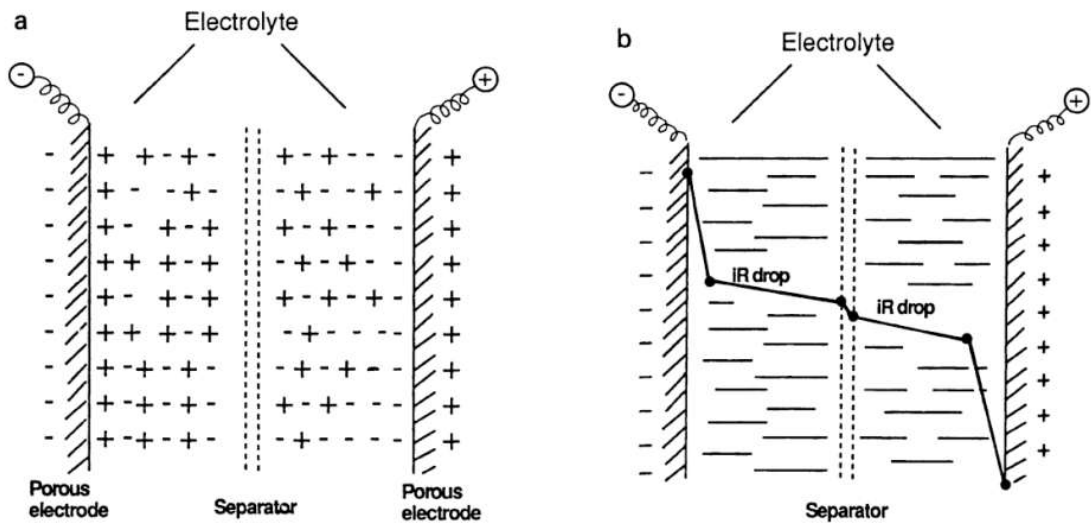


Figure 2.6 Diagrams of electric potential profiles in an ES cell comprising a double-layer at each of two electrodes: (a) charged capacitor in an open circuit, (b) capacitor passing current on discharge with IR drops[3].

The electrostatic force,  $F$ , between two charges  $q_1$  and  $q_2$  with a distance of  $r$  from one another could be determined using Coulomb's Law. The general relation for the force of electrostatic attraction at the double-layer is given by

$$F = \frac{q_1 \cdot q_2}{\epsilon r^2} \quad (2.11)$$

where the  $\epsilon$  is the dielectric constant of a medium.

## 2.4.2 Models and structures

The concept of a double-layer was first described and modeled by von Helmholtz in the 19<sup>th</sup> century, when he investigated the distribution of opposite charges at the interface of colloidal particles. The model was later adapted to the electrode interface. In the Helmholtz model (Figure 2.7a), the double-layer of the electrode interface is consisted of two layers of opposite charge form at the electrode/electrolyte interface, which are separated by an atomic distance. The ions adsorption process was followed by Langmuir's adsorption isotherm. After Helmholtz's model was proposed, it became realized that ions on the solution side of the double-layer could not remain static in a compact array but could be subject to the effects of thermal fluctuation according to the Boltzmann principle. This simple Helmholtz double-layer model was further modified by Gouy and Chapman. The Gouy–Chapman model (Figure 2.7b) states that the continuous distribution of ions in the electrolyte solution could be described by a diffuse layer with a distance of  $d$  due to the thermal fluctuation. In this model, the ions were assumed to be point charges. However, the capacitance of two separated arrays of charges increases inversely with their separation distance according to Eq. 2.5. Therefore, a very large capacitance value is arisen in the case of point charge ions close to the electrode surface. Later, Stern combined the Helmholtz model with the Gouy–Chapman model to explicitly recognize two regions of ion distribution—the inner region called the compact layer and the diffuse region. The compact layer consists of inner Helmholtz plane (IHP) and outer Helmholtz plane (OHP). The IHP

refers to the distance of closest approach of specifically adsorbed ions and OHP refers to that of the non-specifically adsorbed ions. The OHP is also the plane where the diffuse layer begin. In the 1950s, Grahame[27] made a distinction between IHP and OHP in the interfaces which correspond to different distances of closest approach. This difference is mainly caused by the fact that most cations are smaller than common anions and retain solvation shells due to strong ion-solvent dipole interaction. It has been demonstrated that the capacitance of the double-layer is also dependant on the surface properties of electrode, the ions of electrolyte and the solvent[28].

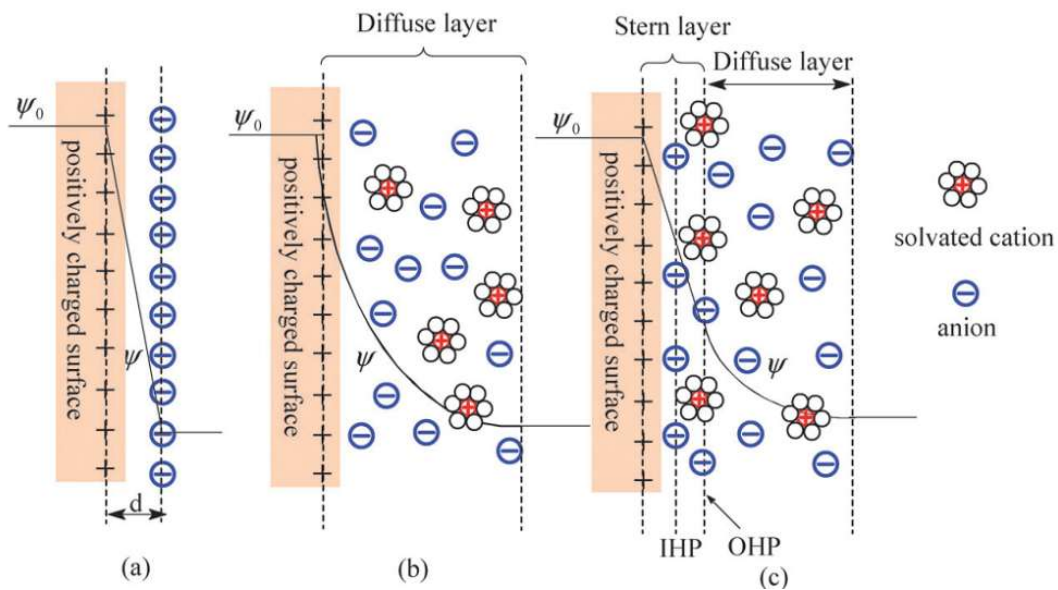


Figure 2.7 Models of the electrical double-layer at a positively charged surface: (a) the Helmholtz model, (b) the Gouy–Chapman model, and (c) the Stern model showing the inner Helmholtz plane (IHP) and outer Helmholtz plane (OHP).  $\psi_0$  and  $\psi$  are the potentials at the electrode surface and the electrode/electrolyte interface, respectively[3].

### 2.4.3 Equivalent circuit representation

The double-layer at the electrode interface could be represented by equivalent circuits. In the Stern model, the capacitance can be treated as a combination of the capacitances from two regions, the Stern type of compact layer and the diffusion region (Figure 2.8).

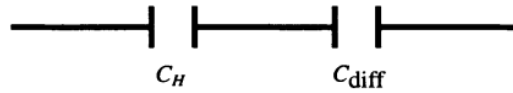


Figure 2.8 Simple equivalent circuit representation of the Stern model of the electrical double-layer[3].

The compact layer of adsorption of ions is taken to correspond to a Helmholtz type of double-layer having a capacitance  $C_H$ , while the remaining ionic charge in the diffuse region of the double-layer has a capacitance  $C_{diff}$ . The overall capacitance of the double-layer is determined by  $C_{diff}$  and  $C_H$  in a series relation related to the equation

$$\frac{1}{C_{dl}} = \frac{1}{C_H} + \frac{1}{C_{diff}} \quad (2.12)$$

On account of the reciprocal form,  $C_{dl}$  is determined by the smaller of the two components  $C_H$  and  $C_{diff}$ . Moreover, it is important to determine if the properties of the double-layer is function of electrode potential and ionic concentration of the electrolyte. The double-layer of interface exhibits ideal capacitive behavior, when the potential difference between electrode and electrolyte is established without any

Faradic charge transfer. The accumulated charge is linearly increased with the applied voltage. In the case where a Faradaic process may take place at the interface of the electrode, an equivalent circuit with Faradaic resistance  $R_F$  will be parallel with the double-layer capacitance.  $R_f$  is exponentially dependent on the electrode potential. In this situation, the capacitance of double-layer, referred to as the pseudocapacitance, is related to the electrode potential. The pseudocapacitive behavior is non-ideal capacitive behavior because the accumulated charge isn't linearly related to the applied voltage.

The basic operation of a single-cell ES consisting of two electrodes with double-layer interface can be illustrated by a simple equivalent RC circuit representation (Figure 2.9).  $C_a$  and  $C_c$  are the capacitance of the anode and cathode, respectively.  $R_s$  is the equivalent series resistance (ESR) of the cell.  $R_F$  is the Faradaic resistance in the case of Faradic reactions are carried out. The notation for anode and cathode resistances are  $R_{Fa}$  and  $R_{Fc}$ . The total capacitance of the cell ( $C_T$ ) is therefore calculated according to

$$\frac{1}{C_T} = \frac{1}{C_a} + \frac{1}{C_c} \quad (2.13)$$

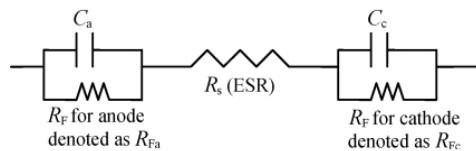


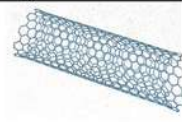
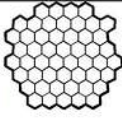
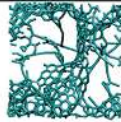
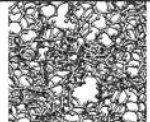
Figure 2.9 Simple equivalent circuit representation of the basic operation of a single-cell ES[29].

## 2.5 Materials for electrode of ES

Selection of electrode materials plays a crucial role in determining the electrochemical performance of an ES. Capacitive charge storage is a surface process, and the surface characteristics of the electrode greatly influence the capacitance of the cell. Carbon is the most widely used electrode material, but considerable research is being conducted into pseudocapacitive materials (metal-oxides and conducting polymers) due to their high specific capacitance. Composite electrodes and hybrid configurations have been developed with the combination of advantages of carbon materials and pseudocapacitive materials.

### 2.5.1 Porous Carbon materials for EDLCs

Table 2.2 Different carbon structures used in EDLCs with onion-like carbon, carbon nanotubes, graphene, activated carbons, carbide-derived carbons and templated carbons[8].

| Material               | Carbon onions   | Carbon nanotubes  | Graphene  | Activated carbon   | Carbide derived carbon  | Templated carbon  |
|------------------------|---|---|---|--|---|---|
| Dimensionality         | 0-D   | 1-D   | 2-D   | 3-D  | 3-D   | 3-D   |
| Conductivity           | High  | High  | High  | Low  | Moderate  | Low   |
| Volumetric Capacitance | Low   | Low   | Moderate  | High   | High  | Low   |
| Cost                   | High  | High  | Moderate  | Low  | Moderate  | High  |
| Structure              |  |  |  |  |  |  |

Carbon materials are considered as prospective electrode materials for commercialization due to their low cost, availability, environmental friendliness and

long history of use. Development of high surface area carbons is required for increasing the capacitance. Table 2.2 shows examples of carbons with different structures and properties for EDLC applications.

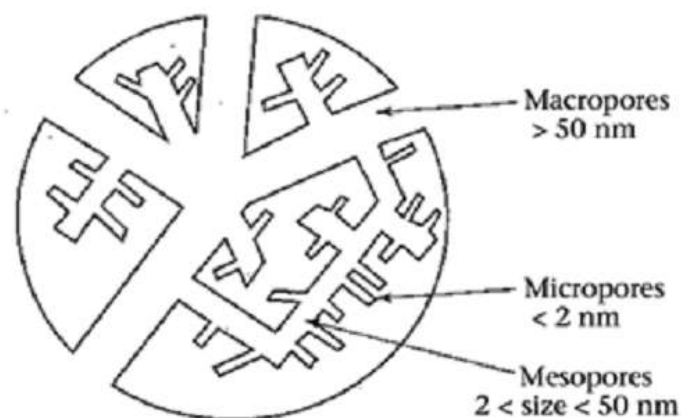


Figure 2.10 Schematic diagram of the pore size network of an activated carbon[30].

High surface area and three-dimensional porous electrodes can be achieved through the activation process. The pore sizes can be further classified into three categories: (1) micropores (<2 nm), (2) mesopores (2-50 nm) and (3) macropores (>50 nm) (Figure 2.10). It has been indicated that the micropores (<2 nm) makes significant contributions to the capacitance of electrodes; however, only ~20 nm in the depth of the surface could be accessed by the electrolyte due to diffusion limitations[31]. Therefore, construction of hierarchical carbon with combination of micropores, mesopores and macropores attracts interests to achieve good capacitive performance[32, 33]. Recent studies have indicated that heteroatom doping is an important method to improve the capacitive performance of carbon-based

electrode[33-35]. The heteroatoms such as N, O, S and B could enhance electrical conductivity, improves the wettability and increase specific capacitance of activated carbon. The N-enriched polymer precursors have been studied to improve the capacitive performance of various carbon frameworks such as carbon nanotubes[36, 37], graphene[38] and carbon fibers[39].

Treatment of carbon materials influences their structure and electrochemical performance. The accessibility of the pores by the electrolyte is very important for EDLCs[40]. Usually, smaller particles result in a larger accessible pore surface-area. The mobility of the ions within the pores is greatly influenced by the electrode's pore size. Small pores have a short distance of ionic charge at the electrode surface, which will enhance the capacitive behaviour. However, if the pores are too small to allow easy access of electrolyte ions, they will not contribute to double-layer capacitance. The pore size must be chosen to suit the electrolyte and thereby ensure that the pore size distribution is optimal based upon the size of the ions[40].

### 2.5.2 Conducting polymers

Conducting polymers are attractive for ESs due to low environmental impact, easy fabrication and high conductivity in a doped state. The typical conducting polymers for ES applications are polypyrrole (PPy), polyaniline (PAni), polythiophene (PTh) and poly(3,4-ethylenedioxythiophene) (PEDOT). Their molecular structures were shown in Figure 2.11.

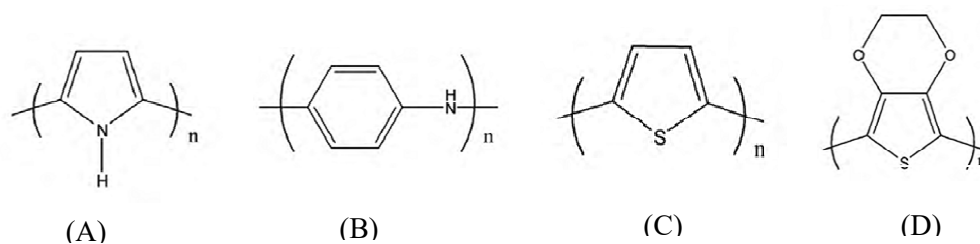


Figure 2.11 Various conducting polymer structures. A) polypyrrole (PPy), B) polyaniline (PAni), C) polythiophene (PTh) and D) poly(3,4-ethylenedioxythiophene) (PEDOT).

Conducting polymers store and release charge through redox processes. Charge and discharge of conducting polymer films could take place throughout the bulk volume of the film, and not just on the surface as is the case with carbon. Therefore, this offers the opportunity of achieving high levels of specific capacitance. There are two different redox types of conducting polymers, p-doped (positively charged) and n-doped (negatively charged). The mechanism of electrochemical doping of a conducting polymer film is described schematically in Figure 2.12. As shown in Figure 2.12a, charging process of p-doped conducting polymers takes place by accumulation of electrons from the polymer backbone through the external circuit. An anion from solution was incorporated into the polymer film to counter balance the positive electronic charge. The mechanism of charging of n-doped conducting polymers is proceeded by reverse of p-doped mechanism shown in Figure 2.12b. Electrons are transported onto the polymer backbone by the external circuit, and

cations enter the polymer from the solution in order to maintain overall charge neutrality.

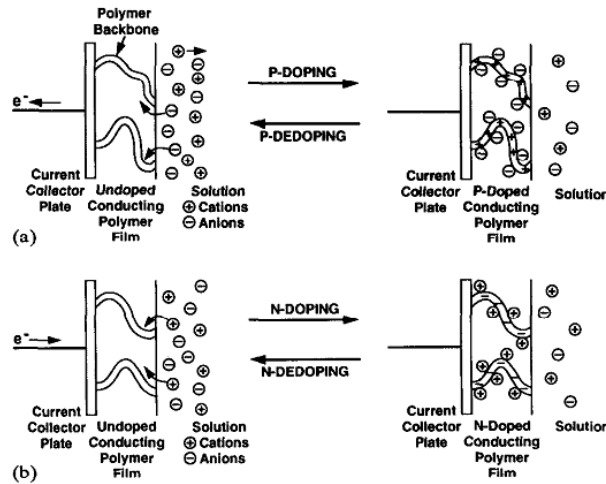


Figure 2.12 Charge and discharge mechanism for a) p-doping and b) n-doping of a conducting polymer.

Three types of conducting polymer based ES devices can be made[41, 42]:

- A. symmetric configuration by using the same p-dopable polymer for both electrodes;
- B. asymmetric configuration by using two different p-dopable polymers with a different range of electroactivity;
- C. symmetric configuration by using the same polymer for both electrodes with the p-doped form used as the positive electrode and the n-doped form used as the negative electrode.

All conducting polymers can only work (supplying charges) within a rigid potential window. Beyond this strict potential range, the polymer may be degraded at more

positive potential, and as the potential is too negative, the polymer may be switched to an insulating state (un-doped state). The selection of a suitable potential range for electrochemical performance is crucial. Table 2.3 gives the potential windows, theoretical capacitances, conductivity and doping type for various conductive polymers for ES applications. It should be noted that PPy and PANi can only be p-doped. PTh and PEDOT are both n- and p-dopable.

Table 2.3 Specific capacitance, conductivity and doping type of conductive polymer[6, 43, 44].

| Polymer | Potential range<br>(V) | Theoretical<br>SC<br>(F g <sup>-1</sup> ) | Conductivity<br>(S cm <sup>-1</sup> ) | Doping<br>type |
|---------|------------------------|---|---------------------------------------|----------------|
| PPy     | -0.5 - 0.4             | 620                                       | 40-200                                | P-doping       |
| PAni    | 0 - 0.8                | 750                                       | 0.1-5                                 | P-doping       |
| PTh     | -0.2 - 0.6             | 485                                       | 300-400                               | n,P-doping     |
| PEDOT   | -0.4 - 0.6             | 210                                       | 300-500                               | n,P-doping     |

A major part of my thesis is focused on polypyrrole (PPy) and polypyrrole(PPy)-based composite electrode for supercapacitors. Compared to most conducting polymer, PPy offers a greater degree of flexibility in electrochemical processing. Furthermore, due to its greater density, PPy has a high capacitance per unit volume (400–500 F cm<sup>-3</sup>). The synthesis of PPy can be accomplished by chemical or electrochemical methods. While the electrochemical synthesis of PPy

involves electrode reactions as the driving force, the chemical method utilizes oxidants for the polymerization, such as  $\text{FeCl}_3$ [45],  $(\text{NH}_4)_2\text{S}_2\text{O}_8$ [46, 47] and  $\text{Fe}_2(\text{SO}_4)_3$ [48]. The reaction formula can be expressed as following.

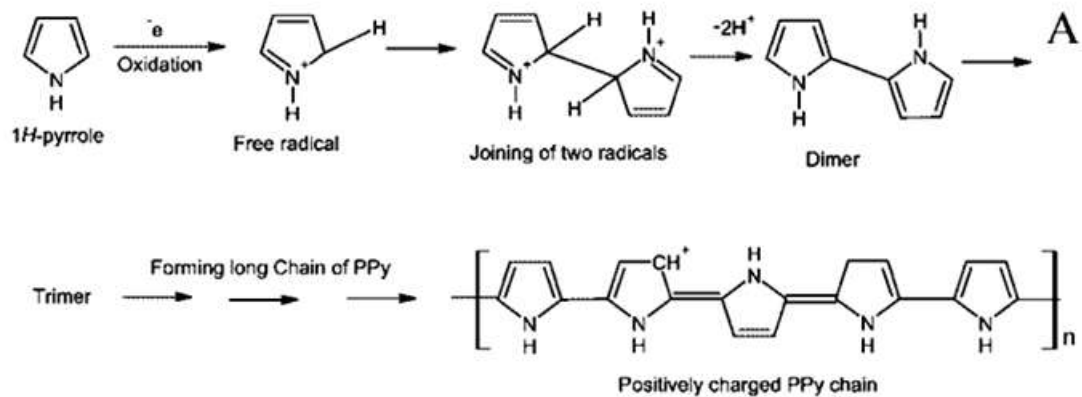
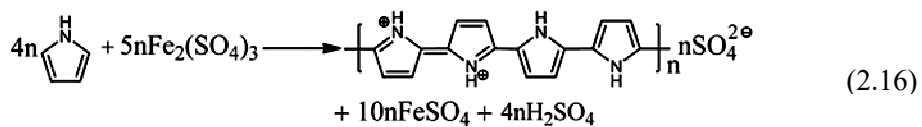
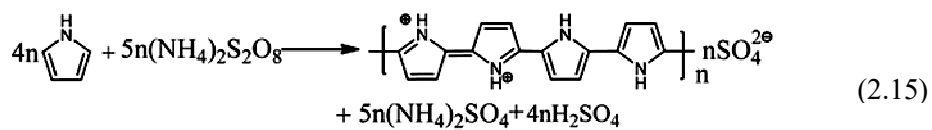
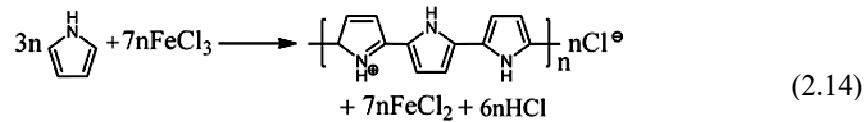


Figure 2.13 Schematic representation of mechanism for the formation of PPy chain proposed by Shubhra[49].

It has been determined that the optimal molar ratios of oxidant to Py monomer are 2.3, 1.25 and 1.25 for  $\text{FeCl}_3$ ,  $\text{Fe}_2(\text{SO}_4)_3$  and  $(\text{NH}_4)_2\text{S}_2\text{O}_8$ , respectively[50]. The anions such

as  $\text{Cl}^-$  and  $\text{SO}_4^{2-}$  interlinked with PPy chains are considered as dopants. The mechanism of PPy polarization process is still a controversial subject. Since the rapid polymerization process and non-crystalline nature of PPy, it is hard to determine the stages of reaction by structure characterization and physical properties analysis. The major mechanism was proposed by Shubhra et. al.[49] as shown in Figure 2.13. In the dopant-oxidant solution, each doping agent on hydrolysis forms its respective counter anionic species. On adding this solution gently to the monomer solution, each neutral pyrrole molecule is oxidized in solution and yields its free cation radical species, which then combines with its consecutive radical species and forms a dimer. This dimer further joins with other free cation radical and forms a trimer and finally results in a chain of positively charged PPy units. Subsequently, the respective negative charged dopant ions attach at the positive site of the PPy back bone, and form series of dopant ion incorporated into the PPy matrix. The charge-discharge mechanism of PPy is still not fully understood. One hypothesis was shown in Figure 2.14, where  $\text{A}^-$  represents anions,  $e^-$  is the electron,  $n$  and  $m$  determine degree of doping and molecular weight, respectively.

High specific capacitance of conducting polymer may be achieved by increasing the doping level. Many studies were focused on the development of advanced anionic dopants for PPy [52-55]. It has been shown that with the variation of the dopant anion, the conductivity of the PPy can differ by three orders of magnitude[56]. Beside affecting conductivity, dopants could also improve the thermal stability[57], surface

morphology[46, 58] and mechanical strength[59] of PPy. The investigation of aromatic dopants, containing sulfonic anionic groups, showed that the conductivity of PPy films increased with increasing charge/mass ratio of the dopant molecules[54, 60]. Considering these facts, it is of great interest to achieve high electrochemical activity of PPy for ES application by developing advanced dopants.

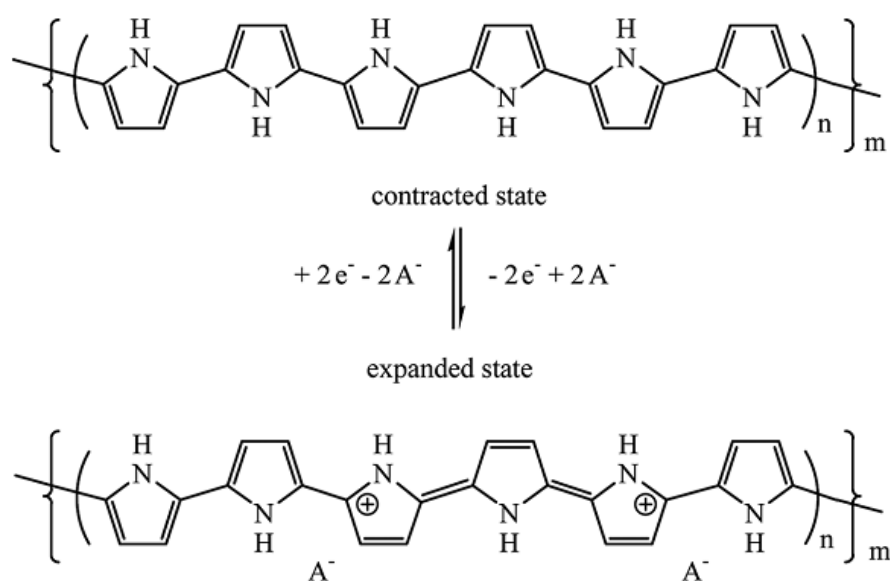


Figure 2.14 Charge storage mechanism for PPy[47, 51].

The main disadvantage of conducting polymer electrodes is long-term stability because swelling and shrinking occur during the intercalating/deintercalating process. Previous studies have shown that conducting polymer based electrodes may remarkably degrade under less than a thousand cycles[61, 62]. According to previous studies, the cycle stability of PPy could be improved by changing structures, improving morphologies of PPy and fabricating composite materials[41, 42, 63].

### 2.5.3 Metal oxides

Metal oxides are promising electrode materials because of high specific capacitance, possibly making it easier to construct high-energy, high-power ESs. Compared to conductive polymer materials, metal oxides have better electrochemical stability. Extensive studies have been focused on ruthenium-oxides in earlier years. Specific capacitance of more than  $1500 \text{ F g}^{-1}$  has been reported[64], but Ru-based electrode are expensive, and small voltage window also limits their applications[13-15].

Currently, researchers are focusing on searching for cheaper metal oxides to use instead of ruthenium-oxides, but the selection has traditionally been limited by the use of concentrated sulfuric acid as an electrolyte. It was believed that high capacitance and fast charging was largely a result of H sorption, so a strong acid was therefore necessary to provide good proton conductivity. This resulted in a narrow range of possible electrode materials since most metal-oxides break down quickly in acidic solutions. Neutral aqueous solutions like  $\text{Na}_2\text{SO}_4$  and  $\text{KCl}$ , have therefore been considered for use with metal-oxides such as  $\text{MnO}_2$ ,  $\text{Co}_3\text{O}_4$ ,  $\text{Fe}_3\text{O}_4$  and  $\text{NiO}$ . Among these metal oxides,  $\text{MnO}_2$  has attracted major attention due to its high theoretical capacitance (about  $1380 \text{ F g}^{-1}$ )[65-68]. The capacitive behaviour of manganese dioxide is attributed to reversible redox transitions involving the exchange of protons ( $\text{H}^+$ ) and/or cations ( $\text{C}^+$ , such as  $\text{K}^+$ ,  $\text{Na}^+$ , etc.) with the electrolyte, as well as the transitions of  $\text{Mn(IV)/Mn(III)}$  and  $\text{Mn(III)/Mn(II)}$  within the electrode potential

window of the electrolyte[65, 69]. The discharge reaction of MnO<sub>2</sub> could be expressed as

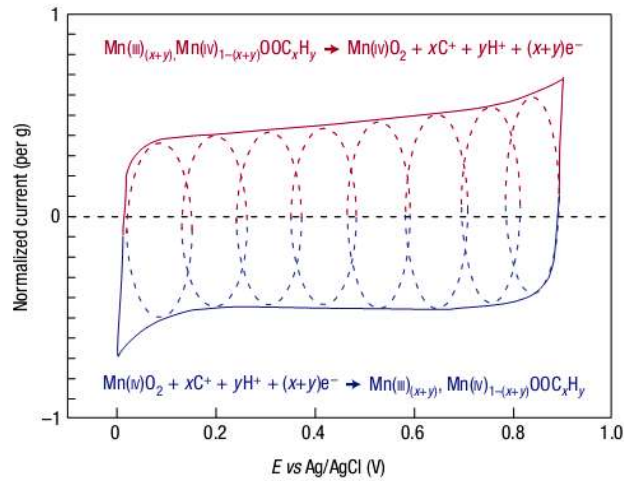
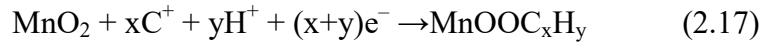


Figure 2.15 Schematic illustration of cyclic voltammetry for a MnO<sub>2</sub>-electrode cell in neutral aqueous electrolyte (0.1 M K<sub>2</sub>SO<sub>4</sub>) shows the successive multiple surface redox reactions leading to the pseudocapacitive charge storage mechanism[2].

The cyclic voltammogram of MnO<sub>2</sub> film in aqueous electrolyte is shown in Figure 2.15. The red (upper) part is related to the oxidation from Mn(III) to Mn(IV) and the blue (lower) part refers to the reduction from Mn(IV) to Mn(III). The main problem of MnO<sub>2</sub> electrode is its low conductivity. High specific capacitance could only be achieved for thin films. Previous studies have been indicated that capacitance retention could be improved by synthesis of nano-structured MnO<sub>2</sub> and combined with conductive carbon materials, such as carbon nanotubes and graphene [70, 71].

### 2.5.4 Composite electrodes and hybrid configurations

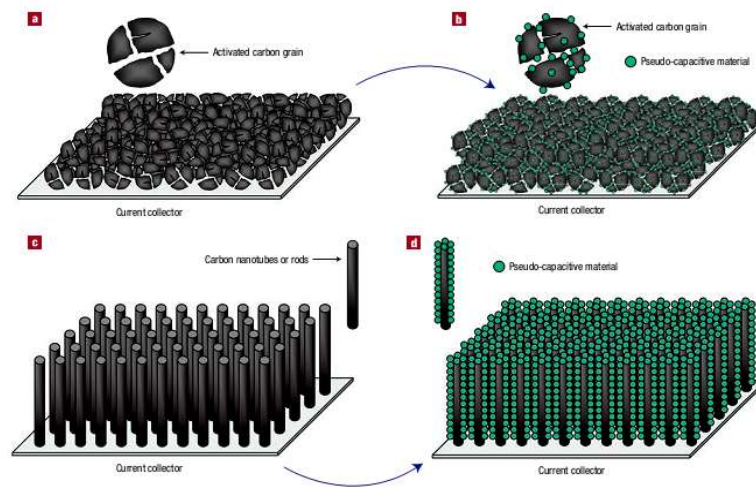


Figure 2.16 Possible strategies to improve both energy and power densities for ESs. a) carbon activation and b) decorating with pseudocapacitive materials on porous carbon; c) highly ordered high surface area carbon nanotubes and d) deposit of pseudocapacitive materials on carbon nanotubes[2].

Carbon materials show good capacitance retention, power performance and cycling stability due to their high conductivity and high specific surface area, but with drawbacks of low energy density. Pseudocapacitive materials (metal oxide/conducting polymer) have high energy density with sacrifice of cycling stability and power delivery because of Faradaic reaction and low conductivity. Composite electrodes consist of one type of materials incorporated into another within the same electrode. The combination of individual materials integrates the advantages of pure species and good overall performance could be achieved. The typical strategies to make composite materials were shown in Figure 2.16. Thin film or high surface area carbon

material is decorated with nano-sized pseudocapacitive material. The fabricated composite electrodes offer opportunities to increase energy density compared with carbon-based EDLCs.

Significant interest has been generated in the fabrication of pseudocapacitive materials-carbon nanotube (CNT) composite electrode. The utilization of CNTs as the additives offers benefits of their high surface area and high electrical conductive. It has been demonstrated that the conductive polymer-CNT electrodes could be fabricated with enhanced cycling stability. For example, in comparison with pure PPy electrode which showed nearly 50% capacitance loss after 500 cycles of charge and discharge, the PPy-CNT composite electrodes indicated improved capacitance retention for the same cycling tests [72]. It is believed that CNT with exceptional mechanical properties can be used as a support for the conductive polymer. The CNTs in the composite electrode offer free space for the swelling and shrinking during the charge and discharge process. The synthesis of MnO<sub>2</sub>-CNT composite electrode has also been investigated extensively[73-76]. The addition of CNT to MnO<sub>2</sub> can form a three-dimensional porous conductive network, extend the working potential and guarantee an effective utilization of MnO<sub>2</sub>. As a result, the MnO<sub>2</sub>-CNT composite electrodes can display higher specific capacitance, higher capacitance retention and higher energy/power density. For example, Xia et al.[73, 77] prepared MnO<sub>2</sub> coated CNT composite by the chemical reaction between KMnO<sub>4</sub> and CNT under hydrothermal conditional. The specific capacitance of MnO<sub>2</sub> coated CNT is 210 F g<sup>-1</sup>

at scan rate of  $2 \text{ mV s}^{-1}$ , which is almost two times higher than pure  $\text{MnO}_2$  ( $110 \text{ F g}^{-1}$ ). The  $\text{MnO}_2$  coated CNT showed very good capacitance retention of 80% as the scan rate of CVs increased from 2 to  $100 \text{ mV s}^{-1}$ . The improved capacitive performance is attributed to the core-shell nano-structure of the composite, which allowed the fast ion and electron transport[77].

Table 2.4 Summary of the different types of hybrid ES[78].

| Type of ES             | Electrode material                         | Charge storage mechanism | Advantage and disadvantage                                  |
|------------------------|--|--------------------------|---|
| Symmetric hybrid ES    | Anode: Metal oxide or conductive polymer   | pseudocapacitance        | High energy density, moderate cost and cycle stability      |
|                        | Cathode: Metal oxide or conductive polymer | pseudocapacitance        |   |
| Asymmetric hybrid ES   | Anode: Metal oxide or conductive polymer   | pseudocapacitance        | High energy density and power density, good cycle stability |
|                        | Cathode: Carbon Material                   | Double-layer capacitance |   |
| Battery-like hybrid ES | Anode: Li-ion intercalation material       | Lithiation/delithiation  | High energy density, but high cost                          |
|                        | Cathode: Carbon Material                   | Double-layer capacitance |   |

Hybrid electrode configurations consist of two different electrodes made of different materials. An appropriate electrode combination can increase the cell voltage, further contributing to improvement in energy and power densities (Eq. 2.3 and 2.4). Currently, three different approaches to hybrid systems have been suggested: (A) different pseudocapacitive materials (symmetric hybrid ES), (B) pseudocapacitive

materials with a carbon electrode (asymmetric hybrid ES), and (C) lithium-insertion electrodes with a carbon electrode (battery-like hybrid ES). A summary of all different hybrid supercapacitors is given in Table 2.4.

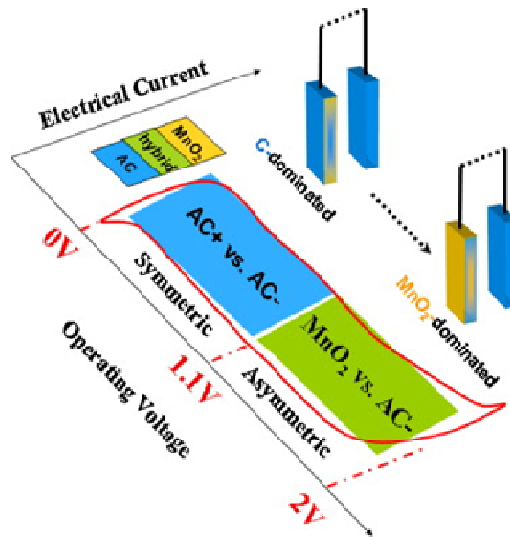


Figure 2.17 The configurations of active carbon (AC) symmetric ES and  $\text{MnO}_2/\text{AC}$  asymmetric ES [19].

In the hybrid system, both double-layer capacitance and pseudocapacitance contribute to energy storage. Several combination of the cathodes and anodes have been proposed in the past[79-83]. Most of the hybrid ESs utilized the Faradic electrode as the cathode, which accumulated the charge through redox electrochemical reactions. For example, as shown in Figure 2.17, the association of a negative porous carbon electrode with positive  $\text{MnO}_2$  electrode allows to obtain 2.0 V ES cell in the neutral aqueous electrolyte due to the water decomposition overvoltage on  $\text{MnO}_2$  and high surface area carbon[84]. A higher ESs cell voltage of 3.0 V was reported by

utilization of the organic electrolyte ( $\text{Et}_4\text{NBF}_4$  in acetonitrile) with similar ES configuration,  $\text{MnO}_2$  and activated carbon as positive and negative electrode, respectively[85].

## **2.6 Electrolyte for ESs**

The electrolyte, which resides between the two electrodes and the separator, is also one of the most important ES components. The electric conductance of the electrolyte reflects the equivalent series resistance (ESR) of device, and thus its power output characteristics. The anion adsorption from the electrolyte control the relative potential to the potential-of-zero charge of electrode. The extent of ionization and dielectric properties of the electrolyte influence the specific capacitance of the electrode and its dependence on the potential. The requirements for selection of an electrolyte in ES include: good electric conductance, high ionic concentration, wide voltage window, high electrochemical stability, low toxicity, low cost as well as high purity.

The two principal factors involved in conductance of the electrolyte are the concentration of free charge carriers and the ionic mobility, which are in turn determined by the solubility of the salt in the solvent and the degree of dissociation of dissolved salts. Three stages of ion pairing, depending on the extent of retention of solvation are presented in Figure 2.18. Hydration shell contact provides high fraction of salts as free charge carriers of electric current (Figure 2.18a). The distance of the solvated ions could be significantly reduced when their solvation shells become

shared (Figure 2.18b). In poorly solvating solvents, the plus and minus ions come into a contact situation (Figure 2.18c).

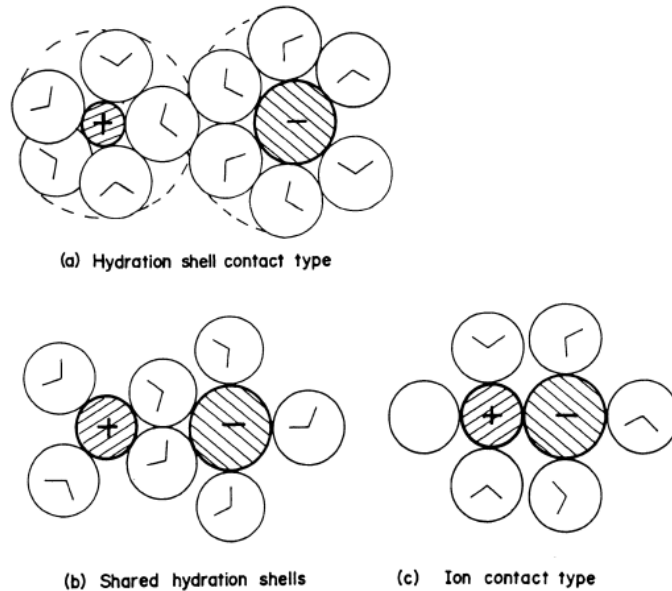


Figure 2.18 Types of ion pairs in an electrolyte solution: (a) solvated-ion pairs, (b) solvent shared ion pairs, and (c) contact ion pairs[3].

Conventional liquid electrolytes used in an ES can be classified into three types: (1) aqueous electrolyte, (2) organic electrolyte and (3) ionic liquid. Very recently, solid electrolyte or gel electrolyte were obtained from proton-conducting polymer electrolytes, which attracted great attention for the fabrication of solid state ES[86-89].

### 2.6.1 Aqueous electrolytes

The aqueous electrolytes, such as  $\text{H}_2\text{SO}_4$ ,  $\text{KOH}$ ,  $\text{KCl}$  and  $\text{Na}_2\text{SO}_4$ , have advantages of low resistance and high ionic concentrations in comparison with organic electrolytes.

ES fabricated by aqueous electrolyte could provide higher power than organic electrolytes due to high conductivity. Furthermore, aqueous electrolyte can be prepared and utilized without stringently controlling the preparation conditions, while the organic electrolytes need strict processes to obtain ultra-pure electrolyte. However, the limitation of aqueous electrolyte is their small voltage window. To improve the voltage window of ES, many efforts have been made to investigate environmentally friendly and cost-effective natural aqueous electrolyte. The results showed that the enlarged voltage window of 1.8-2.2 V could be obtained [90-92].

### 2.6.2 Organic electrolytes

The main advantage of organic electrolytes over aqueous electrolyte is large voltage window as high as 3.5 V. Higher voltage window can increase the energy density because the energy density is proportional to the square of voltage as it can be seen in Equation 2.3. Nevertheless, most organic electrolytes have the drawbacks of high electric resistance, small power capability and complex production conditions. Among organic electrolyte, acetonitrile and propylene carbonate (PC), triethylmethylammonium tetrafluoroborate (TEMABF<sub>4</sub>) are most commonly used solvents. Studies have been made to investigate the relationship between nano-structured activated carbon and the capacitive performance in different electrolytes. The results indicated that capacitance of activated carbon is higher in aqueous electrolytes (100-300 F g<sup>-1</sup>) than in organic electrolytes (50-150 F g<sup>-1</sup>)[93,

94]. One reason is because the effective size of the electrolyte ions in organic solutions is much larger when compared with those in water. Therefore, organic electrolytes increase the number of pores that are smaller than the ions, and decrease the number of pores not contributing to the charge storage. Moreover, the wettability of the electrode is influenced by the chemical affinity between the organic electrolyte and electrode surface.

### 2.6.3 Ionic liquids

Ionic liquids are a class of organic salts with desirable electrolyte properties such as high ionic conductivity, low vapour pressure, non-flammability, wide electrochemical window and high thermal stability. The ionic conductivity of these liquids is low at room temperature, thus they are mainly used at high temperatures. Ionic liquids are entirely composed of cations and anions. The voltage window of ionic liquid is thus determined by the electrochemical stability of ions. The challenge of ionic liquid for energy storage is its chemical stability combined with high ionic conductivity as well as the design of electrode structure capable of assuring proper wettability by the ionic liquid[95, 96]. The development of ionic liquid for ES applications is still in the preliminary stage. Several ESs have been fabricated using ionic liquids and further progress is needed to ensure their full exploitation. M. Lazzari et al.[97] studied the molecular chemistry and structure of the ionic liquid ions for the double-layer capacitive response of carbonaceous electrodes. The results indicated that the specific

capacitance is strongly determined by the cation polarizability of ionic liquid ions. The molecular structure of ions affects the dielectric constant and the thickness of double-layer. G. Yushin[98] reported that a symmetric EDLC prepared by a EMIImBF<sub>4</sub> ionic liquid electrolyte showed a high specific capacitance of 300 F g<sup>-1</sup> at the voltage window of 2.2 V.

#### 2.6.4 Solid-state ES

The conventional ES consists of two electrodes with a separator between them in aqueous or organic electrolyte. However, the liquid electrolytes suffer two major drawbacks for practical applications. Firstly, the electrolyte leakage may lead to reduction in specific capacitance, degradation of electrochemical performance, and even contamination to nearby circuits. Secondly, the ES in such configuration is not an integrated one and not able to move relative to each other under strong flexibility. Therefore, all-solid-state ES (Figure 2.19) prepared by the incorporation of gel electrolyte was proposed to provide safely operations for printable, flexible and wearable devices applications[86, 99]. Commonly, an effective way towards gel electrolyte is adding a polymer, such as polyvinyl alcohol (PVA), polyethylene glycol (PEO) and polyvinylpyrrolidone (PVP), into a proton conducting aqueous solutions, “fixing” water molecules via the formation of 3-D hydrophilic polymer networks. Significant efforts have been dedicated to develop all-solid-state flexible ES including film, paper, textile, woven cotton and fabrics[88, 89, 100, 101]. The

increase of proton conductivity for all-solid-state ES is of significance for development of high performance ES. High proton conductivity of polymer electrolyte could be achieved by fabrication of the thin film with a high degree of hydration. Many efforts have been made to improve the water retention capability and reduce the sensitivity to the environment of polymer electrolyte[102, 103].

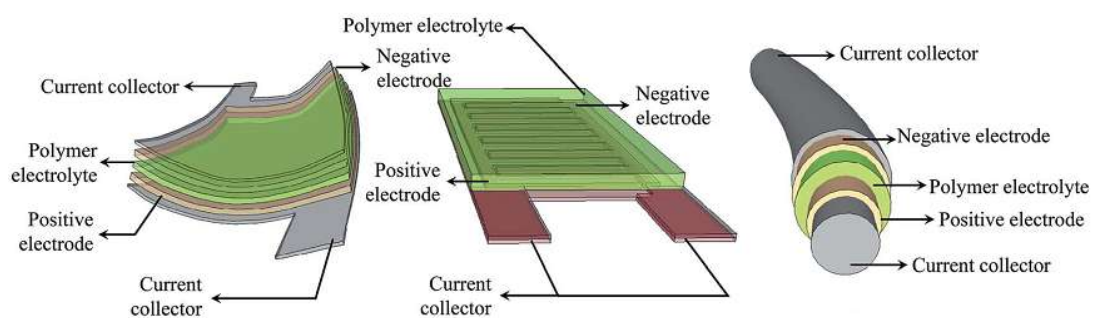


Figure 2.19 Schematic of all-solid-state ES in flexible sandwiched cell configuration (left), interdigitated finger cell configuration (middle), and coaxial fiber cell configuration (right)[86].

## 2.7 New application of ESs technique--Capacitive deionization

ESs address the need in energy storage devices with high capacitance, high power density, fast charge-discharge and cyclic stability. The research in ESs focuses on various aspects of supercapacitor technology, including advanced electrode materials, electrolytes, design and modeling. A new wave of interest in the ES technology is related to the application of ES devices for capacitive water purification [104, 105]. The capacitive water purification is based on capacitive deionization (CDI). It has been demonstrate that CDI is a robust, energy efficient, and cost effective technology

for desalination of water with a low or moderate salt content. The basic mechanism underlying capacitive deionization is similar to the operation of a EDLC and schematically shown in Figure 2.20. During the charging process, the ions were removed from solution and accumulated in electrodes for energy storage in electrical double-layers. The energy, released during the discharge of process, can be used for the charging of neighbouring cells. Therefore, the CDI technology offers the advantages of energy saving.

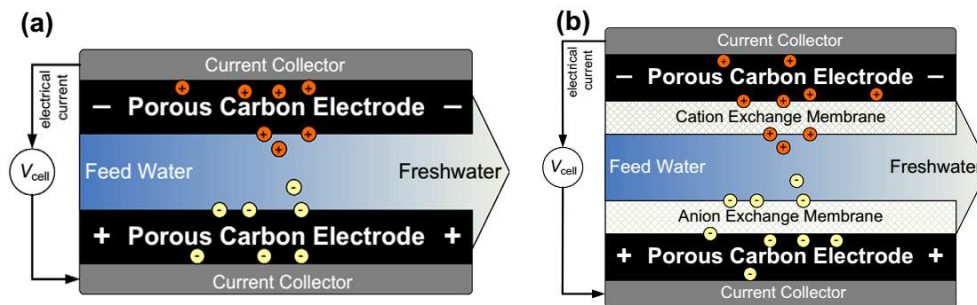


Figure 2.20 Schematic design of a cell for (a) capacitive deionization (CDI) and (b) membrane capacitive deionization (MCDI), where in front of the cathode a cation-exchange membrane is placed, while an anion-exchange membrane is placed in front of the anode[105].

Ongoing research of CDI is focused on the development of ion-exchange membrane capacitive deionization (MCDI) (Figure 2.20b), the optimization of operation modes, investigation of the kinetics of ion removal and development of efficient electrode materials. Special attention is focused on the surface modification of electrode materials. It was demonstrated that high deionization efficiency can be achieved using

high surface area carbon electrodes with high specific capacitance[106-108]. Other important properties of electrode materials are: high chemical stability, high electronic conductivity, surface charge and good wetting behaviour.

The impressive progress in the CDI technology has generated interest in the development of electrodes and devices for capacitive dye removal (CDR). Organic dyes are widely used for many applications, such as solar cells, textile industry, sensors, photocatalysis, lasers, medicine and other applications. The development of methods of dye removal from solutions is a subject of intense experimental works[109-111]. Many investigations were focused on the development of efficient adsorbents. Efforts to increase dye removal efficiency have resulted in the development of adsorbent materials with magnetic properties[112, 113]. Significant progress has been achieved in the development of chemical oxidation and reduction, photocatalytic and ozonation methods[114, 115]. Also of great interest are the electrochemical techniques, such as electrocoagulation, electrochemical reduction, electrochemical oxidation, photoassisted electrochemical methods and other techniques[110, 116, 117]. The limitations of such methods are related to significant energy consumption, electrode degradation and limited range of applications. The diversity and complexity of the dyes have generated the need in new methods of dye removal, which could be addressed by the development of CDR method.

## 2.8 References

- [1]M. Winter, R.J. Brodd, What Are Batteries, Fuel Cells, and Supercapacitors? *Chemical Reviews*, 104(2004) 4245-4270.
- [2]Y. Gogots. Patrice Simon, *Materials for electrochemical capacitors*, *Nature Materials*, 7(2008) 845-854.
- [3]B.E. Conway, *Electrochemical Supercapacitors: Scientific Fundamentals and Technological Applications*, Springer US, 1999.
- [4]M. Pumera, Graphene-based nanomaterials for energy storage, *Energy & Environmental Science*, 3(2011) 668-674.
- [5]L. Hu, M. Pasta, F.L. Mantia, L. Cui, S. Jeong, H.D. Deshazer, J.W. Choi, S.M. Han, Y. Cui, Stretchable, Porous, and Conductive Energy Textiles, *Nano Letters*, 10(2010) 708-714.
- [6]G. Wang, L. Zhang, J. Zhang, A review of electrode materials for electrochemical supercapacitors, *Chemical Society Reviews*, 41(2012) 797-828.
- [7]J.J. Yoo, K. Balakrishnan, J. Huang, V. Meunier, B.G. Sumpter, A. Srivastava, M. Conway, A.L. Mohana Reddy, J. Yu, R. Vajtai, P.M. Ajayan, Ultrathin Planar Graphene Supercapacitors, *Nano Letters*, 11(2011) 1423-1427.
- [8]P. Simon, Y. Gogotsi, Capacitive Energy Storage in Nanostructured Carbon-electrolyte Systems, *Accounts of Chemical Research*, 46(2013) 1094-1103.
- [9]X. Xia, J. Tu, Y. Zhang, J. Chen, X. Wang, C. Gu, C. Guan, J. Luo, H.J. Fan, Porous Hydroxide Nanosheets on Preformed Nanowires by Electrodeposition: Branched Nanoarrays for Electrochemical Energy Storage, *Chemistry of Materials*, 24(2012) 3793-3799.
- [10]L. Hao, B. Luo, X. Li, M. Jin, Y. Fang, Z. Tang, Y. Jia, M. Liang, A. Thomas, J. Yang, L. Zhi, Terephthalonitrile-derived nitrogen-rich networks for high performance supercapacitors, *Energy & Environmental Science*, 5(2012) 9747-9751.
- [11]W. Kim, M.Y. Kang, J.B. Joo, N.D. Kim, I.K. Song, P. Kim, J.R. Yoon, J. Yi, Preparation of ordered mesoporous carbon nanopipes with controlled nitrogen species for application in

- electrical double-layer capacitors, *Journal of Power Sources*, 195(2010) 2125-2129.
- [12]V. Augustyn, P. Simon, B. Dunn, Pseudocapacitive oxide materials for high-rate electrochemical energy storage, *Energy & Environmental Science*, 7(2014) 1597-1614.
- [13]C. Hu, C. Wang, Improving the utilization of ruthenium oxide within thick carbon - ruthenium oxide composites by annealing and anodizing for electrochemical supercapacitors, *Electrochemistry Communications*, 4(2002) 554-559.
- [14]W. Yong-gang, Z. Xiao-gang, Preparation and electrochemical capacitance of RuO<sub>2</sub>/TiO<sub>2</sub> nanotubes composites, *Electrochimica Acta*, 49(2004) 1957-1962.
- [15]C. Hu, K. Chang, M. Lin, Y. Wu, Design and Tailoring of the Nanotubular Arrayed Architecture of Hydrated RuO<sub>2</sub> for Next Generation Supercapacitors, *Nano Letters*, 6(2006) 2690-2695.
- [16]J. Lang, L. Kong, W. Wu, Y. Luo, L. Kang, Facile approach to prepare loose-packed NiO nano-flakes materials for supercapacitors, *Chemical Communications*, (2008) 4213-4215.
- [17]S. Xiong, C. Yuan, X. Zhang, B. Xi, Y. Qian, Controllable Synthesis of Mesoporous Co<sub>3</sub>O<sub>4</sub> Nanostructures with Tunable Morphology for Application in Supercapacitors, *Chemistry-A European Journal*, 15(2009) 5320-5326.
- [18]T. Zhu, J.S. Chen, X.W. Lou, Shape-controlled synthesis of porous Co<sub>3</sub>O<sub>4</sub> nanostructures for application in supercapacitors, *Journal of Materials Chemistry*, 20(2010) 7015-7020.
- [19]Z. Wu, W. Ren, D. Wang, F. Li, B. Liu, H. Cheng, High-Energy MnO<sub>2</sub> Nanowire/Graphene and Graphene Asymmetric Electrochemical Capacitors, *ACS Nano*, 4(2010) 5835-5842.
- [20]A.E. Fischer, K.A. Pettigrew, D.R. Rolison, R.M. Stroud, J.W. Long, Incorporation of Homogeneous, Nanoscale MnO<sub>2</sub> within Ultraporous Carbon Structures via Self-Limiting Electroless Deposition: Implications for Electrochemical Capacitors, *Nano Letters*, 7(2007) 281-286.
- [21]H. Zhang, G. Cao, Z. Wang, Y. Yang, Z. Shi, Z. Gu, Growth of Manganese Oxide Nanoflowers on Vertically-Aligned Carbon Nanotube Arrays for High-Rate Electrochemical Capacitive Energy Storage, *Nano Letters*, 8(2008) 2664-2668.

- [22]D.P. Dubal, S.H. Lee, J.G. Kim, W.B. Kim, C.D. Lokhande, Porous polypyrrole clusters prepared by electropolymerization for a high performance supercapacitor, *Journal of Materials Chemistry*, 22(2012) 3044-3052.
- [23]X. Lu, H. Dou, C. Yuan, S. Yang, L. Hao, F. Zhang, L. Shen, L. Zhang, X. Zhang, Polypyrrole/carbon nanotube nanocomposite enhanced the electrochemical capacitance of flexible graphene film for supercapacitors, *Journal of Power Sources*, 197(2012) 319-324.
- [24]X. Li, I. Zhitomirsky, Electrodeposition of polypyrrole-carbon nanotube composites for electrochemical supercapacitors, *Journal of Power Sources*, 221(2013) 49-56.
- [25]Q. Wu, Y. Xu, Z. Yao, A. Liu, G. Shi, Supercapacitors Based on Flexible Graphene/Polyaniline Nanofiber Composite Films, *ACS Nano*, 4(2010) 1963-1970.
- [26]T.C. Girija, M.V. Sangaranarayanan, Analysis of polyaniline-based nickel electrodes for electrochemical supercapacitors, *Journal of Power Sources*, 156(2006) 705-711.
- [27]D.C. Grahame, The Electrical Double Layer and the Theory of Electrocapillarity., *Chemical Reviews*, 41(1947) 441-501.
- [28]J. Wang, F. Kang, B. Wei, Engineering of MnO<sub>2</sub>-based nanocomposites for high-performance supercapacitors, *Progress in Materials Science*, 74(2015) 51-124.
- [29]L.L. Zhang, X.S. Zhao, Carbon-based materials as supercapacitor electrodes, *Chemical Society Reviews*, 38(2009) 2520-2531.
- [30]C. Hu, K. Chang, M. Lin, Y. Wu, Design and Tailoring of the Nanotubular Arrayed Architecture of Hydrous RuO<sub>2</sub> for Next Generation Supercapacitors, *Nano Letters*, 6(2006) 2690-2695.
- [31]W. Qian, F. Sun, Y. Xu, L. Qiu, C. Liu, S. Wang, F. Yan, Human hair-derived carbon flakes for electrochemical supercapacitors, *Energy & Environmental Science*, 1(7), (2014) 379-386.
- [32]H. Jiang, P.S. Lee, C. Li, 3D carbon based nanostructures for advanced supercapacitors, *Energy & Environmental Science*, 6(2013) 41-53.
- [33]L. Qie, W. Chen, H. Xu, X. Xiong, Y. Jiang, F. Zou, X. Hu, Y. Xin, Z. Zhang, Y. Huang, Synthesis of functionalized 3D hierarchical porous carbon for high-performance supercapacitor,

- Energy & Environmental Science, 8(6), (2013) 2497-2504.
- [34]W. Gu, M. Sevilla, A. Magasinski, A.B. Fuertes, G. Yushin, Sulfur-containing activated carbons with greatly reduced content of bottle neck pores for double-layer capacitors: a case study for pseudocapacitance detection, *Energy & Environmental Science*, 6(2013) 2465-2476.
- [35]B. An, S. Xu, L. Li, J. Tao, F. Huang, X. Geng, Carbon nanotubes coated with a nitrogen-doped carbon layer and its enhanced electrochemical capacitance, *Journal of Materials Chemistry A*, 1(2013) 7222-7228.
- [36]K. Shi, I. Zhitomirsky, Asymmetric Supercapacitors Based on Activated-Carbon-Coated Carbon Nanotubes, *ChemElectroChem*, 2(2015) 396-403.
- [37]H. Wang, Z. Wu, F. Meng, D. Ma, X. Huang, L. Wang, X. Zhang, Nitrogen-Doped Porous Carbon Nanosheets as Low-Cost, High-Performance Anode Material for Sodium-Ion Batteries, *ChemSusChem*, 6(2013) 56-60.
- [38]L. Chen, X. Zhang, H. Liang, M. Kong, Q. Guan, P. Chen, Z. Wu, S. Yu, Synthesis of Nitrogen-Doped Porous Carbon Nanofibers as an Efficient Electrode Material for Supercapacitors, *ACS Nano*, 6(2012) 7092-7102.
- [39]P. Simon, A.F. Burke, Nanostructured carbons: double-layer capacitance and more, *The electrochemical society interface*, 17(2008) 38.
- [40]J. Chmiola, G. Yushin, Y. Gogotsi, C. Portet, P. Simon, P.L. Taberna, Anomalous Increase in Carbon Capacitance at Pore Sizes Less than 1 Nanometer, *Science*, 313(2006) 1760-1763.
- [41]G.A. Snook, P. Kao, A.S. Best, Conducting-polymer-based supercapacitor devices and electrodes, *Journal of Power Sources*, 196(2011) 1-12.
- [42]R. Ramya, R. Sivasubramanian, M.V. Sangaranarayanan, Conducting polymers-based electrochemical supercapacitors — Progress and prospects, *Electrochimica Acta*, 101(2013) 109-129.
- [43]G.A. Snook, P. Kao, A.S. Best, Conducting-polymer-based supercapacitor devices and electrodes, *Journal of Power Sources*, 196(2011) 1-12.

- [44]A. Rudge, J. Davey, I. Raistrick, S. Gottesfeld, J.P. Ferraris, Conducting polymers as active materials in electrochemical capacitors, *Journal of Power Sources*, 47(1994) 89-107.
- [45]Z.H. Dong, Y.L. Wei, W. Shi, G.A. Zhang, Characterisation of doped polypyrrole/manganese oxide nanocomposite for supercapacitor electrodes, *Materials Chemistry and Physics*, 131(2011) 529-534.
- [46]C. Yang, P. Liu, Y. Zhao, Preparation and characterization of coaxial halloysite/polypyrrole tubular nanocomposites for electrochemical energy storage, *Electrochimica Acta*, 55(2010) 6857-6864.
- [47]X. Zhang, Bai, Surface Electric Properties of Polypyrrole in Aqueous Solutions, *Langmuir*, 19(2003) 10703-10709.
- [48]G. Lu, C. Li, G. Shi, Polypyrrole micro- and nanowires synthesized by electrochemical polymerization of pyrrole in the aqueous solutions of pyrenesulfonic acid, *Polymer*, 47(2006) 1778-1784.
- [49]S. Goel, N.A. Mazumdar, A. Gupta, Synthesis and characterization of polypyrrole nanofibers with different dopants, *Polymers for Advanced Technologies*, 21(2010) 205-210.
- [50]L. Qie, L. Yuan, W. Zhang, W. Chen, Y. Huang, Revisit of Polypyrrole as Cathode Material for Lithium-Ion Battery, *Journal of The Electrochemical Society*, 159(2012) A1624-A1629.
- [51]M. Han, Y. Chu, D. Han, Y. Liu, Fabrication and characterizations of oligopyrrole doped with dodecylbenzenesulfonic acid in reverse microemulsion, *Journal of Colloid and Interface Science*, 296(2006) 110-117.
- [52]G.R. Mitchell, F.J. Davis, C.H. Legge, The effect of dopant molecules on the molecular order of electrically-conducting films of polypyrrole, *Synthetic Metals*, 26(1988) 247-257.
- [53]B. Weng, R. Shepherd, J. Chen, G.G. Wallace, Gemini surfactant doped polypyrrole nanodispersions: an inkjet printable formulation, *Journal of Materials Chemistry*, 21(2011) 1918-1924.
- [54]Y. Zhu, I. Zhitomirsky, Influence of dopant structure and charge on supercapacitive behavior of

- polypyrrole electrodes with high mass loading, *Synthetic Metals*, 185, (2013) 126-132.
- [55]Y. Zhu, K. Shi, I. Zhitomirsky, Anionic dopant-dispersants for synthesis of polypyrrole coated carbon nanotubes and fabrication of supercapacitor electrodes with high active mass loading, *Journal of Materials Chemistry A*, 2(2014) 14666-14673.
- [56]P. Wang, J. Yu, Dopant-dependent variation in the distribution of polarons and bipolarons as charge-carriers in polypyrrole thin films synthesized by oxidative chemical polymerization, *Reactive and Functional Polymers*, 72(2012) 311-316.
- [57]P. Syed Abthagir, R. Saraswathi, Thermal stability of polypyrrole prepared from a ternary eutectic melt, *Materials Chemistry and Physics*, 92(2005) 21-26.
- [58]J. Feng, W. Yan, L. Zhang, Synthesis of polypyrrole micro/nanofibers via a self-assembly process, *Microchimica Acta*, 166(2009) 261-267.
- [59]P. Murray, G.M. Spinks, G.G. Wallace, R.P. Burford, In-situ mechanical properties of tosylate doped (pts) polypyrrole, *Synthetic Metals*, 84(1997) 847-848.
- [60]A. Talaie, G.G. Wallace, The effect of the counterion on the electrochemical properties of conducting polymers-a study using resistometry, *Synthetic Metals*, 63(1994) 83-88.
- [61]K. Fic, G. Lota, E. Frackowiak, Electrochemical properties of supercapacitors operating in aqueous electrolyte with surfactants, *Electrochimica Acta*, 55(2010) 7484-7488.
- [62]J. Wang, Y. Xu, X. Chen, X. Du, Electrochemical supercapacitor electrode material based on polypyrrole/poly(3,4-ethylenedioxythiophene) composite, *Journal of Power Sources*, 163(2007) 1120-1125.
- [63]Y. Zhu, K. Shi, I. Zhitomirsky, Polypyrrole coated carbon nanotubes for supercapacitor devices with enhanced electrochemical performance, *Journal of Power Sources*, 268(2014) 233-239.
- [64]C. Hu, W. Chen, K. Chang, How to Achieve Maximum Utilization of Hydrous Ruthenium Oxide for Supercapacitors, *Journal of The Electrochemical Society*, 151(2004) A281-A290.
- [65]S.W. Zhang, G.Z. Chen, Manganese oxide based materials for supercapacitors, *Energy Materials: Materials Science and Engineering for Energy Systems*, 3(2008) 186-200.

- [66]R.N. Reddy, R.G. Reddy, Sol - gel MnO<sub>2</sub> as an electrode material for electrochemical capacitors, *Journal of Power Sources*, 124(2003) 330-337.
- [67]C.Y. Lee, H.M. Tsai, H.J. Chuang, S.Y. Li, P. Lin, T.Y. Tseng, Characteristics and Electrochemical Performance of Supercapacitors with Manganese Oxide-Carbon Nanotube Nanocomposite Electrodes, *Journal of The Electrochemical Society*, 152(2005) A716-A720.
- [68]Q. Qu, P. Zhang, B. Wang, Y. Chen, S. Tian, Y. Wu, R. Holze, Electrochemical Performance of MnO<sub>2</sub> Nanorods in Neutral Aqueous Electrolytes as a Cathode for Asymmetric Supercapacitors, *The Journal of Physical Chemistry C*, 113(2009) 14020-14027.
- [69]W. Wei, X. Cui, W. Chen, D.G. Ivey, Manganese oxide-based materials as electrochemical supercapacitor electrodes, *Chemical Society Reviews*, 40(2011) 1697-1721.
- [70]Y. Wang, I. Zhitomirsky, Electrophoretic Deposition of Manganese Dioxide-Multiwalled Carbon Nanotube Composites for Electrochemical Supercapacitors, *Langmuir*, 25(2009) 9684-9689.
- [71]Y. Wang, H. Liu, X. Sun, I. Zhitomirsky, Manganese dioxide - carbon nanotube nanocomposites for electrodes of electrochemical supercapacitors, *Scripta Materialia*, 61(2009) 1079-1082.
- [72]H. Lee, H. Kim, M.S. Cho, J. Choi, Y. Lee, Fabrication of polypyrrole (PPy)/carbon nanotube (CNT) composite electrode on ceramic fabric for supercapacitor applications, *Electrochimica Acta*, 56(2011) 7460-7466.
- [73]H. Xia, Y. Wang, J. Lin, L. Lu, Hydrothermal synthesis of MnO<sub>2</sub>/CNT nanocomposite with a CNT core/porous MnO<sub>2</sub> sheath hierarchy architecture for supercapacitors, *Nanoscale Research Letters*, 7(2012) 1-10.
- [74]W. Jiang, K. Zhang, L. Wei, D. Yu, J. Wei, Y. Chen, Hybrid ternary rice paper-manganese oxide-carbon nanotube nanocomposites for flexible supercapacitors, *Nanoscale*, 5(2013) 11108-11117.
- [75]L. Zhao, J. Yu, W. Li, S. Wang, C. Dai, J. Wu, X. Bai, C. Zhi, Honeycomb porous MnO<sub>2</sub> nanofibers assembled from radially grown nanosheets for aqueous supercapacitors with high working voltage and energy density, *Nano Energy*, 4(2014) 39-48.

- [76]K. Shi, I. Zhitomirsky, Asymmetric Supercapacitors Based on Activated-Carbon-Coated Carbon Nanotubes, *ChemElectroChem*, 2(2015) 396-403.
- [77]H. Xia, M. Lai, L. Lu, Nanoflaky MnO<sub>2</sub>/carbon nanotube nanocomposites as anode materials for lithium-ion batteries, *Journal of Materials Chemistry*, 20(2010) 6896-6902.
- [78]M. Zhi, C. Xiang, J. Li, M. Li, N. Wu, Nanostructured carbon-metal oxide composite electrodes for supercapacitors: a review, *Nanoscale*, 5(2013) 72-88.
- [79]H. Gao, F. Xiao, C.B. Ching, H. Duan, High-Performance Asymmetric Supercapacitor Based on Graphene Hydrogel and Nanostructured MnO<sub>2</sub>, *ACS Applied Materials & Interfaces*, 4(2012) 2801-2810.
- [80]C. Yang, J. Shen, C. Wang, H. Fei, H. Bao, G. Wang, All-solid-state asymmetric supercapacitor based on reduced graphene oxide/carbon nanotube and carbon fiber paper/polypyrrole electrodes, *Journal of Materials Chemistry A*, (2013).
- [81]Z. Su, C. Yang, C. Xu, H. Wu, Z. Zhang, T. Liu, C. Zhang, Q. Yang, B. Li, F. Kang, Co-electro-deposition of the MnO<sub>2</sub>-PEDOT:PSS nanostructured composite for high areal mass, flexible asymmetric supercapacitor devices, *Journal of Materials Chemistry A*, 1(2013) 12432-12440.
- [82]H. Wang, H. Yi, X. Chen, X. Wang, Asymmetric supercapacitors based on nano-architected nickel oxide/graphene foam and hierarchical porous nitrogen-doped carbon nanotubes with ultrahigh-rate performance, *Journal of Materials Chemistry A*, (2014).
- [83]M. Li, S. Xu, C. Cherry, Y. Zhu, R. Huang, R. Qi, P. Yang, L. Wang, P.K. Chu, Asymmetrical Supercapacitor Composed of Thin Co(OH)<sub>2</sub> Nanoflakes on Three-Dimensional Ni/Si Microchannel Plates with Superior Electrochemical Performance, *Electrochimica Acta*, 149(2014) 18-27.
- [84]V. Khomenko, E. Raymundo-Piñero, F. Béguin, Optimisation of an asymmetric manganese oxide/activated carbon capacitor working at 2.0 V in aqueous medium, *Journal of Power Sources*, 153(2006) 183-190.

- [85]H. Wang, Z. Li, Y. Huang, Q. Li, X. Wang, A novel hybrid supercapacitor based on spherical activated carbon and spherical MnO<sub>2</sub> in a non-aqueous electrolyte, *Journal of Materials Chemistry*, 20(2010) 3883-3889.
- [86]H. Gao, K. Lian, Proton-conducting polymer electrolytes and their applications in solid supercapacitors: a review, *RSC Advances*, 4(2014) 33091-33113.
- [87]C. Zhao, C. Wang, Z. Yue, K. Shu, G.G. Wallace, Intrinsically Stretchable Supercapacitors Composed of Polypyrrole Electrodes and Highly Stretchable Gel Electrolyte, *ACS Applied Materials & Interfaces*, 5(2013) 9008-9014.
- [88]Q. Wang, J. Xu, X. Wang, B. Liu, X. Hou, G. Yu, P. Wang, D. Chen, G. Shen, Core - Shell CuCo<sub>2</sub>O<sub>4</sub>@MnO<sub>2</sub> Nanowires on Carbon Fabrics as High-Performance Materials for Flexible, All-Solid-State, Electrochemical Capacitors, *ChemElectroChem*, (2013) n/a-n/a.
- [89]M. Sawangphruk, M. Suksomboon, K. Kongsupornsak, J. Khuntilo, P. Srimuk, Y. Sanguansak, P. Klunbud, P. Suktha, P. Chiochan, High-performance supercapacitors based on silver nanoparticle-polyaniline-graphene nanocomposites coated on flexible carbon fiber paper, *Journal of Materials Chemistry A*, (2013).
- [90]Q. Gao, L. Demarconnay, E. Raymundo-Pinero, F. Béguin, Exploring the large voltage range of carbon/carbon supercapacitors in aqueous lithium sulfate electrolyte, *Energy & Environmental Science*, 5(2012) 9611-9617.
- [91]K. Fic, G. Lota, M. Meller, E. Frackowiak, Novel insight into neutral medium as electrolyte for high-voltage supercapacitors, *Energy & Environmental Science*, 5(2012) 5842-5850.
- [92]L. Demarconnay, E. Raymundo-Piñero, F. Béguin, A symmetric carbon/carbon supercapacitor operating at 1.6 V by using a neutral aqueous solution, *Electrochemistry Communications*, 12(2010) 1275-1278.
- [93]R. Wang, J. Lang, X. Yan, Effect of surface area and heteroatom of porous carbon materials on electrochemical capacitance in aqueous and organic electrolytes, *Science China Chemistry*, 57(2014) 1570-1578.

- [94]Q. Zhang, J. Rong, D. Ma, B. Wei, The governing self-discharge processes in activated carbon fabric-based supercapacitors with different organic electrolytes, *Energy & Environmental Science*, 4(2011) 2152-2159.
- [95]M. Armand, F. Endres, D.R. MacFarlane, H. Ohno, B. Scrosati, Ionic-liquid materials for the electrochemical challenges of the future, *Nature Materials*, 8(2009) 621-629.
- [96]A. Balducci, R. Dugas, P.L. Taberna, P. Simon, D. Plée, M. Mastragostino, S. Passerini, High temperature carbon-carbon supercapacitor using ionic liquid as electrolyte, *Journal of Power Sources*, 165(2007) 922-927.
- [97]M. Lazzari, M. Mastragostino, F. Soavi, Capacitance response of carbons in solvent-free ionic liquid electrolytes, *Electrochemistry Communications*, 9(2007) 1567-1572.
- [98]L. Wei, M. Sevilla, A.B. Fuertes, R. Mokaya, G. Yushin, Polypyrrole-Derived Activated Carbons for High-Performance Electrical Double-Layer Capacitors with Ionic Liquid Electrolyte, *Advanced Functional Materials*, 22(2012) 827-834.
- [99]C. Meng, C. Liu, L. Chen, C. Hu, S. Fan, Highly Flexible and All-Solid-State Paperlike Polymer Supercapacitors, *Nano Letters*, 10(2010) 4025-4031.
- [100]B. Liu, B. Liu, Q. Wang, X. Wang, Q. Xiang, D. Chen, G. Shen, New Energy Storage Option: Toward ZnCo<sub>2</sub>O<sub>4</sub> Nanorods/Nickel Foam Architectures for High-Performance Supercapacitors, *ACS Applied Materials & Interfaces*, 5(2013) 10011-10017.
- [101]S.T. Senthilkumar, R.K. Selvan, J.S. Melo, C. Sanjeeviraja, High Performance Solid-State Electric Double Layer Capacitor from Redox Mediated Gel Polymer Electrolyte and Renewable Tamarind Fruit Shell Derived Porous Carbon, *ACS Applied Materials & Interfaces*, 5(2013) 10541-10550.
- [102]H. Gao, K. Lian, High rate all-solid electrochemical capacitors using proton conducting polymer electrolytes, *Journal of Power Sources*, 196(2011) 8855-8857.
- [103]S.K. Tripathi, A. Jain, A. Gupta, M. Mishra, Electrical and electrochemical studies on magnesium ion-based polymer gel electrolytes, *Journal of Solid State Electrochemistry*, 16(2012) 1799-1806.

- [104]M.A. Anderson, A.L. Cudero, J. Palma, Capacitive deionization as an electrochemical means of saving energy and delivering clean water. Comparison to present desalination practices: Will it compete? *Electrochimica Acta*, 55(2010) 3845-3856.
- [105]S. Porada, R. Zhao, A. van der Wal, V. Presser, P.M. Biesheuvel, Review on the science and technology of water desalination by capacitive deionization, *Progress in Materials Science*, 8(2013) 1388-1442.
- [106]J. Yang, L. Zou, N.R. Choudhury, Ion-selective carbon nanotube electrodes in capacitive deionisation, *Electrochimica Acta*, 91(2013) 11-19.
- [107]X. Wen, D. Zhang, T. Yan, J. Zhang, L. Shi, Three-dimensional graphene-based hierarchically porous carbon composites prepared by a dual-template strategy for capacitive deionization, *Journal of Materials Chemistry A*, (2013).
- [108]H. Wang, D. Zhang, T. Yan, X. Wen, J. Zhang, L. Shi, Q. Zhong, Three-dimensional macroporous graphene architectures as high performance electrodes for capacitive deionization, *Journal of Materials Chemistry A*, (2013).
- [109]E. Forgacs, T. Cserhádi, G. Oros, Removal of synthetic dyes from wastewaters: a review, *Environment International*, 30(2004) 953-971.
- [110]C.A. Martínez-Huitle, E. Brillas, Decontamination of wastewaters containing synthetic organic dyes by electrochemical methods: A general review, *Applied Catalysis B: Environmental*, 87(2009) 105-145.
- [111]M. Rafatullah, O. Sulaiman, R. Hashim, A. Ahmad, Adsorption of methylene blue on low-cost adsorbents: A review, *Journal of Hazardous Materials*, 177(2010) 70-80.
- [112]S. Zhang, M. Zeng, J. Li, J. Li, J. Xu, X. Wang, Porous magnetic carbon sheets from biomass as an adsorbent for the fast removal of organic pollutants from aqueous solution, *Journal of Materials Chemistry A*, (2014).
- [113]X. Zhu, Y. Liu, C. Zhou, S. Zhang, J. Chen, Novel and High-Performance Magnetic Carbon Composite Prepared from Waste Hydrochar for Dye Removal, *ACS Sustainable Chemistry &*

Engineering, 2(2014) 969-977.

- [114]Z. Zhang, F. Xiao, Y. Guo, S. Wang, Y. Liu, One-Pot Self-Assembled Three-Dimensional TiO<sub>2</sub>-Graphene Hydrogel with Improved Adsorption Capacities and Photocatalytic and Electrochemical Activities, *ACS Applied Materials & Interfaces*, 5(2013) 2227-2233.
- [115]R. Pelegrini, P. Peralta-Zamora, A.R. de Andrade, J. Reyes, N. Durán, Electrochemically assisted photocatalytic degradation of reactive dyes, *Applied Catalysis B: Environmental*, 22(1999) 83-90.
- [116]L. Wang, X. Wu, W. Xu, X. Huang, J. Liu, A. Xu, Stable Organic - Inorganic Hybrid of Polyaniline/ $\alpha$ -Zirconium Phosphate for Efficient Removal of Organic Pollutants in Water Environment, *ACS Applied Materials & Interfaces*, 4(2012) 2686-2692.
- [117]Y. Liu, Z. Chen, C. Shek, C.M.L. Wu, J.K.L. Lai, Hierarchical Mesoporous MnO<sub>2</sub> Superstructures Synthesized by Soft-Interface Method and Their Catalytic Performances, *ACS Applied Materials & Interfaces*, 6(2014) 9776-9784.

### **3. Problem statements and proposed approaches**

#### **3.1 Dispersion of carbon nanotube (CNT) and graphene**

##### 3.1.1 Challenges

Regarding composite electrodes, the combination of high surface area carbon, especially carbon nanotubes (CNTs) and graphene, with pseudocapacitive materials is believed to be an effective solution for improving both capacitive performance and cycle stability of electrodes[1-3]. However, CNTs were generally in a bundled structure as received, whereas graphene showed restacking due to van der Waals attraction. In order to utilize the benefits of CNT and graphene, a homogeneous mixture must be formed.

The methods to disperse CNTs and graphene, including mechanical dispersion, chemical functionalization and physical functionalization, were reported in previous studies[4-6]. It was found that CNTs can be easily and seriously damaged if the mechanical treatments are too aggressive or too long. Chemical functionalization is based on the covalent linkage of functional entities onto carbon scaffold of CNTs. Concentrated acids or strong oxidants are usually used for CNT chemical functionalization, which are environmentally unfriendly and changed the properties of the CNTs.

Non-covalent functionalization using surfactant is an alternative method for tuning the interfacial properties of CNT and graphene. The mechanism of adsorbing surfactant at interface was discussed in ref. [5, 7]. In general, a surfactant has both polar (hydrophilic) and nonpolar (hydrophobic) moieties. At the interface, the molecule can be oriented in different ways. The hydrophilic head is directed toward the bulk water, and the hydrophobic chains orient themselves toward carbon materials through  $\pi$ - $\pi$  interaction. The microscopic pictures of how the adsorbed amphiphilic molecules organize on CNT were studied by C. Richard [8]. Three types of surfactant assembly structures were proposed as shown in Figure 3.1. So far sodium dodecyl sulfate (SDS, surfactant) was recognized as the best surfactant for the dispersion of CNT. However, it required the concentration of SDS to be several to ten times larger than that of CNT[9].

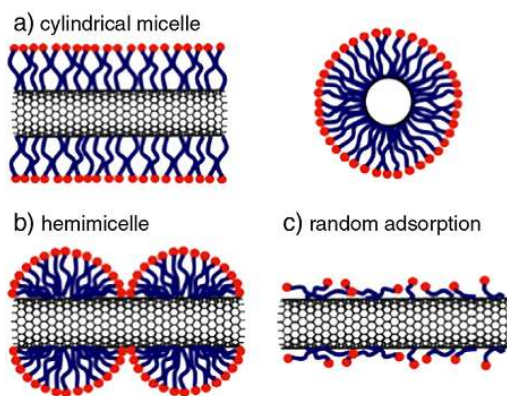


Figure 3.1 Schematic illustration of various surfactant assembly structures on a CNT, including (a) cylindrical micelles, side and cross-section views, (b) hemimicelle, and (c) random adsorption [5].

### 3.1.2 Proposed approaches

Here we are looking for effective and facile ways to disperse both multi-wall carbon nanotube (MWCNT) and graphene. Small organic dispersing agents, such as safranin and malachite green oxalate salt (shown in Figure 3.2), are proposed to disperse individual materials, including MWCNT, graphene and PPy nano-fibers. The criterion we selected cationic aromatic surfactants is related to their non-ionic interaction with the solid surface and small molar weight possible to enhance the charge efficiency. The attachment of the surfactant to MWCNT and graphene was demonstrated in Figure 3.3. One side of aromatic ring could adsorb on either MWCNT or graphene through  $\pi$ - $\pi$  interactions. The primary amine groups and quaternary amine group of molecular, which are highly hydrophilic, could improve the water solubility. Our experiment results have suggested that MWCNT, graphene and PPy nano-fibers could be charged through the adsorption of these small molecules. Such universal dispersing agent offers prospective techniques for the fabrication of advanced composite electrodes, containing MWCNT, graphene and PPy nano-fibers.

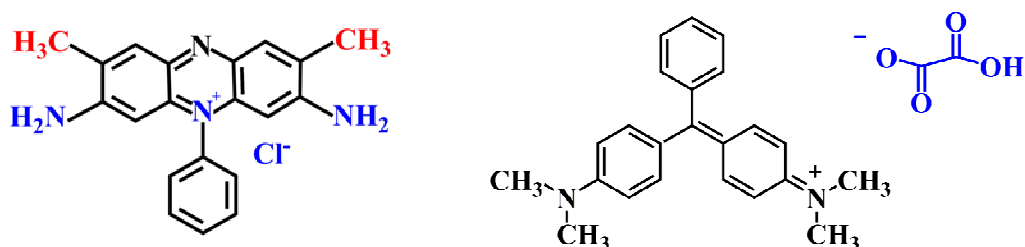


Figure 3.2 Chemical structure of (A) safranin and (B) malachite green oxalate salt.

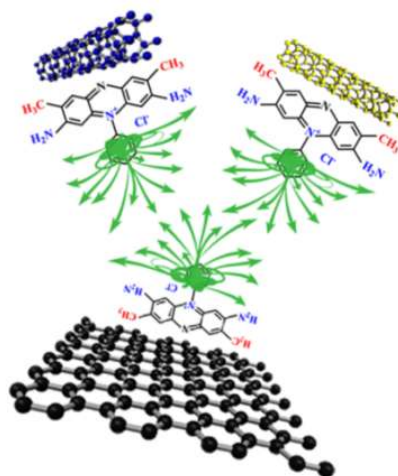


Figure 3.3 Possible adsorption of safranin on MWCNT and graphene.

## 3.2 Energy density of ESs

### 3.2.1 Challenges

Figure 2.2 has compared specific power versus specific energy of modern energy storage devices. ESs suffer from limited energy density ( $0.05\text{-}30 \text{ Wh kg}^{-1}$ ) when compared with batteries ( $>10 \text{ Wh kg}^{-1}$ ). Commercially available ESs provide energy densities of less than  $5 \text{ Wh kg}^{-1}$ . If a large energy capacity is required for an application, a large ES must be constructed, driving up the cost. Improvement of energy density is the major challenge for ES applications.

The energy density of ES could be improved by fabrication of carbon based ES in organic electrolytes or hybrid configuration with high capacitance electrodes. However, most organic electrolytes are relatively expensive, toxic and flammable. Moreover, carbon electrodes showed reduced capacitance and increased impedance in

organic electrolytes. Based on this consideration, many efforts have been made to increase voltage window of carbon based supercapacitors using environmentally friendly, cost-effective and safe aqueous electrolytes.

MnO<sub>2</sub>-activated carbon (AC) hybrid ES are currently under intensive investigation for high energy density aqueous ESs. The interest in MnO<sub>2</sub> for positive ES electrodes is attributed to high specific capacitance of MnO<sub>2</sub>. The use of hybrid ES, containing positive MnO<sub>2</sub> and negative AC electrodes offers the advantage of increased voltage window in aqueous electrolyte due to overvoltage of water decomposition. However, the electronic conductivity of MnO<sub>2</sub> is low. This problem was addressed by the fabrication of MnO<sub>2</sub>-carbon nanotube (CNT) composites. In order to improve the electrical contact of CNT and MnO<sub>2</sub>, composite materials were prepared by the chemical reaction between KMnO<sub>4</sub> and CNT[10, 11]:



It was found that the method allows scalable synthesis of MnO<sub>2</sub> coated CNT, however it generates problems related to carbon consumption in the redox reaction and collapse of carbon bonding structure of CNT, that degrade the electrical conductivity. Additionally, the MnO<sub>2</sub> mass loading on the composite is relative low. Further improvements on the energy performance generates the needs in developing new methods for fabrication of MnO<sub>2</sub>/AC hybrid ES using natural aqueous electrolyte.

## 3.2.2 Proposed approaches

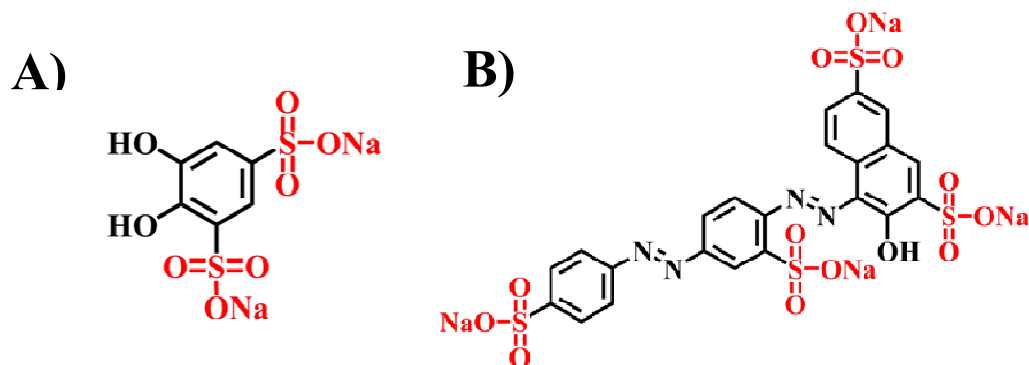


Figure 3.4 Chemical structure of aromatic dopants proposed to improve the capacitive behaviour of PPy. A) Tiron and B) Ponceau S.

According to the Eq. 2.3, the energy density of ESs is determined by specific capacitance and voltage window of the cell. To increase the specific capacitance, we proposed aromatic dopants for PPy electrodes, which belong to aromatic sulfonate family or catechol family. The investigation of electrochemically prepared PPy, containing aromatic sulfonate dopants, showed that film conductivity increased with increasing charge to mass ratio of the dopant molecules[12, 13]. In this regards, Tiron and Ponceau S were selected due to their relatively high charge to mass ratio, compared to other aromatic sulfonate dopants. Their chemical structures were shown in Figure 3.4. Moreover, Tiron is a strong complexing agent due to hydroxyl groups bonded to adjacent carbon atoms of the aromatic ring. The proposed chemisorption mechanism involved the deprotonation of the phenolic hydroxyl groups of the catechol and chelation of metal ions on the inorganic surface[12, 13]. The strong

adhesion of Tiron to various surfaces is attractive for the development of PPy film electrodes using electro-polymerization method.

It has been known that the attached dopant influences the structure of PPy [16-18]. The sulfonic groups of Tiron can be involved in the doping of one PPy molecule or two different polymer chains. Previous study proposed that cooperation of multi-charge dopants to PPy improved its electronic conductivity [19]. The improvement of energy-storage capability of PPy is attributed to unchaining dopant molecule during the charge-discharge process[20].

The electrochemical performance of PPy is influenced by its microstructure. Recently, an interesting nano-fiber morphology of conducting polymers (Figure 3.5) was reported. The nano-fibers were prepared by decomposition of oxidative templates, which were obtained from the chemical reaction between cationic surfactant cetyltrimethylammonium bromide (CTAB) and anionic oxidant ammonium persulfate (APS). PPy nano-fibers showed higher surface area and higher conductivity compared to PPy particles prepared by tradition polymerization method [21]. In our study, the applications of oxidative template were explored. We found that the oxidative template, cetrymonium persulfate  $(CTA)_2S_2O_8$ , was in the form of nano-crystal and showed efficient dispersion as well as electrophoretic deposition (EPD) of MWCNT. The dissociation of  $(CTA)_2S_2O_8$  was catalyzed by MWCNT. The prepared  $(CTA)_2S_2O_8$  nano-crystals were used as multi-functional agents for the synthesis of

PPy-MWCNT composites, as the dispersants for MWCNT and the oxidants for PPy. A core-shell structure PPy coated MWCNT was obtained by dissolution of the nano-crystals. The testing results suggested that PPy coated MWCNT prepared by  $(\text{CTA})_2\text{S}_2\text{O}_8$  showed uniform coating and improved electrochemical performance. In addition, we fabricated ES electrodes containing PPy nano-fibers and PPy nano-fibers/MWCNT composites. The aims of our study are to develop new methods for colloidal processing of individual materials and fabrication of composite electrodes.

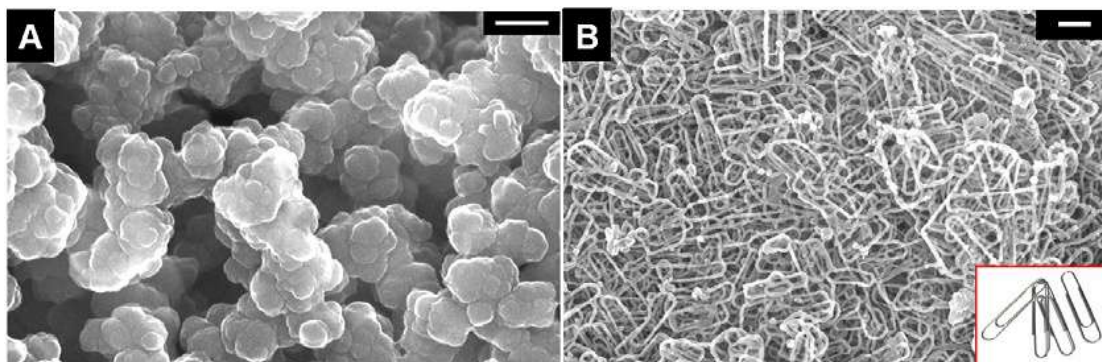


Figure 3.5 SEM images of (A) granular polypyrrole without additive. (scale bar: 200 nm); (B) polypyrrole nano-fibers prepared by  $(\text{CTA})_2\text{S}_2\text{O}_8$  (scale bar 1  $\mu\text{m}$ )[21].

The use of MWCNT as electrode materials offers the advantages of high electronic conductivity and good capacitance retention at high charge-discharge rates[22, 23]. However, the specific capacitance of MWCNT is lower than that of activated carbon (AC). The interest in AC materials is attributed to their high surface area, which allows high specific capacitance. But it is important to note that AC materials are

usually prepared at very high temperatures, which result in relatively large AC size [22, 23]. The large size of AC particles generates problems related to poor contact. Recent investigations indicated that capacitive behaviour of AC can be improved by introducing various heteroatoms, such as N, P and S. It was found that the heteroatom doped AC resulted in higher electronic conductivity, improved wettability and enhanced capacitive performance. The increased specific capacitance is attributed to surface functional groups, which provide additional sites for redox reactions[26-28]. PPy is a good polymer precursor for the fabrication of N-doped carbons. The use of nano-structured PPy allows fabrication of AC materials with small particle size and ultrahigh specific surface area.

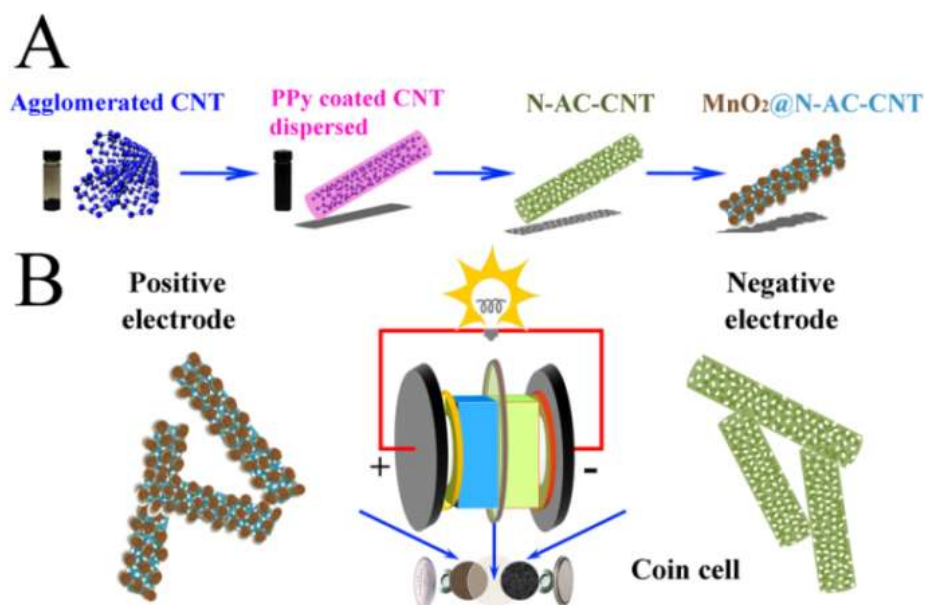


Figure 3.6 Fabrication of (A) MnO<sub>2</sub>@N-AC-MWCNT and (B) coin cells, containing MnO<sub>2</sub>@N-AC-MWCNT positive electrode and N-AC-MWCNT negative electrode.

In our investigation, ES devices were fabricated using N-doped AC coated MWCNT (N-AC-MWCNT), preparing by carbonization and chemical activation of PPy coated MWCNT. We found that the problems related with MWCNT degradation in preparation of MnO<sub>2</sub> coated MWCNT could be avoided by the use of sacrificial AC layer of N-AC-MWCNT. It allowed us to obtain relatively high mass content of MnO<sub>2</sub> in the composite materials. The hybrid ES devices (Figure 3.6) could be fabricated using MnO<sub>2</sub> coated MWCNT (MnO<sub>2</sub>@ N-AC-MWCNT) as positive electrode and N-AC-MWCNT as negative electrode.

### 3.3 Real performance of ESs

#### 3.3.1 Challenges

The specific capacitance ( $C_m$ ), expressed in a unit of  $F\ g^{-1}$ , is often used to evaluate the capacitive behaviour of the electrode. However, mass-normalized capacitance  $C_m$  decreases with increase of materials loading. But this phenomenon is usually omitted from current available papers when they claimed a high  $C_m$ . In 2011, Gogotsi et. al. published their opinions on *Science* regarding to evaluation of the true performance of ES. The paper demonstrated that gravimetric characteristics (such as  $C_m$ ) alone cannot provide realistic picture of material performance, especially at high material loadings[29]. For example, if the current collector is taken into consideration, an electrode with large loading (thick film) has  $C_m$  12 times larger than that of an electrode with small loading (thin film), with only a little sacrificing of power density

(Figure 3.7A). If the capacitance is calculated with respect to electrode volume or area instead of electrode mass, the capacitance of electrode with large loading is about 100 times larger than that of electrode with small loading (Figure 3.7B). For real applications, ES must be composed with large mass loading electrodes. But most current studies are only focusing on improving  $C_m$  of electrode materials and few studies pay attentions on the geometric capacitance performance of ES.

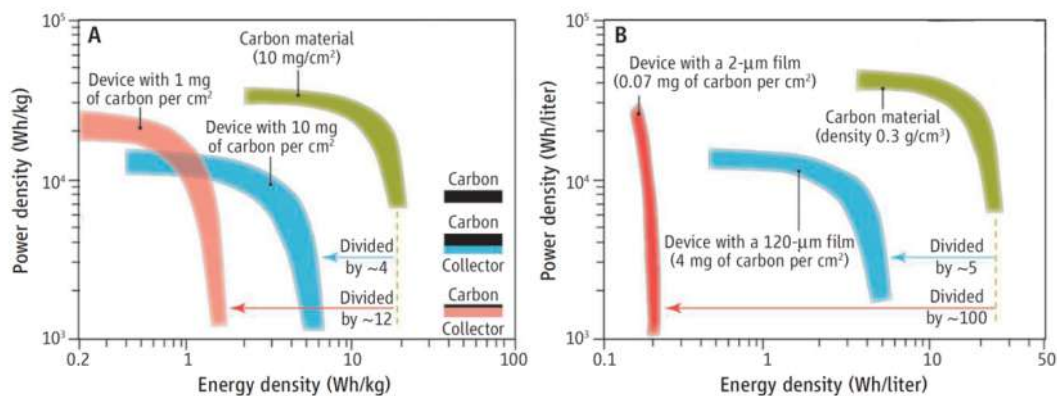


Figure 3.7 The plots for the same electrochemical capacitors are (A) on a gravimetric (per weight) basis and (B) on a volumetric basis[29].

Very recently, area normalized performance have attracted more attention over gravimetric performance, since ESs require power sources delivering the maximum energy in a very limited dimension. Area performance reflects how much and how fast energy can be stored in a unit area of a packed ESs. It is the most important criterion to evaluate the real performance of an ES devices[30, 31]. A good real performance of ES requires the fabrication of high performance electrode with a large materials

loading and effective configuration of ES cell. Unfortunately, the current area normalized performance of different ES devices is still far from a satisfactory level for practical applications.

### 3.3.2 Proposed approaches

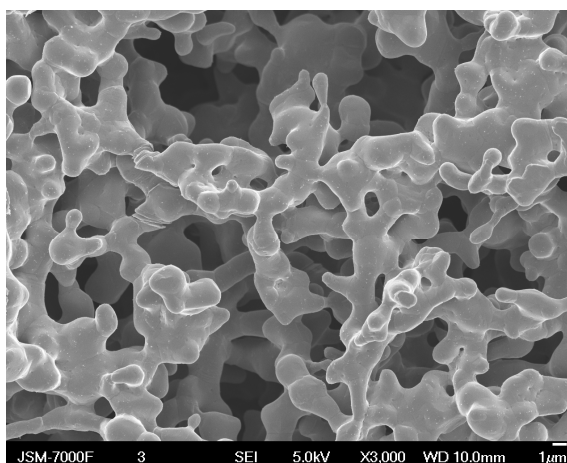


Figure 3.8 SEM picture of as-received Ni plaque.

To optimize capacitive performance of electrodes, both  $C_m$  ( $F g^{-1}$ ) and  $C_s$  ( $F cm^{-2}$ ) are analyzed in our study. Porous current collectors are proposed in order to improve the real performance of ES. Figure 3.8 shows SEM image of micro-porous of Ni plaques for preparation of PPy based electrodes. The pore size of Ni-plaques was in the range of 1-10  $\mu m$ . The pores of Ni plaques could be impregnated with PPy using electric-polymerization method. We expect to obtain high specific capacitance, good capacitance retention and excellent cycle performance by using porous current collectors. The reason is that the high porosity of Ni plaque increases the ions transport and provides more active sites for the charge-transfer reactions.

In the another approach, macro-porous Ni foam was investigated for ES applications. High materials loading electrodes ( $10\text{-}40\text{ mg cm}^{-2}$ ) were obtained using Ni foam as the current collectors. In this approach, the electrode was prepared by slurry impregnation method with the advantages of low cost and facile processing. The slurry was squeezed into Ni foam by two rollers. However, the major challenge of this technique is to obtain homogeneous colloidal suspension of active materials. To solve this challenge, we investigated various dispersants with different chemical structures and functional groups to fabricate the suspensions.

### 3.4 Rate capability of ESs

#### 3.4.1 Challenges

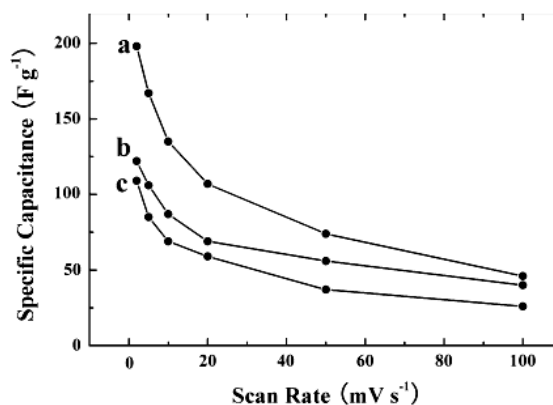


Figure 3.9 Specific capacitance (SC) versus scan rate, demonstrated that SC decrease sharply with increase of the scan rate. The electrode was made by sodium salicylate doped PPy. The PPy was deposited on a stainless steel foil with the film mass of (a)  $165$ , (b)  $373$  and (c)  $658\text{ }\mu\text{g cm}^{-2}$ [2].

Pseudocapacitive materials are promising electrode materials for ES applications with the advantages of faradic processes, high specific capacitance and simple synthesis. However, most of them exhibit poor rate capability, which is one of the most important reasons limiting their wide application. A typical example shown in Figure 3.9 is specific capacitance (SC) versus scan rate of PPy film on a stainless steel. High specific capacitance could be only obtained at a low scan rate with the low film mass. The capacitive behaviour degraded quickly with increase of the scan rate. The reason for the capacitance reduction is the slow diffusion and high film resistance which restricts efficient charge transfer.

Previous studies demonstrated that incorporation of nano-fibers, nano-tubes, nano-rods and nano-wires of different materials between CNT and/or graphene layers allowed to obtain composite electrodes with improved capacitance retention at high rates. Various methods were developed for the fabrication of composites, such as self-assembly[32], chemical vapor deposition[33], microwave[34], hydrothermal syntheses[35] and ultrasonication followed by vacuum filtration[36]. Although the impressive progresses have been achieved in this area, there is a need in the development of simple and versatile methods to obtain composite electrodes. Colloidal techniques are especially attractive for the fabrication of composite nanomaterials with uniform distribution of individual components. In this method, the individual components must be well dispersed in the colloidal suspensions, using

efficient dispersing agents. Several methods based on colloidal processing of composite electrode are proposed below for fabrication of the electrode with improved capacitive behavior.

### 3.4.2 Proposed approaches

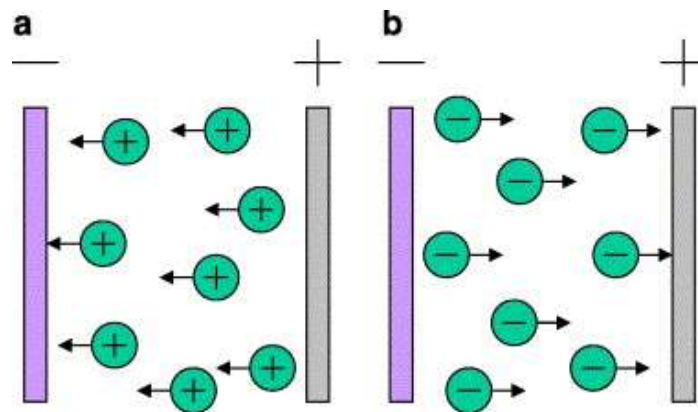


Figure 3.10 Schematic illustration of EPD process. (a) Cathodic EPD and (b) anodic EPD.

Thin films provide shorter transport length for the electrolyte, which improved the utilized efficiency of capacitive materials. Significant interests have been generated in the development of new film deposition techniques [23, 37-39]. Among various techniques, electrophoretic deposition (EPD) is a colloidal processing technique for thin film fabrication. It offers many advantages, e.g., short formation time, high deposition rate, low cost, environmentally friendly, versatility and structure homogeneity. The thickness of deposited films can be easily controlled by adjusting deposition voltage, deposition time and concentration of the colloidal suspensions.

Based on these advantages, it has been investigated for ES technology. The scheme of EPD was shown in Figure 3.10. In colloidal suspension, capacitive nano-particles are charged and dispersed in a liquid medium. Under applied direct current (DC), charged particles are moved along the electric field and deposited on a conductive substrate of opposite charge. So positively charged particles move towards, and are deposited on cathode and vice versa.

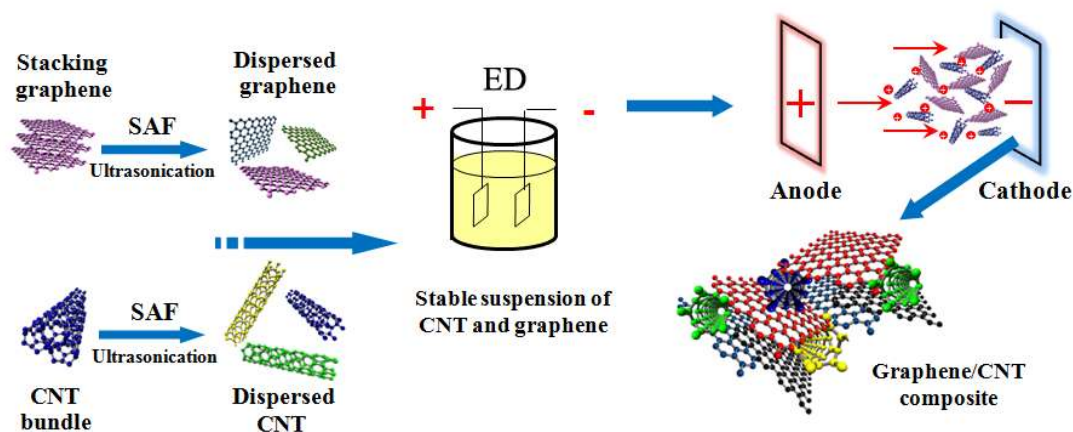


Figure 3.11 Fabrication of suspension and EPD of graphene-MWCNT composite films.

Recent progress has been made by use of CNT and graphene to improve the rate capability because of their superior electrical conductivity and high specific surface area. However, CNT and graphene are in an agglomerated state and randomly oriented with respect to each other. As a result, the pores in the electrodes are partially inaccessible to the electrolyte. In this study, we proposed EPD technique to assemble CNT and graphene on the current collectors. Figure 3.11 shows different steps in the

preparation of mixed graphene-MWCNT suspension and EPD of composite films using safranin as a co-dispersing agent. We found that, in this strategy, MWCNT were used as spacers in the composites and separation of graphene layers was achieved by the combination of MWCNT. Such structures allowed improved electrolyte access to graphene surface, and resulted in improving electrochemical performance of ES electrodes.

To improve the capacitance retention of PPy based electrodes, it is very important to prepare PPy particles with reduced agglomeration and higher specific surface areas. Therefore, pulse current deposition method was proposed in this study. Compared with direct current (DC) method, pulse current (PC) electrochemical polymerization can adopt higher current density which produces nano-crystalline deposits with finer grains and more compact structure. It is expected to get a nano-structured PPy electrode with more active sites on the surface (Figure 3.12) because pulse current (PC) electrochemical polymerization could inhibit grain growth during the deposition relaxation.

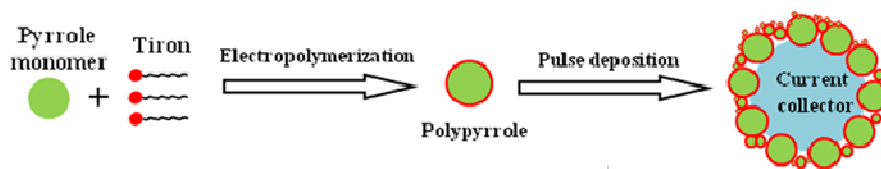


Figure 3.12 Schematic illustration of pulse current electrodeposition PPy.

### **3.5 Cycle stability of PPy-based electrode**

#### 3.5.1 Challenges

Cycle stability of PPy is poor compared with carbon based double-layer capacitive materials. The charge and discharge of double-layer capacitive materials is generally only through the adsorption and desorption of ions. Whereas volume swelling and shrinking may occur during the doping/de-doping (intercalating/deintercalating) process of PPy. These problems often lead to mechanical degradation and fading electrochemical performance during the charge and discharge cycling. The poor stability of PPy-based electrode could reduce the efficiency of ES devices.

#### 3.5.2 Proposed approaches

To improve cycle stability of PPy based electrode, three methods are proposed:

A) Improving morphologies of PPy. Nano-structured materials such as nanofibers, nanorods, nanowires, and nanotubes could alleviate cycling degradation problems because the high surface area and wide distributions of pore structure offer free space for the volumetric changes.

B) Fabrication of PPy-based composite materials for the electrode. According to the literature, composite electrodes could enhance the cycling stability of PPy by improving their chain structure and mechanical stability.

C) Utilization of porous Ni plaque and Ni foam as current collectors. Porous current collectors prevent swelling of PPy during cycling and provide good contact with electrolyte.

### **3.6 Electrode materials for capacitive deionization**

#### **3.6.1 Challenges**

The principle of capacitive deionization (CDI) is based on imposing an external electrostatic field between the electrodes in order to force charged ions to move toward oppositely charged electrodes (Figure 2.20). The charged ions can be held within the electrical double layer formed between the solvent and the electrode interface. A prerequisite for the good deionization performance is the demand for a high electrosorption capacity endowed by the electrode materials[42, 43]. To attain this objective, it is important to employ typical materials with a high specific surface area. Carbon aerogels, CNT, graphene and AC have been investigated as CDI electrodes. However, carbon aerogel has the disadvantage of low conductivity and requires complicated procedure for fabrication. The CNT and graphene were expensive materials but with relatively low specific capacitance. AC is supposed to be the attractive potential candidate for the high efficiency CDI electrodes due to its high specific surface area, high bulk conductivity, mass production and low fabrication cost. But high temperature activation process resulted in large AC particles size, which deteriorates its electrochemical performance.

CDI has been proven to be a very energy efficient water desalination technology in solutions with a relatively low ionic strength, such as for brackish water (lower than 10 mM). When the solution concentration is increased, the charge efficiency would decrease due to the presence of serious co-ions. To address this issue, ion-exchange membranes have been introduced into the CDI process resulting in membrane enhanced capacitive deionization (MCDI)[44, 45]. However, a big problem with the present lab-scale and commercialized MCDI is that it uses an expensive ion exchange membrane, resulting in the increase of the total capital cost of the MCDI desalination plant. An effective solution is to design advanced carbon electrodes with high conductivity, high surface area and good ions selectivity[46]. The electrosorption capacity of CDI could be improved without use of the membrane.

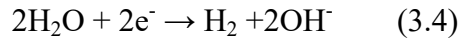
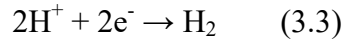
The application of CDI technology for desalination shows possibilities to develop the ES device for capacitive removal of other charged species from aqueous solutions. Of special interest is the possibility of capacitive dye removal (CDR) from the solutions. Organic dyes are widely used for many applications, such as solar cells, transistors, biological and chemical sensors, lasers, medicine and textile industry[43, 47]. The increased utilization of organic dyes for various applications given their rich diversity and complexity mandates the development of robust methods for dye removal from the chemical waste.

### 3.6.2 Proposed aspects

In our study, nano-crystals were developed for synthesis of PPy coated MWCNT. It allowed the fabrication of well-dispersed and uniformly coated MWCNT. This new approach paves the way for the fabrication of nitrogen-doped AC coated MWCNT (N-AC-MWCNT) with high surface area for the applications in efficient electrochemical devices. The problem related with large size of AC particles could be avoided. The testing results suggested that obtained materials showed improved capacitive performance, compared with pristine MWCNT in Na<sub>2</sub>SO<sub>4</sub> electrolyte and organic dyes aqueous solutions.

The development of CDR method requires detailed analysis of influence of chemical structures of dyes, nature of their chemical structure and functional groups on the capacitive performance of ES cells. It appears that dye structure has significant influence on the charge storage efficiency[49]. An important task is to investigate different families of organic dyes and analyze the charge storage mechanisms. The possibility of electrode regeneration and cyclic stability are important characteristics of the CDR devices. By applying a voltage to the aqueous solution, the following electrochemical reactions, involving H<sup>+</sup> consumption or OH<sup>-</sup> generation resulted in the pH increase at the cathode surface:





Reactions (3.2 and 3.3) led to a small pH increase, whereas reaction (3.4) allowed significant pH increase at the cathode surface. The electrochemical reaction at the anode provided  $\text{H}^+$  generation and pH decrease:



From the previous investigation[48, 50], some dyes exhibit pH dependent solubility and pH dependent charge. Such dyes can precipitate at electrodes due to the pH increase at the cathode or pH decrease at the anode surface (Figure 3.13). The precipitation mechanism is triggered by the electrochemical decomposition of water and other electrochemical electrode reactions in aqueous solutions. These dyes can be removed from solutions by cathodic or anodic electrodeposition methods through irreversible reactions. Other dyes exhibit pH independent charge and pH independent solubility. Such dyes can be involved in the formation of electrical double layers at the electrode surface. During the process, the electrostatic adsorption between the dye ions and the electrode is reversible, and could be used for CDR. The CDR process could be accompanied with capacitive energy storage in electrical double layers. Therefore, the goal of our investigation is development of CDR method for the removal of various dyes with different chemical structures from aqueous solutions.

The influence of dye structure, size and charge on capacitive behaviour, voltage window and power-energy characteristics of ES cells will be investigated.

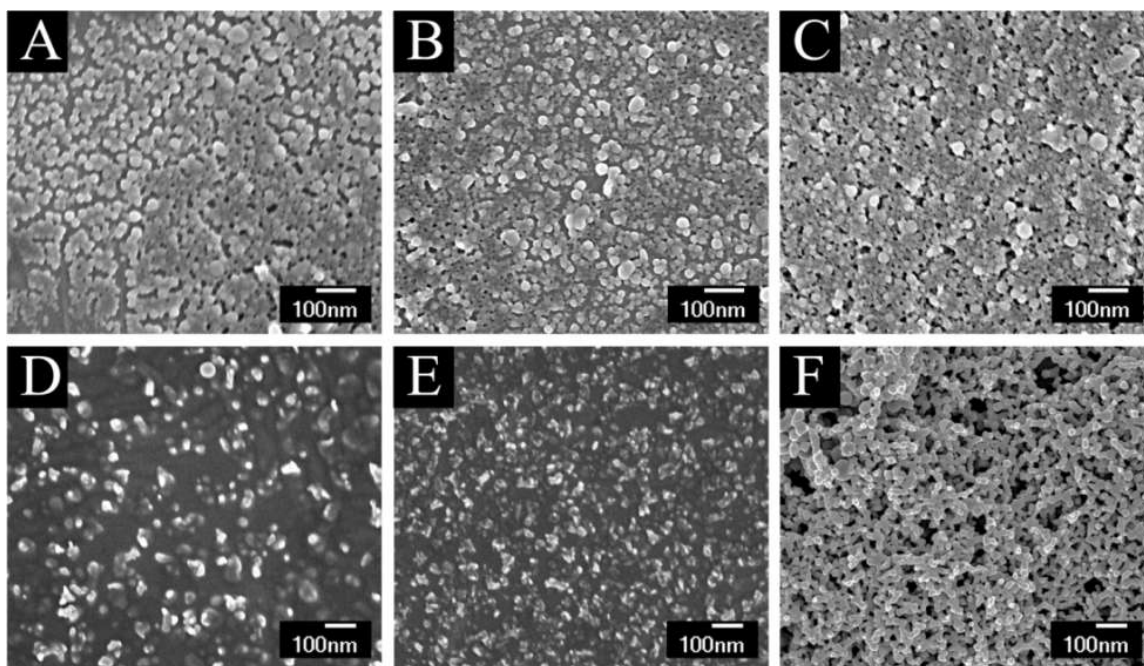


Figure 3.13 SEM images of precipitation of (A-C) cationic basic fuchsin dye at cathode and (D-F) anionic fluorescein dye at anode from  $500 \text{ mg L}^{-1}$  aqueous solutions, at voltage of (A,D) 2, (B,E) 5 and (C,F) 10 V after 10 min[48].

### 3.7 Overall objectives

The overall objective of this study is to develop advanced materials for ES and capacitive water purification applications. This could be achieved through:

- A) Developing advanced anionic dopants to improve the capacitive behaviour of PPy;
- B) Synthesis of nano-structured PPy using anionic dopants and cationic additives;

- C) Developing universal dispersants to make composite electrodes containing PPy, MnO<sub>2</sub>, CNT and graphene;
- D) Studying the electrochemical performance of PPy-based electrodes fabricated using different current collectors, including stainless steels foil, Ni foil, Ni foam and Ni plaque;
- E) Fabricating composite electrodes with high mass loading, good rate capability and excellent cycling stability;
- F) Developing advanced carbon electrodes for capacitive water purification applications;
- G). Fabricating the ES cells for energy storage and water purification and optimizing the configuration of electrodes.

### **3.7 References**

- [1]H. Chang, C. Chang, Y. Tsai, C. Liao, Electrochemically synthesized graphene/polypyrrole composites and their use in supercapacitor, *Carbon*, 50(2012) 2331-2336.
- [2]C. Shi, I. Zhitomirsky, Electrodeposition and Capacitive Behavior of Films for Electrodes of Electrochemical Supercapacitors, *Nanoscale Research Letters*, 5(2010) 518-523.
- [3]C. Shi, I. Zhitomirsky, Electrodeposition of composite polypyrrole/carbon nanotube films, *Surface Engineering*, 27(2011) 655-661.
- [4]L. Vaisman, H.D. Wagner, G. Marom, The role of surfactants in dispersion of carbon nanotubes, *Advances in Colloid and Interface Science*, 128–130(2006) 37-46.

- [5]S.W. Kim, T. Kim, Y.S. Kim, H.S. Choi, H.J. Lim, S.J. Yang, C.R. Park, Surface modifications for the effective dispersion of carbon nanotubes in solvents and polymers, *Carbon*, 50(2012) 3-33.
- [6]P. Ma, N.A. Siddiqui, G. Marom, J. Kim, Dispersion and functionalization of carbon nanotubes for polymer-based nanocomposites: A review, *Composites Part A: Applied Science and Manufacturing*, 41(2010) 1345-1367.
- [7]X. Xie, Y. Mai, X. Zhou, Dispersion and alignment of carbon nanotubes in polymer matrix: A review, *Materials Science and Engineering: R: Reports*, 49(2005) 89-112.
- [8]C. Richard, F. Balavoine, P. Schultz, T.W. Ebbesen, C. Mioskowski, Supramolecular Self-Assembly of Lipid Derivatives on Carbon Nanotubes, *Science*, 300(2003) 775-778.
- [9]B. Vigolo, A. Pénicaud, C. Coulon, C. Sauder, R. Pailler, C. Journet, P. Bernier, P. Poulin, Macroscopic Fibers and Ribbons of Oriented Carbon Nanotubes, *Science*, 290(2000) 1331-1334.
- [10]H. Xia, M. Lai, L. Lu, Nanoflaky MnO<sub>2</sub>/carbon nanotube nanocomposites as anode materials for lithium-ion batteries, *Journal of Materials Chemistry*, 20(2010) 6896-6902.
- [11]H. Xia, Y. Wang, J. Lin, L. Lu, Hydrothermal synthesis of MnO<sub>2</sub>/CNT nanocomposite with a CNT core/porous MnO<sub>2</sub> sheath hierarchy architecture for supercapacitors, *Nanoscale Research Letters*, 7(2012) 1-10.
- [12]Y. Zhu, I. Zhitomirsky, Influence of dopant structure and charge on supercapacitive behavior of polypyrrole electrodes with high mass loading, *Synthetic Metals*, 185-186(2013) 126-132.
- [13]G.R. Mitchell, F.J. Davis, C.H. Legge, The effect of dopant molecules on the molecular order of electrically-conducting films of polypyrrole, *Synthetic Metals*, 26(1988) 247-257.
- [14]M.S. Ata, Y. Liu, I. Zhitomirsky, A review of new methods of surface chemical modification, dispersion and electrophoretic deposition of metal oxide particles, *RSC Advances*, 4(2014) 22716-22732.

- [15]Y. Liu, K. Shi, I. Zhitomirsky, New colloidal route for electrostatic assembly of oxide nanoparticle  
  欵?carbon nanotube composites, *Colloids and Surfaces A: Physicochemical and Engineering  
  Aspects*, 446(2014) 15-22.
- [16]B. Weng, R. Shepherd, J. Chen, G.G. Wallace, Gemini surfactant doped polypyrrole  
  nanodispersions: an inkjet printable formulation, *Journal of Materials Chemistry*, 21(2011)  
  1918-1924.
- [17]X. Zhang, Bai, Surface Electric Properties of Polypyrrole in Aqueous Solutions, *Langmuir*,  
  19(2003) 10703-10709.
- [18]G.R. Mitchell, F.J. Davis, C.H. Legge, The effect of dopant molecules on the molecular order of  
  electrically-conducting films of polypyrrole, *Synthetic Metals*, 26(1988) 247-257.
- [19]E. Håkansson, T. Lin, H. Wang, A. Kaynak, The effects of dye dopants on the conductivity and  
  optical absorption properties of polypyrrole, *Synthetic Metals*, 156(2006) 1194-1202.
- [20]K. Shi, X. Pang, I. Zhitomirsky, Fabrication of Tiron-doped polypyrrole/MWCNT composite  
  electrodes with high mass loading and enhanced performance for supercapacitors, *Journal of  
  Applied Polymer Science*, 32(2015) 42376.
- [21]Z. Liu, X. Zhang, S. Poyraz, S.P. Surwade, S.K. Manohar, Oxidative Template for Conducting  
  Polymer Nanoclips, *Journal of the American Chemical Society*, 132(2010) 13158-13159.
- [22]H. Fu, Z. Du, W. Zou, H. Li, C. Zhang, Carbon nanotube reinforced polypyrrole nanowire network  
  as a high-performance supercapacitor electrode, *Journal of Materials Chemistry A*, 1(2013)  
  14943-14950.
- [23]G.S. Gund, D.P. Dubal, S.S. Shinde, C.D. Lokhande, Architected Morphologies of Chemically  
  Prepared NiO/MWCNTs Nanohybrid Thin Films for High Performance Supercapacitors, *ACS  
  Applied Materials & Interfaces*, 6(2014) 3176-3188.

- [24]H. Li, R. Li, R.M. Worden, S. Calabrese-Barton, Facilitation of High-Rate NADH Electrocatalysis Using Electrochemically Activated Carbon Materials, *ACS Applied Materials & Interfaces*, (2014).
- [25]B. Hsia, M.S. Kim, C. Carraro, R. Maboudian, Cycling characteristics of high energy density, electrochemically activated porous-carbon supercapacitor electrodes in aqueous electrolytes, *Journal of Materials Chemistry A*, 1(2013) 10518-10523.
- [26]H. Jiang, P.S. Lee, C. Li, 3D carbon based nanostructures for advanced supercapacitors, *Energy & Environmental Science*, 6(2013) 41-53.
- [27]Y. Wang, S. Tao, Y. An, S. Wu, C. Meng, Bio-inspired high performance electrochemical supercapacitors based on conducting polymer modified coral-like monolithic carbon, *Journal of Materials Chemistry A*, 1(2013) 8876-8887.
- [28]L. Chen, X. Zhang, H. Liang, M. Kong, Q. Guan, P. Chen, Z. Wu, S. Yu, Synthesis of Nitrogen-Doped Porous Carbon Nanofibers as an Efficient Electrode Material for Supercapacitors, *ACS Nano*, 6(2012) 7092-7102.
- [29]Y. Gogotsi, P. Simon, True Performance Metrics in Electrochemical Energy Storage, *Science*, 334(2011) 917-918.
- [30]J.R. McDonough, J.W. Choi, Y. Yang, F. La Mantia, Y. Zhang, Y. Cui, Carbon nanofiber supercapacitors with large areal capacitances, *Applied Physics Letters*, 95(2009) 243109.
- [31]P. Lv, P. Zhang, Y. Feng, Y. Li, W. Feng, High-performance electrochemical capacitors using electrodeposited MnO<sub>2</sub> on carbon nanotube array grown on carbon fabric, *Electrochimica Acta*, 78(2012) 515-523.
- [32]D. Yu, L. Dai, Self-Assembled Graphene/Carbon Nanotube Hybrid Films for Supercapacitors, *The Journal of Physical Chemistry Letters*, 1(2009) 467-470.
- [33]Z. Fan, J. Yan, L. Zhi, Q. Zhang, T. Wei, J. Feng, M. Zhang, W. Qian, F. Wei, A

Three-Dimensional Carbon Nanotube/Graphene Sandwich and Its Application as Electrode in Supercapacitors, *Advanced Materials*, 22(2010) 3723-3728.

[34]Z. Xu, Z. Li, C.M.B. Holt, X. Tan, H. Wang, B.S. Amirkhiz, T. Stephenson, D. Mitlin, Electrochemical Supercapacitor Electrodes from Sponge-like Graphene Nanoarchitectures with Ultrahigh Power Density, *The Journal of Physical Chemistry Letters*, (2012) 2928-2933.

[35]Z. Wu, W. Ren, D. Wang, F. Li, B. Liu, H. Cheng, High-Energy MnO<sub>2</sub> Nanowire/Graphene and Graphene Asymmetric Electrochemical Capacitors, *ACS Nano*, 4(2010) 5835-5842.

[36]G. Eda, G. Fanchini, M. Chhowalla, Large-area ultrathin films of reduced graphene oxide as a transparent and flexible electronic material, *Nature Nanotechnology*, 3(2008) 270-274.

[37]S.S. Shinde, G.S. Gund, D.P. Dubal, S.B. Jambure, C.D. Lokhande, Morphological modulation of polypyrrole thin films through oxidizing agents and their concurrent effect on supercapacitor performance, *Electrochimica Acta*, 119(2014) 1-10.

[38]P. Xu, J. Kang, J. Choi, J. Suhr, J. Yu, F. Li, J. Byun, B. Kim, T. Chou, Laminated Ultrathin Chemical Vapor Deposition Graphene Films Based Stretchable and Transparent High-Rate Supercapacitor, *ACS Nano*, 8(2014) 9437-9445.

[39]M.E.A. Warwick, A.J. Roberts, R.C.T. Slade, R. Binions, Electric field assisted chemical vapour deposition - a new method for the preparation of highly porous supercapacitor electrodes, *Journal of Materials Chemistry A*, 2(2014) 6115-6120.

[40]L. Fan, J. Maier, High-performance polypyrrole electrode materials for redox supercapacitors, *Electrochemistry Communications*, 8(2006) 937-940.

[41]R.K. Sharma, A.C. Rastogi, S.B. Desu, Pulse polymerized polypyrrole electrodes for high energy density electrochemical supercapacitor, *Electrochemistry Communications*, 10(2008) 268-272.

[42]H. Li, F. Zaviska, S. Liang, J. Li, L. He, H.Y. Yang, A high charge efficiency electrode by

- self-assembling sulphonated reduced graphene oxide onto carbon fibre: towards enhanced capacitive deionization, *Journal of Materials Chemistry A*, 2(2014) 3484-3491.
- [43]Y. Liu, X. Jiang, B. Li, X. Zhang, T. Liu, X. Yan, J. Ding, Q. Cai, J. Zhang, Halloysite nanotubes@reduced graphene oxide composite for removal of dyes from water and as supercapacitors, *Journal of Materials Chemistry A*, 2 (2014) 4264-4269.
- [44]J. Yang, L. Zou, H. Song, Preparing MnO<sub>2</sub>/PSS/CNTs composite electrodes by layer-by-layer deposition of MnO<sub>2</sub> in the membrane capacitive deionisation, *Desalination*, 286(2012) 108-114.
- [45]K.B. Hatzell, E. Iwama, A. Ferris, B. Daffos, K. Urita, T. Tzedakis, F. Chauvet, P. Taberna, Y. Gogotsi, P. Simon, Capacitive deionization concept based on suspension electrodes without ion exchange membranes, *Electrochemistry Communications*, 43(2014) 18-21.
- [46]A.G. El-Deen, N.A.M. Barakat, K.A. Khalil, H.Y. Kim, Development of multi-channel carbon nanofibers as effective electrosorptive electrodes for a capacitive deionization process, *Journal of Materials Chemistry A*, 1(2013) 11001-11010.
- [47]X. Zhu, Y. Liu, C. Zhou, S. Zhang, J. Chen, Novel and High-Performance Magnetic Carbon Composite Prepared from Waste Hydrochar for Dye Removal, *ACS Sustainable Chemistry & Engineering*, 2(4). (2014) 969–977.
- [48]K. Shi, I. Zhitomirsky, Electrodeposition of Carbon Nanotubes Triggered by Cathodic and Anodic Reactions of Dispersants, *Materials and Manufacturing Processes*, 30(2015) 771-777.
- [49]K. Shi, I. Zhitomirsky, Supercapacitor devices for energy storage and capacitive dye removal from aqueous solutions, *RSC Advances* 5(2015) 320-327.
- [50]Y. Sun, M.S. Ata, I. Zhitomirsky, Electrophoretic deposition of TiO<sub>2</sub> nanoparticles using organic dyes, *Journal of Colloid and Interface Science*, 369(2012) 395-401.

## 4. Experimental methods and materials characterization

### 4.1 Starting materials

All chemicals involved in this research were listed in Table 4.1.

Table 4.1 Chemicals used for materials synthesis and device fabrication.

| Category                                    | Chemical Name   | Source                    |
|---|---|---------------------------|
| Monomer for the polypyrrole (PPy) synthesis | Pyrrole (>98%)  | Sigma Aldrich (Canada)    |
| Oxidant for the synthesis                   | Ammonium peroxydisulfate (APS)                            | Sigma Aldrich (Canada)    |
| Dopants of Polypyrrole                      | 4,5-dihydroxy-1,3-benzenedisulfonic acid disodium (Tiron) | Alfa Aesar (USA)          |
|   | Ponceau S (PS)  | Sigma Aldrich (Canada)    |
| Dispersants for fabrication of composites   | Safranin (SAF)  | Sigma Aldrich (Canada)    |
|   | Malachite Green (MG)                                      | Sigma Aldrich (Canada)    |
|   | Cetrimonium Bromide (CTAB)                                | Sigma Aldrich (Canada)    |
| Conductive carbon materials                 | Multi-walled carbon nanotubes (MWCNTs)                    | Bayer Inc. (Germany)      |
|   | Graphene  | Graphene Supermarke (USA) |
| Electrolyte for ES                          | Sodium sulfate ( $\text{Na}_2\text{SO}_4$ )               | Sigma Aldrich (Canada)    |

|  |  |                           |
|--|--|---------------------------|
|  | Sodium chloride (NaCl)   | Sigma Aldrich (Canada)    |
| Organic dyes investigated for capacitive dye removal | Methyl Blue (MB)   | Sigma Aldrich (Canada)    |
|  | Calcon (CL)  | Sigma Aldrich (Canada)    |
|  | Amaranth (AM)  | Sigma Aldrich (Canada)    |
|  | Pyrocatechol violet (PV)   | Sigma Aldrich (Canada)    |
|  | Eriochrome Cyanine R (ECR)                                       | Sigma Aldrich (Canada)    |
|  | Chromotropic Acid Disodium Salt (CHR)                            | Sigma Aldrich (Canada)    |
|  | 2-(phenylazo) Chromotropic Acid Disodium Salt (CHRP)             | Sigma Aldrich (Canada)    |
|  | 2-(1-naphthyl diazenyl)chromotropic acid disodium salt (CHRN)    | Sigma Aldrich (Canada)    |
|  | 7-Bis(2-sulfophenylazo)chromotropic acid tetrasodium salt (CHRB) | Alfa Aesar (USA)          |
|  | Other chemicals  | Potassium hydroxide (KOH) |
| Potassium permanganate (KMnO <sub>4</sub> )          |  | Sigma Aldrich (Canada)    |
| N-methylpyrrolidone                                  |  | Sigma Aldrich (Canada)    |
| Polyvinylidene Fluoride (PVDF)                       |  | Sigma Aldrich (Canada)    |
| Polyvinyl Butyral (PVB) Mw=50000–80000               |  | Sigma Aldrich (Canada)    |
| Current collector                                    | 316L stainless steel foils                                       | Alfa Aesar                |

|  |                             |                     |
|--|-----------------------------|---------------------|
|  |                             | (USA)               |
|  | Ni foil                     | Alfa Aesar<br>(USA) |
|  | Ti foil                     | Alfa Aesar<br>(USA) |
|  | Ni plaques (porosity ~80%)  | Vale (Canada)       |
|  | Nickel foam (porosity ~95%) | Vale (Canada)       |

## 4.2 Capacitive materials preparation

### 4.2.1 Synthesis of PPy

#### 4.2.1.1 Tiron doped PPy synthesized by direct current electro-polymerization

The electro-polymerization cell included a Ni foil or Ni plaque substrate and a Pt counter electrode (Figure 4.1). The distance between the substrate and counter electrode was 15 mm. Direct current electro-polymerization was performed galvanostatically at a current density of  $1 \text{ mA cm}^{-2}$  from an aqueous 0.1 M pyrrole solution containing 0.005 M Tiron. All the deposition experiments were performed from freshly prepared solutions. The obtained films were rinsed with deionized water and then dried in air.

#### 4.2.1.2 Tiron doped PPy synthesized by pulse current electro-polymerization

Pulse electro-polymerization was carried out using the aforementioned electro-polymerization cell (Figure 4.1), containing an aqueous 0.1 M pyrrole solution containing 0.005 M Tiron. Porous Ni plaques were used as current collectors. The PPy films were obtained by pulse deposition with ON and OFF durations of 0.5 s at a

current density of  $1 \text{ mA cm}^{-2}$ . As-prepared PPy films were rinsed with deionized water and then dried in air.

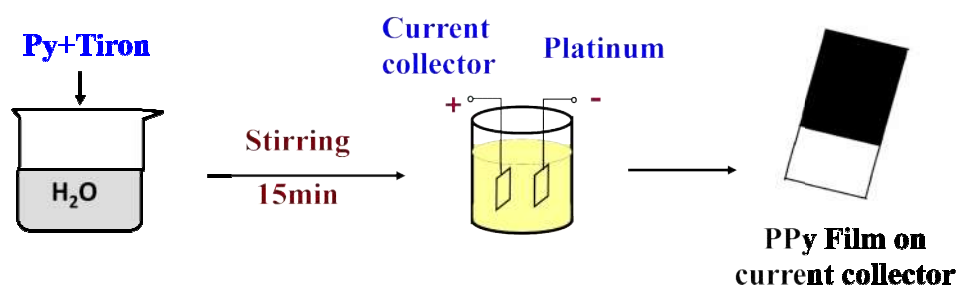


Figure 4.1 Scheme of fabrication of Tiron doped PPy films using electro-polymerization method.

#### 4.2.1.3 Tiron doped PPy synthesized by chemical polymerization

PPy synthesized by chemical polymerization reaction was based on the chemical reaction between pyrrole monomer and APS oxidant. In a typical method, 4.98 g Tiron (15 mmol) was dissolved in 50 mL de-ionized water, followed by injecting 1.04 mL (15 mmol) pyrrole under a vigorous magnetic stirring for 30 min in an ice bath. Then 50 mL of  $0.3 \text{ mol L}^{-1}$  APS solution was slowly added to the above solution. The resultant mixture was subsequently allowed to react for 20 h. To study the influence of Tiron on capacitive performance, PPy was also synthesized using the same concentration of Py and APS but without Tiron. The precipitated PPy solids were filtered and washed by 2 L de-ionized water and 500 mL ethanol. The obtained powders were dried at  $70 \text{ }^{\circ}\text{C}$  for 12 h.

#### 4.2.1.4 PPy nanofibers synthesized using multi-functional nanocrystals

Polypyrrole nanofibers (PPy-NF) were synthesized by a modified oxidative template assembly route[1, 2]. For the fabrication of (CTA)<sub>2</sub>S<sub>2</sub>O<sub>8</sub> oxidative template, 3.64 g (10 mmol) CTAB was dissolved in 120 mL of 1 mol L<sup>-1</sup> HCl solution at 4°C. After being magnetically stirred for 30 min, 1.14 g (0.005 mol) (NH<sub>4</sub>)<sub>2</sub>S<sub>2</sub>O<sub>8</sub> was added to the solution and white (CTA)<sub>2</sub>S<sub>2</sub>O<sub>8</sub> precipitate was formed. The reaction was carried out at 4 °C for 20 h. The obtained precipitates were washed with deionized water using vacuum filtration process and dried in air.

The PS doped PPy powders synthesized using oxidative template and traditional oxidant were compared. In this experiment, PPy powders were prepared from the 100 mL solutions, containing 0.05 mol L<sup>-1</sup> Py monomer and 0-0.025 mol L<sup>-1</sup> PS dopant, using 0.06 mol L<sup>-1</sup> (NH<sub>4</sub>)<sub>2</sub>S<sub>2</sub>O<sub>8</sub> oxidants or (CTA)<sub>2</sub>S<sub>2</sub>O<sub>8</sub> oxidative template for the polymerization reactions. The reactions were carried out at 4 °C for 20 h. The precipitate PPy solids were washed with deionized water using vacuum filtration process and dried in air at 70°C. The filtration system consisted of four components, namely a set of Buchner funnel with sand core (45 mm in diameter), a suction flask, a membrane filter (Nuclepore Whatman, 1 μm pore size) and a water circulation vacuum pump.

## 4.2.2 Preparation of PPy based composites

### 4.2.2.1 Tiron doped PPy/MWCNTs composites fabricated using co-dispersant

SAF was used as a co-dispersant for Tiron doped PPy and MWCNTs to produce composite materials. In this method, 0.34 g of as-prepared Tiron-doped PPy was put into 400 mL solution, containing 0.5 g L<sup>-1</sup> SAF, and sonicated in an ultrasonic bath for 20 min in order to form a homogeneous colloidal solution. 0.06 g MWCNT was then added and further ultrasonicated for 1 hr. A stable Tiron-doped PPy/MWCNT suspension was obtained. The vacuum filtration process was applied to obtain homogeneous Tiron-doped PPy/MWCNT slurry. Excess SAF in the mixture was removed by the vacuum filtration system until the DI-water dropped from the funnel was colorless.

### 4.2.2.2 PPy nanofibers/ MWCNTs composite fabricated using co-dispersant

To prepared PPy-NF/ MWCNTs composite, 0.4 g of PPy-NF were added to 400 mL of 0.5 g L<sup>-1</sup> MG solution and ultrasonicated for 20 min in order to form a homogeneous colloidal suspension. MWCNT were added to the suspensions, the mass ratio of MWCNT to PPy nanofibers was 10 : 90, 20 : 80 and 30 : 70. The mixed PPy-NF and MWCNT suspensions were further ultrasonicated for 1 hr. Obtained stable suspensions were used for the fabrication of homogeneous slurries using vacuum filtration process (Figure 4.2).

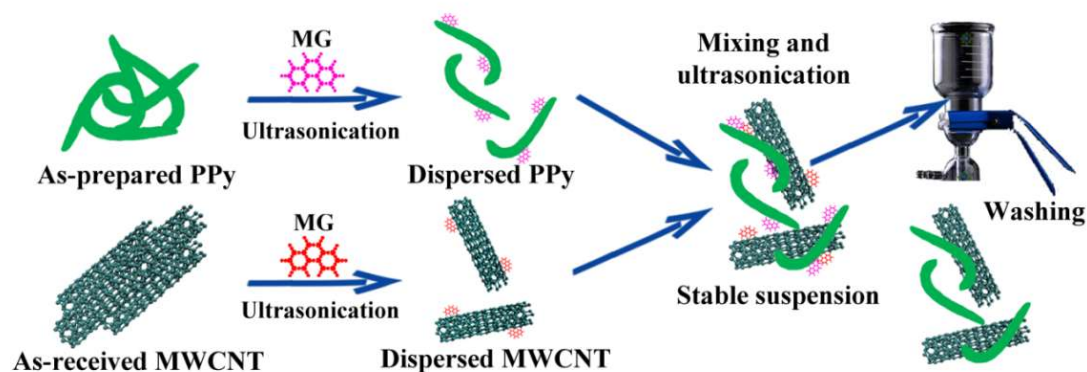


Figure 4.2 Scheme of fabrication of PPy-NF/ MWCNTs composite.

The adsorption of MG on PPy-NF and MWCNT was investigated by analyzing the sedimentation test results, electrokinetic properties, Fourier transform infrared spectroscopy (FTIR) and UV-Vis spectroscopy data. The limitations of zeta potential concept for the analysis of electrokinetic properties of nanoparticles, containing adsorbed organic molecules, were described in the literature [3, 4]. Therefore, the electrokinetic behavior of PPy-NF and MWCNT, containing adsorbed positively charged MG, was investigated by the analysis of electrophoretic deposition (EPD) yield data. EPD was performed from aqueous  $1 \text{ g L}^{-1}$  MWCNT or PPy-NF suspensions, containing  $0.1\text{-}1 \text{ g L}^{-1}$  MG. The suspensions were ultrasonicated for 10 min before the EPD. The EPD cell included Pt electrodes, the distance between the electrodes was 15 mm. The deposition voltage was 30 V. The mass of the deposits was measured after drying in air during 72 h.

## 4.2.2.3 PPy nanofibers/graphene and graphene/MWCNTs composite films fabricated by EPD

Electrophoretic deposition (EPD) was employed to produce PPy-NF/graphene and graphene/MWCNTs composite films (Figure 4.3). The fabrication of stable suspensions, containing well-dispersed charged colloidal particles, is required in EPD method. Here the individual materials of MWCNTs, graphene and PPy-NF were dispersed using SAF as the co-dispersant. EPD was performed from aqueous suspensions of  $1 \text{ g L}^{-1}$  graphene, MWCNT and PPy-NF containing SAF. The concentration of SAF in the suspensions was varied in the range of  $0.1\text{-}1 \text{ g L}^{-1}$ . Cathodic deposits were obtained on Ti foil ( $30 \times 50 \times 0.1 \text{ mm}$ ) substrates. The distance between the substrate and Pt counter electrode was  $15 \text{ mm}$ . The deposition voltage was  $30 \text{ V}$ .

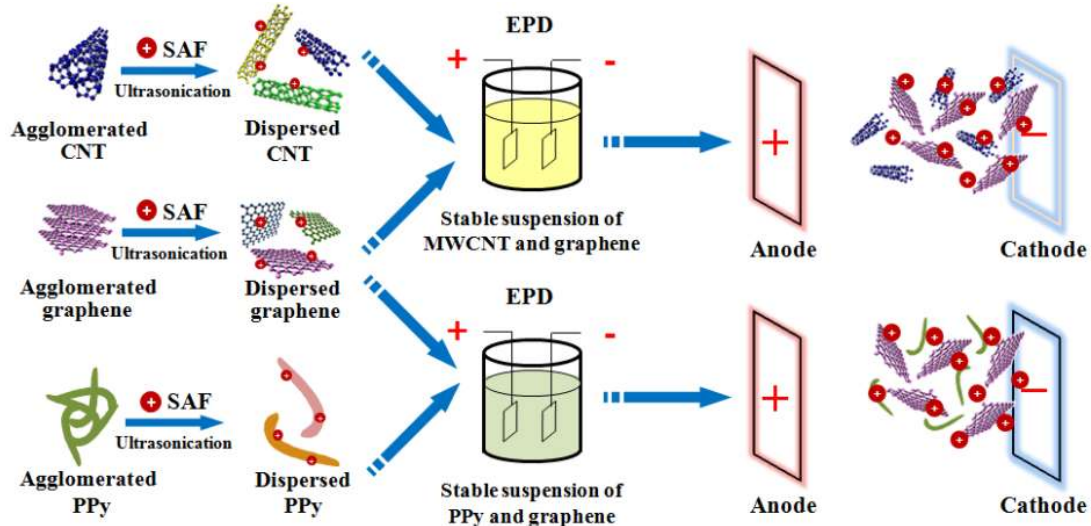


Figure 4.3 Scheme of fabrication of graphene–MWCNT and graphene–PPy composite films by cathodic EPD.

## 4.2.2.4 PPy coated MWCNTs synthesized using multi-functional nano-crystals

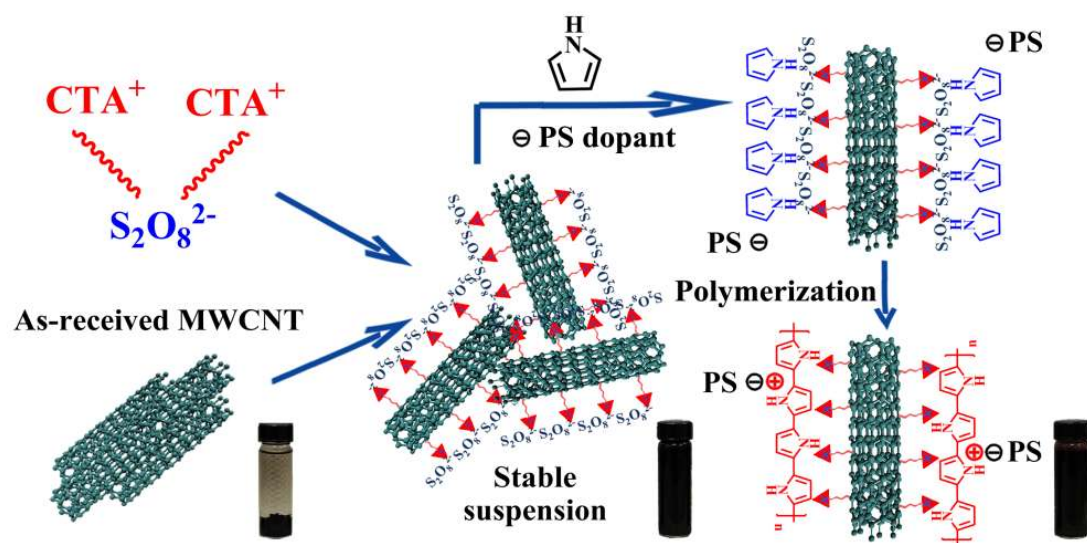


Figure 4.4 Scheme of fabrication of PPy coated MWCNT using  $(\text{CTA})_2\text{S}_2\text{O}_8$  as the dispersants for MWCNT and oxidants for Py.

The obtained oxidative template,  $(\text{CTA})_2\text{S}_2\text{O}_8$  in the form of nano-crystals, was utilized as a multi-functional agent for the synthesis of PPy coated MWCNT (Figure 4.4). In a typical method, a 200 mL suspension, containing MWCNT and  $0.03 \text{ mol L}^{-1}$   $(\text{CTA})_2\text{S}_2\text{O}_8$  was ultrasonicated for 1 h, cooled down to  $4 \text{ }^\circ\text{C}$ . Then a 200 mL solution, containing  $0.05 \text{ mol L}^{-1}$  of Py and  $0.015 \text{ mol L}^{-1}$  PS was added. The mass ratio of MWCNT to pyrrole monomer was in the range of 0.11-0.67. The reaction was performed at  $4 \text{ }^\circ\text{C}$  during 20 h. Obtained material was washed with deionized water dried at  $70 \text{ }^\circ\text{C}$  in air.

## 4.2.3 Preparation of activated carbon by carbonization of PPy

## 4.2.3.1 Activated carbon coated MWCNTs obtained from PPy coated MWCNTs

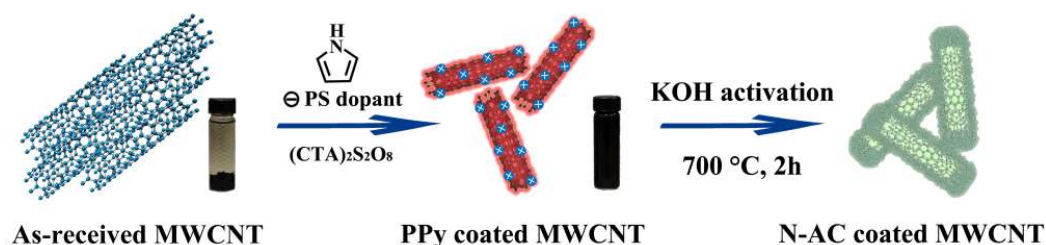


Figure 4.5 Scheme of fabrication of activated carbon coated MWCNTs.

N-doped activated carbon coated MWCNTs (N-AC-MWCNT) were prepared from PPy coated MWCNT by a procedure, which involved carbonization and chemical activation (Figure 4.5). Briefly, 2 g PPy coated MWCNT were dispersed in 50 mL of 4 mol L<sup>-1</sup> KOH. The sedimentation tests showed good dispersibility of PPy coated MWCNT in KOH solution. The prepared suspension was further stirred at 80 °C and dried. The obtained powder was carbonized in a tubular furnace under a nitrogen atmosphere at 700 °C for 2 h and then cooled to room temperature. The carbonized material was washed with 1 M HCl solution and deionized water until the filtrate became neutral. Obtained N-AC-MWCNT was dried in a vacuum oven at 90 °C overnight. For comparison, PPy coated MWCNT was carbonized without KOH activation using a similar procedure to form N-doped carbon coated MWCNT (N-C-MWCNT).

#### 4.2.3.2 MnO<sub>2</sub> coated MWCNTs obtained from activated carbon coated MWCNTs

MnO<sub>2</sub> coated MWCNTs were synthesized using sacrificial N-AC layer of N-AC-MWCNT. In this method, 0.1 M Na<sub>2</sub>SO<sub>4</sub> aqueous solutions were prepared, containing 0.028 M KMnO<sub>4</sub> (solution 1), 0.062 M KMnO<sub>4</sub> (solution 2) and 0.127 M KMnO<sub>4</sub> (solution 3). Then 100 mL of solutions 1-3 were added to suspensions containing 0.6 g N-AC-MWCNT in 100 mL of water at 65 °C. The chemical reaction was performed at 65 °C for 8 h. Na<sub>2</sub>SO<sub>4</sub> was served as a buffer agent to keep the solution neutral during the synthesis. The obtained MnO<sub>2</sub> coated N-AC-MWCNT were washed with deionized water and finally dried at 90 °C for 12 h.

#### 4.2.3.3 Activated carbon nanofibers synthesized from PPy nanofibers

N-doped activated carbon nanofibers (N-AC-NF) were fabricated from PPy-NF, similar to the preparation of N-AC-MWCNT using PPy coated MWCNTs. Firstly, the as-synthesized PPy-NF (3 g) were dispersed and stirred in KOH solution (60 mL, 150 g L<sup>-1</sup>) overnight at 70°C until a black jelly-like slurry was formed. The slurry was then heated in a tubular furnace at a heating rate of 10 °C min<sup>-1</sup> to 700 °C and kept for 2 h under a nitrogen atmosphere. The obtained N-AC-NF material was washed with 1 M HCl solution and deionized water until the filtrate became neutral and dried overnight at 90 °C in a vacuum oven.

### **4.3 Materials characterization**

#### 4.3.1 Adhesion study of deposited films

The measurements of film adhesion were performed according to the ASTM D3359 standard. In a typical procedure, a lattice pattern was made with cuts 1 mm apart in X and Y directions in the film to the substrate. A pressure-sensitive tape was then applied over the lattice pattern and then removed. The adhesion was evaluated by comparison of the lattice pattern after tape removal with a classification table presented in the ASTM D3359 standard.

#### 4.3.2 Morphology study

The morphology was characterized using a JEOL JSM-7000F scanning electron microscope (SEM) and transmission electron microscope (TEM). The JEOL 2010F field emission TEM/STEM, equipped with Gatan imaging filter, high angle annular dark field (HAADF) STEM detector and electron energy loss spectroscopy (EELS) analysis, was employed to study PPy-NF, PPy-NF/MWCNT composites, PPy coated MWCNTs and MnO<sub>2</sub> coated MWCNTs. A FEI's Tecnai Osiris TEM operating at 200 kV, equipped with ChemiSTEM energy dispersive X-ray (EDX) spectroscopy and a high angle annular dark field (HAADF) STEM detector, were used to investigate N-AC-MWCNT and N-AC-NF.

#### 4.3.3 Crystallinity study

X-ray diffraction (XRD) data were collected using a powder diffractometer (Nicolet I2, monochromatised  $\text{Cu}_{K\alpha}$  radiation) at a scanning speed of  $0.5 \text{ min}^{-1}$ .

#### 4.3.4 Composition study

The adsorption of dispersants was studied by Fourier transform infrared spectroscopy (FTIR) and UV–Vis spectroscopy tests. The EPD deposits were removed from the substrates after drying in air for 72 h for the investigations. FTIR tests were performed using Bio-Rad FTS-40 instrument. The UV–Vis spectra were obtained using Cary-50 UV–Vis spectrophotometer. The thermogravimetric analysis (TGA) and differential thermal analysis (DTA) investigations were carried out in air at a heating rate of  $5 \text{ }^\circ\text{C min}^{-1}$  using a Netzsch STA-409 thermoanalyzer.

### **4.4 Fabrication of electrodes and cells for ESs**

#### 4.4.1 Fabrication of electrodes from electro-polymerized and electrophoretically deposited films

The Tiron doped PPy films prepared by direct and pulse current electro-polymerization were used for electrochemical studies. PPy nanofibers/graphene and graphene/MWCNTs composite films, obtained by the EPD method, were washed by deionized water and then dried in air. The working electrodes were prepared from obtained films. The area of the working electrode was  $1 \text{ cm}^2$ .

#### 4.4.2 Fabrication of electrodes using the slurry impregnation method

The synthesized powders, Tiron doped PPy, Tiron doped PPy/MWCNTs, PPy-NF, PPy-NF/MWCNTs, PPy coated MWCNTs, N-AC-MWCNT and N-AC-NF, were fabricated into electrodes using the slurry impregnation method (Figure 4.6). In a typical procedure, capacitive materials were grinded in ethanol with 5 wt% PVB (Polyvinyl butyral) binder. The slurry was then pasted on Ni foam current collector (95 vol% porosity) with an area of  $1 \text{ cm}^2$ . The materials loading of the electrode was  $5\text{-}50 \text{ mg cm}^{-2}$ . After drying, the impregnated Ni foam was further roller pressed to  $\sim 20\%$  of the initial thickness.

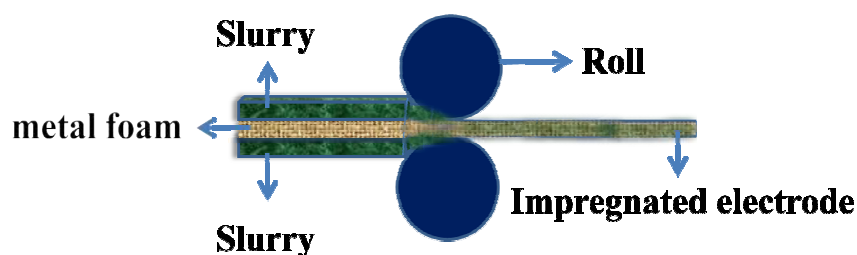


Figure 4.6 Scheme of fabrication electrodes using slurry impregnation.

#### 4.4.3 Fabrication of ES cells

The electrodes obtained by the slurry impregnation method were assembled for ES cells. Symmetric ES cells were produced using two activated carbon electrodes separated by a porous polymer polyethylene membrane (mean pore size 0.4  $\mu\text{m}$ , Vale, Canada) in the electrolyte. Four different symmetric ES cells were fabricated: (I) Tiron doped PPy and Tiron doped PPy/MWCNT composites symmetric ES cells in

saturated  $\text{Na}_2\text{SO}_4$  aqueous electrolyte, (II) N-AC-MWCNT symmetric ES cells in saturated  $\text{Na}_2\text{SO}_4$  aqueous electrolyte, (III) N-AC-MWCNT symmetric ES cells in  $400 \text{ mg L}^{-1}$  SAF, CL and AM dye solutions and (IV) N-AC-NF symmetric ES cells in  $100\text{-}700 \text{ mg L}^{-1}$  PV, ECR, CHR, CHRP, CHRN and CHRB dyes solution.

The asymmetric ES cells contained a positive  $\text{MnO}_2$  coated N-AC-MWCNT electrode and a negative N-AC-MWCNT electrode with active mass loadings of  $10$  and  $25 \text{ mg cm}^{-2}$ , respectively. The positive and negative electrodes were put in the CR2032 type coin cell cases (MTI corporation, USA) and separated by a porous membrane in saturated  $\text{Na}_2\text{SO}_4$  aqueous electrolyte. All ES cells were sealed with a hydraulic crimping machine (MSK-110, MTI Corporation, USA).

## 4.5 Characterization of capacitive performance

### 4.5.1 Cyclic voltammetry

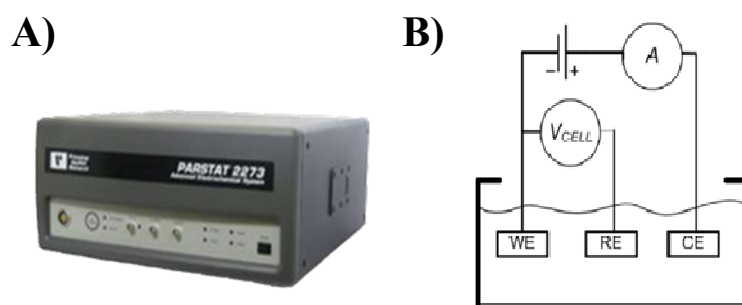


Figure 4.7 (A) Princeton PARSTAT 2273 potentiostat and (B) scheme of three-electrode setup.

Cyclic voltammetry (CV) of single electrodes and ES devices was tested using a potentiostat (PARSTAT 2273, Princeton Applied Research). Single electrodes were tested using three-electrode setup in 0.5 M Na<sub>2</sub>SO<sub>4</sub> aqueous electrolyte (Figure 4.7). The counter electrode was a platinum gauze and the reference electrode was a standard calomel electrode (SCE). Cyclic voltammetry (CV) tests of single electrode were performed at different scan rates<sup>1</sup> within a potential range of -0.5-+0.4 V, 0-0.9 V and -1-0 V for PPy, MnO<sub>2</sub> and activated carbon based electrodes, respectively.

The total capacitance  $C=Q/\Delta V$  was calculated using half the integrated area of the CV curve to obtain the charge Q, and subsequently dividing the charge Q by the width of the potential window  $\Delta V$ . The mass-normalized specific capacitance  $C_m$  (Eq. 4.1) and area-normalized specific capacitance  $C_s$  (Eq. 4.2)) were obtained from the CV data.

$$C_m = \frac{Q}{\Delta V * m} \quad (4.1)$$

$$C_s = \frac{Q}{\Delta V * S} \quad (4.2)$$

#### 4.5.2 Impedance spectroscopy

The impedance spectroscopy (EIS) was performed on a potentiostat (PARSTAT 2273, Princeton Applied Research). The alternating current (AC) complex impedance  $Z^*=Z'-iZ''$  was analyzed in the frequency range of 10 mHz-100 kHz at the amplitude of the AC signal of 5 mV. The complex AC capacitance  $C^*=C'-iC''$  was obtained from the impedance data[5],

$$C' = \frac{Z''}{\omega * |Z|^2} \quad (4.3)$$

$$C'' = \frac{Z'}{\omega * |Z|^2} \quad (4.4)$$

where  $\omega=2\pi f$ ,  $f$  - frequency. The relaxation times  $\tau=1/f_m$  were obtained from the relaxation frequencies  $f_m$ , corresponding to the  $C''_s$  maxima.

#### 4.5.3 Galvanostatic charge-discharge

The fabricated ES cells were investigated for galvanostatic charge-discharge tests. Charge-discharge tests were carried out using a battery analyzer (BST8, MTI corporation, USA) at current densities of 0.5-50 mA cm<sup>-2</sup>. The energy (W) and power (P) of ES devices were calculated using the equations using

$$W = \int_0^t U * I * dt \quad (4.5)$$

$$P = \frac{W}{t} \quad (4.6)$$

, where  $I$  is the current densities,  $U$  is the voltage and  $t$  is the discharging time in unit of hours. The specific energy and specific power in the Ragone plot were obtained using the total mass and total volume of the ES devices. The mass-normalized specific capacitance ( $C_m$ ) and area-normalized specific capacitance ( $C_s$ ) were evaluated by the galvanostatic charge-discharge tests:

$$C_m = 2 * 3.6 * \frac{W}{m * U^2} \quad (4.7)$$

$$C_s = 2 * 3.6 * \frac{W}{s * U^2} \quad (4.8)$$

Where  $m$  and  $s$  are the total mass and area of ES cells.

#### 4.6 Characterization of capacitive water purification

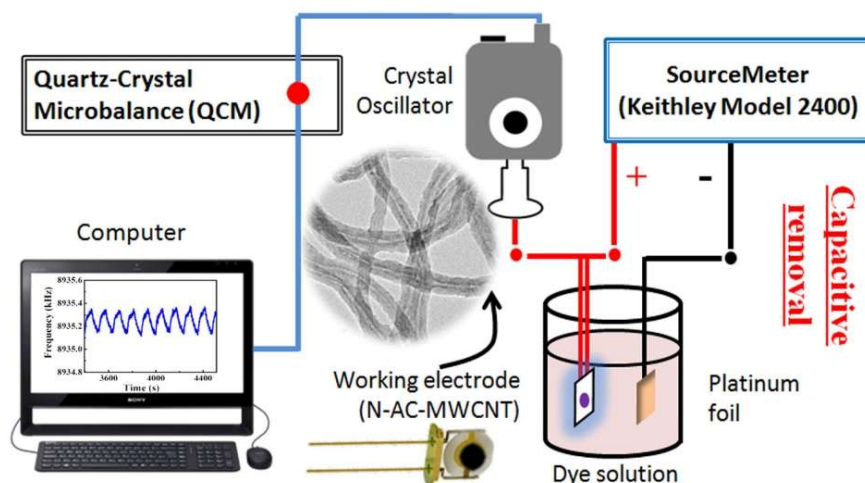


Figure 4.8 Scheme of QCM analysis system for capacitive water purification.

Capacitive adsorption of dyes and NaCl was investigated by Quartz crystal microbalance studies using a microbalance (QCM 922, Princeton Applied Research) controlled by a computer (Figure 4.8). The electrochemical cell included an Au coated 9-MHz quartz resonator working electrode, a Pt wire counter electrode and 50 mg L<sup>-1</sup> dye aqueous electrolyte. The resonators with an area of 0.2 cm<sup>2</sup> were coated with active material. Active material coating was deposited by casting of 0.5  $\mu$ L suspension, containing 20 mg of activated carbon (N-AC-MWCNT and N-AC-NF) and 5% PVDF binder in 1 mL of N-methylpyrrolidone. The coated resonators were dried at 70 °C in the oven.

The QCM studies of capacitive adsorption were performed at a constant voltage (0.6-1 V) and pulse voltage, respectively. In the pulse mode, positive and negative pulses with a constant voltage of 1 V or a series of positive or negative pulses of increasing amplitude in the range of 0.6-1.4 V was applied to the working electrode. The ON and OFF time was 1 min. A sourcemeter (Keithley model 2400) was used as a power supply for QCM studies. The mass gain ( $\Delta m$ ) of the quartz resonators was calculated using the Sauerbrey's equation[6]:

$$-\Delta F = \frac{2F_o^2}{A\sqrt{\rho_q\mu_q}} \times \Delta m \quad (4.9)$$

where  $\Delta F$  is frequency decrease of the QCM,  $F_o$  is the parent frequency of QCM (9 MHz),  $A$  is the area of gold electrode (0.2 cm<sup>2</sup>),  $\rho_q$  is the density of the quartz and  $\mu_q$  is the shear modulus of quartz.

#### 4.7 References

- [1] Z. Liu, X. Zhang, S. Poyraz, S.P. Surwade, S.K. Manohar, Oxidative template for conducting polymer nanoclips, *Journal of the American Chemical Society*, 132 (2010) 13158-13159.
- [2] X. Zhang, J. Zhang, Z. Liu, C. Robinson, Inorganic/organic mesostructure directed synthesis of wire/ribbon-like polypyrrole nanostructures, *Chemical Communications*, (2004) 1852-1853.
- [3] H. Ohshima, Electrophoretic mobility of soft particles, *Journal of Colloid and Interface Science*, 163 (1994) 474-483.
- [4] I. Zhitomirsky, Cathodic electrodeposition of ceramic and organoceramic materials. Fundamental aspects, *Advances in Colloid and Interface Science*, 97 (2002) 279-317.

[5] P. Taberna, P. Simon, J.F. Fauvarque, Electrochemical characteristics and impedance spectroscopy studies of carbon-carbon supercapacitors, *Journal of The Electrochemical Society*, 150 (2003) A292-A300.

[6] G. Sauerbrey, Verwendung von Schwingquarzen zur Wägung dünner Schichten und zur Mikrowägung, *Zeitschrift für Physik A Hadrons and Nuclei*, 155 (1959) 206-222.

## **5. PPy electrodes for energy storage in supercapacitors**

### **5.1 Influence of current collector on the capacitive performance of PPy prepared by the electrochemical polymerization**

Electrochemical polymerization has been investigated for the fabrication of PPy electrodes for ES application[1-3]. In this approach, anodic polymerization of PPy allows the pyrrole monomer, dissolved in a solvent, containing an anionic dopant, to be oxidized at the electrode surface by the applied anodic potential, forming a polymer film[3, 4]. Many studies were focused on the development of advanced anionic dopants for PPy electrochemical polymerization. In the following investigation, the electrochemical polymerization was performed galvanostatically at a current density of  $1 \text{ mA cm}^{-2}$ . Tiron was selected as the anionic dopant for PPy due to high charge/mass ratio and strong adhesion to the substrate. Previous studies of electrochemical polymerization of PPy on Al alloy substrates indicated that Tiron allowed the formation of continuous films and promoted charge transfer [5].

#### **5.1.1 Electrochemical polymerization of PPy on different current collectors**

The inset of Fig. 5.1A shows a chemical structure of Tiron. The anionic properties of Tiron are attributed to  $\text{SO}^{3-}$  groups. Similar to other materials from the catechol family, Tiron has two OH groups, bonded to adjacent carbon atoms of the aromatic ring. Such OH groups are assumed to form bidentate bonding of catechol with metal

atoms on the material surface[6]. It has been known that catechols are important and versatile building blocks of synthetic adhesives and coatings[6, 7].

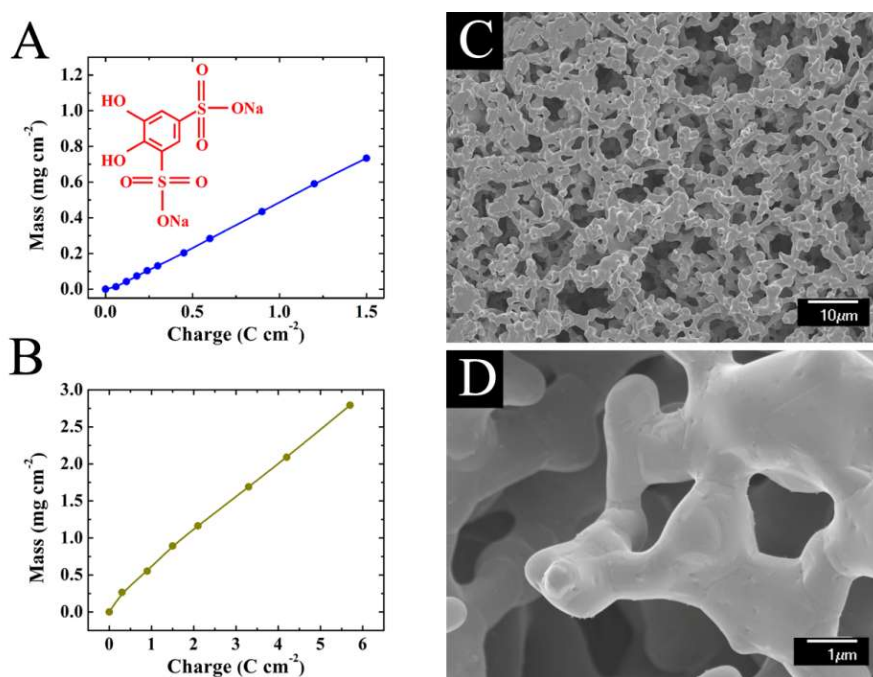


Figure 5.1 (A, B) Deposit mass versus charge passed for deposition on (A) Ni foil (inset shows a chemical structure of Tiron dopant) and on (B) Ni plaque substrates and (C, D) SEM images of Ni plaques at different magnifications.

PPy films were obtained on Ni foil substrates by the electrochemical polymerization from pyrrole solutions containing Tiron. Deposit mass increased with increasing deposition time at a constant current density. Fig. 5.1A shows nearly linear dependence of the deposit mass versus charge passed, which indicated continuous film growth without induction time. It should be noted that induction time [8-10] was observed in experiments performed using other anionic dopants, and was related to

substrate dissolution and passivation. Thin films with mass below  $0.4 \text{ mg cm}^{-2}$  were well adherent to Ni foil substrates. The measurements of film adhesion according to the ASTM D3359 standard showed that adhesion strength corresponded to the 4B classification. However, adhesion decreased with increasing film mass, especially for film mass above  $1 \text{ mg cm}^{-2}$ . In order to increase the mass of PPy deposits, electrochemical polymerization was performed on commercial Ni plaque current collectors, designed for high power battery applications[11]. The deposits mass increased with increasing charge passed, showing nearly linear dependence (Fig. 5.1B) in the range of  $0\text{-}3 \text{ mg cm}^{-2}$ . Relatively high mass of PPy deposits was achieved because of porous microstructure of the Ni plaques (Fig. 5.1C). The pore size of Ni-plaques was in the range of  $1\text{-}10 \text{ }\mu\text{m}$  (Fig. 5.1C and D). Such pores were impregnated with PPy during electrochemical polymerization.

#### 5.1.2 Capacitive performance of PPy deposits

The PPy films formed on Ni substrates showed capacitive behavior in the voltage window of  $-0.5 \text{ - } +0.4 \text{ V}$  versus SCE. Fig. 5.2A shows typical CVs for films in mass range of  $0.10\text{-}0.42 \text{ mg cm}^{-2}$ . Thin films showed nearly box shape CVs, however significant deviation from the ideal box shape CV was observed when film mass was above  $0.3 \text{ mg cm}^{-2}$ . Measurements of  $C_m$  and  $C_s$  at different conditions are important for understanding electrochemical behavior of PPy electrodes and optimizing their performance. The  $C_m$  calculated from the CV data for  $0.1 \text{ mg cm}^{-2}$  film at a scan rate

of  $2 \text{ mV s}^{-1}$  was found to be  $350 \text{ F g}^{-1}$ . The increase in scan rate and mass loading resulted in decreasing  $C_m$  (Fig. 5.2B). The  $C_m$  of the films deposited on Ni substrates was higher, compared to  $C_m$  of films formed on stainless steel[12]. The increase in film mass resulted in increasing  $C_s$  at low scan rates (Fig. 5.2C). In contrast, the  $C_s$  at high scan rates decreased with increasing film mass. It is suggested that diffusion limitations at high scan rates resulted in poor electrolyte access to the bulk of thick PPy films. It is in this regard that corresponding impedance data, presented in a Nyquist plot (Fig. 5.2D), showed the increase in film resistance  $Z'$  with increasing film mass. Therefore, bulk PPy material behaved as a capacitor with low capacitance, connected in series with a surface layer with a high capacitance, and reduced total  $C_s$  of thick PPy films.

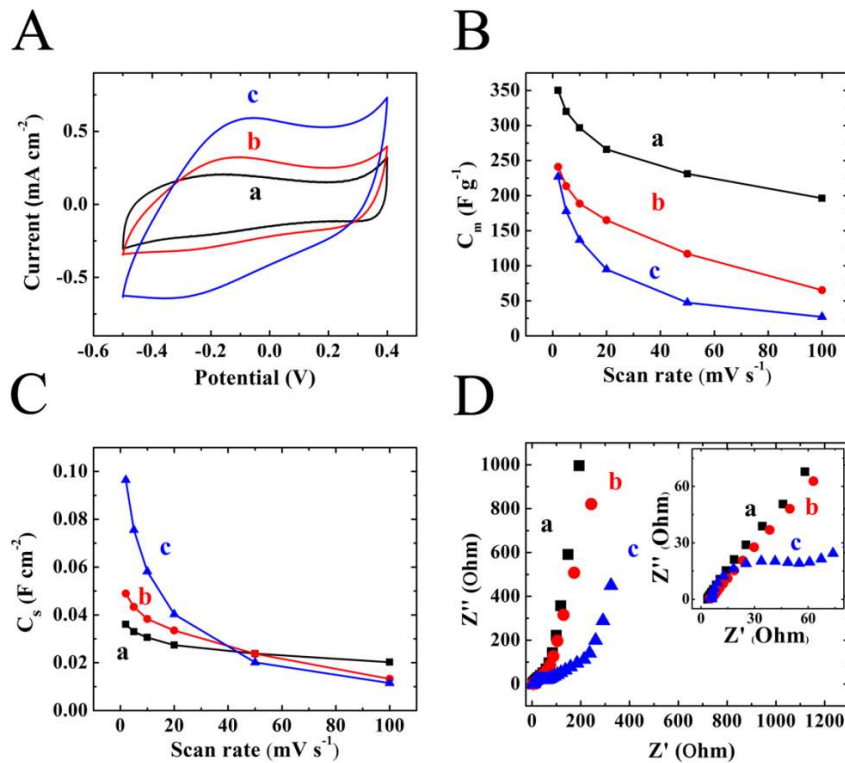


Figure 5.2 (A) CVs at a scan rate of  $5 \text{ mV s}^{-1}$ , (B)  $C_m$  and (C)  $C_s$  obtained from the CV data versus scan rate and (D) Nyquist plot of  $Z^*$  for PPy deposits on Ni foil with PPy mass of (a) 0.10, (b) 0.20 and (c)  $0.42 \text{ mg cm}^{-2}$ , the inset shows high frequency range.

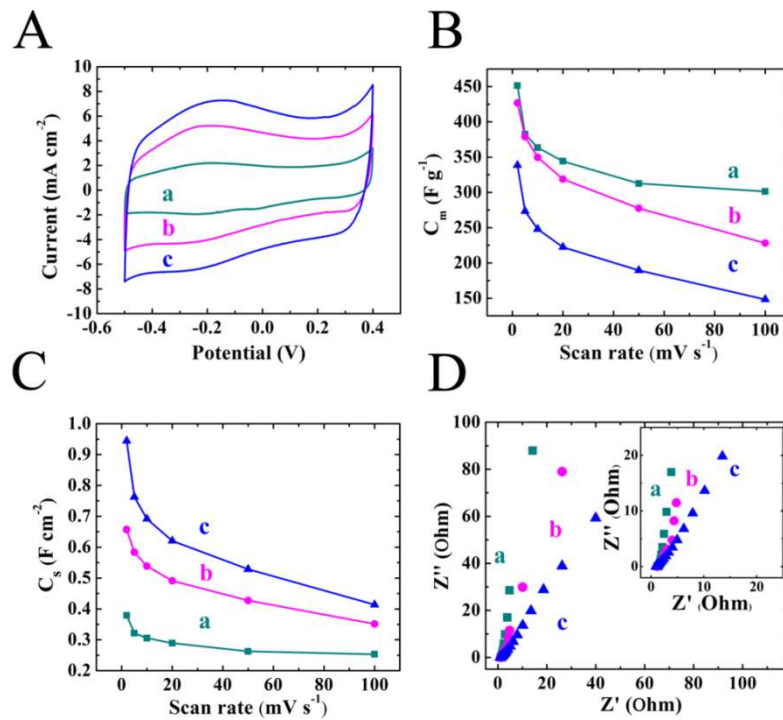


Figure 5.3 (A) CVs at a scan rate of  $5 \text{ mV s}^{-1}$ , (B)  $C_m$  and (C)  $C_s$  obtained from the CV data versus scan rate and (D) Nyquist plot of  $Z^*$  (inset shows high frequency range) for PPy deposits on Ni plaque with PPy mass of (a) 0.84, (b) 1.54 and (c)  $2.80 \text{ mg cm}^{-2}$ .

The comparison of PPy deposits on Ni foil (Fig. 5.2) and Ni plaque (Fig. 5.3) based electrodes showed that significant improvement in capacitive performance at higher materials loading can be achieved using Ni plaque current collectors. The box shape

CVs were observed for materials loadings of 0.84-2.80 mg cm<sup>-2</sup> (Fig. 5.3A). The  $C_m$  values calculated from the CVs at different scan rates showed remarkable improvement in capacitive behavior (Fig. 5.3B). The  $C_m$  at 2 mV s<sup>-1</sup> for the material loading of 0.84 mg cm<sup>-2</sup> (Fig. 5.3B) was 451 F g<sup>-1</sup>, whereas the  $C_m$  for 0.42 mg cm<sup>-2</sup> film (Fig. 5.2B) was only 227 F g<sup>-1</sup>. The difference between the same samples was much more obvious as the scan rate increased to 100 mV s<sup>-1</sup>. The  $C_m$  values of 301 F g<sup>-1</sup> (Fig. 5.3B) and 27 F g<sup>-1</sup> (Fig. 5.2B) were obtained for 0.84 mg cm<sup>-2</sup> Ni plaque and 0.42 mg cm<sup>-2</sup> Ni foil based electrodes, respectively. The experimental results indicated the  $C_m$  decreased with increasing PPy mass (Fig. 5.3B). However, the analysis of corresponding  $C_s$  data (Fig. 5.3C) showed a different behavior, compared to the  $C_s$  data for thin film samples (Fig. 5.2C). The increase in PPy mass resulted in increasing  $C_s$  not only at low scan rates, but also at high scan rates (Fig. 5.3C). This is in contrast to the data for thin film samples formed on Ni foils (Fig. 5.2C), which showed decreasing  $C_s$  with increasing film mass at high scan rates. The impedance measurements showed that electrode resistance  $Z'$  increased with increasing mass of the electrode (Fig. 5.3D). However, the Ni plaques based PPy electrodes showed significantly lower  $Z'$  values, compared to the Ni foil based electrodes of smaller mass (Fig. 5.2D). The lower  $Z''$  values of Ni plaque based PPy electrodes indicated improved capacitive performance. Furthermore, the experimental data presented in Fig. 5.3B and C indicated that the increase in PPy mass in the range of 0.84-2.80 mg cm<sup>-2</sup> resulted in  $C_m$  decrease in the range of 451-339 F g<sup>-1</sup> and corresponding  $C_s$

increase in the range of  $0.4\text{-}0.95\text{ F cm}^{-2}$  at a scan rate of  $2\text{ mV s}^{-1}$ . Previous studies on PPy electrodes[13, 14] prepared by electrochemical polymerization on Ni and stainless steel electrodes with materials loading of  $0.66\text{-}1.0\text{ mg cm}^{-2}$  were in the range of  $100\text{-}350\text{ F g}^{-1}$  for  $C_m$  and  $0.07\text{-}0.34\text{ F cm}^{-2}$  for  $C_s$ . Therefore, the use of Tiron as an anionic dopant for PPy and Ni plaque current collectors offer benefits of relatively high capacitance at higher materials loadings.

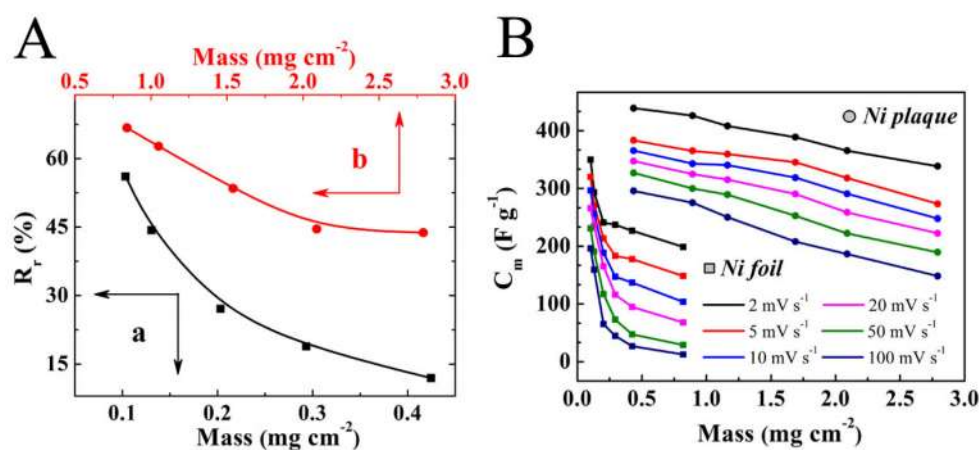


Figure 5.4 (A) Capacitance retention versus mass of PPy deposits on (a) Ni foil and (b) Ni plaque substrates and (B)  $C_m$  at the scan rates from 2 to  $100\text{ mV s}^{-1}$  versus mass of PPy deposits for Ni foil and Ni plaque based electrodes.

The capacitive retention of the electrode,  $R_r = C(100)/C(2)$ , was obtained as a ratio of the specific capacitance measured at the scan rate of  $100\text{ mV s}^{-1}$  to the specific capacitance measured at the scan rate of  $2\text{ mV s}^{-1}$ . Fig. 5.4A compares  $R_r$  for PPy deposits on Ni foils and for Ni-plaques based electrodes. The decrease in  $R_r$  with increase of PPy mass was attributed to diffusion limitations of electrolyte in pores of

PPy electrodes. While the increase in film mass from 0.10 to 0.42 mg cm<sup>-2</sup> resulted in R<sub>r</sub> reduction from 56 to 10% for PPy deposits on Ni foil, the increase in mass loading of PPy on Ni plaque from 0.84 to 2.80 mg cm<sup>-2</sup> resulted in R<sub>r</sub> decrease in the range from 68 to 43%. The Ni plaque based PPy electrodes showed much higher C<sub>m</sub> values even at higher materials loadings as shown in Fig. 5.4B. The results demonstrated that the use of porous Ni plaques allowed better electrolyte access to active material even at much higher materials loadings.

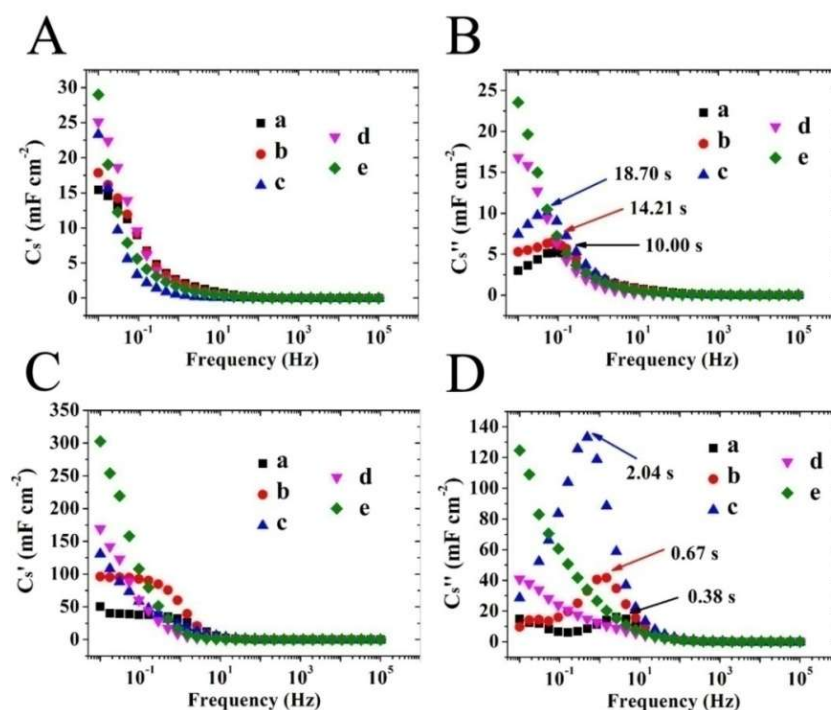


Figure 5.5  $C_s^*$  obtained from impedance data versus frequency for PPy deposits on (A, B) Ni foil with PPy mass of (a) 0.10, (b) 0.13, (c) 0.20, (e) 0.29 and (f) 0.42 mg cm<sup>-2</sup> and (C, D) Ni plaque with PPy mass of (a) 0.84, (b) 1.16, (c) 1.54, (e) 2.09 and (f) 2.80 mg cm<sup>-2</sup>.

Fig. 5.5A shows that  $C_s'$  of thin films decreased with increasing frequency. The corresponding  $C_s''$  curves showed typical relaxation maxima, which shifted to lower frequencies with increasing film mass. The relaxation times  $\tau=1/f_m$  were calculated from the relaxation frequencies  $f_m$ , related to the  $C_s''$  maxima. The  $\tau$  values of 10.00, 14.21 and 18.70 s were obtained for film mass of 0.10, 0.13 and 0.20  $\text{mg cm}^{-2}$ , respectively (Fig. 5.5B). The Ni plaque based PPy electrodes with materials loading of 0.84-2.80  $\text{mg cm}^{-2}$  showed remarkably higher  $C_s'$  values (Fig. 5.5C). Another advantage of Ni plaque based electrodes is related to higher relaxation frequencies. The frequency dependence of  $C_s'$  for 0.84  $\text{mg cm}^{-2}$  electrode showed a plateau below  $\sim 1$  Hz, then the  $C_s'$  decreased at higher frequencies. Such dependence was corresponded to relaxation dispersion. The increase in PPy electrode mass resulted in the relaxation at lower frequencies. The PPy electrode with mass of 1.16  $\text{mg cm}^{-2}$  showed a plateau in the frequency dependence below  $\sim 0.5$  Hz and then  $C_s'$  decreased. The corresponding  $C_s''$  dependencies (Fig. 5D) showed relaxation maxima, which shifted to lower frequencies with increasing electrode mass. The relaxation times  $\tau=1/f_m$  were found to be 0.38, 0.67 and 2.04 s for PPy electrode mass of 0.84, 1.16 and 1.54  $\text{mg cm}^{-2}$ . Therefore, the analysis of  $C^*$  indicated that Ni plaque based electrodes allowed higher capacitance, better capacitance retention at higher frequencies and higher electrode mass. These results are in agreement with the characterization of capacitive performance using cyclic voltammetry discussed above.

## 5.1.3 Cycling stability of PPy deposits on Ni foils and Ni plaques based electrodes

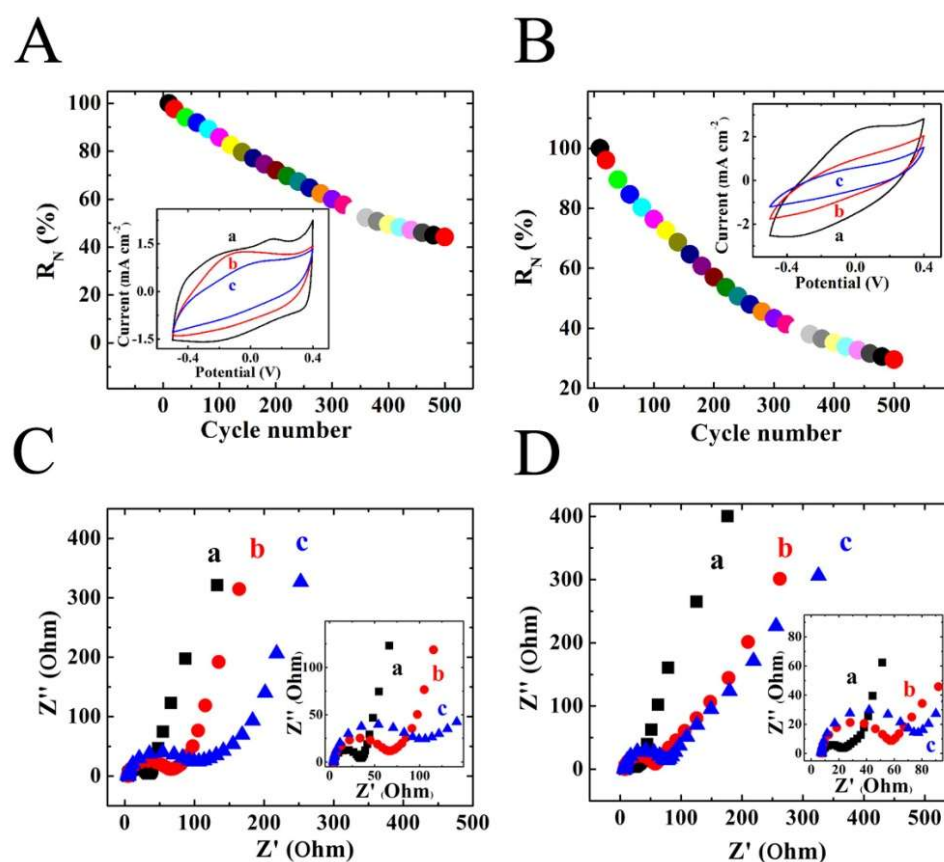


Figure 5.6 (A, B) Capacitance retention versus cycle number (insets show CVs for (a) 10<sup>th</sup> (b) 250<sup>th</sup> and (c) 500<sup>th</sup> cycle) and (C, D) Nyquist plots of  $Z^*$  obtained after the corresponding cycles (insets show high frequency range) for (A, C) 0.15 and (B, D) 0.31 mg cm<sup>-2</sup> deposits on Ni foil.

Fig. 5.6 shows the influence of cycling on electrochemical behavior of PPy films on Ni foil substrates. The capacitance retention,  $R_N = C(50)_N / C(50)_1$ , is the ratio of  $C(50)_N$  for cycle number  $N$  to the  $C(50)_1$  for the first cycle, measured at a scan rate of 50 mV s<sup>-1</sup>. The results indicated that  $R_N$  was decreased with increasing cycle number (Fig. 5.6A). The increase in film mass resulted in reduced capacitance retention (Fig. 5.6B).

The corresponding CV data showed continuous reduction in CV area (Fig. 5.6 A and B insets) with increasing cycle number. The  $R_{500}$  for  $0.31 \text{ mg cm}^{-2}$  electrode was only 29.6%. Fig. 5.6 C and D shows Nyquist plots for impedance measured after 10, 250 and 500 cycles for the same samples. The increase in  $Z'$  and width of high frequency semicircle indicated increasing resistance, which correlated with capacitance measurements for the corresponding cycles. PPy deposit with mass of  $0.31 \text{ mg cm}^{-2}$  (Fig. 5.6D) showed much more significant increase of  $Z'$  compared to the deposit with mass of  $0.15 \text{ mg cm}^{-2}$  (Fig. 5.6C).

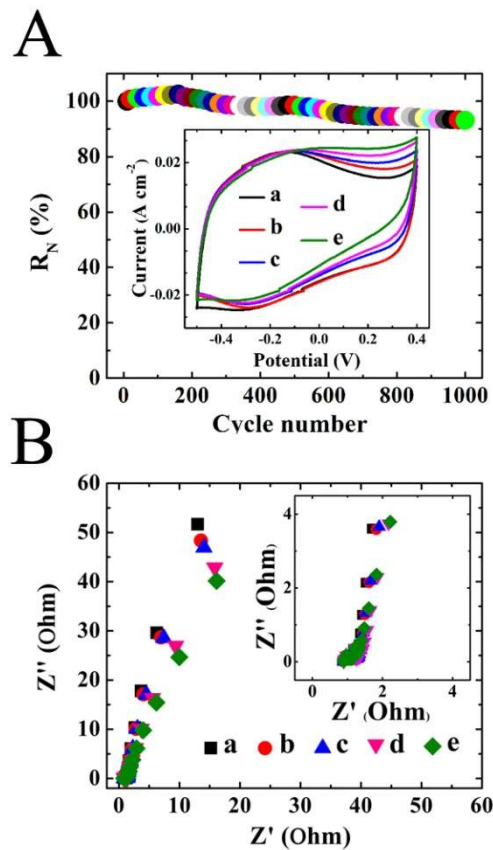


Figure 5.7 (A) capacitance retention versus cycle number (inset shows CVs for (a) 10<sup>th</sup> (b) 150<sup>th</sup>, (c) 500<sup>th</sup>, (d) 750<sup>th</sup> and (e) 1000<sup>th</sup> cycle) and (B) Nyquist plots of  $Z''$

obtained after the corresponding cycles (inset shows high frequency range) for 1.10 mg cm<sup>-2</sup> PPy deposit on a Ni plaque.

The cycle performance of Ni plaque based electrode was presented in Fig. 5.7. Fig. 5.7A shows  $R_N$  as a function of cycle number for PPy deposit with mass of 1.10 mg cm<sup>-2</sup>. The results indicated a small increase in  $R_N$  during the first 150 cycles, then  $R_N$  decreased. The  $R_{500}$  and  $R_{1000}$  values were found to be 97.49% and 93.09%, respectively. The analysis of CVs for 10<sup>th</sup>, 150<sup>th</sup>, 500<sup>th</sup>, 750<sup>th</sup> and 1000<sup>th</sup> cycles (Fig. 5.7A inset) revealed some changes in CV shape, more evident in the potential range of 0-0.4 V. Such change can be attributed to increased resistance. In Fig. 5.7B, impedance spectroscopy data obtained after corresponding cycles showed increase in resistance  $Z'$  with increasing cycle number. However, the changes in resistance for Ni plaque based PPy electrodes (Fig. 5.7B) were relatively small, compared to PPy films on Ni foils (Fig. 5.6C and D).

#### 5.1.4 Morphology of PPy deposits before and after cycling tests

SEM results of PPy electrodes provided information related to the morphology change during cycling tests. Fig. 5.8A shows a SEM image of a PPy film on a Ni foil substrate. The film was relatively dense. The electrolyte diffusion in such films presented difficulties. As a result, the capacitance retention decreased significantly as the mass increased (Fig. 5.4A). Electrochemical cycling resulted in film swelling (Fig. 5.8B), which increased with increasing cycle number. The film partially detached

from the substrates after 1000 cycles. The film swelling and detachment from the substrate resulted in poor electrical contact of the film and Ni foil substrate. Therefore, SEM observations can explain the increase in electrode resistance during cycling (Fig. 5.6C and D) and poor cycling stability (Fig. 5.6A and B).

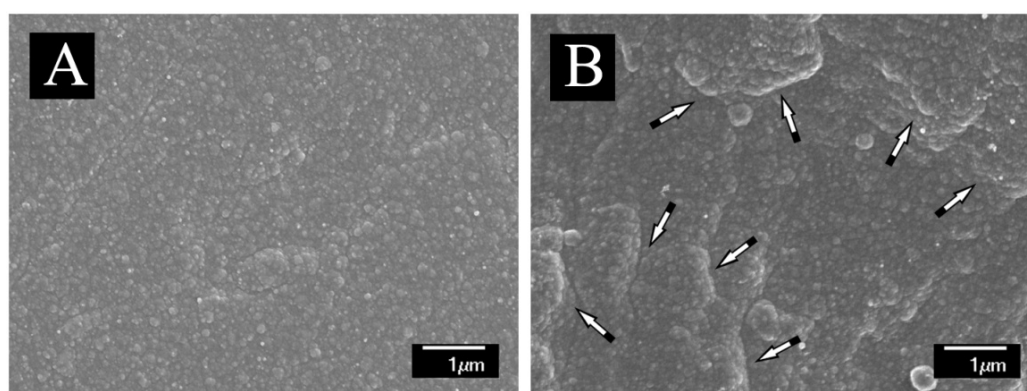


Figure 5.8 SEM images of  $0.15 \text{ mg cm}^{-2}$  PPy deposit on a Ni foil: (A) as prepared and (B) after 500 cycles, arrows show areas of deposit swelling.

The morphology change of PPy on Ni plaque current collector was investigated before and after 1000 cycles (Fig. 5.9). The SEM images of the surface at low magnification showed that the porous Ni plaque was impregnated with PPy (Fig. 5.9A and B). The surface was relatively rough and exhibited cracks. It is suggested that the PPy microstructure is influenced by the microstructure of porous current collector. Large pores in the plaques below the surface PPy layer can promote cracking in the surface layer. Cycling resulted in enhanced cracking of the surface layers and enhanced macroporosity. Such changes can result from PPy swelling during cycling. The SEM image of as-deposited PPy at high magnification showed relatively rough

and dense surface before cycling (Fig. 5.9B). The SEM image of the cycled sample (Fig. 5.9D) revealed microporosity with pore size of about 50 nm. The development of microporosity and cracking in the surface layers can result in improved electrolyte access to the bulk material. Such morphology changes can explain capacitance increase during the first 150 cycles (Fig. 5.7A). However, similar to thin PPy films on Ni foils, the swelling of the surface layers of PPy impregnated plaques can result in reduced capacitance (Fig. 5.7A). However, it is suggested that porous Ni network of Ni plaques limited the swelling of bulk PPy material, which resulted in improved capacitance retention during cycling.

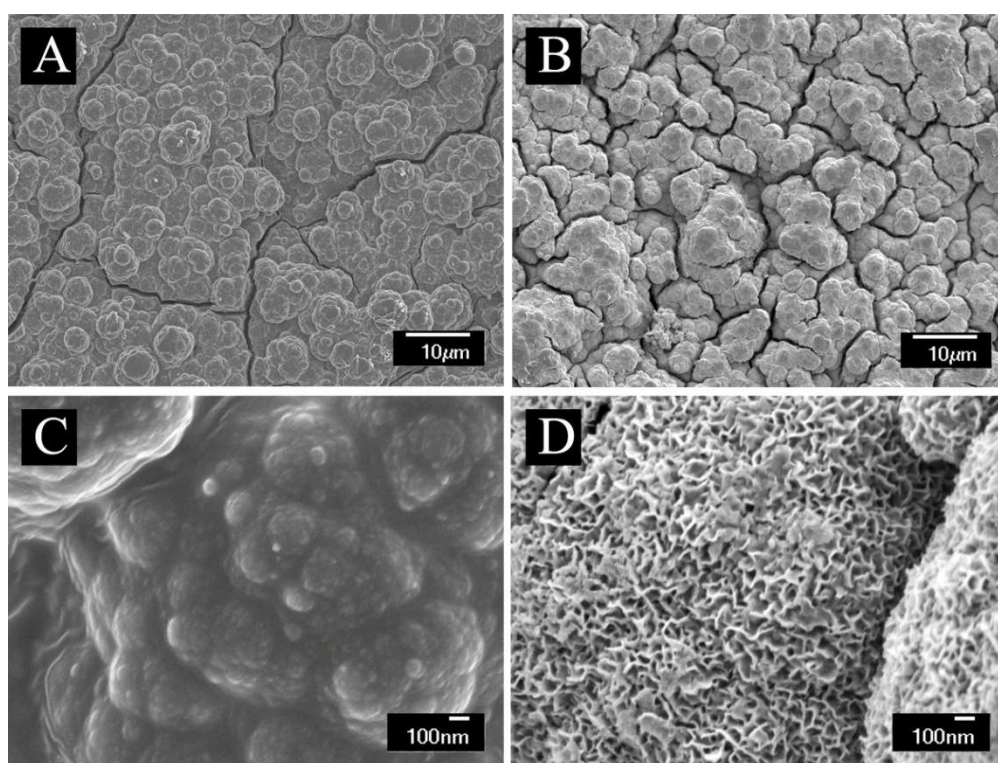


Figure 5.9 (A-D) SEM images of impregnated Ni plaques at different magnifications: (A, C) before cycling and (B, D) after 1000 cycles.

## 5.1.5 Discussion

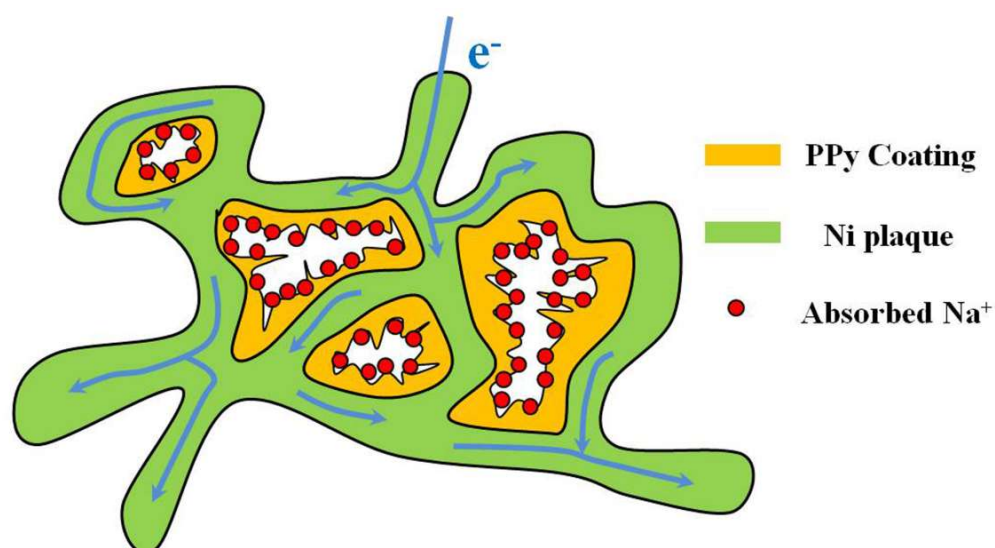


Figure 5.10 Scheme of electron transportation within the porous Ni plaque electrodes.

Compared to Ni foil current collectors, the use of Ni plaques allowed increased  $C_m$  and  $C_s$  at high materials loadings, improved capacitance retention at high scan rates and good cycling stability. The improved capacitive performance of PPy electrodes based on Ni plaque is attributed to their porous architecture and high surface area. As showed in Figure 5.10, porous Ni plaque serves as channels for electron transport. The advantages of porous structure are summarized: (1) the high porosity increases ionic conduction of the electrode; (2) nano-structured PPy shorts traveling distance of the electrolyte, improving electronic conduction within the electrochemical double-layer; and (3) the high contact area provides more active sites, and therefore facilitates fast charge-transfer reactions.

The main drawback of PPy for applications of ES is its poor cycling stability[15, 16]. The charge and discharge instability of PPy is mainly due to structural pulverization and counterion drain effect[17]. The repeated swelling and shrinking of PPy chains leads to structural pulverization, resulting capacitance loss. For the counterion drain effect, the ion channels of PPy could collapse and form a compact structure when anions diffuse back into electrolyte during reduction process[16]. As a result, the Coulombic efficiency of the electrode is reduced. In this investigation, Ni plaque with high porosity and surface area was employed as the current collector, which provided more active sites for reversible redox reaction. Tiron as the dopant improved the capacitive behavior and adhesion of the deposited film

Additionally, the approach developed in this investigation offers processing advantages. It is in this regard that in many recent investigations the improved capacitive behavior was achieved by the development of PPy based composites, containing various additives, such as MWCNT[18], MnO<sub>2</sub>[19] and graphene[20, 21]. However, in this investigation we obtained higher capacitance and good capacitance retention of pure PPy electrodes, compared to PPy based composites[18-21]. This was achieved using Tiron as an anionic dopant and Ni plaque current collectors. Eliminating the use of additives offers important processing advantages, because the problems related to additive preparation, dispersion, electrodeposition and control of deposit composition can be avoided.

### 5.1.6 Conclusions

PPy was deposited by the electrochemical polymerization on Ni foil and Ni plaque current collectors, respectively. The use of Tiron, as an anionic dopant with chelating properties, allowed the formation of adherent PPy films on the Ni substrates. The obtained PPy films were investigated as the electrodes for applications in ES. The results indicated that the  $C_m$  of 339-451 F g<sup>-1</sup> and  $C_s$  of 0.4-0.95 F cm<sup>-2</sup> can be achieved for pure PPy electrodes for material loadings of 0.84-2.80 mg cm<sup>-2</sup>. Compared to Ni foil current collectors, the use of Ni plaques allowed increased capacitance at high materials loadings, improved capacitance retention at high scan rates and good cycling stability. Additionally, Ni plaques limited PPy swelling during cycling and allowed improved cycling stability.

### **5.2 Pulse electrochemical polymerization of PPy using Ni plaque as the current collector**

Galvanostatic and pulse current polymerization are different methods for electrochemical fabrication of PPy films [22, 23]. It was found that films with finer grains can be produced by the pulse method[24]. The previous study[25] showed that pulse current polymerization of PPy decreased resistance and increased capacitance of electrodes. Here, we investigated capacitive performance of Tiron doped PPy electrodes prepared by pulse polymerization. Ni plaques were employed as current collectors for the electrodes.

### 5.2.1 Morphology characterization

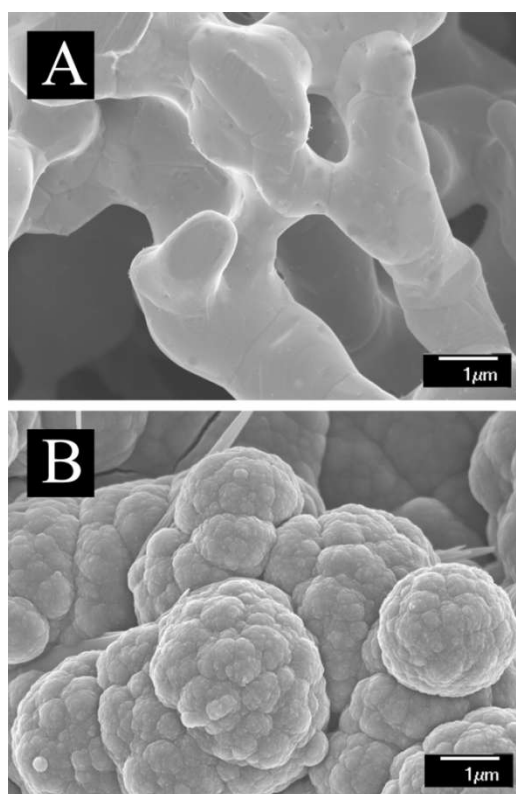


Figure 5.11 SEM images of Ni plaque: (A) as-received and (B) after impregnation with PPy mass loading of  $2.54 \text{ mg cm}^{-2}$ .

SEM studies showed a microstructure of Ni plaques before pulse current polymerization (Fig. 5.11A). The typical Ni grain size is about  $1 \mu\text{m}$ . The porosity and conductivity of commercial Ni plaques are beneficial for the fabrication of PPy electrodes with high material loadings and improved contact of PPy with the current collector. Pulse electrochemical polymerization was used for the impregnation of Ni plaques, because galvanostatic electrochemical polymerization resulted in the formation of surface layers, which blocked the impregnation of the bulk of the Ni plaques[26]. Fig. 5.11B shows a SEM image of an impregnated plaque. The results

indicated that Ni plaques were coated with PPy and exhibited a porous microstructure, which was beneficial for the improved electrolyte access to the PPy surface. PPy coating was formed on micron size Ni grains, however the size of PPy grains was about 100 nm. This is in agreement with the SEM observations of thin films, prepared using 5-sulfosalicylic acid as a dopant, which showed that pulse deposition allows smaller grain size compared to galvanostatic electrochemical polymerization[26, 27]. It is known [28, 29] that during the OFF periods of pulse deposition, the polypyrrole chains are stabilized, making nucleation of new chains more favorable during subsequent ON polymerization pulses, rather than enlarging previous chains.

### 5.2.2 Specific capacitance and capacitance retention

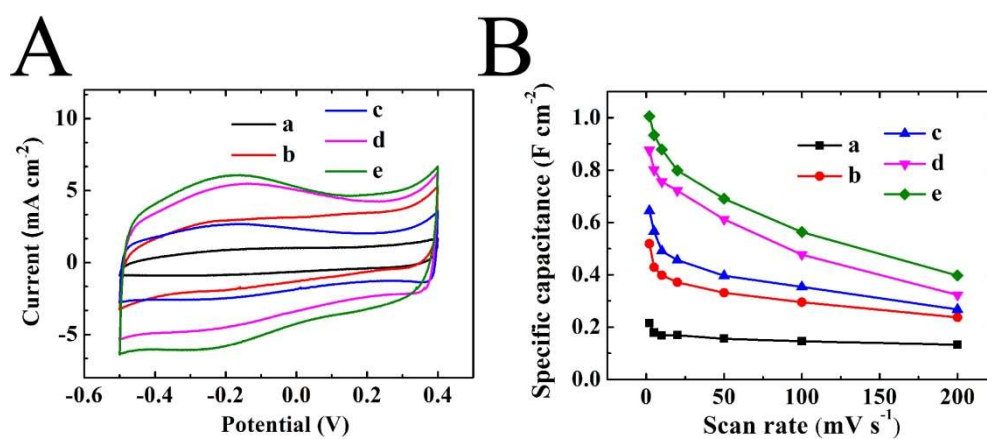


Figure 5.12 Capacitance retention versus cycle number for 1.94 mg cm<sup>-2</sup> PPy electrode. Inset shows CVs at a scan rate of 50 mV s<sup>-1</sup>.

The investigations of PPy electrodes, formed on Ni plaque current collectors revealed good capacitive behaviour, as indicated by the box shape CVs (Fig. 5.12A). The

current increased with increasing PPy mass, indicating the increase in capacitance. Fig. 5.12B shows capacitance versus scan rate dependencies at different material loadings. The increase in PPy mass resulted in a higher area capacitance. The capacitance of  $1.01 \text{ F cm}^{-2}$  at mass loading of  $2.54 \text{ mg cm}^{-2}$  was achieved at a scan rate of  $2 \text{ mV s}^{-1}$ . It is in this regard that thin film samples, prepared by pulse deposition, showed a capacitance of  $0.1 \text{ F cm}^{-2}$  at materials loading of  $0.2 \text{ mg cm}^{-2}$ [25]. Therefore, the use of Ni plaque current collectors allowed the increase in capacitance by one order of magnitude, compared to thin film samples. The advantages of Ni plaque current collectors are especially evident at high scan rates. Thin film deposits showed significant reduction in capacitance with increasing scan rate from 2 to  $100 \text{ mV s}^{-1}$ . The capacitance retention at  $100 \text{ mV s}^{-1}$  was only 20%[25]. In contrast, Ni plaque based PPy electrodes with mass loading of 0.47, 1.01 and  $2.54 \text{ mg cm}^{-2}$  showed capacitance retention of 68, 56 and 54%, respectively. Compared to the previous work[5, 25, 30, 31], both specific capacitance and the retention rate were improved by pulse current polymerization using Ni plaque as the current collectors.

### 5.2.3 Cycling stability

The results of cycling stability of PPy electrode, prepared by pulse electrochemical polymerization, were presented in Fig. 5.13. It was found that the electrode could retain 90.3% of capacitance after 1,000 cycles (Fig. 5.13). The inset shows some

representative CV curves, which are practically overlapping with each other, indicating good long-term cycling stability.

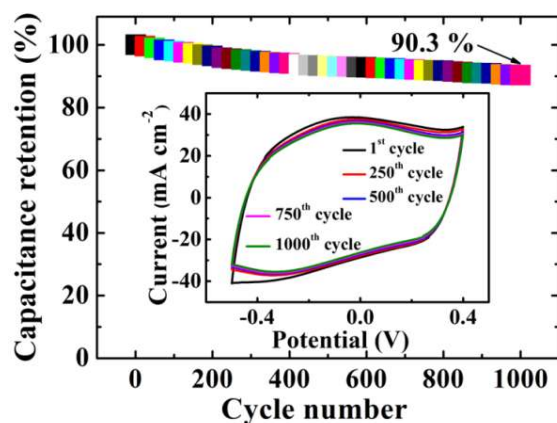


Figure. 5.13 Capacitance retention versus cycle number for  $1.94 \text{ mg cm}^{-2}$  PPy electrode. Inset shows CVs at a scan rate of  $50 \text{ mV s}^{-1}$ .

It has been suggested that the film detachment was caused by PPy swelling during the charge and discharge cycles. The lost of film adhesion usually results in increasing resistance and decreasing capacitance. However, the investigations of Ni plaque based PPy electrodes showed very small changes in impedance during cycling (Fig. 5.14). The impedance data at high frequencies (Fig. 5.14A inset), indicates low resistance. The slope of the  $Z''$  versus  $Z'$  curve was close to  $90^\circ$ , indicating good capacitive behavior. With increase of the cycle number, the slope of the  $Z''$  versus  $Z'$  dependence in the Nyquist plots slightly decreased and then remained at a constant level, reflecting good cycling stability of the PPy electrode. The capacitive behavior was also analyzed using impedance data and presented in the form of Bode plots for

complex AC capacitance (Fig. 5.14B and C). The real part of capacitance  $C'$  showed relaxation at frequencies above 0.1 Hz, the corresponding dependence for the imaginary part  $C''$  showed a relaxation maximum with a time constant  $\tau$  of 6.28 s. The time constant was comparable with that reported for carbon electrodes[32]. During 1000 cycles only relatively small decrease in  $C'$  was observed (Fig. 5.14B inset). The maxima in the frequency dependence of  $C''$  shifted to slightly lower frequencies (Fig. 5.14C inset), indicating the time constant  $\tau$  change from 6.28 to 7.39s. The results indicated that the electrodes, prepared by pulse current polymerization, allowed good capacitance retention at high scan rates and AC frequencies and cycling stability.

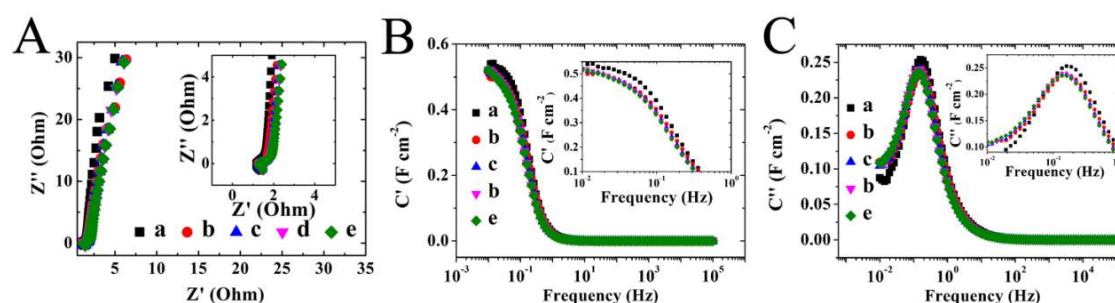


Figure 5.14 (A) Nyquist plots of complex impedance (inset shows high frequency range) and corresponding Bode plots of (B)  $C'$  and (C)  $C''$  (insets show low frequency range) for the PPy electrode with a mass loading of  $1.94 \text{ mg cm}^{-2}$  after (a) 1<sup>st</sup>, (b) 250<sup>th</sup>, (c) 500<sup>th</sup>, (d) 750<sup>th</sup> and (e) 1,000<sup>th</sup> cycles.

#### 5.2.4 Conclusions

PPy electrodes were prepared by pulse electrochemical polymerization using Tiron as an anionic dopant and Ni plaque current collectors. The highest area-normalized

capacitance of  $1.01 \text{ F cm}^{-2}$  was obtained at a scan rate of  $2 \text{ mV s}^{-1}$  with PPy mass loading of  $2.54 \text{ mg cm}^{-2}$ . Cycling voltammetry data coupled with the results of impedance spectroscopy investigations during cycling showed good capacitance retention at high scan rates and good cycling stability.

### 5.3 References

- [1] B. Muthulakshmi, D. Kalpana, S. Pitchumani, N.G. Renganathan, Electrochemical deposition of polypyrrole for symmetric supercapacitors, *Journal of Power Sources*, 158 (2006) 1533-1537.
- [2] P.A. Mini, A. Balakrishnan, S.V. Nair, K.R.V. Subramanian, Highly super capacitive electrodes made of graphene/poly(pyrrole), *Chemical Communications*, 47 (2011) 5753-5755.
- [3] D.P. Dubal, S.H. Lee, J.G. Kim, W.B. Kim, C.D. Lokhande, Porous polypyrrole clusters prepared by electropolymerization for a high performance supercapacitor, *Journal of Materials Chemistry*, 22 (2012) 3044-3052.
- [4] G.A. Snook, P. Kao, A.S. Best, Conducting-polymer-based supercapacitor devices and electrodes, *Journal of Power Sources*, 196 (2011) 1-12.
- [5] D.E. Tallman, C. Vang, G.G. Wallace, G.P. Bierwagen, Direct Electrodeposition of Polypyrrole on Aluminum and Aluminum Alloy by Electron Transfer Mediation, *Journal of The Electrochemical Society*, 149 (2002) C173-C179.
- [6] E. Faure, C. Falentin-Daudre, C. Jerome, J. Lyskawa, D. Fournier, P. Woisel, C. Detrembleur, Catechols as versatile platforms in polymer chemistry, *Progress in Polymer Science*, 38(1), (2013) 236-270.
- [7] B.P. Lee, P.B. Messersmith, J.N. Israelachvili, J.H. Waite, Mussel-Inspired Adhesives and Coatings, *Annual Review of Materials Research*, 41 (2011) 99-132.
- [8] W.J. Hamer, L. Koene, J.H.W. De Wit, Formation and electrochemical behaviour of poly(pyrrole) coatings on steel substrates, *Materials and Corrosion*, 55 (2004) 653-658.
- [9] W. Su, J.O. Iroh, Formation of polypyrrole coatings onto low carbon steel by electrochemical process, *Journal of Applied Polymer Science*, 65 (1997) 417-424.

- [10] A. De Bruyne, J.L. Delplancke, R. Winand, Comparison between polypyrrole films obtained on mild steel by electropolymerization from oxalic acid and sodium sulphate aqueous solutions, *Surface and Coatings Technology*, 99 (1998) 118-124.
- [11] A.Y. Zaitsev, D.S. Wilkinson, G.C. Weatherly, T.F. Stephenson, The preparation of highly porous structures from filamentary nickel powders, *Journal of Power Sources*, 123 (2003) 253-260.
- [12] C. Shi, I. Zhitomirsky, Electrodeposition of composite polypyrrole-carbon nanotube films, *Surface Engineering*, 27 (2011) 655-661.
- [13] C. Shi, I. Zhitomirsky, Electrodeposition and Capacitive Behavior of Films for Electrodes of Electrochemical Supercapacitors, *Nanoscale research letters*, 5 (2010) 518-523.
- [14] Z.H. Dong, Y.L. Wei, W. Shi, G.A. Zhang, Characterisation of doped polypyrrole/manganese oxide nanocomposite for supercapacitor electrodes, *Materials Chemistry and Physics*, 131 (2011) 529-534.
- [15] C. Arbizzani, M. Mastragostino, L. Meneghello, Polymer-based redox supercapacitors: A comparative study, *Electrochimica Acta*, 41 (1996) 21-26.
- [16] H. Olsson, G. Nyström, M. Strømme, M. Sjödin, L. Nyholm, Cycling stability and self-protective properties of a paper-based polypyrrole energy storage device, *Electrochemistry Communications*, 13 (2011) 869-871.
- [17] Y. Song, T.-Y. Liu, X.-X. Xu, D.-Y. Feng, Y. Li, X.-X. Liu, Pushing the Cycling Stability Limit of Polypyrrole for Supercapacitors, *Advanced Functional Materials*, 25 (2015) 4626-4632.
- [18] X. Li, I. Zhitomirsky, Electrodeposition of polypyrrole-carbon nanotube composites for electrochemical supercapacitors, *Journal of Power Sources*, 221 (2013) 49-56.
- [19] R.K. Sharma, A. Karakoti, S. Seal, L. Zhai, Multiwall carbon nanotube-poly(4-styrenesulfonic acid) supported polypyrrole/manganese oxide nano-composites for high performance electrochemical electrodes, *Journal of Power Sources*, 195 (2010) 1256-1262.
- [20] H.-H. Chang, C.-K. Chang, Y.-C. Tsai, C.-S. Liao, Electrochemically synthesized graphene/polypyrrole composites and their use in supercapacitor, *Carbon*, 50 (2012) 2331-2336.
- [21] P. Mini, A. Balakrishnan, S.V. Nair, K. Subramanian, Highly super capacitive electrodes made of graphene/poly (pyrrole), *Chemical Communications*, 47 (2011) 5753-5755.

- [22] S. Demoustier-Champagne, J. Duchet, R. Legras, Chemical and electrochemical synthesis of polypyrrole nanotubules, *Synthetic Metals*, 101 (1999) 20-21.
- [23] S. Sadki, P. Schottland, N. Brodie, G. Sabouraud, The mechanisms of pyrrole electropolymerization, *Chemical Society Reviews*, 29 (2000) 283-293.
- [24] I. Kosta, E. Vallés, E. Gómez, M. Sarret, C. Müller, Nanocrystalline CoP coatings prepared by different electrodeposition techniques, *Materials Letters*, 65 (2011) 2849-2851.
- [25] X. Li, I. Zhitomirsky, Capacitive behaviour of polypyrrole films prepared on stainless steel substrates by electropolymerization, *Materials Letters*, 76 (2012) 15-17.
- [26] X. Li, I. Zhitomirsky, Electrodeposition of polypyrrole-carbon nanotube composites for electrochemical supercapacitors, *Journal of Power Sources*, 221 (2013) 49-56.
- [27] K. Shi, I. Zhitomirsky, Influence of current collector on capacitive behavior and cycling stability of Tiron doped polypyrrole electrodes, *Journal of Power Sources*, 240 (2013) 42-49.
- [28] T.D. Nguyen, M. Keddad, H. Takenouti, Device to Study Electrochemistry of Iron at a Defect of Protective Coating of Electronic Conducting Polymer, *Electrochemical and Solid-State Letters*, 6 (2003) B25-B28.
- [29] R.K. Sharma, A.C. Rastogi, S.B. Desu, Pulse polymerized polypyrrole electrodes for high energy density electrochemical supercapacitor, *Electrochemistry Communications*, 10 (2008) 268-272.
- [30] Y. Fang, J. Liu, D.J. Yu, J.P. Wicksted, K. Kalkan, C.O. Topal, B.N. Flanders, J. Wu, J. Li, Self-supported supercapacitor membranes: Polypyrrole-coated carbon nanotube networks enabled by pulsed electrodeposition, *Journal of Power Sources*, 195 (2010) 674-679.
- [31] K. Qi, Y. Qiu, X. Guo, Pulse electrochemical incorporation of graphene oxide into polypyrrole films for supercapacitor electrode materials, *Electrochimica Acta*, 137 (2014) 685-692.
- [32] C. Portet, P.L. Taberna, P. Simon, E. Flahaut, C. Laberty-Robert, High power density electrodes for Carbon supercapacitor applications, *Electrochimica Acta*, 50 (2005) 4174-4181.

## **6. PPy based composite electrodes for energy storage in supercapacitors**

### **6.1 Tiron doped PPy/MWCNTs composite prepared using SAF as the co-dispersant**

It has been known that fabrication of the electrodes with high mass loading using electrochemical polymerization is very time consuming [1, 2]. For practical applications of ES, it is always desirable to increase active material loading and achieve high capacitance at high charge-discharge rates[3, 4]. Chemical polymerization of PPy is an attractive method for ES applications with the advantage for fabrication of electrode with high mass loadings. Additionally, a great advancement has been achieved by using carbon nanotube (CNT) to improve the rate capability of PPy-based electrode because of their superior electrical conductivity and high specific surface area[5-7]. However, both CNT and PPy are prone to agglomeration in the fabrication process. In the following study, PPy was chemically polymerized by APS using Tiron as an anionic dopant. A facile route for fabrication of PPy nano-composites with multiwalled carbon nanotube (MWCNT) has been developed using safranin (SAF) as a co-dispersant. Good dispersion of the MWCNT resulted in obtaining supercapacitor electrodes with improved capacitance retention at high charge-discharge rates.

### 6.1.1 Morphology of PPy, prepared by chemical polymerization

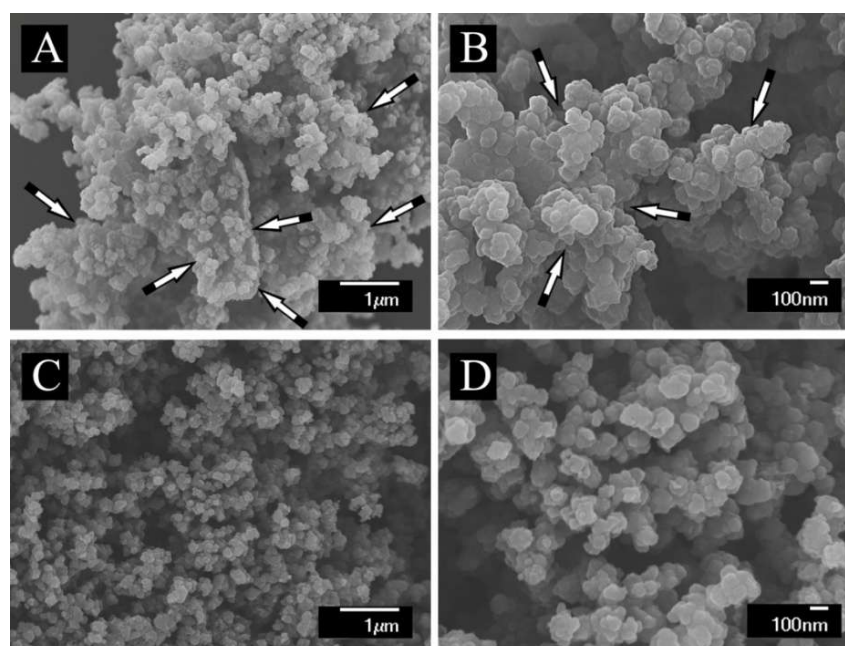


Figure 6.1 SEM images at different magnifications of (A, B) PPy prepared without Tiron, arrows show agglomerates of particles; and (C, D) Tiron doped PPy.

PPy powders were prepared by chemical polymerization as-described in Section 4.2.1.3. Figs. 6.1A and 1B show the SEM images of PPy, prepared without Tiron. The morphology exhibits an agglomerated cauliflower-like structure, consisting of many spherical particles. The mechanism of chemical polymerization of PPy in the presence of dopants and oxidants was discussed in the literature[8, 9]. Upon the addition of oxidant solution to the monomer solution, each neutral pyrrole molecule is oxidized by APS and yields a free cationic radical, which then combines with another radical to form a dimer. The dimers are further combined with other free cationic radicals to form trimers and so on, finally resulting in chains of positively charged PPy units. The

anionic dopants are incorporated into the polymer matrix and compensate the positive charge of PPy[10, 11]. Fig. 6.1C and 6.1D show that the Tiron doped PPy has a fine structure. The results demonstrated that Tiron could reduce the agglomeration of PPy particles.

### 6.1.2 Fabrication of PPy/MWCNT composites

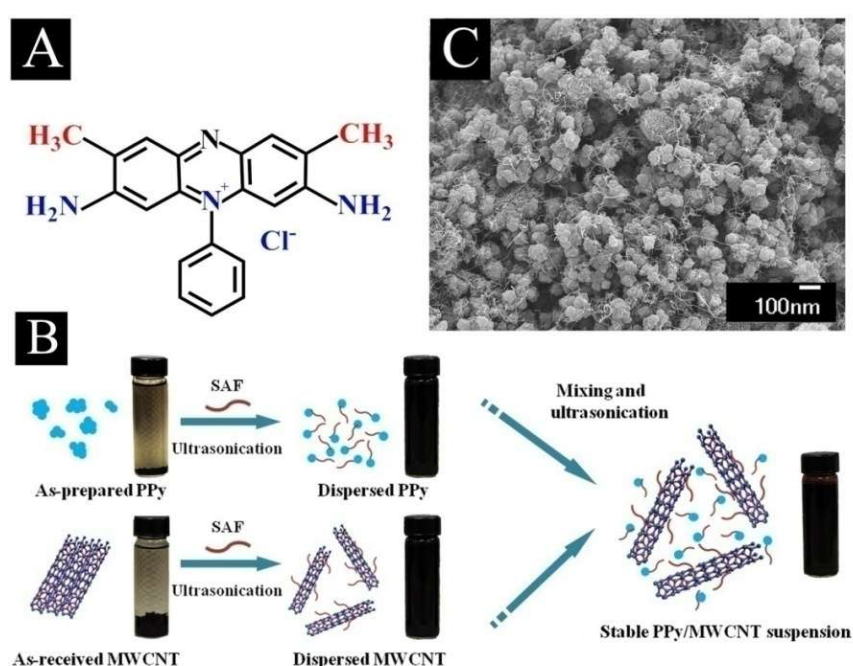


Figure 6.2 (A) Chemical structure of SAF, (B) Scheme of Tiron doped PPy/MWCNT suspension fabrication and (C) SEM image of Tiron doped PPy/MWCNT composite obtained from a mixed Tiron doped PPy/MWCNT suspension.

Tiron doped PPy/MWCNT composites were prepared using SAF as the co-dispersant (Section 4.2.2.1). The sedimentation test showed that as-prepared PPy was not stable in the aqueous suspension. It is suggested that fine PPy particles in suspension formed

agglomerates, which promoted PPy precipitation. It is known that particle agglomeration results in reduced surface area, which deteriorates the capacitive behavior of active materials[12]. In this study, we found that Tiron doped PPy and MWCNT can be well dispersed using SAF as a co-dispersant. Fig. 6.2A shows the molecular structure of cationic polyaromatic SAF, which includes two methyl groups and two NH<sub>2</sub> groups. SAF offers advantages for dispersion, compared to long chain surfactants, which are widely used for the dispersion of carbon nanotubes[13]. In general, surfactants have both polar (hydrophilic) and nonpolar (hydrophobic) moieties[14, 15]. The hydrophilic head of adsorbed surfactant is directed toward the bulk water, and the hydrophobic tail provides adsorption on the carbon nanotube surface via hydrophobic interactions. The adsorbed long chain surfactants create insulating layers on the carbon nanotube surface, which reduce the efficiency of carbon nanotubes for application as conductive additives in the composites. Due to the weak hydrophobic interactions, relatively large concentrations of surfactants are required for the carbon nanotube dispersion. It was found that surfactants can provide dispersion at relatively low carbon nanotube concentrations[16-19]. It is in this regard that the smaller size of SAF molecules is beneficial for the dispersion of MWCNT. The adsorption of SAF on both PPy and MWCNT involves the  $\pi$ - $\pi$  interactions. The positive charge of adsorbed SAF results in electrostatic repulsion of PPy and MWCNT and improves dispersion of both materials. Fig. 6.2B is the scheme of Tiron doped PPy/MWCNT suspension fabrication. The pristine Tiron doped PPy and

MWCNT show a very quick precipitation after 1-2 hours. After adding SAF into MWCNT and Tiron doped PPy, the suspensions showed no precipitation after two weeks. Mixed Tiron doped PPy and MWCNT suspensions were homogenous and stable. SEM images (Fig. 6.2C) showed the Tiron doped PPy/MWCNT composite fabricated by mixing suspensions followed by a vacuum filtration process. The results indicated that MWCNTs were well dispersed in PPy matrix. Good dispersion of MWCNTs allowed the fabrication of PPy electrode with improved capacitive performance.

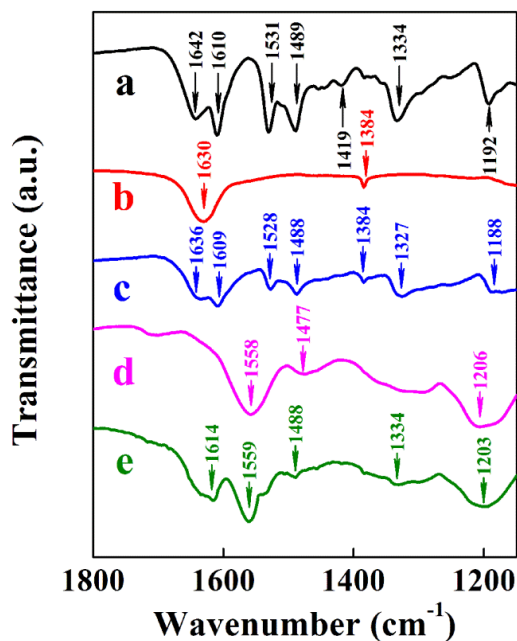


Figure 6.3 FTIR for (a) SAF, (b) pristine MWCNT, (c) SAF dispersed MWCNT (d) Tiron doped PPy, (e) SAF dispersed Tiron doped PPy.

The MWCNT and Tiron doped PPy were analyzed by FTIR (Fig. 6.3a-e). The FTIR spectrum of SAF (Fig. 6.3a) was in agreement with literature data[20, 21]. The C=C

stretching of the benzene rings contributed to the bands at 1531 and 1489  $\text{cm}^{-1}$ . The absorption at 1610  $\text{cm}^{-1}$  is attributed to the  $\text{NH}_2$ - asymmetric deformation. The C=N stretching appears at the 1642 and 1334  $\text{cm}^{-1}$ . The FTIR spectrum of MWCNT (Fig. 6.3b) showed the absorption at 1630-1635  $\text{cm}^{-1}$ , related to the C=O stretching of quinone groups of MWCNT. The bending vibration of the -OH group contributed to the band at 1384  $\text{cm}^{-1}$ [22]. The peaks at 1558 and 1477  $\text{cm}^{-1}$  in Fig. 6.3d are assigned to C-N and C-C asymmetric and symmetric ring-stretching of PPy, respectively. Additionally, strong peak near 1206  $\text{cm}^{-1}$  is attributed to symmetric and asymmetric stretching vibration of  $\text{SO}_3\text{Na}$  group of Tiron dopant[23]. The IR absorption of doping band and its intensity is associated with changes in the conjugated structure of conductive polymer[23, 24]. Rodriguez et. al.[25] suggested that it is depended on the oxidation-state and charge carriers of the PPy chains. In comparison with the spectra of pristine MWCNT and Tiron doped PPy, the spectra of dispersed materials (Fig. 6.3c and e) showed additional adsorptions at 1609, 1528, 1488, 1327  $\text{cm}^{-1}$  for dispersed MWCNT and at 1614 and 1334  $\text{cm}^{-1}$  for dispersed Tiron doped PPy. Taking into account that similar absorptions were observed in the spectrum of SAF, it was concluded that the dispersed MWCNT and Tiron doped PPy contained adsorbed SAF.

### 6.1.3 Capacitive performance of single electrode

Fig. 6.4A shows typical cyclic voltammograms for the different electrodes. The incorporation of Tiron into the PPy matrix significantly increased the capacitive

behavior, as indicated by the differences in current between undoped PPy (Fig. 6.4A(a)) and Tiron doped PPy (Fig. 6.4A(b)). The cyclic voltammogram area for doped PPy is significantly larger than that for undoped PPy, indicating a higher capacitance of the doped material. While the Tiron doped sample with a mass of 14 mg cm<sup>-2</sup> showed a nearly box-shaped cyclic voltammogram (Fig. 6.4A(b)), a deviation from the ideal box-shaped cyclic voltammogram was observed when the mass loading was increased to 27 mg cm<sup>-2</sup> (Fig. 6.4A(c)). The CV curve of SAF dispersed composite electrode with the same mass (Fig. 6.4A(d)) has a nearly box shape, suggesting the capacitive performance was improved by utilization of MWCNT and a co-dispersant.

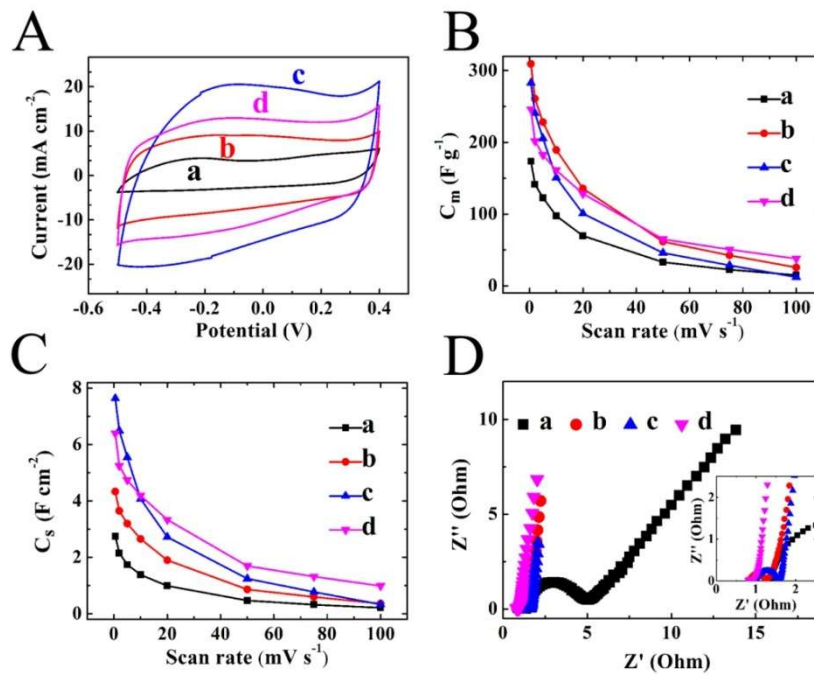


Figure 6.4 (A) CV data at a scan rate of 2 mV s<sup>-1</sup>, (B) C<sub>m</sub> and (C) C<sub>s</sub> obtained from the CV data versus scan rate and (D) Nyquist plot of Z\* (inset shows high frequency

range) for (a) PPy without Tiron with a mass of  $14 \text{ mg cm}^{-2}$ ; (b) Tiron doped PPy with a mass of  $14 \text{ mg cm}^{-2}$ ; (c) Tiron doped PPy with a mass of  $27 \text{ mg cm}^{-2}$ ; (d) Tiron doped PPy/MWCNT composite with a mass of  $27 \text{ mg cm}^{-2}$ .

Measurements of  $C_m$  and  $C_s$  at different conditions are important for understanding the electrochemical behavior of PPy electrodes and optimizing their performance. As shown in Fig. 6.4B, the  $C_m$  calculated from the CV data for  $14 \text{ mg cm}^{-2}$  undoped PPy was only  $174 \text{ F g}^{-1}$  at a scan rate of  $0.5 \text{ mV s}^{-1}$ . The Tiron doped PPy showed a capacitance of  $309 \text{ F g}^{-1}$ . The increase in the scan rate and mass loading resulted in a decreasing  $C_m$ . It has been demonstrated that high  $C_m$  values of electrode materials do not necessarily indicate good capacitive behavior due to the strong dependence of  $C_m$  on the electrode mass[26]. Therefore,  $C_s$  data for the composite electrode were presented in Fig. 6.4C. The Tiron doped PPy showed an increased  $C_s$  of  $4.4 \text{ F cm}^{-2}$  at a mass loading of  $14 \text{ mg cm}^{-2}$  (Fig. 6.4C(b)), compared with  $2.8 \text{ F cm}^{-2}$  for the undoped PPy (Fig. 6.4C(a)). With an increase of mass loading to  $28 \text{ mg cm}^{-2}$ , Tiron doped PPy showed a  $C_s$  of  $6.5 \text{ F cm}^{-2}$ . However, the  $C_s$  was only  $0.3 \text{ F cm}^{-2}$  at a scan rate of  $100 \text{ mV s}^{-1}$  (Fig. 6.4C(c)). The SAF dispersed composite electrode showed improved capacitance retention at high scan rates. A  $C_s$  of  $1.1 \text{ F cm}^{-2}$  was obtained at a scan rate of  $100 \text{ mV s}^{-1}$  (Fig. 6.4C(d)). It is known that MWCNT has relatively low SC ( $\sim 20 \text{ F g}^{-1}$ )[27, 28] but Tiron doped PPy showed SC of  $309 \text{ F g}^{-1}$ . Therefore, the contribution of CNT in capacitance measurement could be neglected for the composite electrode with the mass ratio 7:3 between Tiron doped PPy and MWCNT.

The impedance measurements (Fig. 6.4D) showed that the undoped PPy has a large electrode resistance  $Z'$  compared to the Tiron doped PPy. The increase in the mass loading enlarged the width of the high frequency semicircle. Compared with pure PPy, the  $Z'$  was reduced for Tiron doped PPy/MWCNT composite.

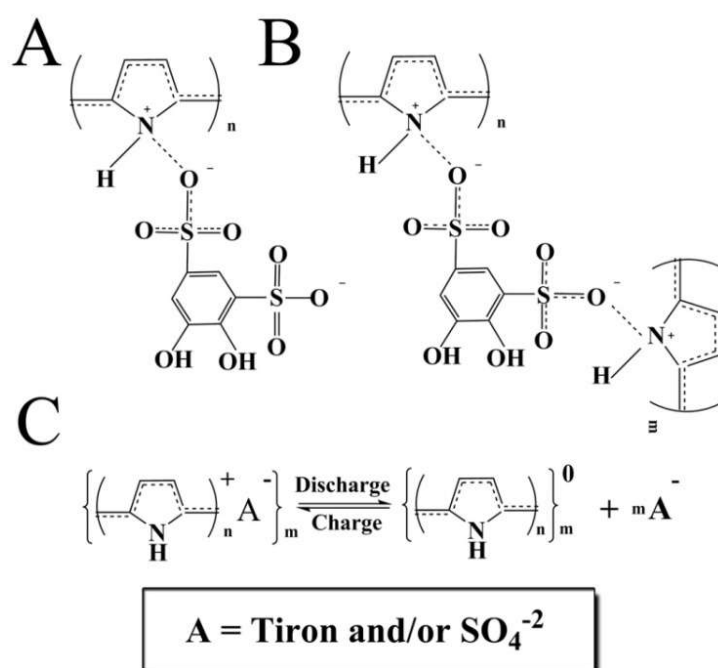


Figure 6.5 (A,B) Tiron doping of PPy: (A) in the same chain and (B) in different polymer chains, and (C) the charge-discharge mechanism of Tiron doped PPy.

The sulfonic groups of Tiron can be involved in the doping of one PPy molecule (Fig. 6.5A) or two different polymer chains (Fig. 6.5B). In the latter case the dopant can enhance the interchain mobility of charge carriers and improve the electrical conductivity of the PPy [29]. The charge and discharge mechanism of Tiron doped PPy electrode in Na<sub>2</sub>SO<sub>4</sub> as the electrolyte is proposed in Fig. 6.5C. During the

discharge process, the PPy is reduced (de-doped) to its neutral state by unchaining the incorporated anions  $A^-$ . For the undoped PPy, the released ions  $A^-$  is  $SO_4^{2-}$ . Tiron allows the improvement of charge storage of PPy because the dopant anions can be released during the reduction[30, 31]. The anions could migrate back to the polymers during the charging process.

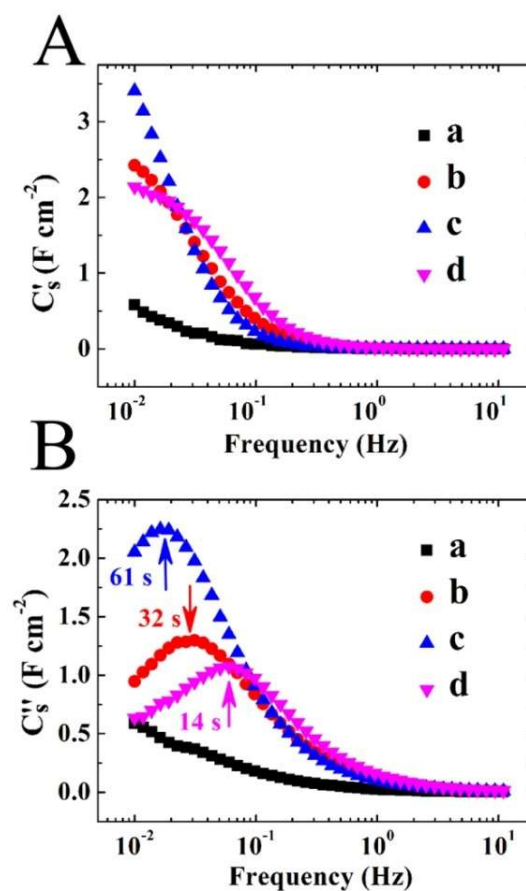


Figure 6.6 (A)  $C_s'$  and (B)  $C_s''$  obtained from the impedance data versus frequency for (a) undoped PPy with a mass of 14 mg cm<sup>-2</sup>; (b) Tiron doped PPy with a mass of 14 mg cm<sup>-2</sup>; (c) Tiron doped PPy with a mass of 27 mg cm<sup>-2</sup>; and (d) Tiron doped PPy/MWCNT composite with a mass of 27 mg cm<sup>-2</sup>.

The analysis of capacitive behavior from EIS data showed higher capacitance of Tiron doped PPy compared with undoped PPy (Fig. 6.6 A and B). It was found that  $C_s'$  are 0.6 and 2.5 F cm<sup>-2</sup> at frequency of 0.01 Hz for undoped PPy and Tiron doped PPy with a mass of 14 mg cm<sup>-2</sup>, respectively (Fig. 6.6 A). The improved capacitance behavior might be mainly ascribed to the smaller particle sizes and lower impedance of Tiron doped PPy. An increase in the mass loading resulted in a higher  $C_s'$  at the low frequency; however, the capacitance decreased sharply with the increase of frequency. The corresponding  $C_s''$  curves (Fig. 6.6B) showed typical relaxation maxima. With an increasing mass loading, the relaxation frequencies shifted to lower frequencies. The relaxation times  $\tau=1/f_m$ , related to the  $C_s''$  maxima, were found to be 32, 61 and 14 s for 14 mg cm<sup>-2</sup> Tiron doped PPy, 27 mg cm<sup>-2</sup> Tiron doped PPy and 27 mg cm<sup>-2</sup> Tiron doped PPy-MWCNT composite, respectively. The results of  $C^*$  analysis further confirmed that the Tiron doped electrodes exhibited improved capacitive performance compared to the undoped PPy. SAF dispersed PPy/MWCNT composite preserved the capacitance behavior at higher frequencies. This phenomenon could be explained by the charge storage nature of the bulk pseudo-capacitive material, which is controlled by both diffusion process and charge transfer process[32-34]. Diffusion limitations at high scan rates or high frequencies will result in poor electrolyte access to the bulk of composite PPy electrode. Furthermore, PPy has difficulty in transferring Faradaic charges compared with the PPy/MWCNT composite, because the pure PPy has a higher resistance than the PPy/MWCNT composite, as shown in Fig. 6.4D. The

difficulty of PPy to transfer charges causes its pseudo-capacitive properties to become negligible at high scan rates. The decrease of differential capacitance (Fig. 6.6A and B), derived from the impedance data, with the increasing frequency correlates with the decrease in integral capacitance with the increasing scan rate, as shown in Fig. 6.4B and C respectively.

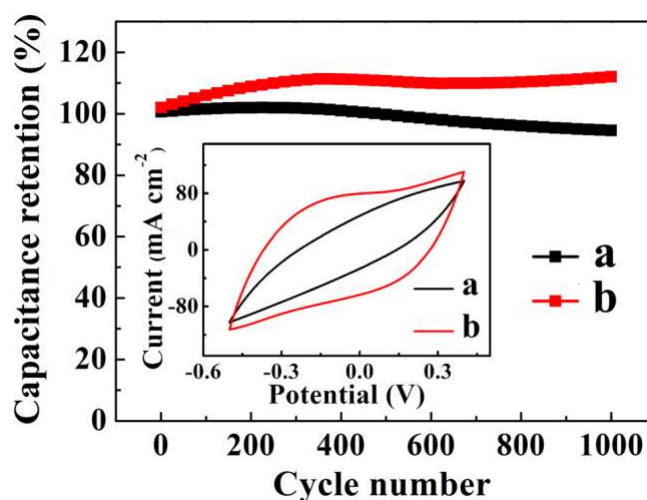


Figure 6.7 Capacitance retention as a function of cycle number, inset shows corresponding CVs after 1,000 cycles at a scan rate of  $50 \text{ mV s}^{-1}$  for (a) Tiron doped PPy and (b) Tiron doped PPy/MWCNT composite with a mass of  $27 \text{ mg cm}^{-2}$ .

The cycling performance of Tiron doped PPy and SAF dispersed composite was shown in Fig. 6.7. The capacitance slightly increased during the initial cycles. After 400 cycles, no obvious capacity fading was observed for any of the electrodes. The capacitance retentions after 1,000 cycles are 94% and 112% for Tiron doped PPy and PPy/MWCNT composite electrode, respectively. The CV of Tiron doped

PPy/MWCNT remains a quasi-rectangular shape at a scan rate of  $50 \text{ mV s}^{-1}$  after 1,000 cycles (Fig. 6.7, inset). Fig. 6.8 shows the microstructures of the Tiron doped PPy after 1,000 cycles. The SEM results indicate that cycling resulted in increasing porosity and fibrous microstructure, which may result in the increase of capacitance during the first 250 cycles.

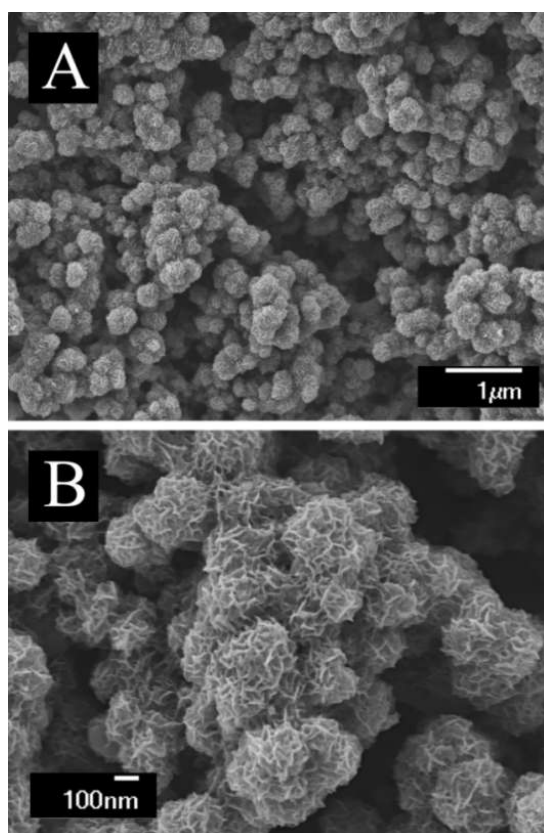


Figure 6.8 SEM images of Tiron doped PPy after 1,000 CV cycles at different magnifications.

The capacitive performance of Tiron doped PPy was studied during cycles using the impedance data (Fig. 6.9 A-D). The real part of capacitance  $C'$  decreased at frequencies above 0.1 Hz (shown in Fig. 6.9 (A) and (C)). The corresponding

dependence for the imaginary part  $C''$  indicated the time constant  $\tau$  of 36 s and 25 s for PPy without (Fig. 6.9 (B)) and with (Fig. 6.9 (D)) MWCNT, respectively. An increase of  $C^*$  in the first 250 cycles was observed for both samples. The maxima in the frequency dependence of  $C''$  shifted to slightly lower frequencies during cycling. These results confirmed good capacitive behavior and cycling stability of Tiron doped PPy electrode with a high mass loading.

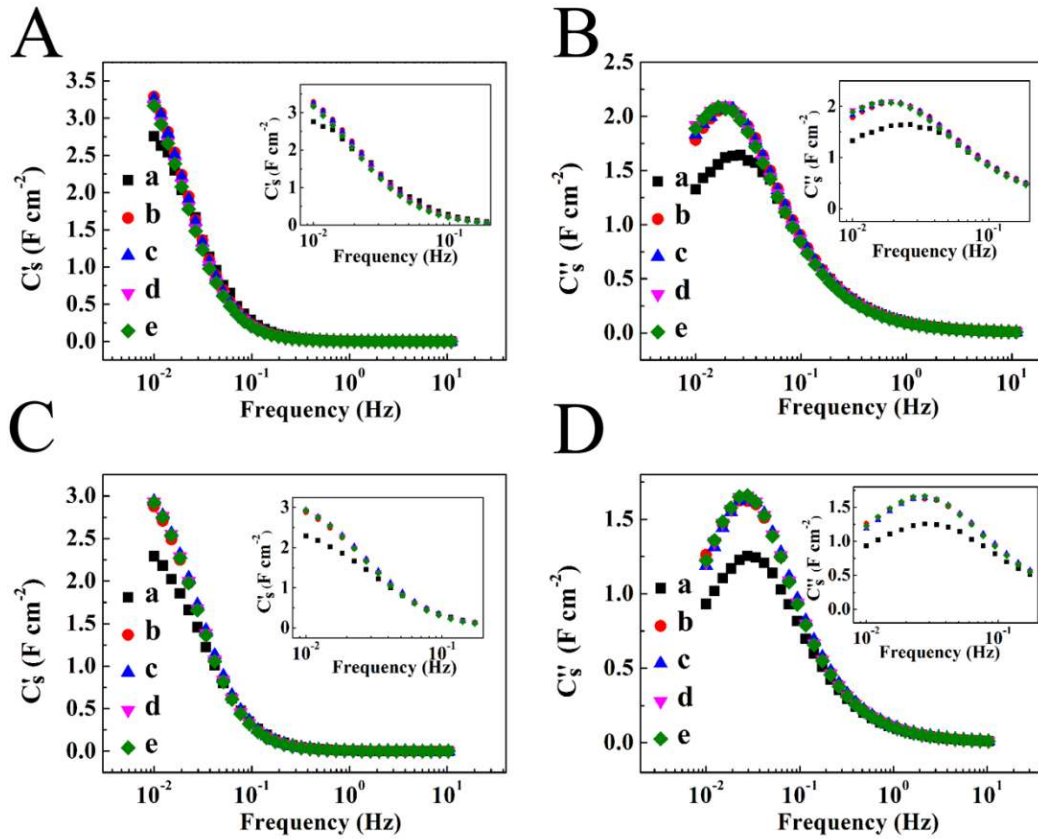


Figure 6.9 (A)  $C_s'$  and (B)  $C_s''$  for Tiron doped PPy and (C)  $C_s'$  and (D)  $C_s''$  for Tiron doped PPy/MWCNT composite with a mass of  $27\ mg\ cm^{-2}$  after (a) 1<sup>st</sup>, (b) 250<sup>th</sup>, (c) 500<sup>th</sup>, (d) 750<sup>th</sup> and (e) 1,000<sup>th</sup> cycle, insets show low frequency range.

6.1.4 Capacitive performance of symmetric supercapacitor

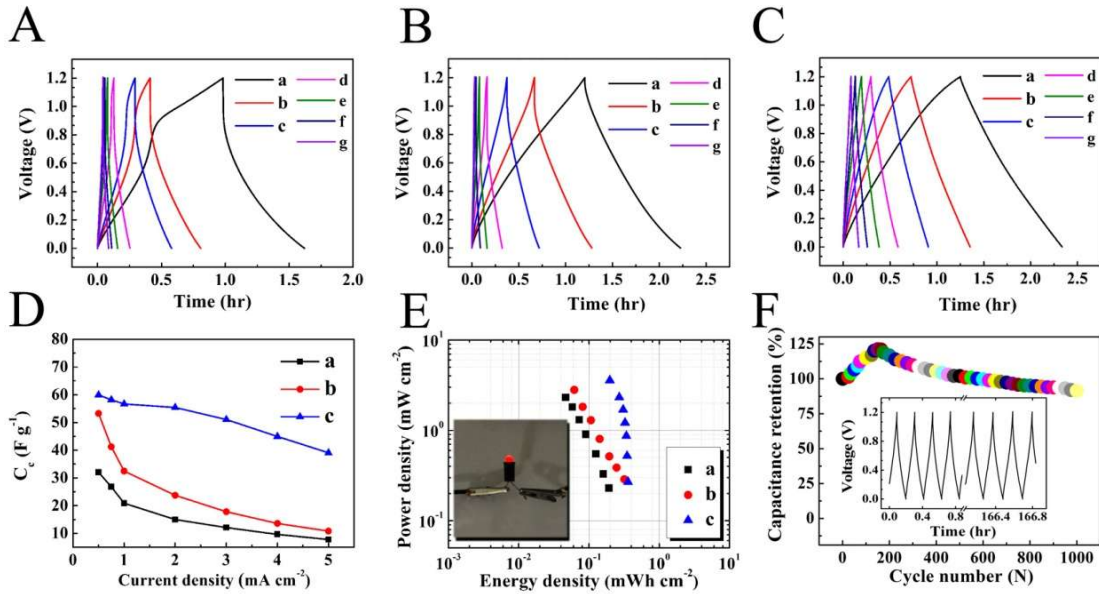


Figure 6.10 Galvanostatic charge-discharge curves of ES fabricated from (A) PPy without Tiron, (B) Tiron doped PPy and (C) Tiron doped PPy/MWCNT composite at current densities: (a) 0.5, (b) 0.75, (c) 1, (d) 2, (e) 3, (f) 4 and (g) 5 mA cm<sup>-2</sup>. (D) C<sub>c</sub> versus current density obtained from the galvanostatic discharge data and (E) Ragone plot of the ES devices for (a) PPy without Tiron, (b) Tiron doped PPy and (c) Tiron doped PPy/MWCNT composite (inset shows LED powered by a ES module). (F) Capacitance retention as a function of cycle number for Tiron doped PPy/MWCNT composite ES, inset shows the charge/discharge curves at a constant current density of 5 mA cm<sup>-2</sup> for the initial cycles and after 1,000<sup>th</sup> cycle.

Finally, we constructed symmetric ES devices with 15 mg on each electrode using different active materials. Galvanostatic charge/discharge properties of undoped PPy at different current densities are shown in Fig. 6.10A. Non-linear curves were

observed for the PPy without dopant electrode. It was attributed to the limited contact area[35] between the conducting polymer and electrolyte due to agglomeration of PPy particles. The curves of the Tiron doped PPy (Fig. 6.10B) had nearly symmetrical triangular shape during the charge–discharge process at various current densities, which means that the Tiron doped electrode exhibits better capacitive performance compared with undoped PPy. However, the IR drop increased significantly with an increase in the current density. The Tiron doped PPy/MWCNT composite ES shows a lower IR drop and longer charge-discharge times at the high current densities (Fig. 6.10C).  $C_c$  values calculated from the galvanostatic discharge data were plotted in Fig. 6.10D. The SC of Tiron doped PPy symmetric supercapacitor is  $54 \text{ F g}^{-1}$  at a current density of  $0.5 \text{ mA cm}^{-2}$ , while the undoped PPy is only  $32 \text{ F g}^{-1}$ . However, as the scan rate increases to  $5 \text{ mA cm}^{-2}$ ,  $C_c$  of Tiron doped PPy sharply decreases to only  $10 \text{ F g}^{-1}$ . The Tiron doped PPy/MWCNT composite shows a specific capacitance of  $60 \text{ F g}^{-1}$  at a current density of  $0.5 \text{ mA cm}^{-2}$  and remains  $39 \text{ F g}^{-1}$  as the scan rate increases to  $5 \text{ mA cm}^{-2}$ . These results further prove that Tiron increases the specific capacitance and MWCNT allows to improve the capacitance retention of the electrodes. The specific energy and specific power of the fabricated symmetric ES were estimated in the Ragone plot as shown in Fig. 6.10E. The maximum energy densities of undoped PPy and Tiron doped PPy are  $0.16$  and  $0.26 \text{ mWh cm}^{-2}$ , respectively. Tiron doped PPy without MWCNT revealed a significant decrease in specific energy with an increase of specific power. The specific energy values of Tiron doped PPy/MWCNT

composite electrode remained in the range of 0.20-0.34 mWh cm<sup>-2</sup>, while the power density was in the range 0.52-3.68 mW cm<sup>-2</sup>. The inset in Fig. 6.10E shows LED bulbs with a nominal current of 20 mA, powered by the coin cells. Fig. 6.10F shows cyclic behaviour of the symmetric supercapacitor and corresponding charge-discharge curves, which had similar triangular shape at the beginning and at the end of the cycling. The capacitance retention was found to be 91.4% after 1,000 cycles. The increase in capacitance at the first 250 cycles can be attributed to the changes in the microstructure of the electrode material during cycling (Fig. 6.8).

#### 6.1.5 Conclusions

Tiron doped PPy has been synthesized using chemical polymerization. SEM analysis indicated that Tiron reduced agglomeration and the particle size of PPy. The electrochemical tests demonstrated that at a scan rate of 0.5 mV s<sup>-1</sup>, C<sub>m</sub> of 180 F g<sup>-1</sup> was obtained for undoped PPy electrode with a material loading of 14 mg cm<sup>-2</sup>. Tiron allowed the improvement of charge storage of PPy, showing C<sub>m</sub> of 310 F g<sup>-1</sup>. SAF enabled the efficient dispersion of prepared PPy and MWCNT. FTIR data proved the adsorption of SAF molecules on PPy and MWCNT surface. The electron microscopy studies coupled with impedance spectroscopy measurements during cycling provided an insight into the cycle performance of Tiron doped PPy and microstructure changes during cycling. The ES, prepared using PPy/MWCNT composite was able to deliver a

maximum energy density of  $0.36 \text{ mWh cm}^{-2}$  and showed a good cycle stability with 91.4% capacitance retention after 1,000 cycles.

## **6.2 PPy nano-fiber/MWCNTs composite prepared using MG as the co-dispersant**

Nano-structured PPy exhibited unique electrical and electrochemical properties[36, 37], which open new possibilities for the applications of supercapacitors with improved performance. Different nano-architectures of PPy have been successfully synthesized, including colloidal PPy nano-particles[38], PPy nano-tubes[39], PPy nano-spirals[40] and PPy nano-fibers[41]. Recently, significant interest has been generated in the development of nano-structured PPy-carbon nanotube (CNT) composites[42-44]. It is known[45, 46] that morphology control is important for the fabrication of efficient PPy-CNT composite electrodes. Good electrolyte access to the PPy surface can be achieved in porous electrodes, containing non-agglomerated PPy nano-architecture. The goal of this investigation was to fabricate PPy nano-fiber/multiwalled carbon nanotube (MWCNT) composite electrodes for ES applications. New approach is based on the use of malachite green (MG) dye for electrosteric dispersion of PPy nano-fibers and MWCNT. Good dispersion of PPy nano-fibers and MWCNT using MG resulted in the formation of 3-D fibrous nano-network, in which individual material was well dispersed. The composite electrode prepared by the co-dispersant allowed to fabricate ES electrode with high conductivity, high capacitance and high materials loading.

### 6.2.1 Morphology of PPy nano-fiber

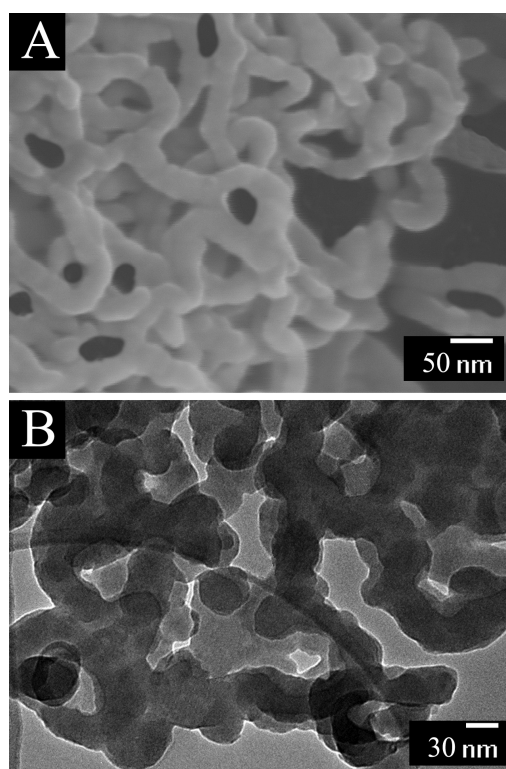


Figure 6.11 (A) SEM and (B) TEM images of PPy nano-fiber.

PPy nano-fibers were synthesized using oxidative templates (Section 4.2.1.4). Previous investigation showed that the porous morphology of PPy is favorable for ionic diffusion and improved contact between active materials and electrolyte[35]. Fig. 6.11 shows electron microscopy images of as-prepared PPy nano-fibers. The diameter of the nano-fibers was in the range of 30-50 nm. The synthesized PPy nano-fibers formed a 3-D fibrous porous network. However, the obtained PPy were unstable in aqueous suspensions. The suspensions of PPy nano-fibers showed rapid sedimentation immediately after ultrasonication. The addition of MG allowed the formation of stable suspensions. The possibility of dispersion of MWCNT and PPy nano-fibers allowed

the fabrication of stable suspensions containing PPy and MWCNT. The filtration and washing of the suspensions allowed the formation of PPy nano-fiber/MWCNT composite.

### 6.2.2 Investigation of MG adsorption

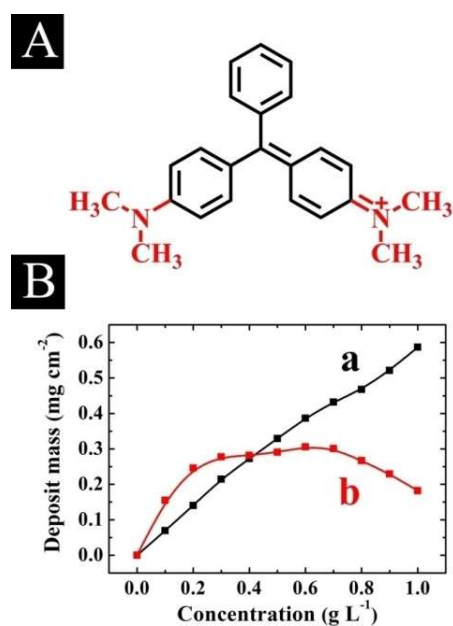


Figure 6.12 (A) Chemical structure of MG, (B) electrophoretic deposition mass for the films, prepared at a deposition voltage of 10 V and deposition time of 5 min versus MG concentration in (a) 1 g L<sup>-1</sup> MWCNT and (b) 1 g L<sup>-1</sup> PPy nano-fiber suspensions.

MG was employed as the co-dispersant to prepare PPy nano-fiber/MWCNT composite (Section 4.2.2.2). Fig. 6.12A shows a chemical structure of MG, used in this investigation. MG is a cationic organic dye, containing conjugated bonds. MG has numerous industrial applications, which exploit intense color of this material and

its affinity to different substrates. The adsorption of MG on PPy nano-fibers and MWCNT allowed their efficient dispersion. It is suggested that the adsorption mechanism is governed by  $\pi$ - $\pi$  interactions of MG with PPy and MWCNT. The adsorption of cationic MG allowed electrosteric stabilization of nano-fiber PPy and MWCNT in the suspensions.

The adsorption of MG on PPy nano-fibers and MWCNT was confirmed by the electrophoretic deposition (EPD) experiments, FTIR and UV-Vis spectroscopy analysis. Cathodic deposits were obtained after addition of MG to PPy nano-fiber and MWCNT suspensions. Therefore, adsorbed MG imparted a positive charge to MWCNT and PPy nano-fibers. Electric field provided electrophoretic motion of PPy nano-fibers and MWCNT, containing adsorbed cationic MG, toward the cathode surface, where pH increased due to the following electrode reaction:



It is suggested that the charge neutralization of cationic MG resulted in the formation of MG base[47, 48] (MG-OH) at the cathode surface:



The formation of MG base (carbinol form) reduced the electrostatic repulsion of adsorbed  $\text{MG}^+$  species at the electrode surface and promoted deposition.

The deposition yield of MWCNT increased with increasing MG concentration in the suspensions (Fig. 6.12B(a)). Nearly linear dependence was observed at MG concentrations below  $0.6 \text{ g L}^{-1}$ , at higher concentrations a deviation from the linear dependence was observed. It is suggested that the increase in MG concentration in the suspensions resulted in increasing adsorption of  $\text{MG}^+$  on MWCNT, which resulted in higher charge and higher deposition rate. The addition of MG to the PPy nano-fiber suspensions resulted (Fig. 6.12B(b)) in significant increase in the deposition yield at concentrations below  $0.2 \text{ g L}^{-1}$ , and relatively small increase in the deposition rate was observed with increasing MG concentration in the range of  $0.2\text{-}0.7 \text{ g L}^{-1}$ . The deposition yield decreased at higher MG concentrations (Fig. 6.12B(b)).

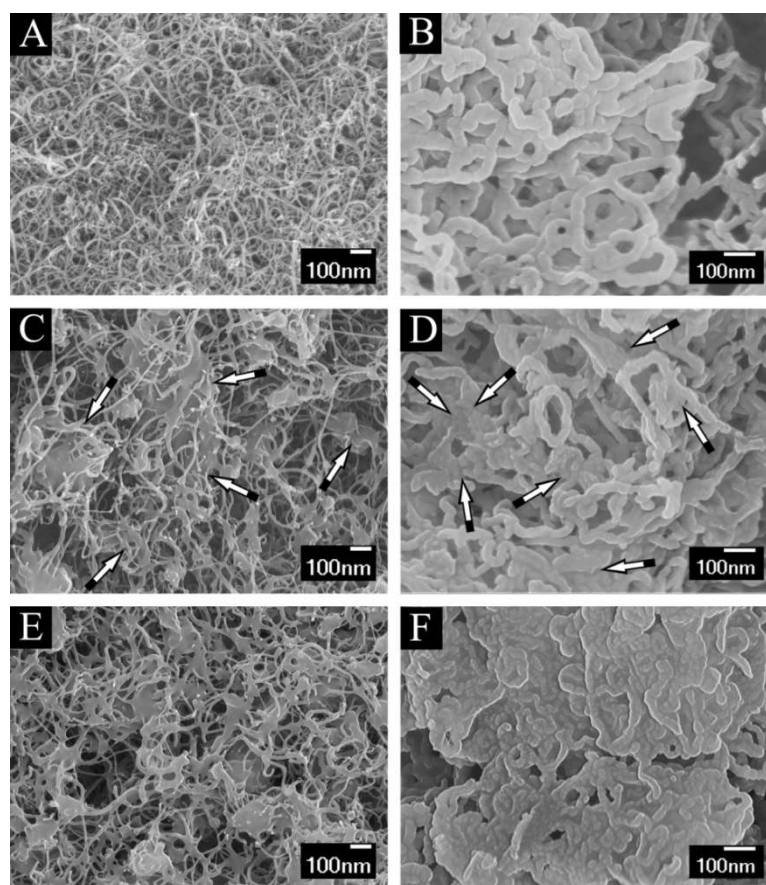


Figure 6.13 SEM images of the films prepared from suspensions, containing (A,B) 0.2, (C,D) 0.5, (E,F) 0.8 g L<sup>-1</sup> MG and (A), (C), (E) 1 g L<sup>-1</sup> MWCNT or (B), (D), (F) 1 g L<sup>-1</sup> PPy nano-fibers, arrows in Fig. 6.13C and D show co-deposited MG.

The SEM images of the deposits prepared from 1 g L<sup>-1</sup> suspensions of MWCNT and PPy nano-fibers, containing 0.2 g L<sup>-1</sup> MG showed the formation of porous films of MWCNT (Fig. 6.13A) and PPy nano-fibers (Fig. 6.13B). The increase in MG concentration in the suspensions resulted in deposition of MG-OH in voids between MWCNT and PPy nano-fibers (Fig. 6.13C-F). The increase in the MG concentration from 0.5 to 0.8 g L<sup>-1</sup> resulted in the formation of relatively dense areas, containing PPy nano-fibers and MGOH (Fig. 6.13F). The deposition of insulating MG-OH can explain the reduction of the deposition rate with increasing MG concentration above 0.7 g L<sup>-1</sup> in the PPy nano-fiber suspensions (Fig. 6.12B(b)). The increasing deposition of insulating MG-OH led to higher voltage drop in the deposited film and corresponding reduction of the electric field in the bulk of the suspensions, which resulted in decreasing deposition rate in agreement with the Hamaker equation[49]. The use of MG for deposition PPy opens a new an unexplored route for the electrodeposition of neutral polymers. Cathodic EPD offers advantages, because the problem related to oxidation of non-noble substrates during anodic PPy electrochemical polymerization[50]. Moreover, the electrodes fabricated by EPD or electrochemical polymerisation have low materials loadings, which limited their applications. The results presented below indicated that high materials loading can be

achieved by impregnation of Ni foam current collectors from colloidal suspensions of PPy nano-fibers and MWCNT containing MG co-dispersant.

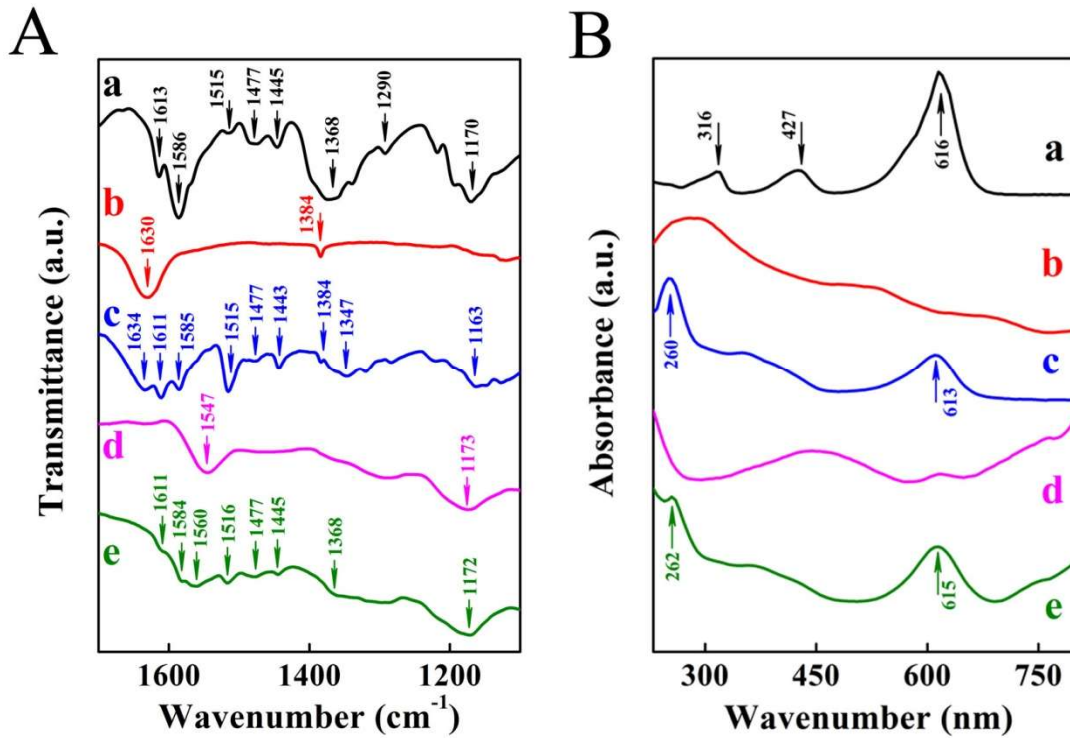


Figure 6.14 (A) FTIR and (B) UV-Vis spectra for (a) MG, (b) pristine MWCNT, (c) deposited MWCNT (d) pristine PPy nano-fiber, (e) deposited PPy nano-fiber.

The as-received MG, MWCNT and deposits removed from the substrates were used for FTIR and UV-Vis studies. The FTIR studies of as-received MG (Fig. 6.14A(a)) showed absorptions at 1613, 1586, 1515 and 1477 cm<sup>-1</sup>, attributed to C—C and C=C stretching [47, 51, 52]. Asymmetric and symmetric C-H bending in CH<sub>3</sub> contributed to absorptions[53] at 1445 and 1368 cm<sup>-1</sup>. The absorption at 1170 cm<sup>-1</sup> was attributed to C—H stretching in aromatic ring[53, 54]. Weak absorption at 1290 cm<sup>-1</sup> was

assigned to stretching C—N vibration[55]. The FTIR spectrum of as-received MWCNT (Fig. 6.14 A(b)) was the analyzed in section 6.1.2. The broad peak at  $1630\text{ cm}^{-1}$  of MWCNT was attributed to C—C vibrations and stretching vibration of surface carbonyl groups[56]. Small absorption at  $1384\text{ cm}^{-1}$  was assigned to stretching vibration of surface  $\text{COO}^-$  groups[57]. The spectrum of deposited MWCNT (Fig. 6.14A(c)) showed peaks at 1611, 1585, 1515, 1477, 1443, 1347,  $1163\text{ cm}^{-1}$ , which were not observed in the spectrum of as-received MWCNT. However, similar peaks were observed in the spectrum of MG. Therefore, deposited MWCNT contained adsorbed MG species. The FTIR spectrum of as-prepared PPy nano-fibers (Fig. 6.14A(d)) showed broad absorption peaks at 1547 and  $1172\text{ cm}^{-1}$ , attributed to C—C and C=C stretching [47, 51, 52, 58] and C—H stretching [53, 54], respectively. The FTIR spectrum of deposited PPy nano-fibers(Fig. 6.14A(e)) showed additional absorptions, which were also observed in the spectrum of MG. Therefore, the FTIR data confirmed that deposited PPy nano-fibers contained adsorbed MG species.

The UV-Vis data (Fig. 6.14B(a-e)) provided additional information, related to the MG adsorption. The UV-Vis spectrum of as-received MG (Fig. 6.14B(a)) showed absorptions at 616, 427 and 316 nm in agreement with the literature data[48, 51]. The spectra of deposited MWCNT (Fig. 6.14B(c)) and PPy nano-fibers (Fig. 6.14B(e)) showed peaks at 613 and 615 nm, respectively. Such peaks were not observed in the spectra of as-received MWCNT (Fig. 6.14B(b)) and as-prepared PPy (Fig. 6.14B(d)). Moreover, the UV-Vis spectra of deposited MWCNT and PPy showed peaks at 260

and 262 nm, respectively. Such peaks were not observed in the spectrum of as-received MG. Literature data indicated that such peaks were observed in the spectrum of MG-OH[47, 48]. Therefore, the UV-Vis data confirmed that MG species were incorporated in the deposits as MG-OH, which agreed with Eq. (2).

### 6.2.3 Morphology of PPy nano-fiber/MWCNT composites

The adsorption of MG on MWCNT and PPy nanofibers allowed efficient dispersion of both materials and fabrication of composites. The SEM and TEM images of the composites are presented in Fig. 6.15. The results show PPy nano-fibers and MWCNT, which have smaller diameter as indicated by the arrows. Increasing of the MWCNT suspension concentration resulted in the increased MWCNT content in the composites. The SEM and TEM results indicated that MWCNT are well distributed between the PPy nano-fibers. Good dispersion of MWCNT in the PPy nano-fiber matrix allowed the fabrication of composite electrodes with improved capacitive behavior.

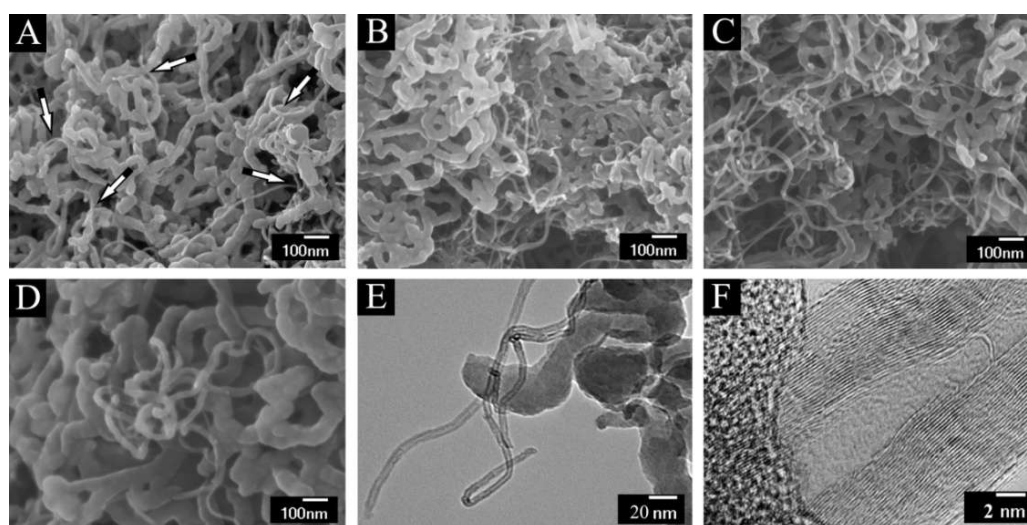


Figure 6.15 (A-D) SEM images of composites obtained from mixed PPy nano-fiber/MWCNT suspension containing (A) 10, (B) 20 and (C) 30 wt.% MWCNT, (D) high magnification image of composite (A) and (E,F) TEM images of composite (A) at different magnifications.

#### 6.2.4 Capacitive performance of PPy nano-fiber based electrodes

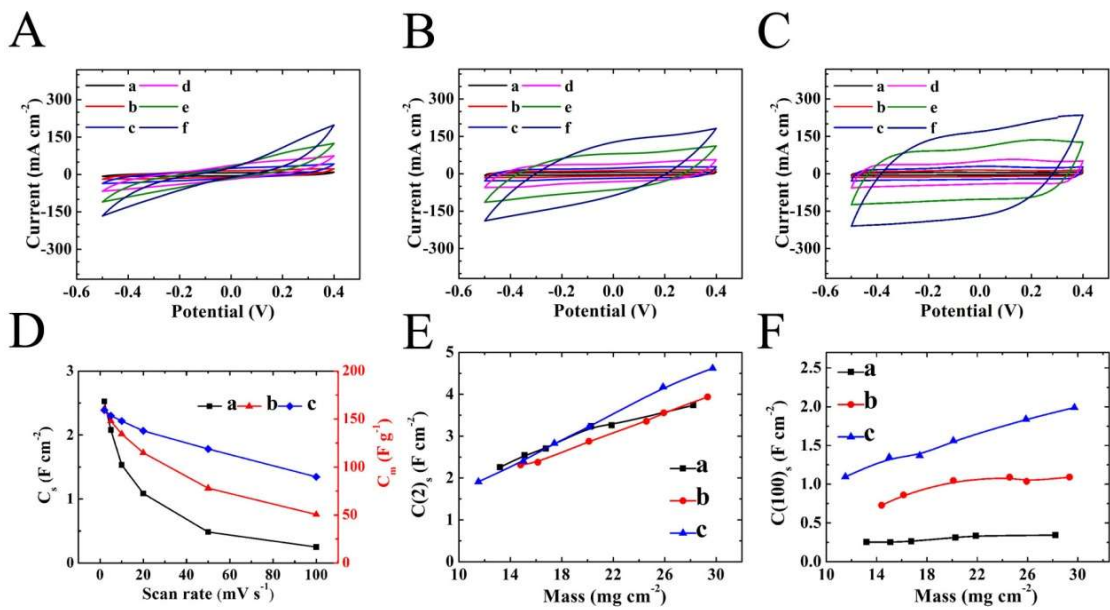


Figure 6.16 (A,B,C) CVs for different electrodes with mass loading of 15 mg cm<sup>-2</sup>: (A) PPy nano-fiber, (B) PPy nano-fiber/MWCNT (10 wt.%) composite, prepared without dispersant and (C) PPy nano-fiber/MWCNT (10 wt.%) composite dispersed using MG at scan rates of (a) 2, (b) 5, (c) 10, (d) 20, (e) 50 and (f) 100 mV s<sup>-1</sup> and (D) corresponding C<sub>s</sub> and C<sub>m</sub> values obtained from the CV data versus scan rate. (E) C<sub>s</sub> at scan rate of 2 mV s<sup>-1</sup> (C<sub>s</sub>(2)) and (F) C<sub>s</sub> at scan rate of 100 mV s<sup>-1</sup> (C<sub>s</sub>(100)) versus mass for different electrodes: (a) PPy nano-fiber, (b) PPy nano-fiber/MWCNT (10

wt.%) composite, prepared without dispersant and (c) PPy nano-fiber/MWCNT (10 wt.%) composite, prepared using MG.

Fig. 6.16A, B and C compares CVs for  $15 \text{ mg cm}^{-2}$  electrodes of pure PPy, PPy nano-fiber/MWCNT composites prepared without dispersant and PPy nano-fiber/MWCNT electrodes, prepared using MG. The PPy nano-fiber/MWCNT composites prepared without MG (Fig. 6.16B) showed improved capacitive behavior at high scan rates, compared to PPy nano-fiber electrodes (Fig. 6.16A) of the same mass. The larger area of CVs at high scan rate indicates higher capacitance. Further improvement in the capacitive behavior was achieved in PPy nano-fiber/MWCNT electrodes, prepared using MG as a dispersant (Fig. 6.16C). The obtained CVs showed nearly box shape as a scan rate of  $100 \text{ mV s}^{-1}$ , indicating good capacitive performance.

The  $C_s$  and  $C_m$  data obtained from the CV data are presented in Fig. 6.16D. As pointed out above, the specific capacitance of MWCNT is lower than  $20 \text{ F g}^{-1}$ [27, 28]. To achieve good capacitive performance, the MWCNT content in the composite must be optimized and MWCNT must be well dispersed in the PPy nano-fiber matrix. The  $C_s$  of pure PPy nano-fiber electrodes with materials loading of  $15 \text{ mg cm}^{-2}$  at a scan rate of  $2 \text{ mV s}^{-1}$  was found to be  $2.53 \text{ F cm}^{-2}$ . The composite electrodes of the same mass showed lower  $C_s$  at the same scan rate. The lower  $C_s$  of the composite electrodes was attributed to lower capacitance of MWCNT, compared with PPy nano-fiber.

However, the composites showed higher  $C_s$  and  $C_m$  compared to pure PPy nano-fiber electrodes in the range of 5-100  $\text{mV s}^{-1}$ . The composites, prepared with MG dispersant showed higher capacitance, compared to the composites, prepared without dispersant. Testing results indicated good capacitance retention of the composite electrodes at high scan rates. The  $C_s$  of pure PPy electrodes at a scan rate of 100  $\text{mV s}^{-1}$  was only  $0.25 \text{ F cm}^{-2}$ , whereas  $C_s$  of  $1.36 \text{ F cm}^{-2}$  was achieved by MG dispersed PPy nano-fiber/MWCNT composite electrode.

Fig. 6.16E and F provides further evidence of the benefit of the composites and MG dispersant. The  $C_s$  measured at a scan rate of  $2 \text{ mVs}^{-1}$  ( $C(2)_s$ ) was plotted as a function of materials loading in Fig. 6.16E. The  $C(2)_s$  of composite electrodes, prepared without dispersant, was lower, than that of pure PPy nano-fiber electrodes. The composite electrodes, prepared using MG dispersant showed slightly lower  $C(2)_s$  values at materials loadings below  $15 \text{ mg cm}^{-2}$ , compared to the pure PPy nano-fiber electrodes of the same mass. However significantly higher  $C(2)_s$  values were obtained for composite electrodes with materials loadings above  $20 \text{ mg cm}^{-2}$ . The highest  $C_s$  of  $4.62 \text{ F cm}^{-2}$  was achieved for composite PPy nano-fiber/MWCNT electrodes with materials loading of  $30 \text{ mg cm}^{-2}$ , prepared using MG dispersant. The  $C_s$  measured at  $100 \text{ mV s}^{-1}$  ( $C(100)_s$ ) was plotted versus electrode mass in Fig. 6.16F. The increase in electrode mass didn't result in increase in  $C(100)_s$  of pure PPy nano-fiber electrodes. The composite electrodes, prepared without MG showed higher  $C(100)_s$  values. The  $C(100)_s$  slightly increased with increasing electrode mass in the range below  $20 \text{ mg}$

$\text{cm}^{-2}$ , however no increase in  $C(100)_s$  was observed at higher mass loadings. The composite electrodes prepared using MG dispersant showed higher  $C(100)_s$ , compared to the composites prepared without dispersant and pure nano-fiber PPy electrodes. The  $C(100)_s$  showed nearly linear increase with increasing mass loading, indicating good materials utilization at high scan rates. The  $C_s$  of composite electrodes, prepared using MG as a dispersant, was significantly higher, compared to the data in the previous studies[59, 60].

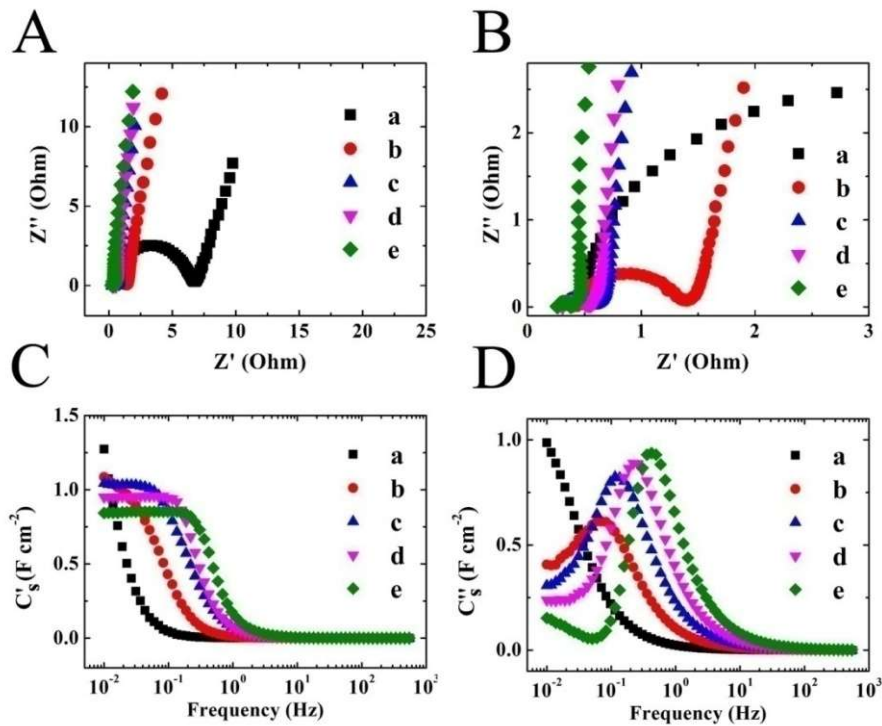


Figure 6.17(A) Nyquist plot of complex impedance  $Z^*=Z'-iZ''$  and (B) high frequency range of  $Z^*$ , (C)  $C_s'$  and (D)  $C_s''$  calculated from the impedance data versus frequency for different electrodes: (a) PPy nano-fiber, (b) PPy nano-fiber/MWCNT composite, prepared without dispersant and (c,d,e) PPy nano-fiber/MWCNT composite, prepared

using MG dispersant and containing (c) 10, (d) 20 and (e) 30 wt.% MWCNT. All electrodes have mass loading of  $15 \text{ mg cm}^{-2}$ .

Fig. 6.17A and B shows impedance spectroscopy data in different frequency ranges for the pure nano-fiber PPy and composite electrodes. The composite electrodes showed significant reduction in  $Z'$  values, compared to pure PPy electrodes. The composite electrodes prepared using MG showed lower  $Z'$ , compared to the composites prepared without MG. The Nyquist plot for pure PPy electrodes showed relatively large semicircle, which indicated high charge transfer resistance[60-62]. The impedance data for the composite electrodes showed significantly lower diameters of the semicircles. Fig. 6.17C and D shows  $C_s^*$  values, calculated from the impedance data[63]. The frequency dependences of complex  $C_s^*$  showed a relaxation behavior. The  $C'_s$  and  $C''_s$  of pure PPy electrodes decreased rapidly with increasing frequency below 0.1 Hz (Fig. 6.17C(a) and 6.17D(a)). The composite electrodes, prepared without MG, showed relaxation at higher frequencies (Fig. 6.17C(b)). The corresponding  $C''_s$  curve exhibited (Fig. 6.17D(b)) a relaxation maximum at 72 mHz ( $\tau=13.88 \text{ s}$ ). The composites, prepared using MG dispersant, showed relaxations at higher frequencies. The  $C'_s$  showed plateaux at low frequencies and typical relaxation type decrease at higher frequencies (Fig. 6.17C(c,d,f)). The cut-off frequency[64] increased from 92 to 213 mHz with increasing MWCNT content in the composites from 10 to 30 mass%, however the low frequency capacitance, measured at 10 mHz ( $C_{\text{max}}$ ), decreased from 1.04 to 0.84  $\text{F cm}^{-2}$ . The  $C''_s$  versus frequency dependences

(Fig. 6.17D (c,d,e)) showed maxima at 199 mHz ( $\tau=5.02$  s), 247 mHz ( $\tau=4.05$  s) and 441 mHz ( $\tau=2.27$  s) for MWCNT content of 10, 20 and 30 mass%, respectively. The results indicated that composite electrodes, prepared using MG, can be utilized for ES, operating at higher frequencies, compared ES, based on pure PPy nano-fiber electrodes. The frequency range can be increased by more than one order of magnitude (Fig. 6.17C and D).

### 6.2.5 Influence of mass loading on the capacitive performance

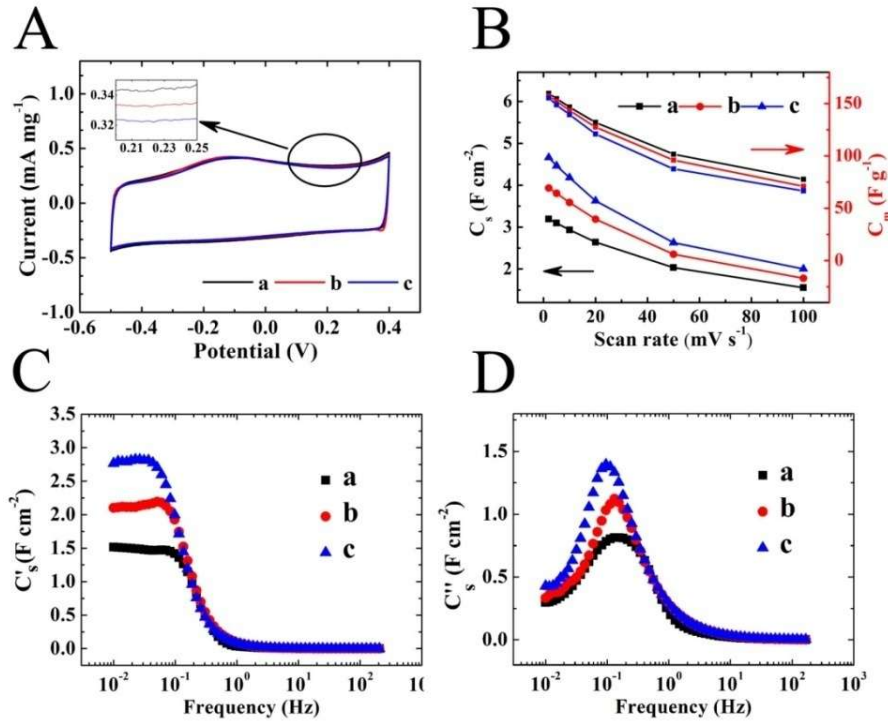


Figure 6.18 (A) CVs at a scan rate of  $2 \text{ mV s}^{-1}$ , (B)  $C_s$  and  $C_m$  obtained from the CV data versus scan rate, (C)  $C_s'$  and (D)  $C_s''$  calculated from impedance data versus frequency for PPy nano-fiber/MWCNT (10 wt.%) composite electrodes, prepared using MG, with mass loading of (a) 20, (b) 25 and (c)  $30 \text{ mg cm}^{-2}$ .

In Fig 6.18, the capacitive performance of the electrodes was investigated in mass range of 20-30 mg cm<sup>-2</sup>. The experimental results indicated that good electrochemical performance can be achieved for composite electrodes with high materials loadings. The CVs recorded at a scan rate of 2 mVs<sup>-1</sup> were practically of the same shape. The inset in Fig. 6.18A indicated relatively small reduction in mass normalized current with increasing electrode mass. The corresponding C<sub>m</sub> versus scan rate data (Fig. 6.18B) didn't show significant reduction in C<sub>m</sub> with increasing electrode mass. The capacitance retention in the range of 2-100 mV s<sup>-1</sup> was about 50 %. The C<sub>s</sub> increased with increased materials loading, indicating good material utilization. The C\*<sub>s</sub> data (Fig. 6.18C and D) showed that the cut-off frequencies were 81 mHz, 53 mHz, 35 mHz and corresponding relaxation frequencies 182 mHz (τ=5.50 s), 159 mHz (τ=6.29 s) and 115 mHz (τ=8.70 s) for material loadings of 20, 25 and 30 mg cm<sup>-2</sup>, respectively. The decrease in cut-off and relaxation frequencies is attributed to reduction in conductivity with increased electrode mass. The low frequency capacitance C'<sub>s</sub> increased with increasing materials loading.

#### 6.2.6 Cycling stability of the PPy nano-fiber/MWCNT electrode

Fig. 6.19A shows cyclic behavior of the composite electrode. The specific capacitance increased during the first 250 cycles and then slightly decreased. The capacitance after 1000 cycles was 104.2% of the initial value. The shape of the CV remained unchanged during cycling. The CV, corresponding to 250<sup>th</sup> cycle, has the largest area

(Fig. 6.19A, inset). The increase in capacitance can result from changes in electrode material morphology during cycling[59]. The impedance measurements during cycling didn't show significant changes in  $Z^*=Z'-iZ''$  (Fig. 6.19B) and  $C^*=C'-iC''$  (Fig. 6.19C and D) data. The  $C'_s$  measured at a frequency of 10 mHz showed 5% increase during cycling (Fig. 6.19C, inset). The cut-off frequency and relaxation frequency remained practically unchanged. The results indicated good cyclic stability of the composite electrodes.

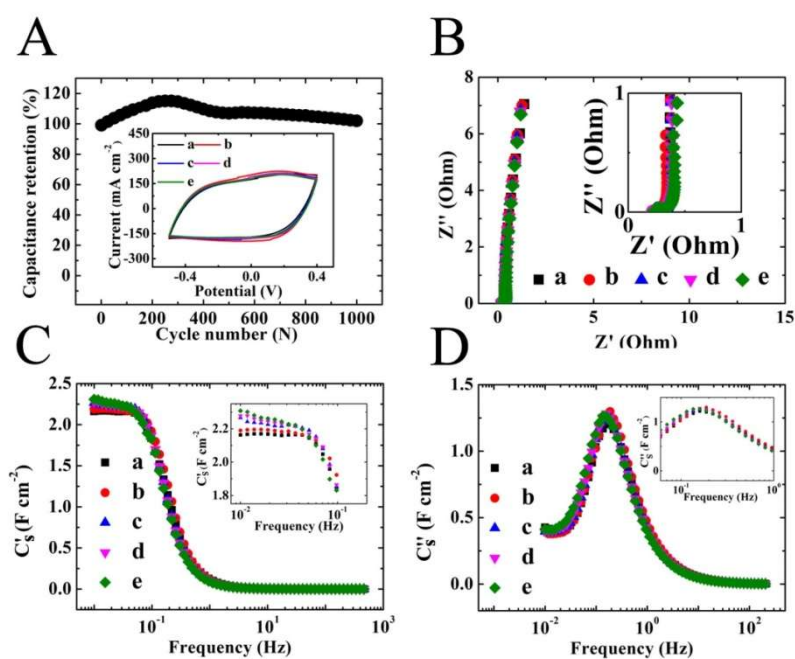


Figure 6.19 (A) Capacitance retention versus cycle number  $N$  (inset shows CVs at a scan rate of  $50 \text{ mV s}^{-1}$ ), (B) Nyquist plots of complex impedance, (C)  $C'_s$  and (D)  $C''_s$  (insets show low frequency range) calculated from impedance data versus frequency for PPy nano-fiber/MWCNT (10 wt.%) composite electrodes, prepared using MG,

with a mass loading of  $27 \text{ mg cm}^{-2}$  after (a) 1<sup>st</sup>, (b) 250<sup>th</sup>, (c) 500<sup>th</sup>, (d) 750<sup>th</sup> and (e) 1,000<sup>th</sup> cycles.

### 6.2.7 Conclusions

MG is efficient dispersing agent for the colloidal nanotechnology of PPy nano-fibers and MWCNT. Sedimentation testing results, investigation of EPD kinetics and analysis of FTIR and UV-Vis data showed that MG adsorbed on PPy nano-fibers and MWCNT and provided their electrosteric dispersion. The possibility of dispersion individual materials, using MG as a co-dispersant, allows fabricating composite electrodes with material loadings of  $10\text{-}30 \text{ mg cm}^{-2}$ . The highest  $C_s$  of  $4.62 \text{ F cm}^{-2}$  was obtained at materials loading of  $30 \text{ mg cm}^{-2}$ . The composite PPy nano-fiber/MWCNT electrodes, prepared using MG as a dispersant, showed better capacitive performance compared to the pure PPy and composite electrodes, prepared without dispersant. The composite electrodes, prepared using MG showed significant improvement in capacitance retention at high scan rate, frequencies and mass loadings. Such electrodes also showed good cycling stability.

### **6.3 Graphene/MWCNTs and Graphene/PPy nano-fibers composite films prepared by electrophoretic deposition**

Graphene is attractive for applications in electrodes of ES due to high capacitance and conductivity, large voltage window and good chemical stability[65-67]. Many applications of graphene require the fabrication of thin films, which are of special

interest for the fabrication of flexible ES[68, 69]. Recent investigations were focused on the development of composites, containing various functional materials, incorporated between the graphene layers[65]. The separation of graphene layers has been achieved by the introduction of CNT or nanotubes, nanofibers, nanorods and nanowires of different materials between the graphene layers [70-73]. The obtained nano-composites were investigated for energy storage, electronic and optoelectronic applications[74, 75]. Various methods were developed for the fabrication of graphene-CNT composites, such as self-assembly[71], chemical vapor deposition[72], microwave[73] and hydrothermal[70] syntheses, ultrasonication followed by vacuum filtration[76, 77]. In another investigation[78], polyaniline nano-fibers were prepared by chemical polymerization in the presence of graphene, dispersed using sodium dodecyl benzenesulfonate as surfactant. The obtained polyaniline nano-fibers/graphene[78] and polypyrrole nano-tubes/graphene[39] composite films were used for the fabrication of efficient electrodes for ES applications.

Although the impressive progress has been achieved in this area, there is a need in the development of simple and versatile methods for the fabrication of graphene based composite films. Colloidal techniques are especially attractive for the fabrication of nano-composites with uniform distribution of individual components. In these methods, the individual components must be well dispersed in the colloidal suspensions, using efficient dispersing agents. The goal of this investigation was the fabrication of graphene-MWCNT and graphene-PPy nano-fiber films for electrodes of

ES. The composite electrodes were fabricated by cathodic electrophoretic deposition (EPD) from colloidal suspensions, containing safranin (SAF) as a dispersing and charging agent. Compared with the previous studies, the EPD method offers advantages of the short formation time, simple apparatus and suitability for mass production.

### 6.3.1 Dispersion of MWCNT, graphene and PPy nano-fiber

Fig. 6.20A shows a chemical structure of SAF used in this investigation. SAF is a cationic organic dye, soluble in water. Many important properties of SAF are attributed to phenazine and aromatic groups[79]. It was found that SAF allowed efficient dispersion of MWCNT, PPy nano-fiber and graphene (Fig. 6.20(B-J)). The suspensions of MWCNT, PPy nano-fiber and graphene without SAF were unstable and showed sedimentation 1 h after the ultrasonic agitation. In contrast, the suspensions, containing 0.5-1 g L<sup>-1</sup> SAF were stable for more than 2 months. It is suggested that  $\pi$ - $\pi$  interactions[80] promoted SAF adsorption on MWCNT, graphene and PPy nano-fiber. The adsorbed cationic SAF provided electrostatic dispersion of MWCNT, graphene and PPy nano-fiber.

Previous studies [76, 77] indicated that the stability of CNT and graphene suspensions could be improved by mixing the suspensions of individual materials. The results of sedimentations tests were in agreement with the literature data and indicated that graphene-MWCNT suspensions without SAF were stable for 3-4 h. In contrast,

graphene-MWCNT suspensions with SAF showed superior stability, compared to the suspensions without SAF (Fig. 6.20).

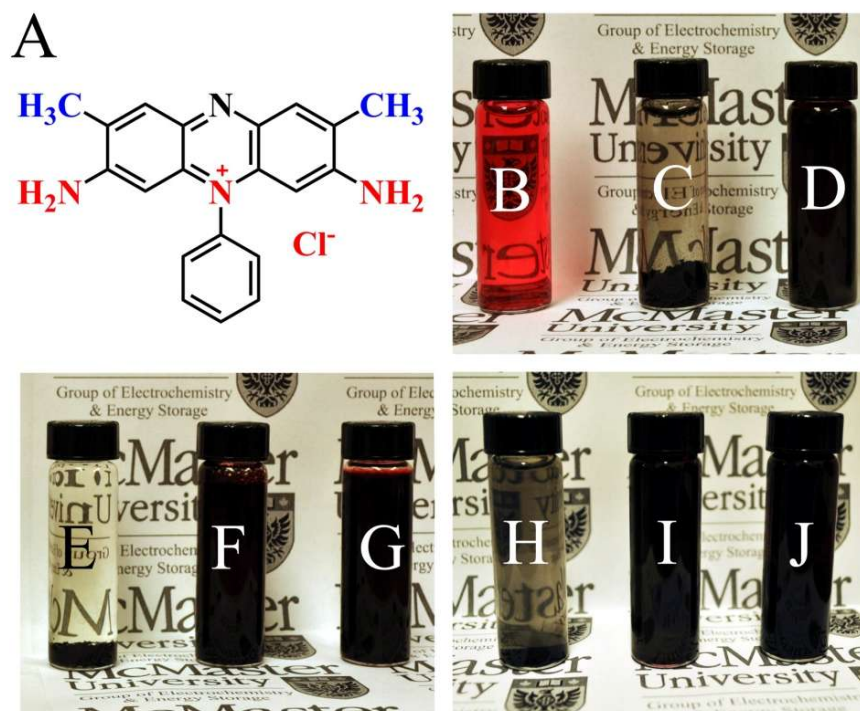


Figure 6.20 (A) Chemical structure of SAF, and (B) SAF (C) MWCNT, (D) MWCNT and SAF, (E) graphene, (F) graphene and SAF, (G) graphene, MWCNT and SAF, (H) PPy nano-fiber, (I) PPy nano-fiber and SAF, (J) graphene, PPy nano-fiber and SAF in water. Suspensions D, F, G, I and J were stable for more than two months.

### 6.3.2 Electrophoretic deposition of MWCNT, graphene and PPy nano-fiber

The MWCNT, graphene and PPy nano-fiber suspensions, containing SAF, were used for EPD (Section 4.2.2.3). The results of deposition yield measurements are presented in Fig. 6.21. The addition of SAF to the suspension allowed the formation of cathodic deposits. Significant increase in the deposition rate was observed at SAF

concentrations below 0.6, 0.5 and 0.3 g L<sup>-1</sup> for MWCNT, graphene and PPy suspensions, respectively (Fig. 6.21A, C and E). The deposit mass increased with increasing deposition time. The dependencies (Fig.6.21 B, D and F) deviated from a linear plot as deposition time increased. Such deviation can be attributed to voltage drop in the deposited layers or other factors, discussed in the literature[81-83]. The deposition yield (Fig. 6.21) can be varied by the variation of SAF concentration in the suspension or deposition time. It is suggested that SAF adsorbed on MWCNT, graphene and PPy nano-fiber and provided a positive charge for EPD.

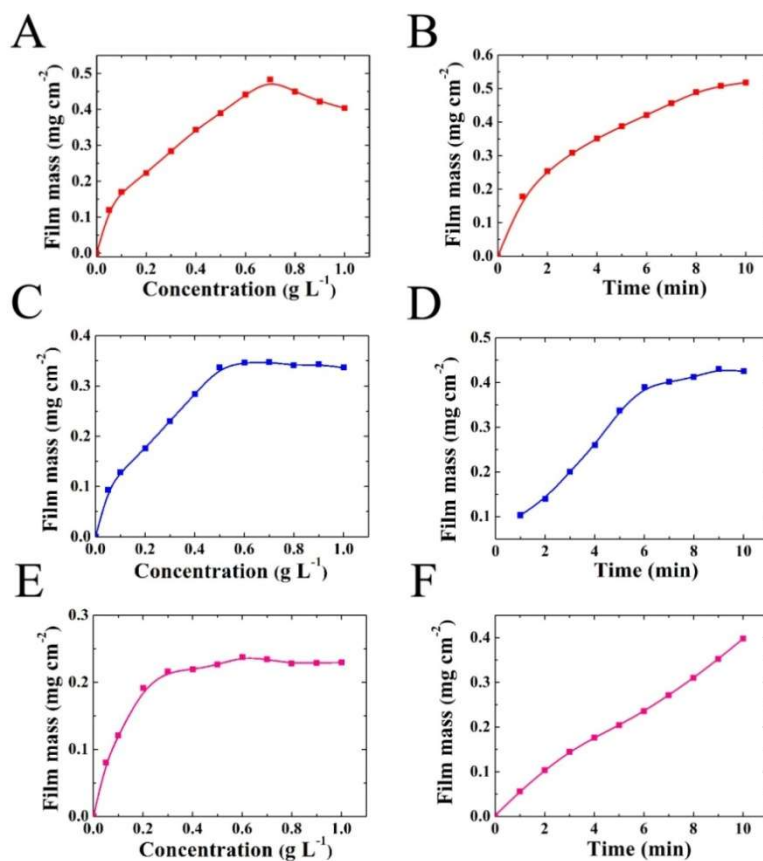


Figure 6.21 Deposit mass for (A,B) 1g L<sup>-1</sup> MWCNT, (C,D) 1g L<sup>-1</sup> graphene, (E,F) 1g L<sup>-1</sup> PPy nano-fiber suspensions versus (A,C,E) SAF concentration in the

suspensions at a deposition time of 5 min and versus (B,D,F) deposition time at SAF concentration of 0.5 g L<sup>-1</sup>.

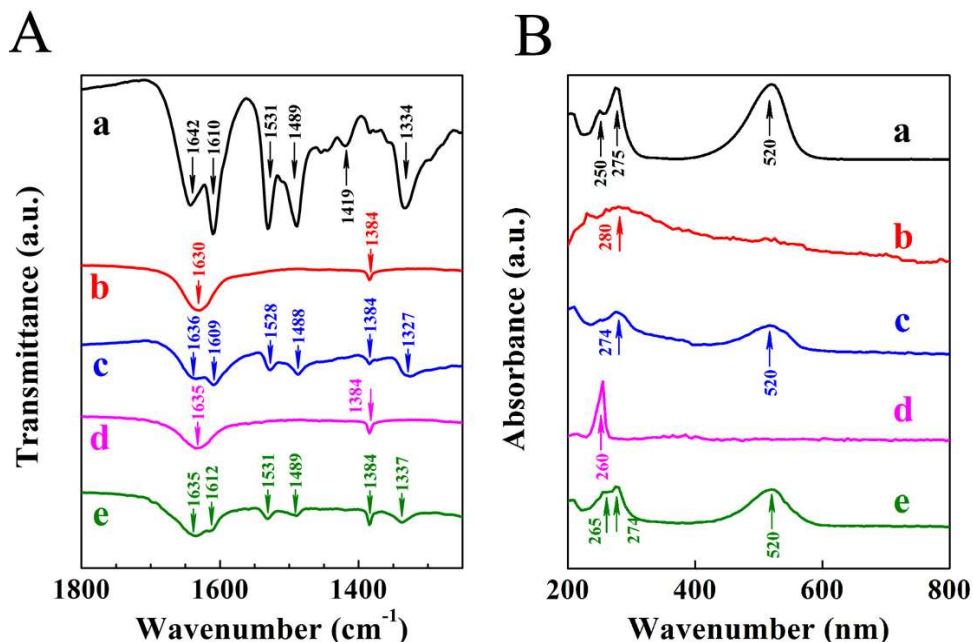


Figure 6.22 (A) FTIR and (B) UV-Vis spectra for (a) SAF, (b) pristine MWCNT, (c) deposited MWCNT, (d) pristine graphene, (e) deposited graphene.

The adsorption of SAF was confirmed by the FTIR and UV-Vis studies. Fig. 6.22 compares the results of FTIR and UV-Vis studies of the deposits, prepared from MWCNT and graphene suspensions, containing SAF, with corresponding data for as-received SAF, graphene and MWCNT. The FTIR spectrum of SAF (Fig. 6.22A(a)) was in agreement with literature data[84]. The absorptions at 1642, 1419 cm<sup>-1</sup> were assigned to phenazine-type C-C vibrations. The absorption at 1610 cm<sup>-1</sup> was attributed to NH<sub>2</sub> scissoring. Aromatic C-C vibrations resulted in absorptions at 1531

and  $1489\text{ cm}^{-1}$ . Stretching C-N vibrations contributed to absorption at  $1334\text{ cm}^{-1}$ . The FTIR spectra of MWCNT and graphene (Fig. 6.22A(b,d)) showed broad peaks at  $1630$  and  $1635\text{ cm}^{-1}$ , respectively, which were attributed to C-C vibrations and stretching vibration of surface carbonyl groups[56]. Small absorptions at  $1384\text{ cm}^{-1}$  were assigned to stretching vibration of surface  $\text{COO}^-$  groups[57]. In comparison with the spectra of pristine MWCNT and graphene, the spectra of deposited materials (Fig. 6.22A(c,e)) showed additional absorptions at  $1609$ ,  $1528$ ,  $1488$ ,  $1327\text{ cm}^{-1}$  for deposited MWCNT and at  $1612$ ,  $1531$ ,  $1489$  and  $1337\text{ cm}^{-1}$  for deposited graphene. Taking into account that similar absorptions were observed in the spectra of SAF, it was concluded that deposited MWCNT and graphene contained adsorbed SAF. UV-Vis spectra provided further evidence of SAF adsorption. The UV-Vis spectrum of SAF (Fig. 6.22B(a)) showed absorptions at  $520$ ,  $275$  and  $250\text{ nm}$  in agreement with reported data[85, 86]. Similar absorptions were observed in the spectra of deposited MWCNT and graphene (Fig.6.22B(c,e)) in addition to the absorptions of corresponding pristine materials (Fig 6.22B(b,d)).

The results of FTIR and UV-Vis studies of as-prepared and deposited PPy nano-fiber were compared in Fig. 6.23. The FTIR spectrum of as-prepared PPy nano-fiber (Fig. 6.23A(a)) showed broad absorptions at  $1547$ ,  $1463$  and  $1291\text{ cm}^{-1}$ , attributed to fundamental ring vibrations, C-N stretching vibrations and C-H in-plane vibration, respectively [87, 88]. The FTIR spectrum of the deposited PPy nano-fiber (Fig. 6.23A(b)) showed absorptions at  $1634$ ,  $1610$ ,  $1530$  and  $1488\text{ cm}^{-1}$  which were not

observed in the spectrum of as-prepared PPy. However, similar absorptions were observed in the spectrum of SAF (Fig. 6.22A(a)). Therefore, the FTIR data indicated that deposited PPy nano-fiber contained adsorbed SAF. The analysis of the UV-Vis spectra (Fig. 6.23B (a,b)) for the same samples showed that deposited PPy nano-fiber exhibited absorption peaks at 520, 275 and 249 nm, which were not observed in the spectrum of as-prepared PPy nano-fiber. Such peaks were observed in the spectrum of SAF (Fig. 6.22B(a)). Therefore, UV-Vis data showed SAF adsorption on deposited PPy nano-fiber.

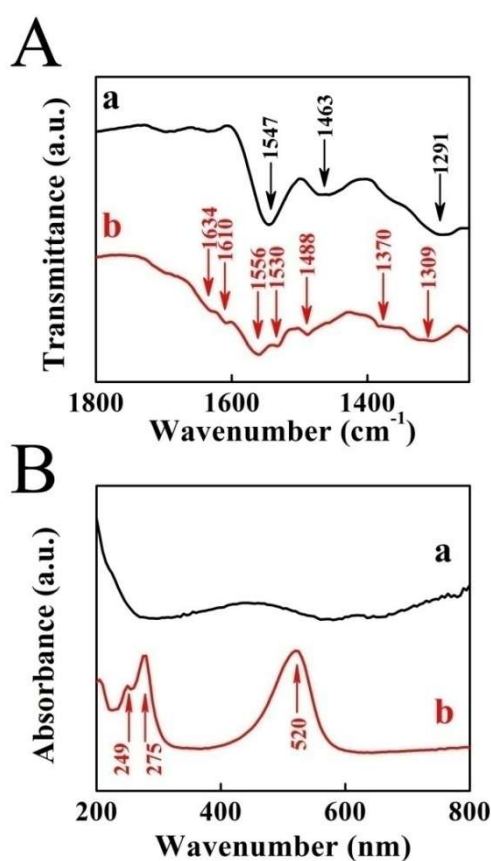


Figure 6.23 (A) FTIR and (B) UV-Vis spectra for (a) as-prepared and (b) deposited PPy nano-fiber.

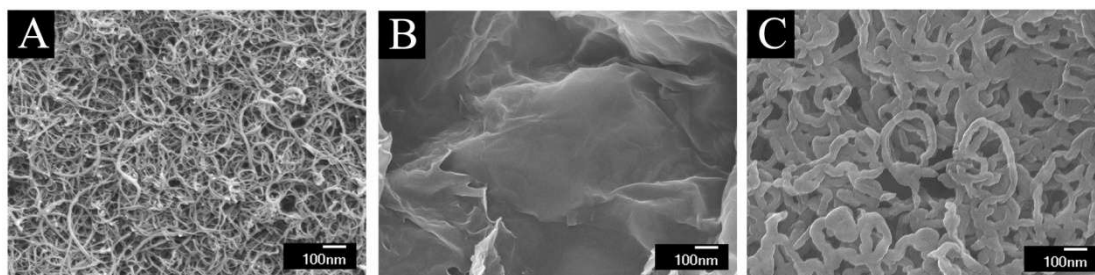


Figure 6.24 SEM images of (A) MWCNT, (B) graphene and (C) PPy films prepared by EPD.

The MWCNT, graphene and PPy nano-fiber films prepared by EPD method were studied by SEM. The studies showed the formation of continuous films, consisted of well dispersed materials. The high magnification SEM images showed MWCNT (Fig.6.24A), graphene (Fig.6.24B) and PPy nanofibers (Fig.6.24C), which formed a continuous network.

### 6.3.3 Composite films fabricated by electrophoretic deposition

EPD was employed for the fabrication of graphene-MWCNT and graphene-PPy composite films. Previous studies showed that one of the major problems in the EPD of composite materials is the selection of dispersing and charging agents suitable for EPD of all individual components[89, 90]. The use of dispersion and charging agent allows for the co-deposition of individual components from one suspension and for the fabrication of multilayer or functionally graded films from different suspensions[89, 91]. The possibility of deposition of MWCNT, graphene and PPy

nanofibers using SAF paved the way for the co-deposition of the materials and fabrication of composites by EPD.

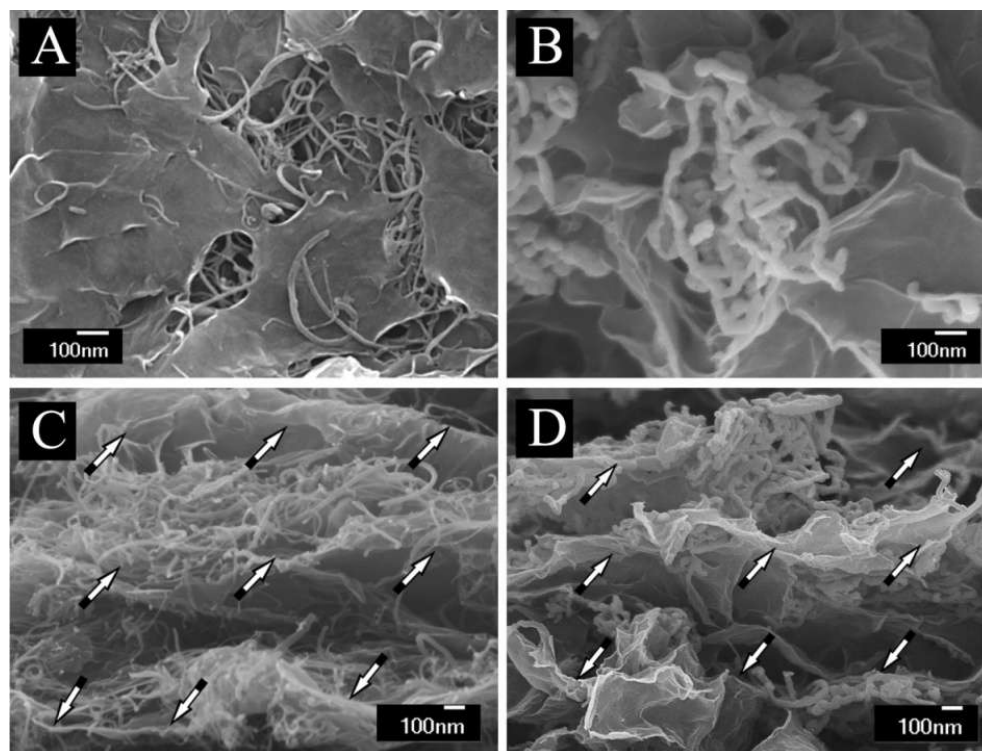


Figure 6.25 SEM images of (A,B) surfaces and (C,D) cross sections (fractures) of composite (A,C) graphene/MWCNT and (B,D) graphene/PPy nano-fiber films. Arrows in (C,D) show graphene.

The use of SAF allowed the dispersion of individual components and fabrication of mixed suspensions. Cathodic EPD allowed the fabrication of composite films. Fig. 6.25 shows SEM images of surfaces and cross sections of the composite films. The SEM images showed graphene and MWCNT (Fig. 6.25A and C) or graphene and PPy (Fig. 6.25B and D). The results indicated that the EPD method allowed to prepare composite films with 3-D nano-architecture (Fig. 6.25A and B). MWCNT and fibrous

PPy were distributed between graphene layers, preventing them from re-stacking (Fig. 6.25C and D). Therefore, SEM studies prove successful co-deposition of graphene, MWCNT and PPy and fabrication of composite graphene/MWCNT and graphene/PPy nano-fiber films.

### 6.3.4 Capacitive performance of deposited films

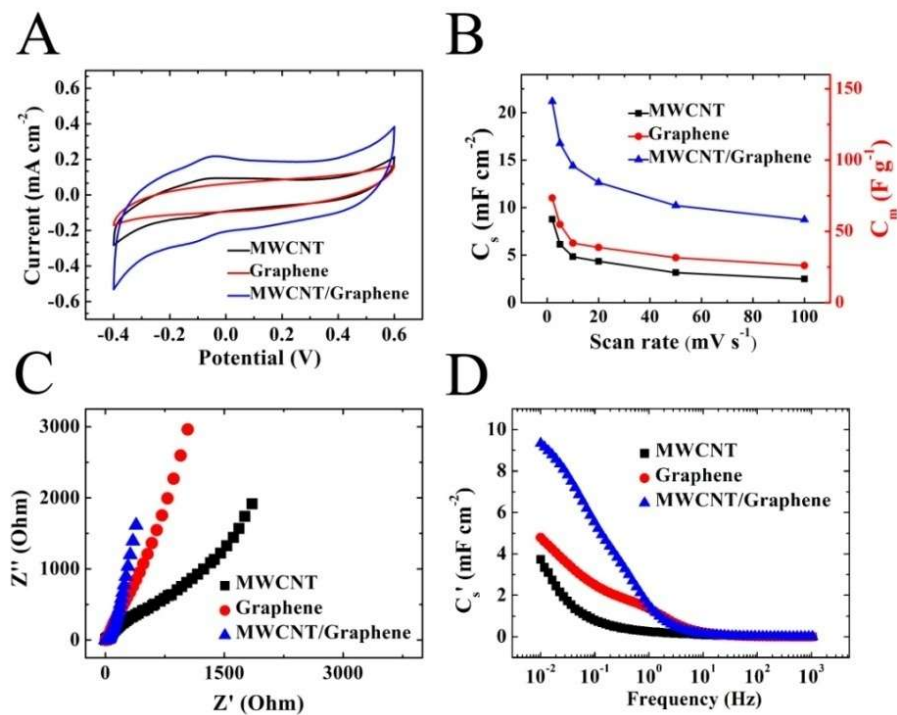


Figure 6.26 (A) CVs at a scan rate of  $10 \text{ mV s}^{-1}$ , (B) capacitance calculated from CV data versus scan rate, (C) EIS data presented in a Nyquist plot and (D) capacitance calculated from EIS data versus frequency for  $0.15 \text{ mg cm}^{-2}$  films of MWCNT, graphene and graphene/MWCNT composite.

The films fabricated by cathodic EPD were studied for application in electrodes of ES.

Fig. 6.26 compares testing results for composite graphene/MWCNT films with

corresponding data for pure graphene and MWCNT films of the same mass. The CV data showed capacitive performance of the films (Fig. 6.26A). The larger area of the composite film indicated higher capacitance. Fig. 6.26B shows capacitance of the films at different scan rates, calculated from the CV data. The capacitance of the composite films decreased from  $21.2 \text{ mF cm}^{-2}$  ( $141.2 \text{ F g}^{-1}$ ) to  $8.7 \text{ mF cm}^{-2}$  ( $58.2 \text{ F g}^{-1}$ ) with increasing scan rate from 2 to  $100 \text{ mV s}^{-1}$ . The graphene and MWCNT films of the same mass showed significantly lower SC. The SC of  $11.0 \text{ mF cm}^{-2}$  ( $73.5 \text{ F g}^{-1}$ ) and  $8.8 \text{ mF cm}^{-2}$  ( $58.5 \text{ F g}^{-1}$ ) were obtained at a scan rate of  $2 \text{ mV s}^{-1}$  for graphene and MWCNT films, respectively. Fig. 6.26C shows the results of EIS studies presented in the Nyquist plot. The composite films showed lower  $Z'$  values, indicating higher conductivity of the composite electrode in the electrolyte solutions. The capacitance was also calculated from the EIS data and plotted as  $C_s'$  versus frequency in the low frequency range (Fig. 6.26D). The composite film showed higher  $C_s'$ , compared with the corresponding  $C_s'$  data for pure graphene and MWCNT films.

The CV of graphene/PPy nano-fiber film exhibited nearly box shape, indicating good capacitive behavior (Fig. 6.27A). The capacitance of pure PPy nano-fiber films, calculated from the CV data (Fig. 6.27B), decreased from  $46.9 \text{ mF cm}^{-2}$  ( $312.8 \text{ F g}^{-1}$ ) to  $10.4 \text{ mF cm}^{-2}$  ( $69.1 \text{ F g}^{-1}$ ) with increasing scan rate from 2 to  $100 \text{ mV s}^{-1}$ . The composite graphene/PPy nano-fiber films showed higher capacitance compared to pure graphene and PPy nano-fiber films of the same mass. Moreover, the composite graphene/PPy nano-fiber films showed significant improvement in capacitance

retention at high scan rates. The capacitance of the composite films, calculated from the CV data (Fig. 6.27B), decreased from  $53.1 \text{ mF cm}^{-2}$  ( $354.2 \text{ F g}^{-1}$ ) to  $33.8 \text{ mF cm}^{-2}$  ( $225.6 \text{ F g}^{-1}$ ) with increasing scan rate from 2 to  $100 \text{ mV s}^{-1}$ . The EIS data showed lower  $Z'$  of the graphene/PPy nano-fiber film (Fig. 6.27C), compared to pure PPy film (Fig. 6.27C) and pure graphene film (Fig. 6.26C). The analysis of capacitance values, obtained from the impedance data showed higher  $C_s'$  and improved capacitance retention for composite graphene-PPy film (Fig. 6.27D), compared to the corresponding values for PPy film (Fig. 6.27D) and graphene film (Fig. 6.26D).

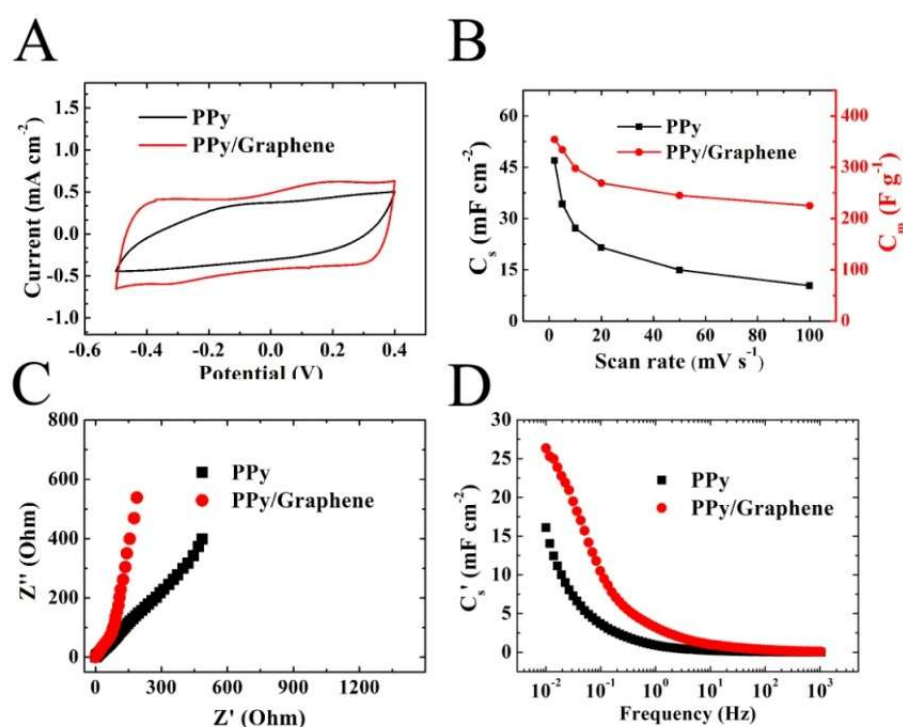


Figure. 6.27 (A) CVs at a scan rate of  $10 \text{ mV s}^{-1}$ , (B) capacitance calculated from CV data versus scan rate, (C) EIS data presented in a Nyquist plot and (D) capacitance

calculated from EIS data versus frequency for  $0.15 \text{ mg cm}^{-2}$  films of PPy nano-fiber and graphene/PPy nano-fiber composite.

The electrochemical testing results showed higher capacitance and lower impedance of composite films, compared to the films of the individual components. The incorporation of MWCNT and PPy nano-fibers between the dispersed graphene layers allowed improved electrolyte access to graphene. As a result, the high surface area of graphene was utilized better in the composite, resulting in higher capacitance and lower resistance. It is suggested that the lower resistance of graphene/PPy nano-fiber films, compared to pure PPy film, is also attributed to higher electronic conductivity of graphene. The higher ionic and electronic conductivity of composite graphene/PPy nano-fiber composites resulted in higher capacitance, especially at high scan rates.

### 6.3.5 Conclusions

EPD method has been developed for the fabrication of MWCNT, graphene and PPy nano-fibers films. The results of sedimentation tests, deposition yield measurements, FTIR, UV-Vis and SEM studies showed that SAF adsorbed on MWCNT, graphene and PPy nano-fibers, provided their dispersion and charging and allowed film formation by cathodic EPD. The possibility of efficient dispersion, charging and EPD of individual materials using SAF, allowed their efficient co-deposition and fabrication of composite graphene/MWCNT and graphene/PPy nano-fiber films. The composite films showed higher capacitance, lower resistance and improved

capacitance retention at high scan rates, compared to the films of individual components. The improved capacitive performance is attributed to efficient dispersion of MWCNT, graphene and PPy nano-fibers and beneficial effect of composite microstructure.

#### **6.4 PPy coated MWCNTs synthesized by multi-functional nano-crystals**

PPy/CNT composite presented high electrical conductivity, improved mechanical and electrochemical properties. It was found that the structure of nano-composite is an important factor controlling electrochemical, electrical and mechanical properties. The percolating CNT network allowed reduced volumetric changes of PPy during cycling and improved cycling behavior of the composite materials. PPy coated CNT has demonstrated great potential for improving the overall capacitive performance. Methods for fabricating of such composites have been developed in the past few years [43, 92-94]. However, the major difficulties in the fabrication of PPy coated CNT are efficient dispersion of CNT during polymerization and control of coating uniformity.

The goal of this investigation was to fabricate PPy coated MWCNT electrodes for ES applications. The new approach is based on the use of nano-crystals as multifunctional oxidant  $(\text{CTA})_2\text{S}_2\text{O}_8$  (Fig. 6.28A) for chemical polymerization of PPy, which allowed excellent dispersion of MWCNT and fabrication of uniformly coated MWCNT. The use of Ponceau S (PS) (Fig. 6.28B) as a new dopant allowed the fabrication of PPy based electrodes with improved capacitive behavior.

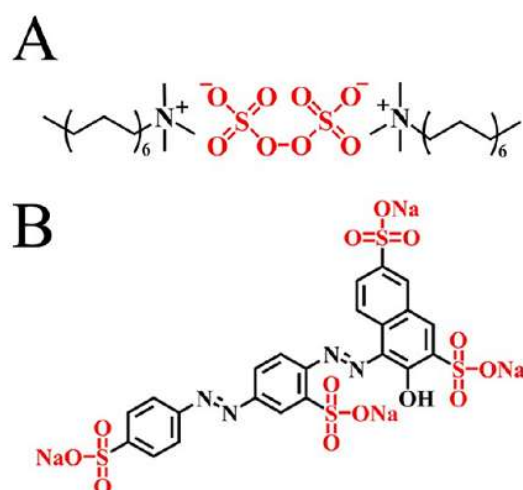


Figure 6.28 Chemical structure of (A)  $(\text{CTA})_2\text{S}_2\text{O}_8$  and (B) Ponceau S.

#### 6.4.1 PPy synthesized by $(\text{NH}_4)_2\text{S}_2\text{O}_8$ and $(\text{CTA})_2\text{S}_2\text{O}_8$

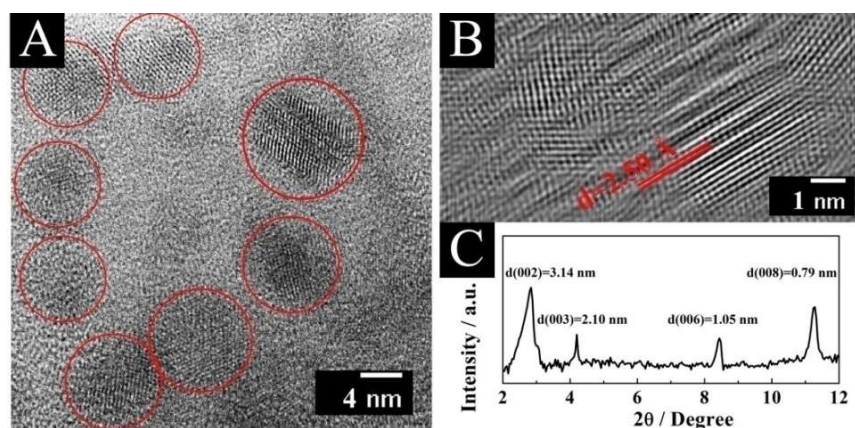


Figure 6.29 (A, B) HRTEM of  $(\text{CTA})_2\text{S}_2\text{O}_8$  nano-crystals formed by mixing CTAB and  $(\text{NH}_4)_2\text{S}_2\text{O}_8$  solutions and (C) Low-angle XRD pattern of  $(\text{CTA})_2\text{S}_2\text{O}_8$ .

Nano-crystals  $(\text{CTA})_2\text{S}_2\text{O}_8$  were prepared by the chemical reaction between cationic surfactant cetyltrimethylammonium bromide (CTAB) and anionic oxidant ammonium persulfate ( $(\text{NH}_4)_2\text{S}_2\text{O}_8$ ). The obtained  $(\text{CTA})_2\text{S}_2\text{O}_8$  nano-crystals were investigated in Fig. 6.29. The HRTEM results (Fig. 6.29A and B) indicated that typical size of the  $(\text{CTA})_2\text{S}_2\text{O}_8$

nano-crystals was in the range of 5-10 nm. The X-ray diffraction data (Fig. 6.29C) showed well defined diffraction peaks, indicating the formation of a periodic structure, containing  $\text{CTA}^+$  and  $\text{S}_2\text{O}_8^{2-}$  bi-layers[95-97].

Fig. 6.30 compares the SEM images of PPy powders, prepared using  $(\text{NH}_4)_2\text{S}_2\text{O}_8$  and  $(\text{CTA})_2\text{S}_2\text{O}_8$  oxidants. The PPy powder, prepared using  $(\text{NH}_4)_2\text{S}_2\text{O}_8$ , contained agglomerates of PPy particles with primary particle size of about 100 nm (Fig. 6.30A). It is known that PPy, synthesized without dopants, exhibits relatively low conductivity[98]. The use of efficient dopants is important for the development of advanced PPy electrodes for ES. It has been known that polyaromatic dopants with high charge to mass ratio are beneficial for the fabrication of PPy with high capacitance, improved cycling stability and high conductivity[99, 100]. Fig. 6.28B indicated that PS is a polyaromatic molecule, containing four anionic  $\text{SO}_3^-$  groups. Therefore, PS is a promising material for application as a new dopant for PPy polymerization. The PPy powder, prepared in the presence of PS (Fig. 6.30B), showed reduced agglomeration and smaller particle size, compared to the PPy powder, prepared without PS (Fig. 6.30A). It is suggested that anionic PS provided electrostatic repulsion of PPy particles during polymerization, resulting in reduced agglomeration and lower particle size.

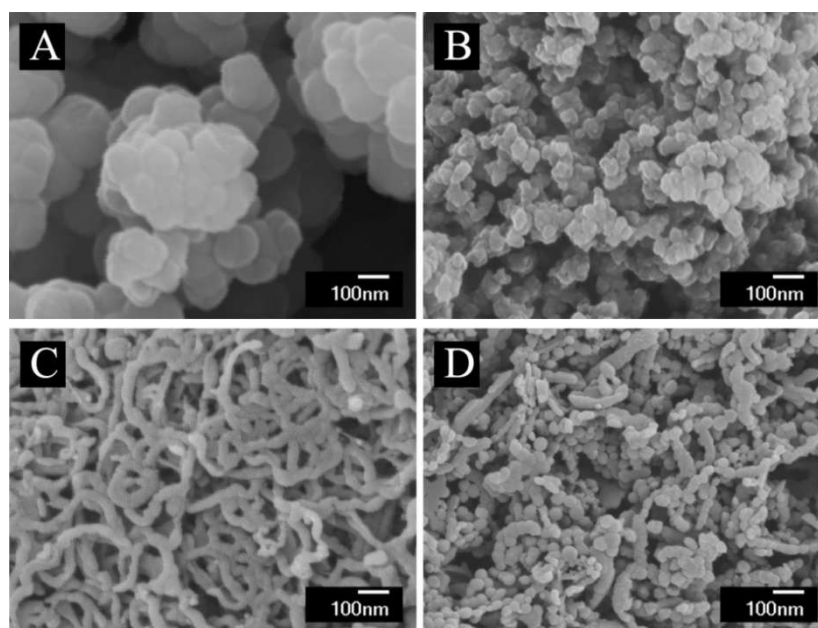


Figure 6.30 SEM images of PPy powders, prepared from  $0.05 \text{ mol L}^{-1}$  Py solutions, using (A,B)  $0.06 \text{ mol L}^{-1}$   $(\text{NH}_4)_2\text{S}_2\text{O}_8$  or (C,D)  $0.06 \text{ mol L}^{-1}$   $(\text{CTA})_2\text{S}_2\text{O}_8$  oxidants; (A,C) without PS and (B,D) with  $0.015 \text{ mol L}^{-1}$  PS.

SEM studies (Fig. 6.30C) of PPy, prepared using  $(\text{CTA})_2\text{S}_2\text{O}_8$ , revealed fibrous morphology of PPy particles. The obtained PPy nano-fibers have typical diameters of 25-30 nm and lengths of about 200-500 nm. The synthesis of fibrous PPy was reported in other investigations[101]. However, Py was added to the CTAB solution before the addition of  $(\text{NH}_4)_2\text{S}_2\text{O}_8$  and the CTAB: $(\text{NH}_4)_2\text{S}_2\text{O}_8$  molar ratio of 1:3 was different from that, corresponding to the  $(\text{CTA})_2\text{S}_2\text{O}_8$  stoichiometry[101]. It was suggested[101] that hydrophobic Py molecules were located at the interior of CTAB micelles in aqueous solutions. The addition of  $(\text{NH}_4)_2\text{S}_2\text{O}_8$  led to the formation of a  $\text{CTA}^+\text{-Py-S}_2\text{O}_8^{2-}$  template, with Py monomers located inside it. The polymerization resulted in the degradation of the template and formation of fibrous PPy. In contrast,

in our investigation,  $(\text{CTA})_2\text{S}_2\text{O}_8$  was prepared in the form of nano-crystals before the polymerization. Therefore, the mechanism, involving the templates, containing Py[101] or other monomers[102] inside or between the CTA layers cannot explain the formation of fibrous PPy, shown in Fig. 6.30C. Our investigation indicated that fibrous PPy can be formed using small nano-crystals of the  $(\text{CTA})_2\text{S}_2\text{O}_8$  oxidant for PPy polymerization, which was similar to previous investigations[40, 103].

It is known[104] that  $(\text{CTA})_2\text{S}_2\text{O}_8$  has low solubility in water ( $1 \times 10^{-5}\text{M}$ ). However, the consumption of  $\text{S}_2\text{O}_8^{2-}$  species in the redox reactions with Py monomers resulted in the gradual decomposition of the nano-crystals, containing weakly bonded  $\text{CTA}^+$  layers. It is in this regard that the size of  $\text{CTA}^+$  is about 2 nm[105, 106]. Therefore, the obtained nano-crystals could be easily decomposed in the redox reactions with Py. It is suggested that  $\text{CTA}^+$ , released from the decomposed  $(\text{CTA})_2\text{S}_2\text{O}_8$  structure, adsorbed on the PPy and influenced the anisotropic nucleation and growth of PPy. From the available literature it has been demonstrated that CTAB is an important shape-controlling surfactant, for the synthesis of nanowires and nanorods[107-109].

The PPy powders, prepared in the presence of PS and  $(\text{CTA})_2\text{S}_2\text{O}_8$ , contained PPy nano-particles and PPy nano-fibers (Fig. 6.30D). The fibrous PPy was consisted of individual spherical particles, with typical size of 20-30 nm. This observation supports our suggestion that the mechanism of PPy nano-fibers formation in the presence of  $(\text{CTA})_2\text{S}_2\text{O}_8$  nano-particles involved the formation of individual PPy

nano-particles and their 1-D agglomeration. The analysis of SEM images indicated that PS allowed reduced particle size, while  $(\text{CTA})_2\text{S}_2\text{O}_8$  nano-crystals promoted PPy nano-fiber formation.

#### 6.4.2 Capacitive performance of PPy

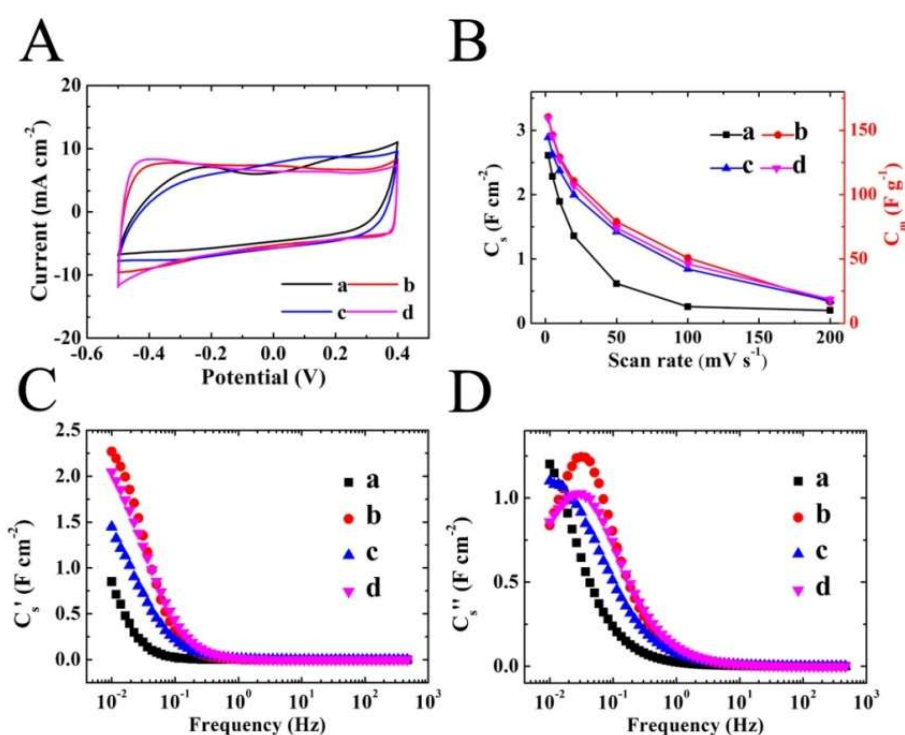


Figure 6.31 (A) CVs at  $2 \text{ mV s}^{-1}$ , (B)  $C_s$  and  $C_m$  versus scan rate, (C)  $C_s'$  and (D)  $C_s''$  versus frequency for  $20 \text{ mg cm}^{-2}$  PPy electrodes; (a),(b),(c),(d) present data for powders, shown in (A), (B), (C), (D) of Fig. 6.30, respectively.

The PPy powders were used for the fabrication of ES electrodes. Fig. 6.31A(a-d) presents CV data for the electrodes, prepared from the powders, shown in Fig. 6.30A-D. The comparison of the CV data revealed the beneficial effect of PS, which allowed nearly box shapes of CVs, indicating improved capacitive behavior (Fig.

6.31A(b,d)). For powders, prepared using  $(\text{NH}_4)_2\text{S}_2\text{O}_8$  oxidant, the addition of PS resulted in higher capacitance, especially at high scan rates (Fig. 6.31B(a,b)). The undoped PPy, prepared using  $(\text{CTA})_2\text{S}_2\text{O}_8$  (Fig. 6.31B(c)), showed higher capacitance, compared to undoped PPy, prepared in the presence of  $(\text{NH}_4)_2\text{S}_2\text{O}_8$  oxidant (Fig. 6.31B(a)). Further improvement in the capacitive behavior was achieved by adding PS (Fig. 6.31B(d)). The PPy electrodes (Fig. 6.31B(d)) showed highest  $C_m$  and  $C_s$  of  $159 \text{ F g}^{-1}$  and  $3.21 \text{ F cm}^{-2}$ , respectively at a scan rate of  $2 \text{ mV s}^{-1}$ . However, the capacitance retention at  $200 \text{ mV s}^{-1}$  was only 12%.

The components of complex AC capacitance  $C^*=C'-iC''$ , obtained from the impedance data are plotted in the Fig. 6.31C and D versus frequency. The  $C_s'$  data showed improved capacitance retention at higher frequencies for PS doped samples, compared to the undoped samples (Fig. 6.31C). The  $C_s''$  versus frequency plot for PS doped PPy showed a typical relaxation maximum (Fig. 6.31D). It indicated that the PS doped PPy, prepared by  $(\text{CTA})_2\text{S}_2\text{O}_8$ , showed improved specific capacitance and capacitive frequency range.

#### 6.4.3 Dispersion of MWCNT using $(\text{CTA})_2\text{S}_2\text{O}_8$

The development of efficient ES for high power applications requires good capacitive behavior at high scan rates and high AC frequencies. The improved capacitance retention of electrodes at high charge-discharge rates can be achieved by the fabrication of PPy coated MWCNT. Our new strategy was based on the use of

(CTA)<sub>2</sub>S<sub>2</sub>O<sub>8</sub> nano-crystals for the dispersion of MWCNT and fabrication of PPy coated MWCNT. Difficulties in the formation of PPy coatings on MWCNT are attributed to poor dispersibility of MWCNT in water and low suspension stability. However, our sedimentation tests showed that the MWCNT suspensions, containing (CTA)<sub>2</sub>S<sub>2</sub>O<sub>8</sub> were stable for more than one month.

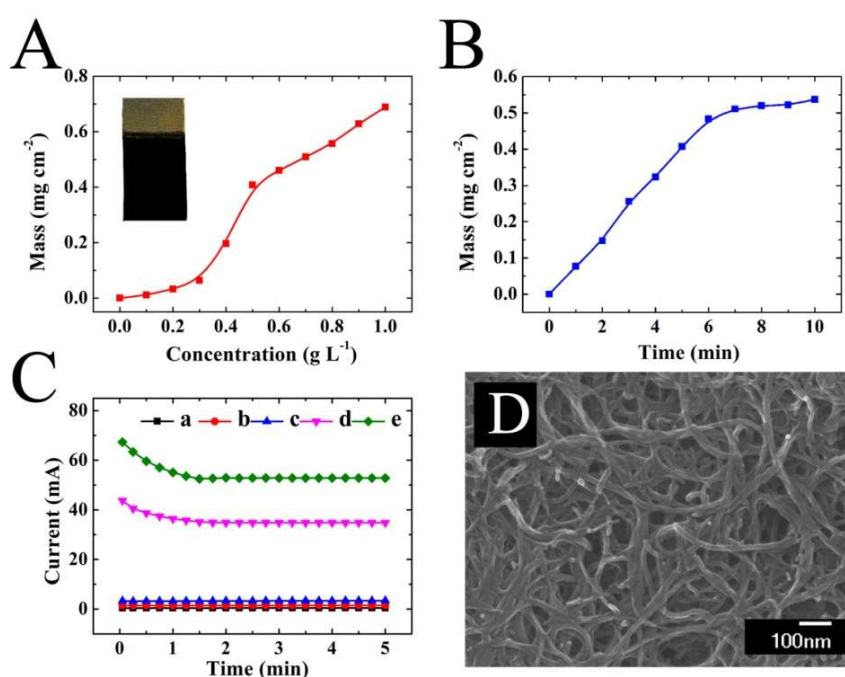


Figure 6.32. (A,B) Deposit mass for 1 g L<sup>-1</sup> MWCNT suspension versus (A) (CTA)<sub>2</sub>S<sub>2</sub>O<sub>8</sub> concentration at a deposition time of 5 min (inset shows a MWCNT film on stainless steel) and (B) deposition time at (CTA)<sub>2</sub>S<sub>2</sub>O<sub>8</sub> concentration of 0.5 g L<sup>-1</sup>; (C) deposition current versus deposition time for (a) 1 g L<sup>-1</sup> MWCNT, (b) 0.5 g L<sup>-1</sup> (CTA)<sub>2</sub>S<sub>2</sub>O<sub>8</sub>, (c) 1 g L<sup>-1</sup> (CTA)<sub>2</sub>S<sub>2</sub>O<sub>8</sub>, (d) 1 g L<sup>-1</sup> MWCNT and 0.5 g L<sup>-1</sup> (CTA)<sub>2</sub>S<sub>2</sub>O<sub>8</sub> and (e) 1 g L<sup>-1</sup> MWCNT and 1 g L<sup>-1</sup> (CTA)<sub>2</sub>S<sub>2</sub>O<sub>8</sub> suspensions; (D) SEM image of the MWCNT film obtained by cathodic EPD.

The dispersion mechanism was analyzed using EPD method, as presented in Fig. 6.32. It was not possible to deposit films by EPD from 0.5-1 g L<sup>-1</sup> MWCNT or 0.5-1 g L<sup>-1</sup> (CTA)<sub>2</sub>S<sub>2</sub>O<sub>8</sub> suspensions. However, cathodic deposits were obtained from 1 g L<sup>-1</sup> MWCNT suspensions, containing (CTA)<sub>2</sub>S<sub>2</sub>O<sub>8</sub>. The deposition yield increased with increasing (CTA)<sub>2</sub>S<sub>2</sub>O<sub>8</sub> concentration in the suspensions and deposition time (Fig. 6.32A and B). The method resulted in the formation of continuous films (Fig. 6.32A, inset). The decrease in the deposition rate with increasing deposition time (Fig. 6.32B) can be attributed to the decreasing electric field in the suspension due to increasing voltage drop in the growing deposit[82]. The formation of cathodic deposits indicated that MWCNT were positively charged in the suspensions. The results of electric current measurements during EPD at a constant voltage provided important information related to the charging and dispersion mechanism. Electric current in the 1 g L<sup>-1</sup> MWCNT, 0.5 g L<sup>-1</sup> (CTA)<sub>2</sub>S<sub>2</sub>O<sub>8</sub> and 1 g L<sup>-1</sup> (CTA)<sub>2</sub>S<sub>2</sub>O<sub>8</sub> suspensions was very low (Fig. 6.32C). As pointed out above, no deposit formation was achieved from such suspensions. However, the addition of 1 g L<sup>-1</sup> MWCNT to 0.5 g L<sup>-1</sup> (CTA)<sub>2</sub>S<sub>2</sub>O<sub>8</sub> or 1 g L<sup>-1</sup> (CTA)<sub>2</sub>S<sub>2</sub>O<sub>8</sub> suspensions resulted in significant increase in electric current (Fig. 6.32C). The starting current in the mixed 1 g L<sup>-1</sup> MWCNT and 1 g L<sup>-1</sup> (CTA)<sub>2</sub>S<sub>2</sub>O<sub>8</sub> suspensions was at least 20 times higher compared to the currents in the suspensions of individual components. The decrease in current with time (Fig. 6.32C(d,e)) is related to the decreasing electric field in the suspensions due to increasing voltage drop in the growing films. SEM image of the film, deposited from 1 g L<sup>-1</sup> MWCNT

and  $1 \text{ g L}^{-1}$   $(\text{CTA})_2\text{S}_2\text{O}_8$  suspension, showed a continuous network of MWCNT (Fig. 6.32D).

It is known that electrode reactions are not involved in the EPD process[110]. As pointed out above, the solubility of  $(\text{CTA})_2\text{S}_2\text{O}_8$  in water is very low. It is suggested that  $(\text{CTA})_2\text{S}_2\text{O}_8$  nano-crystals were adsorbed on the MWCNT and dissociation of  $(\text{CTA})_2\text{S}_2\text{O}_8$  was catalyzed by MWCNT. The MWCNT catalyzed dissociation of  $(\text{CTA})_2\text{S}_2\text{O}_8$  resulted in increasing ionic strength of the suspensions, as indicated by high starting current and high current during EPD (Fig.6.32C(d,e)). We suggested that  $\text{CTA}^+$  species were adsorbed on MWCNT, providing electrosteric stabilization and positive charge for cathodic EPD. The  $\text{CTA}^+$  and  $\text{S}_2\text{O}_8^{2-}$  species formed an electrical double layer.

The addition of Py to the suspensions, stabilized with  $\text{CTA}^+$  and  $\text{S}_2\text{O}_8^{2-}$  species, resulted in the oxidation of Py by the  $\text{S}_2\text{O}_8^{2-}$  in the double layer, polymerization and formation of PPy coatings. The sedimentation tests were carried out for the prepared materials in aqueous suspensions (Fig. 6.33). Testing results indicated that the suspensions of PPy coated MWCNT, prepared using  $(\text{CTA})_2\text{S}_2\text{O}_8$  nano-crystals in the presence of PS, were stable for more than one month after fabrication(Fig. 6.33D). In contrast, the suspensions prepared using  $(\text{NH}_4)_2\text{S}_2\text{O}_8$  instead of  $(\text{CTA})_2\text{S}_2\text{O}_8$  showed precipitation after 12h (Fig. 6.33C). The good dispersion of PPy coated MWCNT is not related to PPy coating, because PPy particles, prepared without MWCNT using

(CTA)<sub>2</sub>S<sub>2</sub>O<sub>8</sub>, showed precipitation after 48 h (Fig. 6.33A and B). These results further confirmed that colloidal stability of PPy coated MWCNT, prepared using (CTA)<sub>2</sub>S<sub>2</sub>O<sub>8</sub>, is related to adsorbed CTA<sup>+</sup>, which provided electrosteric dispersion.

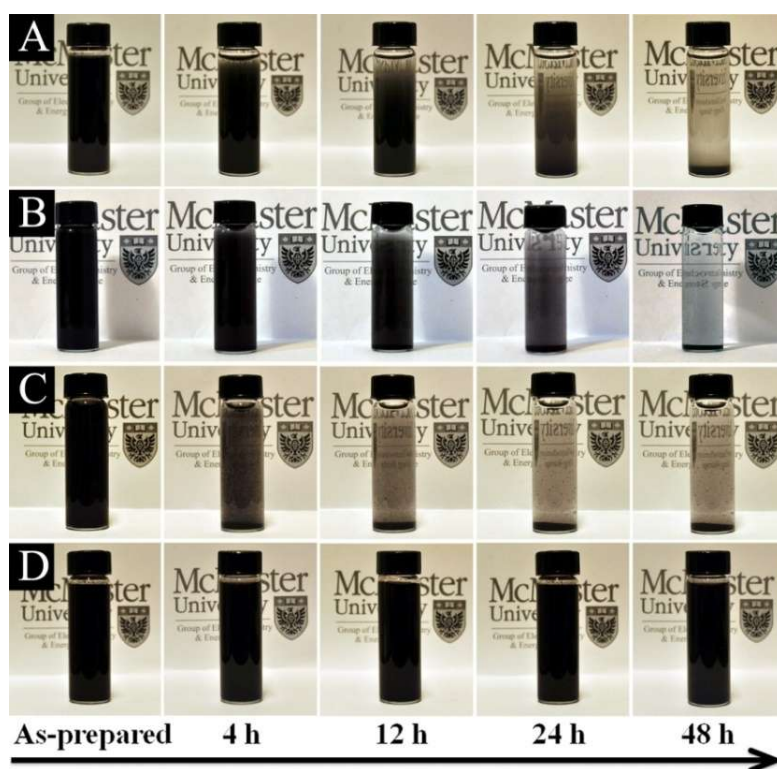


Figure 6.33 Sedimentation tests for aqueous suspensions of (A) 1 g L<sup>-1</sup> PPy nano-fibers, prepared using (CTA)<sub>2</sub>S<sub>2</sub>O<sub>8</sub>, (B) 1 g L<sup>-1</sup> PPy, prepared using PS and (CTA)<sub>2</sub>S<sub>2</sub>O<sub>8</sub>, (C) 1 g L<sup>-1</sup> PPy-MWCNT composite, prepared using PS and (NH<sub>4</sub>)<sub>2</sub>S<sub>2</sub>O<sub>8</sub> and (D) 1 g L<sup>-1</sup> PPy coated MWCNT, prepared using PS and (CTA)<sub>2</sub>S<sub>2</sub>O<sub>8</sub>, mass ratio MWCNT:Py 3:7.

The use of (CTA)<sub>2</sub>S<sub>2</sub>O<sub>8</sub> nano-crystals offered many advantages for MWCNT dispersion and fabrication of PPy coatings on MWCNT. A critical property of a

dispersant is its adsorption on a particle surface. Adsorbed dispersant provides particle dispersion, however non-adsorbed dispersant acts as an electrolyte[83]. The non-adsorbed ionic dispersant increases the ionic strength of the suspensions and promotes particle flocculation[83]. Therefore, a dispersant must be adsorbed on the particles and the concentration of non-adsorbed dispersant must be minimized. Due to the low solubility of  $(\text{CTA})_2\text{S}_2\text{O}_8$ , the ionic concentration of  $(\text{CTA})_2\text{S}_2\text{O}_8$  solutions was low. The interaction of  $(\text{CTA})_2\text{S}_2\text{O}_8$  nano-crystals with MWCNT resulted in decomposition of  $(\text{CTA})_2\text{S}_2\text{O}_8$  and adsorption of  $\text{CTA}^+$  on the MWCNT surface. As a result, efficient dispersion and EPD of MWCNT was achieved at  $(\text{CTA})_2\text{S}_2\text{O}_8/\text{MWCNT}$  mass ratio of 0.5, which is five times lower than the use of CTAB as the charging agent [111-114].

#### 6.4.4 PPy/MWCNT nano-composites synthesized by $(\text{NH}_4)_2\text{S}_2\text{O}_8$ and $(\text{CTA})_2\text{S}_2\text{O}_8$

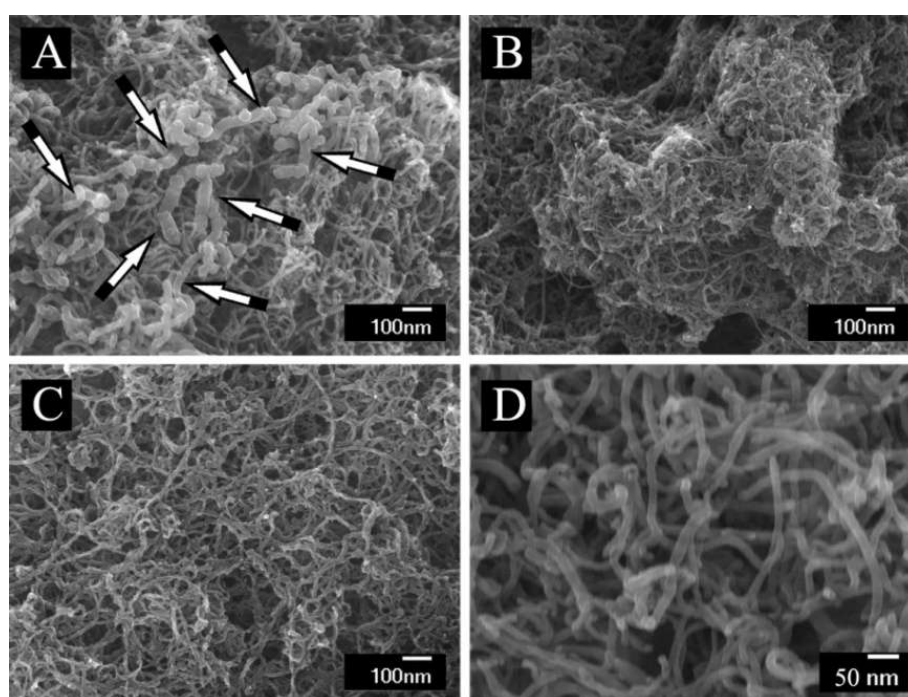


Figure 6.34. SEM images of PPy-MWCNT powders prepared using (A)  $(CTA)_2S_2O_8$  (arrows show PPy nano-fibers), (B) PS and  $(NH_4)_2S_2O_8$ , (C,D) PS and  $(CTA)_2S_2O_8$  at different magnifications, mass ratio MWCNT:Py =3:7.

The  $(NH_4)_2S_2O_8$  and  $(CTA)_2S_2O_8$  were investigated as oxidants to synthesize PPy/MWCNT nano-composites (Section 4.2.2.4). The obtained materials were investigated by electron microscopy. It was found that the morphology of PPy/MWCNT nano-composite is influenced by  $(CTA)_2S_2O_8$  and PS. The SEM and TEM images of powders, prepared without PS are shown in Fig. 6.34(A and B) and Fig. 6.35(A and B). The powders, prepared using  $(CTA)_2S_2O_8$  contained PPy coated MWCNT and PPy nano-fibers (Fig. 6.34A and Fig. 6.35A). The use of  $(NH_4)_2S_2O_8$  as an oxidant resulted in the formation of highly agglomerated particles, containing MWCNT and PPy (Fig. 6.34B and Fig. 6.35B). Uniformly coated MWCNT were obtained when Py and PS were added to the MWCNT suspensions, containing  $(CTA)_2S_2O_8$  (Fig. 6.34C,D and Fig. 6.35C,D). This result indicated that PS prevented the formation of fibrous PPy in the bulk of the suspensions. The formation of PPy coated MWCNT was confirmed by the analysis of high magnification TEM images. Fig. 6.35D shows typical TEM image of PPy coated MWCNT and inset shows the PPy-MWCNT interface. The SEM images (Fig 6.34C and D) and TEM images (Fig 6.35C and D)) indicated the formation of non-agglomerated and uniformly coated MWCNT with coating thickness of about 5 nm. The results of EELS studies were presented in Fig. 6.35E and F. Line scans were performed by rastering the electron

beam in a line perpendicular to the PPy coated MWCNT in 0.5 nm steps, measuring the spectrum for each step (Fig. 6.35E). The spectra in the energy range of 250-500 eV showed both the C-K and N-K edges at about 285 eV and 401 eV, respectively. The elemental distribution profile for nitrogen has a saddle shape with two maxima on both sides of the MWCNT, related to PPy coating (Fig. 6.35F). The carbon dominates in the middle of the profile with two small maxima from the both sides due to the hollow structure of MWCNT and PPy coating (Fig. 6.35F). The results of SEM, TEM and EELS data indicated that use of  $(CTA)_2S_2O_8$  in the form of nano-crystals as a dispersant for MWCNT and oxidant for Py polymerization allowed the fabrication of PPy coated MWCNT.

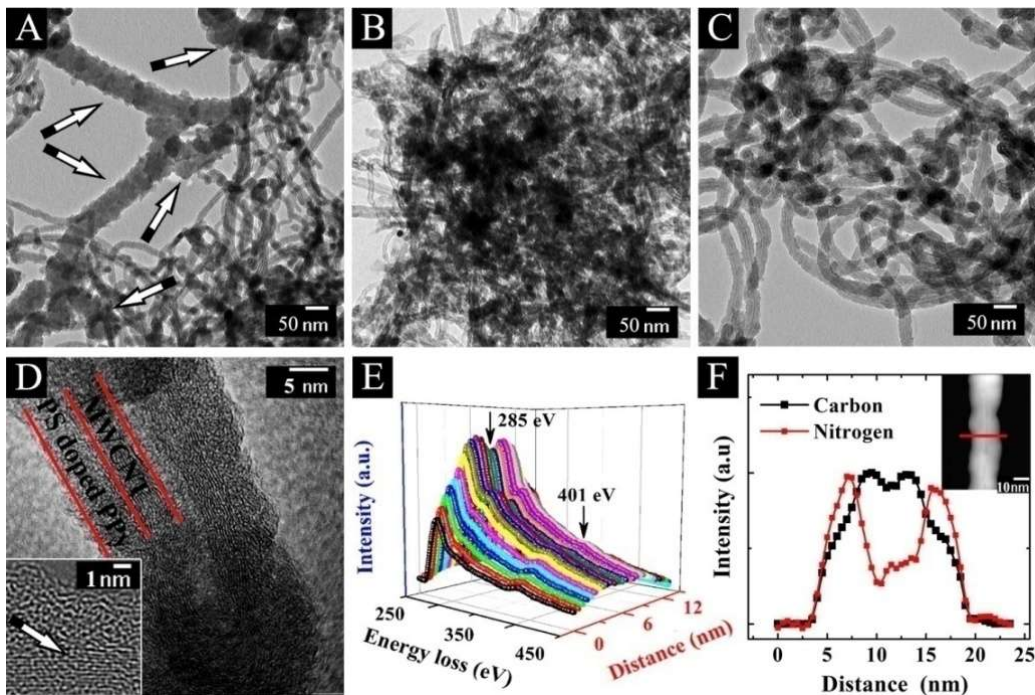


Figure. 6.35 TEM images of PPy-MWCNT powders prepared using (A)  $(CTA)_2S_2O_8$  (arrows show PPy fibers), (B) PS and  $(NH_4)_2S_2O_8$ , (C,D) PS and  $(CTA)_2S_2O_8$  at

different magnifications, arrow in (D) inset shows HRTEM image of PPy-MWCNT interface; (E) set of resolved EELS spectra measured along a line across PPy coated MWCNT (F) Element distribution obtained from the EELS data, inset shows HAADF image of a region for analysis, concentrations of Py, PS,  $(\text{NH}_4)_2\text{S}_2\text{O}_8$  and  $(\text{CTA})_2\text{S}_2\text{O}_8$  were the same as in Fig. 6.30, mass ratio MWCNT:Py = 3:7.

Another important factor, controlling the formation of PPy coatings was the MWCNT:Py ratio in the solutions (Fig. 6.36). When MWCNT/Py ratio was 1:9 the coatings were non-uniform (Fig. 6.36A). Individual PPy nano-particles were observed for MWCNT/Py ratio below 2:8. The uniformity of PPy coating improved when the ratio was increased (Fig. 6.36B). Uniformly coated MWCNT were obtained at MWCNT/Py ratio of 3:7 (Fig. 6.36C).

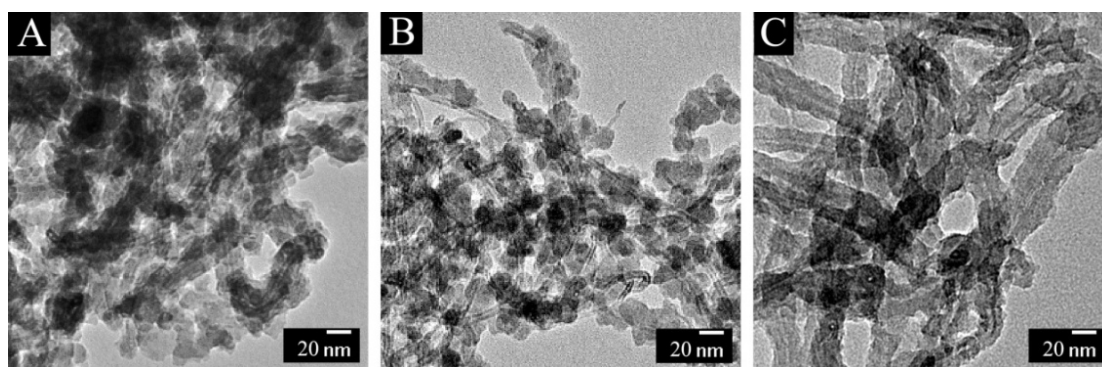


Figure 6.36. TEM images of PPy coated MWCNT, prepared from  $0.05 \text{ mol L}^{-1}$  Py solutions, using  $0.06 \text{ mol L}^{-1}$   $(\text{CTA})_2\text{S}_2\text{O}_8$  and  $0.015 \text{ mol L}^{-1}$  PS, mass ratio MWCNT:Py (A) 1:9, (B) 2:8, (C) 3:7.

#### 6.4.5 Capacitive performance of PPy/MWCNT nano-composites

The electrochemical tests showed that the use of PPy coated MWCNT allowed significant improvement in capacitance retention at high scan rates. Fig. 6.37 (A,B,C) presents CVs for the electrodes, prepared using powders shown in Fig. 6.35(A,B,C). The larger CV area for the PPy electrodes, prepared using  $(\text{CTA})_2\text{S}_2\text{O}_8$  and PS, indicates higher capacitance. The investigation of the capacitance, calculated from the CV data, showed capacitance retention of 63% at a scan rate of  $200 \text{ mV s}^{-1}$ . Moreover, relatively high capacitance of  $1.4 \text{ F cm}^{-2}$  ( $72 \text{ F g}^{-1}$ ) was achieved at a scan rate of  $200 \text{ mV s}^{-1}$  (Fig. 6.37D). The capacitance, calculated from the impedance data was plotted versus AC frequency in Fig. 6.37E and F. The  $C_s'$  data showed relaxation behavior (Fig. 6.37E), as indicated by the rapid decrease in the  $C_s'$  above relaxation frequencies. The maxima of  $C_s''$  appeared at higher frequency for PPy coated MWCNT (Fig. 6.37F(c)). The comparison of the data presented in Fig. 6.31(C,D) and Fig. 6.37(E,F) showed that the use of PPy coated MWCNT allowed significant improvement in capacitance retention at high AC frequencies. Additionally, the PPy coated MWCNT, prepared in the presence of  $(\text{CTA})_2\text{S}_2\text{O}_8$  and PS, showed significantly higher  $C_s'$  in the frequency range below 1 Hz, compared to PPy powders (Fig. 6.31C) and the relaxation maximum shifted to 293 mHz (Fig. 6.37F(c)). It have been demonstrated that specific capacitances of conductive polymers, calculated from the AC impedance data are significantly lower, compared to the capacitances, calculated from the CV data [115, 116]. Such data analysis is usually performed at the same time scale,

because the voltammetric capacitance depends on a scan rate, whereas AC capacitance depends on frequency[115]. Tanguy et al. suggested that some “deeply trapped” dopant counterions can be immobile at low AC voltages[116]. Such ions can be released at higher voltages in CV experiments and contribute to higher capacitance. In other investigations, the discrepancy between the AC and voltammetric capacitances was attributed to chemical and physical heterogeneity and existence of sites with wide range of redox potentials[115, 117, 118].

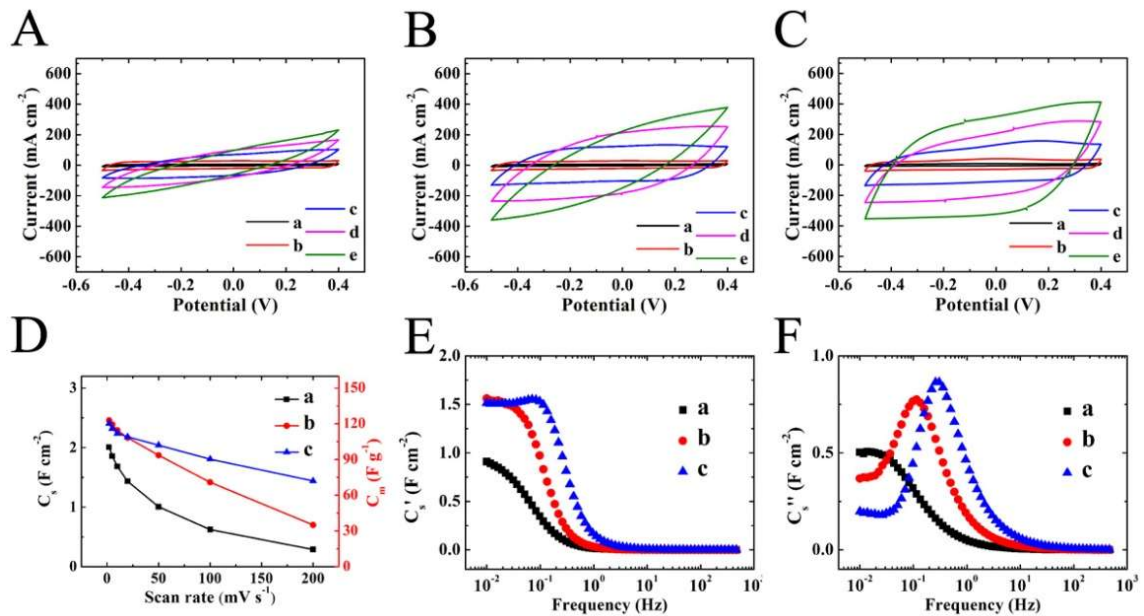


Figure 6.37 (A,B,C) CVs at scan rates of (a)2, (b)10, (c)50, (d)100 and (e)200  $\text{mV s}^{-1}$ , (D)  $C_s$  and  $C_m$  versus scan rate (E)  $C_s'$  and (F)  $C_s''$  versus AC frequency, (A,B,C) in Fig. 6.37 and (a),(b),(c) in Fig. 6.37(D-F) present data for powders shown in A,B,C of Fig. 6.35, respectively, for electrode mass of  $20 \text{ mg cm}^{-2}$ .

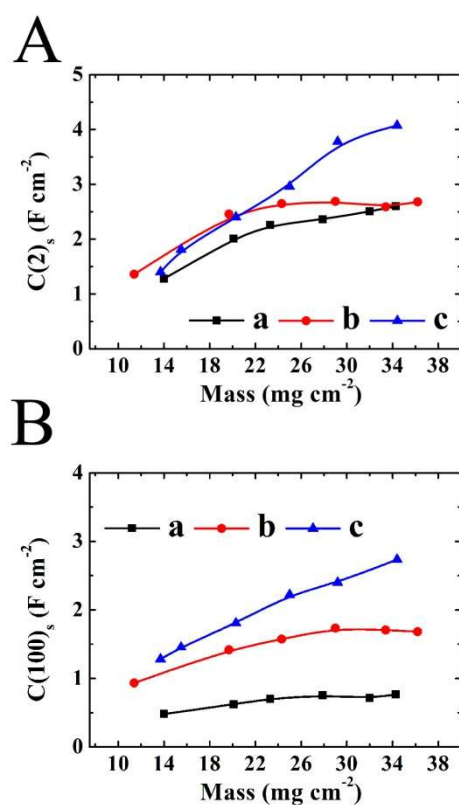


Figure 6.38  $C_s$  versus electrode mass obtained at scan rates of (A) 2 and (B) 100  $\text{mV s}^{-1}$ , (a),(b),(c) present data for powders, shown in (A), (B), (C) of Fig. 6.35, respectively.

The advantage of PPy coated MWCNT is also evident from the capacitance versus electrode mass dependencies. The specific capacitance  $C_s(2)$  and  $C_s(100)$ , measured at scan rates of 2 and 100  $\text{mV s}^{-1}$ , were presented in Fig. 6.38A and B, respectively. The results showed that  $C_s(2)$  and  $C_s(100)$  of PPy coated MWCNT increased with increasing materials loading (Fig. 6.38A(c) and B(c)). In contrast, the electrodes, prepared without PS or with  $(\text{NH}_4)_2\text{S}_2\text{O}_8$  oxidant showed lower capacitance and no increase in  $C_s$  was observed with increasing material loading above 20  $\text{mg cm}^{-2}$  (Fig.

6.38A(a,b) and B(a,b)). The highest  $C(2)_s$  of  $4.1 \text{ F cm}^{-2}$  was obtained for material loading of  $35 \text{ mg cm}^{-2}$ . Moreover, remarkably high  $C(100)_s$  of  $2.8 \text{ F cm}^{-2}$  was obtained. The linear increase of  $C_s$  with electrode mass for PPy coated MWCNT indicated efficient utilization of the active materials.

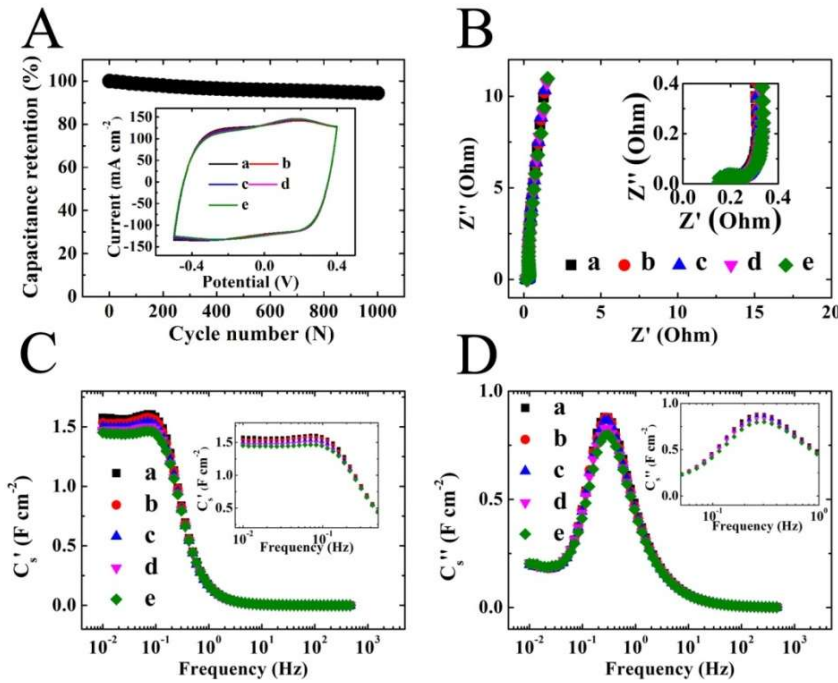


Figure 6.39 (A) Capacitance retention versus cycle number, inset shows corresponding CVs at  $50 \text{ mV s}^{-1}$ , (B) Nyquist plot of complex impedance, inset shows high frequency range, (C)  $C_s'$  and (D)  $C_s''$  versus frequency, insets in (C,D) show low frequency range, after (a)1<sup>st</sup>, (b)250<sup>th</sup>, (c) 500<sup>th</sup>, (d)750<sup>th</sup>, (e)1000<sup>th</sup> cycles, prepared from powder shown in Fig. 6.35C.

Fig 6.39 showed cycling performance of the electrodes, containing PPy coated MWCNT, with active mass of  $20 \text{ mg cm}^{-2}$ . The capacitive retention after 1000 cycles

is 94.4% (Fig. 6.39A). The shape of the CV (Fig. 6.39A, inset) and resistance value  $R=Z'$  (Fig. 6.39B) remained practically unchanged during cycling. The 6% decrease in the  $C_s'$  after 1000 cycles (Fig. 6.39C) correlated with corresponding reduction in  $C_s$ , obtained from the CV data (Fig. 6.39A). However, no changes in the relaxation frequency were observed during cycling (Fig. 6.39D). The results indicated that the use of PPy coated MWCNT, prepared using  $(CTA)_2S_2O_8$  nano-crystals, which served as a dispersant and oxidant, and PS as a new anionic dopant, allowed the fabrication of electrodes with high capacitance, high material loading, good capacitance retention at high scan rates and good cycling stability.

#### 6.4.6 Conclusions

PS was used as a new anionic dopant and  $(CTA)_2S_2O_8$  nano-crystals were used as an oxidant for chemical polymerization of PPy. Testing results demonstrated that PS allowed reduced PPy particle size and improved electrochemical performance, whereas  $(CTA)_2S_2O_8$  nano-crystals promoted the formation of PPy nano-fibers. The PPy powders prepared using PS and  $(CTA)_2S_2O_8$  nano-crystals showed improved capacitive behavior, while the PPy coated MWCNT showed superior capacitive behavior compared to PPy nano-particles. We demonstrated that  $(CTA)_2S_2O_8$  nano-crystals can be used for efficient dispersion of MWCNT. The dispersion mechanism was investigated by EPD method. It is found that the  $(CTA)_2S_2O_8$  dissociation was catalyzed by MWCNT. In this approach, efficient dispersion was

achieved at low CTA<sup>+</sup> concentration. The use of (CTA)<sub>2</sub>S<sub>2</sub>O<sub>8</sub> nano-crystals as a dispersant for MWCNT and oxidant for PPy and the use of PS as an anionic dopant and PPy structure controlling agent allowed the fabrication of uniformly coated MWCNT. The PPy coated MWCNT prepared by (CTA)<sub>2</sub>S<sub>2</sub>O<sub>8</sub> showed improved dispersibility, compared with PPy nano-particles and PPy/MWCNT prepared by (NH<sub>3</sub>)<sub>2</sub>S<sub>2</sub>O<sub>8</sub>. The method allowed the fabrication of ES electrodes with high materials loading, excellent capacitance retention at high charge-discharge rates and excellent cycling stability. The highest C<sub>s</sub> of 4.1 F cm<sup>-2</sup> was obtained at a scan rate of 2 mV s<sup>-1</sup> for material loading of 35 mg cm<sup>-2</sup>.

## 6.5 References

- [1] C. Pirvu, C.C. Manole, A.B. Stoian, I. Demetrescu, Understanding of electrochemical and structural changes of polypyrrole/polyethylene glycol composite films in aqueous solution, *Electrochimica Acta*, 56 (2011) 9893-9903.
- [2] G. Zhang, H. Zhou, J. Zhang, X. Han, J. Chen, Y. Kuang, Electropolymerization of pyrrole in ionic liquid microemulsion, *Journal of Applied Polymer Science*, 125 (2012) 2342-2347.
- [3] Z. Yu, C. Li, D. Abbitt, J. Thomas, Flexible, sandwich-like Ag-nanowire/PEDOT:PSS-nanopillar/MnO<sub>2</sub> high performance supercapacitors, *Journal of Materials Chemistry A*, 2 (2014) 10923-10929.
- [4] Z. Yu, L. Tetard, L. Zhai, J. Thomas, Supercapacitor electrode materials: nanostructures from 0 to 3 dimensions, *Energy & Environmental Science*, 8 (2015) 702-730.
- [5] Y. Hu, Y. Zhao, Y. Li, H. Li, H. Shao, L. Qu, Defective super-long carbon nanotubes and polypyrrole composite for high-performance supercapacitor electrodes, *Electrochimica Acta*, 66 (2012) 279-286.

- [6] X. Lu, F. Zhang, H. Dou, C. Yuan, S. Yang, L. Hao, L. Shen, L. Zhang, X. Zhang, Preparation and electrochemical capacitance of hierarchical graphene/polypyrrole/carbon nanotube ternary composites, *Electrochimica Acta*, 69 (2012) 160-166.
- [7] R. Xu, F. Guo, X. Cui, L. Zhang, K. Wang, J. Wei, High performance carbon nanotube based fiber-shaped supercapacitors using redox additives of polypyrrole and hydroquinone, *Journal of Materials Chemistry A*, (2015).
- [8] S. Goel, N.A. Mazumdar, A. Gupta, Synthesis and characterization of polypyrrole nanofibers with different dopants, *Polymers for Advanced Technologies*, 21 (2010) 205-210.
- [9] I. Sultana, M.M. Rahman, S. Li, J. Wang, C. Wang, G.G. Wallace, H.-K. Liu, Electrodeposited polypyrrole (PPy)/para (toluene sulfonic acid) (pTS) free-standing film for lithium secondary battery application, *Electrochimica Acta*, 60 (2012) 201-205.
- [10] M. Han, Y. Chu, D. Han, Y. Liu, Fabrication and characterizations of oligopyrrole doped with dodecylbenzenesulfonic acid in reverse microemulsion, *Journal of Colloid and Interface Science*, 296 (2006) 110-117.
- [11] B. Weng, R. Shepherd, J. Chen, G.G. Wallace, Gemini surfactant doped polypyrrole nanodispersions: an inkjet printable formulation, *Journal of Materials Chemistry*, 21 (2011) 1918-1924.
- [12] K. Shi, I. Zhitomirsky, Fabrication of Polypyrrole-Coated Carbon Nanotubes Using Oxidant-Surfactant Nano-crystals for Supercapacitor Electrodes with High Mass Loading and Enhanced Performance, *ACS Applied Materials & Interfaces*, 5 (2013) 13161-13170.
- [13] L. Vaisman, H.D. Wagner, G. Marom, The role of surfactants in dispersion of carbon nanotubes, *Advances in Colloid and Interface Science*, 128-130 (2006) 37-46.
- [14] X.-L. Xie, Y.-W. Mai, X.-P. Zhou, Dispersion and alignment of carbon nanotubes in polymer matrix: A review, *Materials Science and Engineering: R: Reports*, 49 (2005) 89-112.
- [15] S.W. Kim, T. Kim, Y.S. Kim, H.S. Choi, H.J. Lim, S.J. Yang, C.R. Park, Surface modifications for the effective dispersion of carbon nanotubes in solvents and polymers, *Carbon*, 50 (2012) 3-33.
- [16] Y. Sun, Y. Wang, I. Zhitomirsky, Dispersing agents for electrophoretic deposition of TiO<sub>2</sub> and TiO<sub>2</sub>-carbon nanotube composites, *Colloids and Surfaces A: Physicochemical and Engineering Aspects*, 418 (2013) 131-138.

- [17] Y. Liu, M.S. Ata, K. Shi, G.z. Zhu, G.A. Botton, I. Zhitomirsky, Surface modification and cathodic electrophoretic deposition of ceramic materials and composites using celestine blue dye, *RSC Advances*, 4 (2014) 29652-29659.
- [18] Y. Liu, K. Shi, I. Zhitomirsky, New colloidal route for electrostatic assembly of oxide nanoparticle – carbon nanotube composites, *Colloids and Surfaces A: Physicochemical and Engineering Aspects*, 446 (2014) 15-22.
- [19] K. Shi, I. Zhitomirsky, Electrophoretic nanotechnology of graphene–carbon nanotube and graphene–polypyrrole nanofiber composites for electrochemical supercapacitors, *Journal of Colloid and Interface Science*, 407 (2013) 474-481.
- [20] S.A. Curran, A.V. Ellis, A. Vijayaraghavan, P.M. Ajayan, Functionalization of carbon nanotubes using phenosafranin, *The Journal of Chemical Physics*, 120 (2004) 4886-4889.
- [21] G. Ćirić-Marjanović, N.V. Blinova, M. Trchová, J. Stejskal, Chemical Oxidative Polymerization of Safranines, *The Journal of Physical Chemistry B*, 111 (2007) 2188-2199.
- [22] P.C. Ma, J.-K. Kim, B.Z. Tang, Functionalization of carbon nanotubes using a silane coupling agent, *Carbon*, 44 (2006) 3232-3238.
- [23] L.R.B. Santos, T. Chartier, C. Pagnoux, J.F. Baumard, C.V. Santilli, S.H. Pulcinelli, A. Larbot, Tin oxide nanoparticle formation using a surface modifying agent, *Journal of the European Ceramic Society*, 24 (2004) 3713-3721.
- [24] F.-H. Hsu, T.-M. Wu, In situ synthesis and characterization of conductive polypyrrole/graphene composites with improved solubility and conductivity, *Synthetic Metals*, 162 (2012) 682-687.
- [25] I. Rodríguez, B.R. Scharifker, J. Mostany, In situ FTIR study of redox and overoxidation processes in polypyrrole films, *Journal of Electroanalytical Chemistry*, 491 (2000) 117-125.
- [26] Y. Gogotsi, P. Simon, True Performance Metrics in Electrochemical Energy Storage, *Science*, 334 (2011) 917-918.
- [27] K. Shi, M. Ren, I. Zhitomirsky, Activated Carbon-Coated Carbon Nanotubes for Energy Storage in Supercapacitors and Capacitive Water Purification, *ACS Sustainable Chemistry & Engineering*, 2 (2014) 1289-1298.

- [28] K. Shi, I. Zhitomirsky, Asymmetric Supercapacitors Based on Activated - Carbon - Coated Carbon Nanotubes, *ChemElectroChem*, 2 (2015) 396-403.
- [29] G.R. Mitchell, F.J. Davis, C.H. Legge, The effect of dopant molecules on the molecular order of electrically-conducting films of polypyrrole, *Synthetic Metals*, 26 (1988) 247-257.
- [30] A. Talaie, G.G. Wallace, The effect of the counterion on the electrochemical properties of conducting polymers -a study using resistometry, *Synthetic Metals*, 63 (1994) 83-88.
- [31] X. Zhang, Bai, Surface Electric Properties of Polypyrrole in Aqueous Solutions, *Langmuir*, 19 (2003) 10703-10709.
- [32] S. Ardizzone, G. Fregonara, S. Trasatti, "Inner" and "outer" active surface of RuO<sub>2</sub> electrodes, *Electrochimica Acta*, 35 (1990) 263-267.
- [33] D. Baronetto, N. Krstajić, S. Trasatti, Reply to "note on a method to interrelate inner and outer electrode areas" by H. Vogt, *Electrochimica Acta*, 39 (1994) 2359-2362.
- [34] H. Vogt, Note on a method to interrelate inner and outer electrode areas, *Electrochimica Acta*, 39 (1994) 1981-1983.
- [35] M.S. Kim, J.H. Moon, P.J. Yoo, J.H. Park, Hollow Polypyrrole Films: Applications for Energy Storage Devices, *Journal of The Electrochemical Society*, 159 (2012) A1052-A1056.
- [36] A.N. Aleshin, H.J. Lee, Y.W. Park, K. Akagi, One-Dimensional Transport in Polymer Nanofibers, *Physical Review Letters*, 93 (2004) 196601.
- [37] J.G. Park, S.H. Lee, B. Kim, Y.W. Park, Electrical resistivity of polypyrrole nanotube measured by conductive scanning probe microscope: The role of contact force, *Applied Physics Letters*, 81 (2002) 4625-4627.
- [38] J.Y. Hong, H. Yoon, J. Jang, Kinetic Study of the Formation of Polypyrrole Nanoparticles in Water - Soluble Polymer/Metal Cation Systems: A Light - Scattering Analysis, *Small*, 6 (2010) 679-686.
- [39] J. Liu, J. An, Y. Ma, M. Li, R. Ma, Synthesis of a Graphene-Polypyrrole Nanotube Composite and Its Application in Supercapacitor Electrode, *Journal of The Electrochemical Society*, 159 (2012) A828-A833.

- [40] Y. Wang, W. Chen, D. Zhou, G. Xue, Synthesis of Conducting Polymer Spiral Nanostructures Using a Surfactant Crystallite Template, *Macromolecular Chemistry and Physics*, 210 (2009) 936-941.
- [41] Z. Liu, X. Zhang, S. Poyraz, S.P. Surwade, S.K. Manohar, Oxidative Template for Conducting Polymer Nanoclips, *Journal of the American Chemical Society*, 132 (2010) 13158-13159.
- [42] T. Chen, Z. Cai, L. Qiu, H. Li, J. Ren, H. Lin, Z. Yang, X. Sun, H. Peng, Synthesis of aligned carbon nanotube composite fibers with high performances by electrochemical deposition, *J. Mater. Chem. A*, 1 (2013) 2211-2216.
- [43] Y. Fang, J. Liu, D.J. Yu, J.P. Wicksted, K. Kalkan, C.O. Topal, B.N. Flanders, J. Wu, J. Li, Self-supported supercapacitor membranes: Polypyrrole-coated carbon nanotube networks enabled by pulsed electrodeposition, *Journal of Power Sources*, 195 (2010) 674-679.
- [44] X. Lu, H. Dou, C. Yuan, S. Yang, L. Hao, F. Zhang, L. Shen, L. Zhang, X. Zhang, Polypyrrole/carbon nanotube nanocomposite enhanced the electrochemical capacitance of flexible graphene film for supercapacitors, *Journal of Power Sources*, 197 (2012) 319-324.
- [45] H. Wang, L. Bian, P. Zhou, J. Tang, W. Tang, Core-sheath structured bacterial cellulose/polypyrrole nanocomposites with excellent conductivity as supercapacitors, *J. Mater. Chem. A*, 1 (2013) 578-584.
- [46] S. Chen, W. Xing, J. Duan, X. Hu, S.Z. Qiao, Nanostructured morphology control for efficient supercapacitor electrodes, *J. Mater. Chem. A*, 1 (2013) 2941-2954.
- [47] P. Golding, T. King, L. Maddocks, D. Drucker, A. Blinkhorn, Photosensitization of *Staphylococcus aureus* with malachite green isothiocyanate: inactivation efficiency and spectroscopic analysis, *Journal of Photochemistry and Photobiology B: Biology*, 47 (1998) 202-210.
- [48] V. Chernyak, R. Reisfeld, Spectroscopic behaviour of malachite green in sol-gel glasses, *Chemical Physics Letters*, 181 (1991) 39-44.
- [49] O.O. Van der Biest, L.J. Vandeperre, Electrophoretic deposition of materials, *Annual Review of Materials Science*, 29 (1999) 327-352.
- [50] D.K. Ariyanayagamkumarappa, I. Zhitomirsky, Electropolymerization of polypyrrole films on stainless steel substrates for electrodes of electrochemical supercapacitors, *Synthetic Metals*, 162 (2012) 868-872.

- [51] M.-H. Baek, C.O. Ijagbemi, D.-S. Kim, Spectroscopic studies on the oxidative decomposition of Malachite Green using ozone, *Journal of Environmental Science and Health Part A*, 45 (2010) 630-636.
- [52] I.A. Jankovic, Z.V. Saponjic, M.I. Comor, J.M. Nedeljkovic, Surface Modification of Colloidal TiO<sub>2</sub> Nanoparticles with Bidentate Benzene Derivatives, *The Journal of Physical Chemistry C*, 113 (2009) 12645-12652.
- [53] S.K. Bajpai, A. Jain, Equilibrium and Thermodynamic Studies for Adsorption of Crystal Violet onto Spent Tea Leaves (STL), *Water Journal*, 4 (2012) 52-71.
- [54] K.D. Dobson, A.J. McQuillan, In situ infrared spectroscopic analysis of the adsorption of aromatic carboxylic acids to TiO<sub>2</sub>, ZrO<sub>2</sub>, Al<sub>2</sub>O<sub>3</sub>, and Ta<sub>2</sub>O<sub>5</sub> from aqueous solutions, *Spectrochimica Acta A*, 56 (2000) 557-565.
- [55] S. Tunesi, M.A. Anderson, Surface effects in photochemistry: an in situ cylindrical internal reflection-Fourier transform infrared investigation of the effect of ring substituents on chemisorption onto TiO<sub>2</sub> ceramic membranes, *Langmuir*, 8 (1992) 487-495.
- [56] C. Zeng, N. Hossieny, C. Zhang, B. Wang, Synthesis and Processing of PMMA Carbon Nanotube Nanocomposite Foams, *Polymer*, 51 (2010) 655-664.
- [57] Y. Sun, Y. Wang, I. Zhitomirsky, Dispersing Agents for Electrophoretic Deposition of TiO<sub>2</sub> and TiO<sub>2</sub>-Carbon Nanotube Composites, *Colloids Surf., A*, 418 (2013) 131-138.
- [58] X. Zhang, J. Zhang, W. Song, Z. Liu, Controllable Synthesis of Conducting Polypyrrole Nanostructures, *The Journal of Physical Chemistry B*, 110 (2005) 1158-1165.
- [59] K. Shi, I. Zhitomirsky, Influence of current collector on capacitive behavior and cycling stability of Tiron doped polypyrrole electrodes, *Journal of Power Sources*, 240 (2013) 42-49.
- [60] Z.H. Dong, Y.L. Wei, W. Shi, G.A. Zhang, Characterisation of doped polypyrrole/manganese oxide nanocomposite for supercapacitor electrodes, *Materials Chemistry and Physics*, 131 (2011) 529-534.
- [61] R. Ramya, R. Sivasubramanian, M. Sangaranarayanan, Conducting polymers-based Electrochemical Supercapacitors-Progress and Prospects, *Electrochimica Acta*, 101 (2013) 109-129.

- [62] J. Wang, Y. Xu, X. Chen, X. Du, Electrochemical supercapacitor electrode material based on poly (3, 4-ethylenedioxythiophene)/polypyrrole composite, *Journal of Power Sources*, 163 (2007) 1120-1125.
- [63] P.L. Taberna, P. Simon, J.F. Fauvarque Electrochemical Characteristics and Impedance Spectroscopy Studies of Carbon-Carbon Supercapacitors, *Journal of The Electrochemical Society*, 150 (2003) A292-A300.
- [64] R. Kötz, M. Carlen, Principles and applications of electrochemical capacitors, *Electrochimica Acta*, 45 (2000) 2483-2498.
- [65] D.A.C. Brownson, D.K. Kampouris, C.E. Banks, An overview of graphene in energy production and storage applications, *Journal of Power Sources*, 196 (2011) 4873-4885.
- [66] Y. Huang, J. Liang, Y. Chen, An overview of the applications of graphene-based materials in supercapacitors, *Small*, 8 (2012) 1805-1834.
- [67] H.-J. Choi, S.-M. Jung, J.-M. Seo, D.W. Chang, L. Dai, J.-B. Baek, Graphene for energy conversion and storage in fuel cells and supercapacitors, *Nano Energy*, 1 (2012) 534-551.
- [68] A. Yu, I. Roes, A. Davies, Z. Chen, Ultrathin, transparent, and flexible graphene films for supercapacitor application, *Applied Physics Letters*, 96 (2010) 253105.
- [69] B.G. Choi, S.-J. Chang, H.-W. Kang, C.P. Park, H.J. Kim, W.H. Hong, S. Lee, Y.S. Huh, High performance of a solid-state flexible asymmetric supercapacitor based on graphene films, *Nanoscale*, 4 (2012) 4983-4988.
- [70] Y. Wang, Y. Wu, Y. Huang, F. Zhang, X. Yang, Y. Ma, Y. Chen, Preventing Graphene Sheets from Restacking for High-Capacitance Performance, *J. Phys. Chem. C*, 115 (2011) 23192-23197.
- [71] D. Yu, L. Dai, Self-Assembled Graphene/Carbon Nanotube Hybrid Films for Supercapacitors, *J. Phys. Chem. Lett.*, 1 (2010) 467-470.
- [72] K. Yu, G. Lu, Z. Bo, S. Mao, J. Chen, Carbon Nanotube with Chemically Bonded Graphene Leaves for Electronic and Optoelectronic Applications, *J. Phys. Chem. Lett.*, 2 (2011) 1556-1562.
- [73] Z. Xu, Z. Li, C.M.B. Holt, X. Tan, H. Wang, B.S. Amirkhiz, T. Stephenson, D. Mitlin, Electrochemical Supercapacitor Electrodes from Sponge-like Graphene Nanoarchitectures with Ultrahigh Power Density, *J. Phys. Chem. Lett.*, 3 (2012) 2928-2933.

- [74] D. Yu, K. Goh, H. Wang, L. Wei, W. Jiang, Q. Zhang, L. Dai, Y. Chen, Scalable synthesis of hierarchically structured carbon nanotube-graphene fibres for capacitive energy storage, *Nat Nano*, 9 (2014) 555-562.
- [75] Q. Bao, H. Zhang, J.x. Yang, S. Wang, D.Y. Tang, R. Jose, S. Ramakrishna, C.T. Lim, K.P. Loh, Graphene-polymer nanofiber membrane for ultrafast photonics, *Advanced Functional Materials*, 20 (2010) 782-791.
- [76] Q. Cheng, J. Tang, J. Ma, H. Zhang, N. Shinya, L.-C. Qin, Graphene and Carbon Nanotube Composite Electrodes for Supercapacitors with Ultra-High Energy Density, *Phys. Chem. Chem. Phys.*, 13 (2011) 17615-17624.
- [77] L. Qiu, X. Yang, X. Gou, W. Yang, Z.-F. Ma, G.G. Wallace, D. Li, Dispersing Carbon Nanotubes with Graphene Oxide in Water and Synergistic Effects between Graphene Derivatives, *Chem. Europ. J.*, 16 (2010) 10653-10658.
- [78] L. Mao, K. Zhang, H.S. On Chan, J. Wu, Surfactant-stabilized graphene/polyaniline nanofiber composites for high performance supercapacitor electrode, *Journal of Materials Chemistry*, 22 (2012) 80-85.
- [79] G. Ciric-Marjanovic, N.V. Blinova, M. Trchova, J. Stejskal, Chemical oxidative polymerization of safranines, *Journal of Physical Chemistry B*, 111 (2007) 2188-2199.
- [80] Z. Zhang, H. Huang, X. Yang, L. Zang, Tailoring Electronic Properties of Graphene by  $\pi$ - $\pi$  Stacking with Aromatic Molecules, *J. Phys. Chem. Lett.*, 2 (2011) 2897-2905.
- [81] B. Ferrari, R. Moreno, EPD kinetics: A review, *Journal of the European Ceramic Society*, 30 (2010) 1069-1078.
- [82] I. Zhitomirsky, Electrophoretic hydroxyapatite coatings and fibers, *Materials Letters*, 42 (2000) 262-271.
- [83] I. Zhitomirsky, Cathodic Electrodeposition of Ceramic and Organoceramic Materials. Fundamental Aspects, *Adv. Colloid Interface Sci.*, 97 (2002) 277-315.
- [84] G. Ciric-Marjanovic, N.V. Blinova, M. Trchova, J. Stejskal, Chemical Oxidative Polymerization of Safranines, *J. Phys. Chem., B*, 111 (2007) 2188-2199.

- [85] M. Drabik, J. Touskova, J. Hanus, H. Kobayashi, H. Biederman, Properties of Composite Films of Titania Nanofibers and Safranin O Dye, *Synth. Met.*, 160 (2010) 2564-2572.
- [86] S. Gokturk, M. Tuncay, Spectral Studies of Safranin-O in Different Surfactant Solutions, *Spectrochim. Acta A*, 59 (2003) 1857-1866.
- [87] B. Pourabbas, F. Pilati, Polypyrrole grafting onto the surface of pyrrole-modified silica nanoparticles prepared by one-step synthesis, *Synthetic Metals*, 160 (2010) 1442-1448.
- [88] Y. Liu, H. Nan, Q. Cai, H. Li, Fabrication of halloysite@polypyrrole composite particles and polypyrrole nanotubes on halloysite templates, *Journal of Applied Polymer Science*, 125 (2012) E638-E643.
- [89] I. Zhitomirsky, Cathodic electrodeposition of ceramic and organoceramic materials. Fundamental aspects, *Advances in colloid and interface science*, 97 (2002) 279-317.
- [90] A.R. Boccaccini, I. Zhitomirsky, Application of electrophoretic and electrolytic deposition techniques in ceramics processing, *Current Opinion in Solid State and Materials Science*, 6 (2002) 251-260.
- [91] A. Boccaccini, S. Keim, R. Ma, Y. Li, I. Zhitomirsky, Electrophoretic deposition of biomaterials, *Journal of the Royal Society Interface*, 7 (2010) S581-S613.
- [92] Y. Han, M. Shen, X. Lin, B. Ding, L. Zhang, H. Tong, X. Zhang, Ternary phase interfacial polymerization of polypyrrole/MWCNT nanocomposites with core-shell structure, *Synthetic Metals*, 162 (2012) 753-758.
- [93] N.G. Sahoo, Y.C. Jung, H.H. So, J.W. Cho, Polypyrrole coated carbon nanotubes: Synthesis, characterization, and enhanced electrical properties, *Synthetic Metals*, 157 (2007) 374-379.
- [94] M. Hughes, G.Z. Chen, M.S. Shaffer, D.J. Fray, A.H. Windle, Electrochemical capacitance of a nanoporous composite of carbon nanotubes and polypyrrole, *Chemistry of Materials*, 14 (2002) 1610-1613.
- [95] G. Wu, Y. Katsumura, G. Chu, Photolytic and radiolytic studies of SO<sub>4</sub><sup>2-</sup> in neat organic solvents, *Physical Chemistry Chemical Physics*, 2 (2000) 5602-5605.
- [96] W. Chen, G. Xue, Formation of conducting polymer nanostructures with the help of surfactant crystallite templates, *Front. Mater. Sci. China*, 4 (2010) 152-157.

- [97] T. Chen, B. Du, Z. Fan, Organic–Inorganic Hybrid Mesoporous Polymers Fabricated by Using (CTA)<sub>2</sub>S<sub>2</sub>O<sub>8</sub> as Self-Decomposed Soft Templates, *Langmuir*, 28 (2012) 15024-15032.
- [98] Y. Kudoh, Properties of polypyrrole prepared by chemical polymerization using aqueous solution containing Fe<sub>2</sub>(SO<sub>4</sub>)<sub>3</sub> and anionic surfactant, *Synthetic Metals*, 79 (1996) 17-22.
- [99] Y. Zhu, K. Shi, I. Zhitomirsky, Polypyrrole coated carbon nanotubes for supercapacitor devices with enhanced electrochemical performance, *Journal of Power Sources*, 268 (2014) 233-239.
- [100] Y. Zhu, K. Shi, I. Zhitomirsky, Anionic dopant–dispersants for synthesis of polypyrrole coated carbon nanotubes and fabrication of supercapacitor electrodes with high active mass loading, *Journal of Materials Chemistry A*, 2 (2014) 14666-14673.
- [101] X. Zhang, J. Zhang, Z. Liu, C. Robinson, Inorganic/organic mesostructure directed synthesis of wire/ribbon-like polypyrrole nanostructures, *Chem. Commun.*, (2004) 1852-1853.
- [102] X. Hu, H. Bao, P. Wang, S. Jin, Z. Gu, Mechanism of formation of polyaniline flakes with high degree of crystallization using a soft template in the presence of cetyltrimethylammonium bromide, *Polymer International*, 61 (2012) 768-773.
- [103] Y. Wang, C. Yu, Z. Li, D. Zhou, W. Chen, G. Xue, Synthesis of ordered spiral and ring-like polypyrrole nanowires in cetyltrimethylammonium bromide crystalline suspension, *Colloid and Polymer Science*, 287 (2009) 1325-1330.
- [104] G. Wu, Y. Katsumura, G. Chu, Photolytic and radiolytic studies of SO<sub>4</sub><sup>2-</sup> in neat organic solvents, *Physical Chemistry Chemical Physics*, 2 (2000) 5602-5605.
- [105] P. Mohanty, J. Lee, K. Glover, K. Landskron, Discoid Bicelles as Efficient Templates for Pillared Lamellar Periodic Mesoporous Silicas at pH 7 and Ultrafast Reaction Times, *Nanoscale Res Lett*, 6 (2011) 61.
- [106] C. Wu, Laser Light Scattering Determination of the Surfactant Interface Thickness of Spherical Polystyrene Microlatices, *Macromolecules*, 27 (1994) 7099-7102.
- [107] S. De, S. Mandal, Surfactant-assisted shape control of copper nanostructures, *Colloids and Surfaces A: Physicochemical and Engineering Aspects*, 421 (2013) 72-83.
- [108] N.R. Jana, L. Gearheart, C.J. Murphy, Wet chemical synthesis of high aspect ratio cylindrical gold nanorods, *The Journal of Physical Chemistry B*, 105 (2001) 4065-4067.

- [109] N.R. Jana, L. Gearheart, C.J. Murphy, Wet chemical synthesis of silver nanorods and nanowires of controllable aspect ratio Electronic supplementary information (ESI) available: UV-VIS spectra of silver nanorods. See <http://www.rsc.org/suppdata/cc/b1/b100521i>, Chemical Communications, (2001) 617-618.
- [110] P. Sarkar, P.S. Nicholson, Electrophoretic Deposition (EPD): Mechanisms, Kinetics, and Application to Ceramics, Journal of the American Ceramic Society, 79 (1996) 1987-2002.
- [111] J.-Y. Shin, T. Premkumar, K.E. Geckeler, Dispersion of single-walled carbon nanotubes by using surfactants: Are the type and concentration important?, Chemistry - A European Journal, 14 (2008) 6044-6048.
- [112] J. Luo, Z. Duan, H. Li, The influence of surfactants on the processing of multi-walled carbon nanotubes in reinforced cement matrix composites, Physica Status Solidi (a), 206 (2009) 2783-2790.
- [113] C. Guo, Y. Zuo, X. Zhao, J. Zhao, J. Xiong, Effects of surfactants on electrodeposition of nickel-carbon nanotubes composite coatings, Surface and Coatings Technology, 202 (2008) 3385-3390.
- [114] X. Zhang, J. Zhang, R. Wang, Z. Liu, Cationic surfactant directed polyaniline/CNT nanocables: Synthesis, characterization, and enhanced electrical properties, Carbon, 42 (2004) 1455-1461.
- [115] X. Ren, P.G. Pickup, The origin of the discrepancy between the low frequency AC capacitances and voltammetric capacitances of conducting polymers, Journal of Electroanalytical Chemistry, 372 (1994) 289-291.
- [116] J. Tanguy, N. Mermilliod, M. Hoclet, Capacitive Charge and Noncapacitive Charge in Conducting Polymer Electrodes, Journal of The Electrochemical Society, 134 (1987) 795-802.
- [117] B.J. Feldman, P. Burgmayer, R.W. Murray, The potential dependence of electrical conductivity and chemical charge storage of poly(pyrrole) films on electrodes, Journal of the American Chemical Society, 107 (1985) 872-878.
- [118] P.G. Pickup, R.A. Osteryoung, Electrochemical polymerization of pyrrole and electrochemistry of polypyrrole films in ambient temperature molten salts, Journal of the American Chemical Society, 106 (1984) 2294-2299.

## **7. Activated carbon electrodes for energy storage in supercapacitors**

### **7.1 Symmetric supercapacitors fabricated based on activated carbon coated MWCNT**

The use of CNT[1, 2] as an electrode material offers the advantages of high electronic conductivity and good capacitance retention at high charge-discharge rates. However, the specific capacitance of CNT is lower than that of activated carbon. The interest in activated carbon (AC) materials[3-5] is attributed to their high surface area, which allows high specific capacitance. However, the electronic conductivity of activated carbon is lower than that of carbon nanotubes. The problem was addressed by the development of composites[4, 6, 7], containing activated carbon and conductive additives, such as carbon nanotubes and graphene.

Recent investigations showed that capacitive performance of carbon materials can be improved using various dopants, such as N and S[8-10]. It was found that the use of dopants resulted in higher electronic conductivity and capacitance, attributed to the redox reactions[3] of surface functional groups. Impressive progress[11-14] has been made in the development of heteroatom doped carbons with controlled porosity as well as investigation of charge-discharge mechanism. Significant interest has been generated in the use of N-enriched polymers as precursors for fabrication of N-doped carbon materials. The use of N-enriched polymers allows the fabrication of advanced

carbon materials with controlled N content. Polypyrrole and polyaniline are important conductive polymer materials for fabrication of N-doped activated carbons[15-17]. Investigations were focused on development of doped carbon nanotubes, nanowires and nanosheets using polymer precursors[18-21].

In section 6.4, the well dispersed PPy coated MWCNT was prepared by  $(CTA)_2S_2O_8$  nano-crystals. This new approach paves the way for the fabrication of nitrogen doped activated carbon coated MWCNT (N-AC-MWCNT) with high surface area for the application in efficient ES devices.

#### 7.1.1 Characterization of N-AC-MWCNT

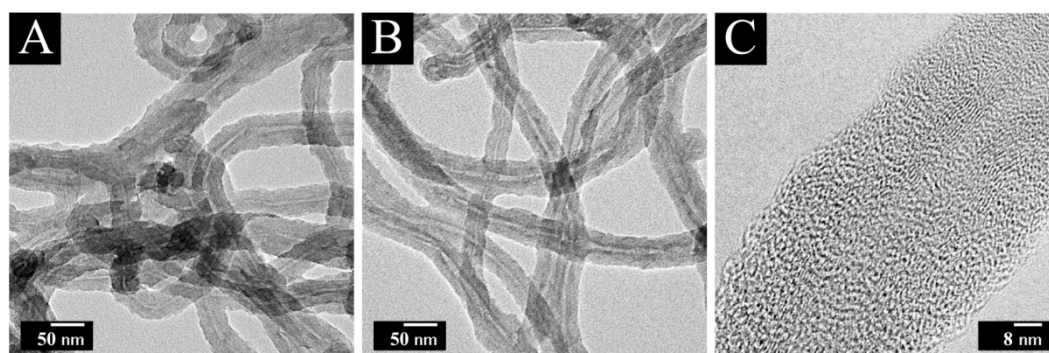


Figure 7.1 (A,B) TEM and (C) HRTEM images for (A) PPy-MWCNT and (B,C) N-AC-MWCNT.

PPy coated MWCNT was synthesized using multi-functional  $(CTA)_2S_2O_8$  nano-crystals, which are dispersants for MWCNT and oxidants for Py. The use of non-agglomerated MWCNT, uniformly coated with PPy, allowed the fabrication of non-agglomerated N-AC-MWCNT through carbonization and chemical activation.

The chemical activation was carried out using KOH at 700 °C for 2 h (section 4.2.3.1). In comparison with N-AC-MWCNT, N-doped carbon-coated MWCNT (N-C-MWCNT) was prepared without KOH activation using a similar procedure. The morphology of PPy-MWCNT and N-AC-MWCNT were showed in Fig. 7.1A and B. The analysis of HRTEM images (Fig. 7.1C) showed the amorphous and disordered characteristics of AC coating, with a thickness in the range of 12-15 nm.

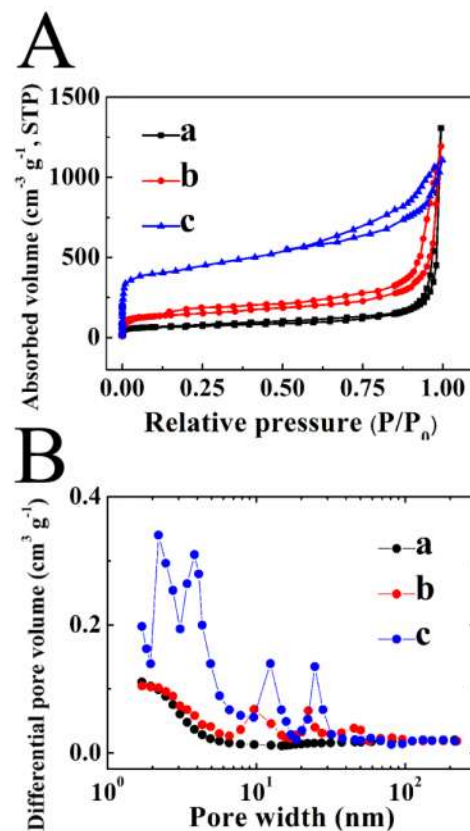


Figure 7.2. (A) Nitrogen adsorption-desorption isotherms at -196 °C and (B) corresponding pore-size distributions calculated with the Barrett-Joyner-Halenda (BJH) method for (a) pristine MWCNT, (b) N-C-MWCNT and (c) N-AC-MWCNT.

The nitrogen adsorption-desorption isotherms and corresponding pore-size distribution curves of pristine MWCNT, N-C-MWCNT and N-AC-MWCNT are shown in Fig. 7.2. The pristine MWCNT showed an intermediate adsorption curve between types II and IV (in the IUPAC classification) with a small hysteresis loop extending from  $P/P_0 = 0.82$  to  $0.99$ . For N-C-MWCNT, there is an increase of  $N_2$  adsorption at high partial pressures indicating increase of pores volume and the hysteresis is also more pronounced than in the pristine tubes. After the chemical activation, the N-AC-MWCNT showed close to type IV dependence with steep uptakes below  $P/P_0 = 0.01$  and clear hysteresis loops, which indicated the coexistence of micropores ( $<2$  nm) and mesopores (2~50 nm) in the coating (Fig 7.2B). The textural parameters of these porous carbons are listed in Table 7.1. The higher  $N_2$  adsorption capacities imply higher surface areas and pore volumes. It was found that specific surface area increased in the order 325.5 (MWCNT), 489.4 (N-C-MWCNT) and 1889.1  $m^2 g^{-1}$  (N-AC-MWCNT). The average pore diameter changed in the order of 5.32 (MWCNT), 6.23(N-C-MWCNT), and 3.78 nm (N-AC-MWCNT). The high specific surface area, large porosity volume and hierarchical porous characteristics of N-AC-MWCNT can provide a sufficient electrode-electrolyte interface for accumulation of ions.

Table 7.1 BET surface area, total porosity volume ( $V_{total}$ ), microporosity (diameter $<2$ nm) volume ( $V_{micro}$ ), average pore diameter and density of investigated materials.

---

---

|                | BET surface area               | $V_{\text{total}}$              | $V_{\text{micro}}$              | Average Pore  | Density                |
|----------------|--------------------------------|---------------------------------|---------------------------------|---------------|------------------------|
|                | ( $\text{m}^2 \text{g}^{-1}$ ) | ( $\text{cm}^3 \text{g}^{-1}$ ) | ( $\text{cm}^3 \text{g}^{-1}$ ) | diameter (nm) | ( $\text{g cm}^{-3}$ ) |
| Pristine MWCNT | 325.48                         | 0.24                            | 0.09                            | 5.32          | 0.72                   |
| N-C MWCNT      | 489.39                         | 0.37                            | 0.11                            | 6.23          | 0.68                   |
| N-AC-MWCNT     | 1889.12                        | 1.72                            | 0.61                            | 3.78          | 0.24                   |

---

The XPS survey spectra of MWCNT and N-AC-MWCNT are shown in Fig. 7.3A. The spectrum of N-AC-MWCNT revealed N1s peak. Weak S1s peak in the spectrum of N-AC-MWCNT was observed due to the use of S-containing PS dye as an anionic dopant for PPy polymerization. The XPS results on chemical composition indicated that the oxygen, nitrogen and sulfur contents in N-AC-MWCNT were 7.89, 6.71 and 2.28 wt%, respectively. The high-resolution N1s spectrum (Fig. 7.3B) can be deconvoluted into three peaks located at 400.9, 399.8 and 398.2 eV, which are attributed to quaternary (N-Q), pyrrolic (N-5), and pyridinic nitrogen (N-6) groups, respectively[22]. It is known that N-Q and N-6 groups have a stronger donor electron character and thus improve electron transfer in supercapacitor electrodes at high current loads[23]. In addition N-Q, and N-5 nitrogens located at the edges of graphene layers enhanced the pseudo-capacitance effect, wettability and hydrophilicity of the electrode[11].

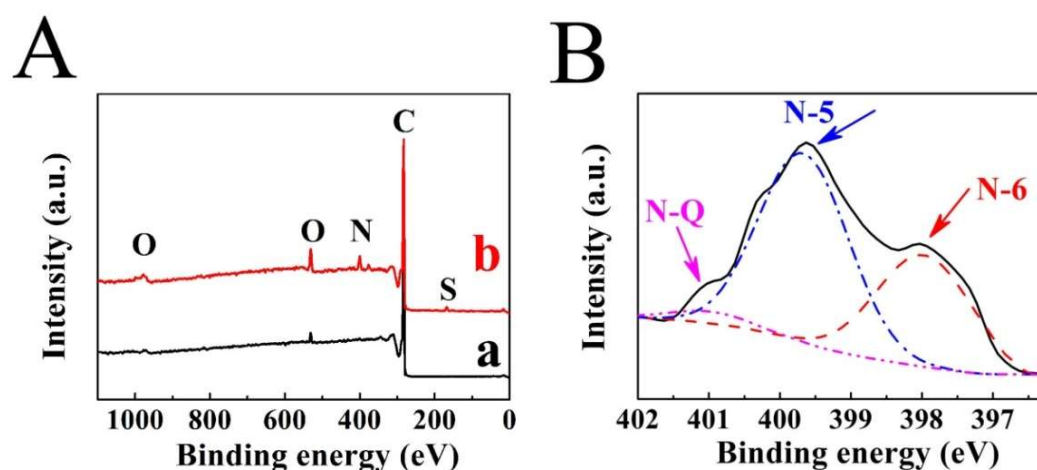


Figure 7.3 (A) Survey XPS spectra for (a) pristine MWCNT and (b) N-AC-MWCNT, (B) High-resolution XPS spectra for N1s of N-AC-MWCNT, showing contributions of nitrogen containing functional groups: N5 (pyrrole), N6 (pyridine) and N-Q (quaternary).

Raman spectroscopy was used to investigate the degrees of graphitization of N-AC-MWCNT. The Raman spectrum (Fig. 7.4) shows the D-band peak at  $\sim 1330\text{ cm}^{-1}$  and G-band at  $\sim 1520\text{ cm}^{-1}$ . The peak at  $\sim 1330\text{ cm}^{-1}$  (D-band) corresponds to the defects and edge planes. The peak at  $\sim 1520\text{ cm}^{-1}$  (G-band) can be attributed to the stretching vibration of any pair of  $sp^2$  sites inside of the graphitic pattern[6]. The N-AC-MWCNT (Fig. 7.4b) exhibited very weak G-band peak, compared to pristine MWCNT (Fig. 7.4a). It indicated a low degree of graphitization and a significant amount of disordered sections of N-AC-MWCNT, which was consisted with HRTEM results shown in Fig. 7.1C.

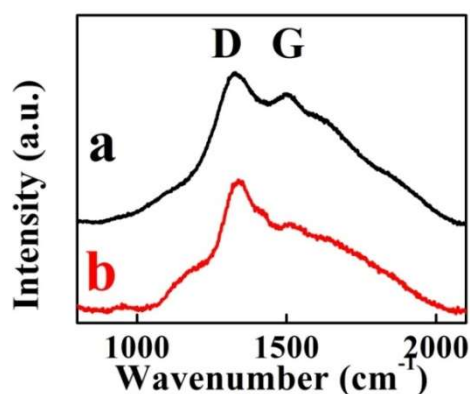


Figure 7.4 Raman spectrum of (a) pristine MWCNT and (b) N-AC-MWCNT.

### 7.1.2 Capacitive performance of the N-AC-MWCNT electrodes

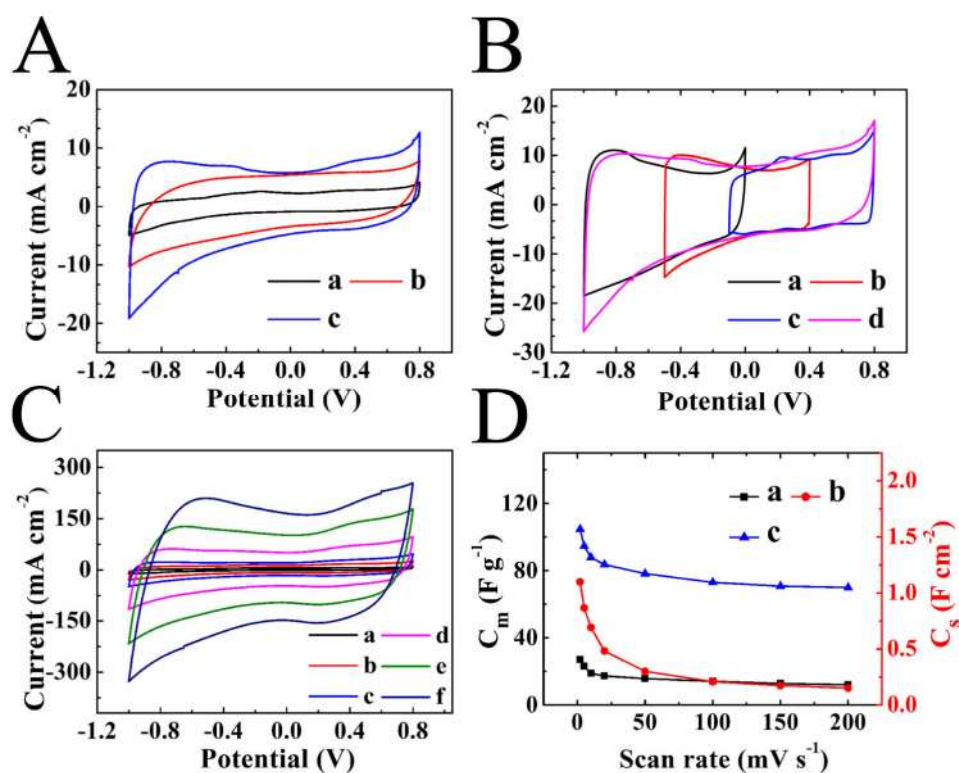


Figure 7.5 (A) CVs at a scan rate of  $5 \text{ mV s}^{-1}$  for (a) pristine MWCNT, (b) N-C-MWCNT and (c) N-AC-MWCNT. (B) CVs for N-AC-MWCNT in voltage windows of (a)  $-1 - 0 \text{ V}$ , (b)  $-0.5 - +0.4 \text{ V}$ , (c)  $-0.1 - +0.8 \text{ V}$  and (d)  $-1 - +0.8$  at a scan

rate of  $5 \text{ mV s}^{-1}$ . (C) CVs for N-AC-MWCNT at scan rates of (a) 2, (b) 10, (c) 20, (d) 50, (e) 100, (f)  $200 \text{ mV s}^{-1}$ . (D)  $C_m$  and  $C_s$  versus scan rate for (a) pristine MWCNT, (b) N-C-MWCNT and (c) N-AC-MWCNT. All electrodes have mass loading of  $15 \text{ mg cm}^{-2}$ .

Recent investigations were focused on developing high energy and power ES with environmentally friendly, cost-effective and safe components. The enhancement of energy storage of ES cells can be essentially realized by improving voltage using electrolytes with a large stability potential range. Here, the capacitive performance of obtained materials was evaluated in aqueous  $0.5 \text{ M Na}_2\text{SO}_4$  electrolyte in different voltage windows. Fig. 7.5A compares CVs for pristine MWCNT, N-C-MWCNT and N-AC-MWCNT electrodes in a three electrode cell. The electrodes showed nearly box shape CVs in aqueous  $0.5 \text{ M Na}_2\text{SO}_4$  electrolyte in a voltage window of  $-1.0 - +0.8 \text{ V}$  versus SCE. It is important to note that cell voltage in aqueous electrolytes is usually limited by potential window of water decomposition ( $1.2\text{V}$ )[24]. However, voltage window of  $1.7\text{-}1.8 \text{ V}$  in aqueous  $\text{Na}_2\text{SO}_4$  electrolytes was reported for single activated carbon electrodes[24, 25]. It is known that the enlarged voltage window of porous carbon in neutral  $\text{Na}_2\text{SO}_4$  electrolyte is attributed to the high over-potential for di-hydrogen evolution[26-28]. The box shape CVs obtained in different voltage windows (Fig. 7.5B) indicated a possibility of the fabrication of a supercapacitor device, containing two N-AC-MWCNT electrodes. The increase in the scan rate resulted in increasing current (Fig. 7.5C), indicating good capacitive behavior in a

voltage window of 1.8 V. Fig. 7.5D compares capacitance versus scan rate dependencies for MWCNT, N-C-MWCNT and N-AC-MWCNT electrodes with active mass loading of 15 mg cm<sup>-2</sup>. The N-AC-MWCNT electrodes showed significantly higher capacitance compared to MWCNT and N-C-MWCNT electrodes (Fig. 7.5). The difference was especially evident (Fig. 7.5D) at scan rates above 50 mV s<sup>-1</sup>, where N-AC-MWCNT electrodes showed significant improvement in capacitance retention. The N-AC-MWCNT electrodes showed C<sub>m</sub> of 105.4 and 70.5 F g<sup>-1</sup> and at scan rates of 2 and 200 mV s<sup>-1</sup>, respectively.

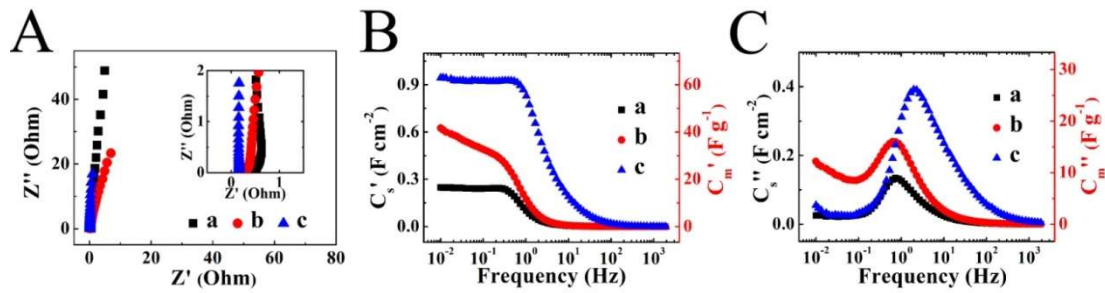


Figure 7.6 (A) Nyquist plot of complex impedance, inset shows high frequency range, (B) C<sub>s</sub>' and C<sub>m</sub>' and (C) C<sub>s</sub>'' and C<sub>m</sub>'' calculated from the impedance data versus frequency for (a) pristine MWCNT, (b) N-C-MWCNT and c) N-AC-MWCNT. All electrodes have mass loading of 15 mg cm<sup>-2</sup>.

Fig. 7.6 compares impedance spectroscopy data for MWCNT, N-C-MWCNT and N-AC-MWCNT electrodes with active mass loading of 15 mg cm<sup>-2</sup>. The experimental data presented in the Nyquist plot (Fig. 7.6A) showed relatively low resistance R=Z'. The large slope of the Z'' versus Z' curves indicated good capacitive behavior. The

analysis of capacitive behavior (Fig. 7.6B and C) showed higher capacitance of N-AC-MWCNT compared to that of MWCNT and N-C-MWCNT. It was found that  $C'$  of N-AC-MWCNT was practically frequency independent below 0.7 Hz (Fig. 7.6B). At higher frequencies a relaxation type of dispersion[29, 30] was observed, as indicated by rapid decrease in  $C'$  with frequency in the range of 0.7 – 190 Hz (Fig. 7.6B) and corresponding maximum in the frequency dependence of  $C''$  at 2.1 Hz (Fig. 7.6C). The N-AC-MWCNT showed relaxation type frequency dispersion of capacitance at much higher frequencies, compared to MWCNT and N-C-MWCNT. This indicates improved capacitance retention in frequency response, which was in agreement with the results of cyclic voltammetry (Fig. 7.5). The improved capacitance behavior of N-AC-MWCNT can be attributed to larger surface area (Fig. 7.2) and better wetting of AC coating by the electrolyte. It is known that wettability is an important factor, controlling electrochemical performance of carbon electrodes[31, 32], which allows higher capacitance values.

The analysis of cyclic stability of individual electrodes in the voltage window of 1.8 V showed that capacitance retention was about 98.0 % after 1000 cycles (Fig. 7.7A). The analysis of CVs and impedance spectroscopy data did not show significant changes in the CV shape and impedance during cycling (Fig. 7.7B). The frequency dependence of AC capacitance remained practically unchanged during cycling (Fig. 7.7C and D).

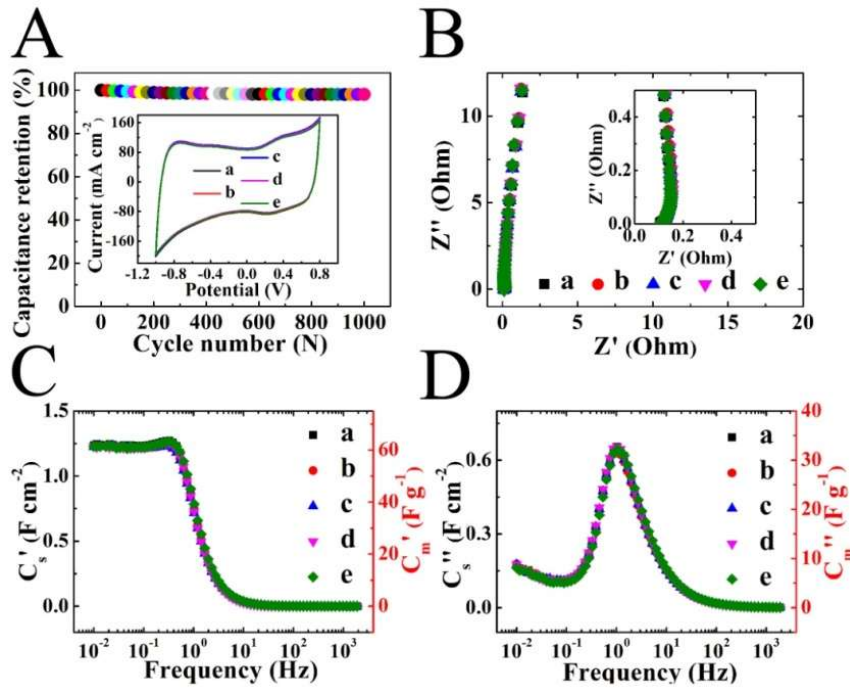


Figure 7.7 (A) Capacitance retention versus cycle number, inset shows corresponding CVs at  $100 \text{ mV s}^{-1}$ , (B) Nyquist plot of complex impedance, inset shows high frequency range, (C)  $C_s'$  and  $C_m'$  and (D)  $C_s''$  and  $C_m''$  versus frequency after (a)1<sup>st</sup>, (b)250<sup>th</sup>, (c) 500<sup>th</sup>, (d)750<sup>th</sup>, (e)1000<sup>th</sup> cycles for  $20 \text{ mg cm}^{-2}$  electrodes, prepared from N-AC-MWCNT.

### 7.1.3 Capacitive performance of the symmetric ES cell

The individual N-AC-MWCNT electrodes were combined for the fabrication of two-electrode ES cells. Fig. 7.8(A and B) compares the CV and charge-discharge data for ES cells in different voltage windows. The CV shapes deviated significantly from the ideal box shape for cell voltages above 1.8 V (Fig. 7.8A). The corresponding charge-discharge curves become essentially non-linear above 1.8 V (Fig. 7.8B). The capacitance  $C_{cm}$  increased with increasing cell voltage and showed a maximum at 1.9

V (Fig. 7.8C). The Coulombic efficiency showed very small changes at cell voltages in the range of 1.4-1.8 V and decreased significantly for higher cell voltages. The decrease in the Coulombic efficiency was attributed to electrochemical decomposition of water. Therefore, the cell voltage of 1.8 V was chosen for further investigation of the electrochemical performance of the ES device.

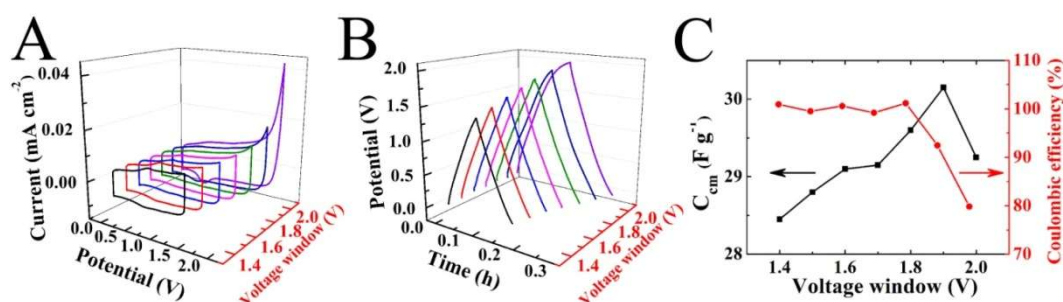


Figure 7.8 Capacitive behavior for a symmetric ES cell, containing two N-AC-MWCNT electrodes: (A) CVs at scan rate of  $5 \text{ mV s}^{-1}$  for different potential windows, (B) charge-discharge curves at a current of  $4 \text{ mA cm}^{-2}$  for different potential windows, (C)  $C_{\text{cm}}$  calculated from charge-discharge curves and Coulombic efficiency versus width of the potential window. The mass loading of individual electrodes is  $15 \text{ mg cm}^{-2}$ .

Fig. 7.9 shows cell testing results for the optimized voltage window of 1.8 V. The cell capacitances  $C_{\text{cm}}$  and  $C_{\text{cs}}$ , calculated from the CV data (Fig. 7.9A) decreased from 50.9 to  $25.9 \text{ F g}^{-1}$  and from 1.54 to  $0.77 \text{ F cm}^{-2}$  (Fig.7.9B), respectively, with increasing scan rate from 2 to  $100 \text{ mV s}^{-1}$ . The cell capacitances,  $C_{\text{cm}}$  and  $C_{\text{cs}}$ , calculated from the charge-discharge data (Fig. 7.9C) decreased from 36.6 to  $27.6 \text{ F}$

$\text{g}^{-1}$  and 1.0 to  $0.76 \text{ F cm}^{-2}$  (Fig. 7.9D), respectively, with increasing current from 1 to  $10 \text{ mA cm}^{-2}$ .

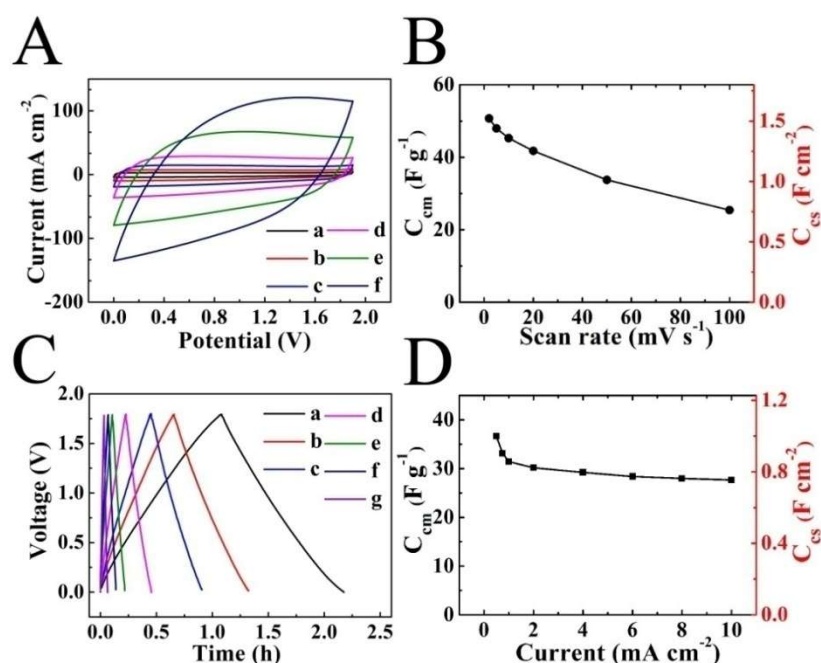


Figure 7.9 Capacitive behaviour of a symmetric ES cell, containing two N-AC-MWCNT electrodes: (A) CVs at scan rates of (a) 2, (b) 5, (c) 10, (d) 20, (e) 50 and (f)  $100 \text{ mV s}^{-1}$ . (B)  $C_{\text{cm}}$  and  $C_{\text{cs}}$  calculated from CVs versus scan rate. (C) charge-discharge curves at currents of (a) 0.5, (b) 0.75, (c) 1, (d) 2, (e) 4, (f) 6 and (g)  $10 \text{ mA cm}^{-2}$ . (D)  $C_{\text{cm}}$  and  $C_{\text{cs}}$  calculated from the charge-discharge curves versus current. The mass loading of individual electrodes is  $15 \text{ mg cm}^{-2}$ .

In Fig. 7.10A, the Ragone plot presented indicates that energy density of  $16.1 \text{ mWh g}^{-1}$  and power density of  $14.4 \text{ W g}^{-1}$  were obtained. The insets in the Fig. 7.10A show coin cells and LED bulbs powered by the coin cells. The analysis of cycling behavior of the cells showed 8.1% decrease in the capacitance after 1000 cycles, then relatively

small decrease in the capacitance was observed (Fig.7.10B). The capacitance retention after 5000 cycles was 89.5%. The charge-discharge curves maintained linear shape during the cycle tests, indicated that the fabricated symmetric cells were stable at voltage of 1.8 V (Fig. 7.10B, inset). Although a high capacitance and energy density could be obtained using the ionic liquids as the electrolyte, the natural aqueous electrolyte in this study offer advantages of lower price and environment friendliness. The high-performance symmetric ES with a high voltage of 1.8 V could be obtained using the N-AC-MWCNT as the electrodes and the neutral  $\text{Na}_2\text{SO}_4$  aqueous solution as the electrolyte.

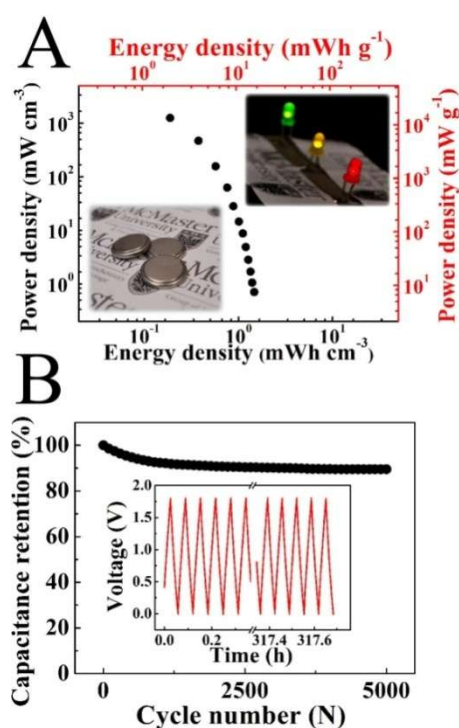


Figure 7.10 (A) Ragone plot for a coin cell, containing two activated carbon coated MWCNT electrodes, insets show the coin cells and the light emitting diodes powered

by coin cells. (B) Capacitance retention of a coin cell versus cycle number, inset shows the initial and final charge-discharge curves in the cycle performance test.

#### 7.1.4 Conclusions

The non-agglomerated N-AC-MWCNT materials with high surface area has been developed for the ES electrode applications. The electrochemical tests indicated that the highest capacitance of  $3.6 \text{ F cm}^{-2}$  was achieved in a voltage window of 1.8 V using aqueous  $\text{Na}_2\text{SO}_4$  electrolyte. The ES cells, based on N-AC-MWCNT electrodes, exhibited excellent performance with energy density of  $16.1 \text{ mWh g}^{-1}$  and power density of  $14.4 \text{ W g}^{-1}$  in a voltage window of 1.8 V. The individual electrodes and ES cells showed good capacitance retention at high charge-discharge rates and good cycling stability.

#### **7.2 Asymmetric supercapacitor fabricated by activated carbon coated MWCNT**

$\text{MnO}_2$ -AC asymmetric ESs are currently under intensive investigation for advanced energy storage applications[33]. The interest in  $\text{MnO}_2$  for positive ES electrodes is attributed to high specific capacitance[34, 35] of  $\text{MnO}_2$ . The use of asymmetric ES, containing positive  $\text{MnO}_2$  and negative AC electrodes offers the advantage of increased voltage window in aqueous electrolytes[36, 37].

Recent investigations[38-42] were focused on the morphology and microstructure control in order to improve the electrochemical performance of  $\text{MnO}_2$  electrodes. However, the electronic conductivity of  $\text{MnO}_2$  is low. This problem was addressed by

the fabrication of MnO<sub>2</sub>-carbon nanotube (CNT) composites[43, 44]. In order to improve the electrical contact of CNT and MnO<sub>2</sub>, MnO<sub>2</sub> coated CNT was prepared by reduction of Mn<sup>7+</sup> species in KMnO<sub>4</sub> solutions, containing CNT suspension [45-47].



This method allowed the fabrication of flexible ES devices[48]; however, the method generates problems related to carbon consumption in the redox reaction and collapse of carbon bonding structure of CNT [43], that degrade the electrical conductivity. In order to reduce the chemical degradation of CNT, cathodic electrosynthesis of MnO<sub>2</sub> was performed from KMnO<sub>4</sub> solutions on CNT coated substrates, prepared by a chemical vapour deposition technique[49]. However, relatively low MnO<sub>2</sub> mass loading was achieved[49].

The goal of this investigation was to fabricate asymmetric device, containing MnO<sub>2</sub> coated N-AC-MWCNT positive electrode and N-AC-MWCNT negative electrode. In this strategy, the problems related to the degradation of MWCNT during MnO<sub>2</sub>-MWCNT composite synthesis (eq. 7.1) can be avoided using AC coating as a sacrificial layer. The experimental results presented below indicated that MnO<sub>2</sub> coated N-AC-MWCNT composites can be obtained with relatively large MnO<sub>2</sub> content and reduced MnO<sub>2</sub> particle size.

7.2.1 Fabrication of  $\text{MnO}_2$  coated N-AC-MWCNT and asymmetric ES cells

Fig.7.11A shows different steps in the fabrication of N-AC-MWCNT (section 4.2.3.1) and  $\text{MnO}_2$  coated N-AC-MWCNT (section 4.2.3.2). The  $\text{MnO}_2$  coated N-AC-MWCNT was synthesized by the chemical reaction between  $\text{KMnO}_4$  and N-AC-MWCNT (eq. 7.1). AC coating of N-AC-MWCNT allows to protect MWCNT from oxidation. Asymmetric ES device was fabricated based on N-AC-MWCNT as a negative electrode and  $\text{MnO}_2$  coated N-AC-MWCNT as a positive electrode (Fig.7.11B).

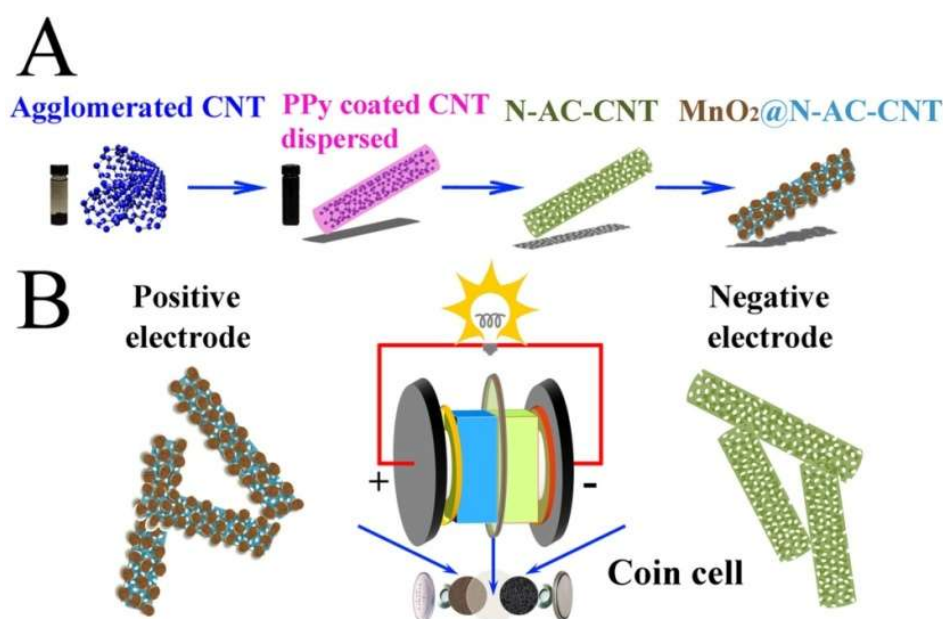


Figure 7.11 Fabrication of (A)  $\text{MnO}_2$  coated N-AC-MWCNT: dispersion of CNT, fabrication of PPy coating, formation of N-AC coated CNT and synthesis of  $\text{MnO}_2$  coating and (B) coin-cell ES, containing  $\text{MnO}_2$  coated N-AC-MWCNT positive electrode and N-AC-MWCNT negative electrode.

## 7.2.2 Materials characterization

Fig. 7.12 shows SEM and TEM images of the N-AC-MWCNT powder. The electron microscopy data indicated that nitrogen doped activated carbon (N-AC) formed relatively uniform coatings on MWCNT (Fig. 7.12A and B). The high magnification TEM image showed that the thickness of the coating was about 10 nm (Fig. 7.12C). The reaction of the N-AC-MWCNT powder with  $\text{KMnO}_4$  solutions was used for the formation of  $\text{MnO}_2$  coatings on the N-AC-MWCNT surface.

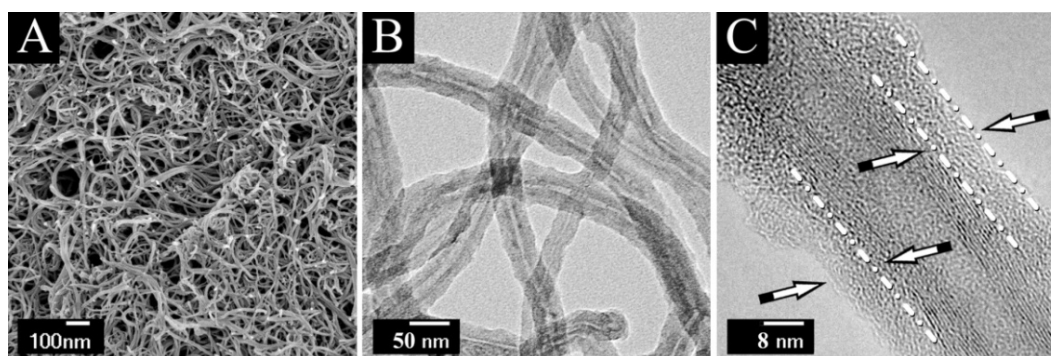


Figure 7.12 (A) SEM, (B) TEM and (C) HRTEM images of N-AC-MWCNT. Arrows in C show thickness of N-AC layer on MWCNT.

Electron microscopy studies (Fig. 7.13) showed that the powders, prepared using solutions 1-3, contained flaky  $\text{MnO}_2$  nano-particles, attached to N-AC-MWCNT. However, the TEM images of the powders, prepared using solution 1, revealed many partially uncoated N-AC-MWCNT. The powders, prepared using solutions 2 and 3 with higher  $\text{KMnO}_4$  concentrations, contained only  $\text{MnO}_2$  coated N-AC-MWCNT due to larger  $\text{MnO}_2$  content in the composite. The analysis of the TEM images for the

powders, prepared using solutions 2 and 3, indicated that the increase in the  $\text{KMnO}_4$  concentration resulted in increasing number of the flaky  $\text{MnO}_2$  particles, which formed bridges between the N-AC-MWCNT fibers. The TEM images (Fig. 7.13C, E and I) at high magnification of  $\text{MnO}_2$  coated N-AC-MWCNT revealed small crystals of  $\text{MnO}_2$ .

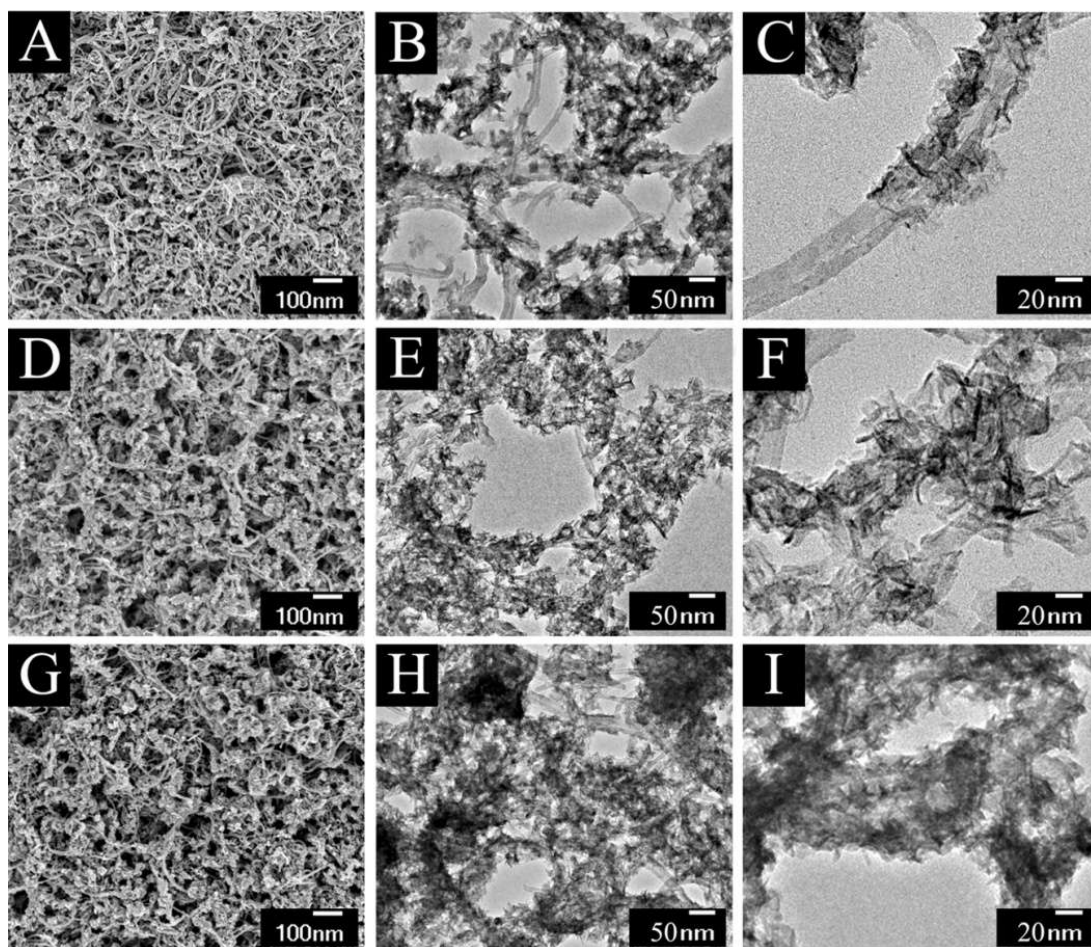


Figure 7.13 Electron microscopy images for  $\text{MnO}_2$  coated N-AC-MWCNT, prepared using (A,B,C) solution 1, (D,E,F) solution 2 and (G,H,I) solution 3 (experiments were described in section 4.2.3.2); (A, D, G) SEM and (B, C, E, F, H, I) TEM images at different magnifications.

The formation of  $\text{MnO}_2$  was also confirmed by the results of TGA/DTA analysis (Fig. 7.14). The TGA analysis (Fig. 7.14a) showed mass loss below  $300^\circ\text{C}$ , which can mainly be attributed to dehydration. The corresponding DTA curve showed (Fig. 7.14b) a broad endothermic minimum at  $100^\circ\text{C}$ , related to the dehydration process. A step in mass loss was observed in the TGA data in the range of  $300\text{--}400^\circ\text{C}$  (Fig. 7.14a); the DTA data showed a corresponding exothermic peak at  $370^\circ\text{C}$  (Fig. 7.14b). The sample mass gradually decreased in the temperature range  $400\text{--}900^\circ\text{C}$ . The reduction in sample mass in the range of  $300\text{--}900^\circ\text{C}$  and the exothermic effect are related to burning out of N-AC-MWCNT. The sample mass of 41% of the initial mass at  $900^\circ\text{C}$  is mainly attributed to  $\text{MnO}_2$ . An additional step in TGA data (Fig. 7.14a) was observed in the range of  $900\text{--}950^\circ\text{C}$ , which corresponded to  $\text{MnO}_2\text{--Mn}_3\text{O}_4$  transformation[50, 51].

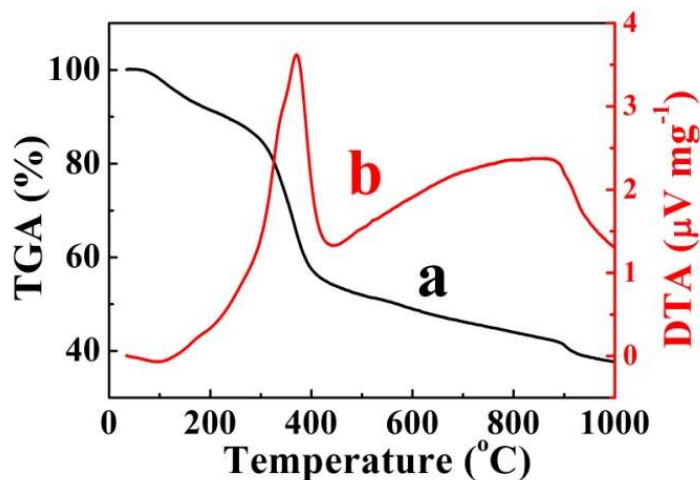


Figure 7.14 (a) TGA and (b) DTA data of  $\text{MnO}_2$  coated N-AC-MWCNT, prepared using solution 2.

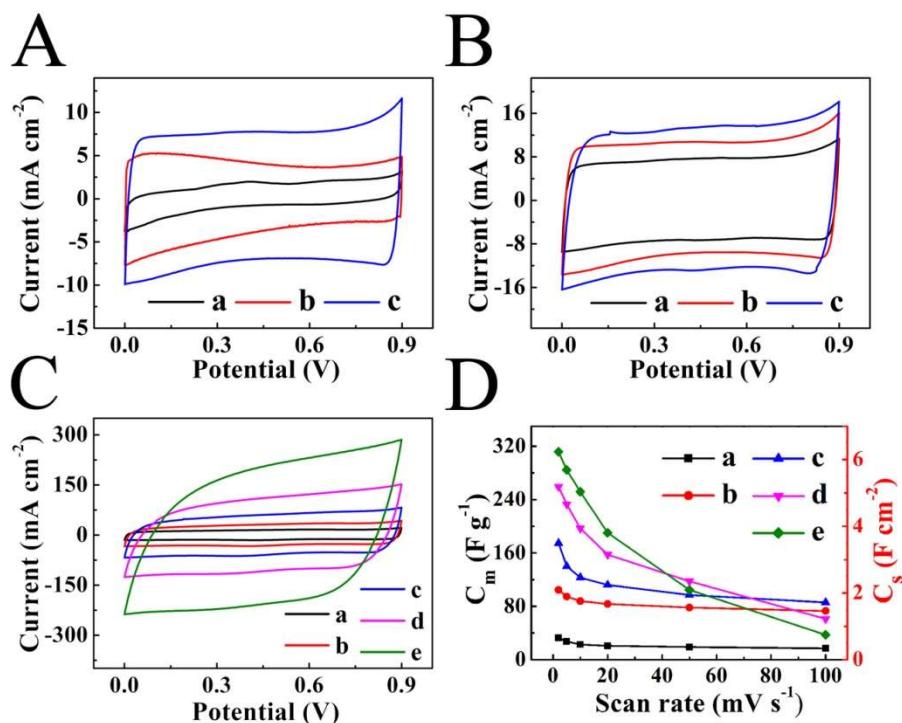
7.2.3 Capacitive performance of the MnO<sub>2</sub> coated N-AC-MWCNT electrodes

Figure 7.15 (A) CVs at a scan rate of  $2 \text{ mV s}^{-1}$  for (a) pristine MWCNT, (b) N-AC-MWCNT and (c) MnO<sub>2</sub> coated N-AC-MWCNT, prepared using solution 1; (B) CVs at  $2 \text{ mV s}^{-1}$  for MnO<sub>2</sub> coated N-AC-MWCNT, prepared using (a) solution 1, (b) solution 2 and (c) solution 3; (C) CVs for MnO<sub>2</sub> coated N-AC-MWCNT, prepared from solution 1 at scan rates of (a) 5, (b) 10, (c) 20, (d) 50 and (e)  $100 \text{ mV s}^{-1}$ ; (D)  $C_m$  and  $C_s$  versus scan rate for (a) pristine MWCNT, (b) N-AC-MWCNT and (c-e) MnO<sub>2</sub> coated N-AC-MWCNT, prepared using (c) solution 1, (d) solution 2 and (e) solution 3. All electrodes have mass loading of  $20 \text{ mg cm}^{-2}$ .

The N-AC-MWCNT and MnO<sub>2</sub> coated N-AC-MWCNT materials were used for the fabrication of ES electrodes. Fig. 7.15A compares CVs for MWCNT,

N-AC-MWCNT and MnO<sub>2</sub> coated N-AC-MWCNT in the potential window of 0-0.9 V at a scan rate of 2 mV s<sup>-1</sup>. The area of the CVs increased in the order MWCNT < N-AC-MWCNT < MnO<sub>2</sub> coated N-AC-MWCNT, indicating improved capacitive behavior. It is important to note that the capacitance of MWCNT and N-AC-MWCNT is related to the double layer charge storage mechanism. Therefore, the large surface area of N-AC-MWCNT allowed higher capacitance. The charge storage mechanism of MnO<sub>2</sub> is related to pseudocapacitance, which is higher than the double layer capacitance. Therefore, the higher capacitance of MnO<sub>2</sub> coated N-AC-MWCNT was attributed to the contribution of the surface MnO<sub>2</sub> layer. The comparison of CVs at a scan rate of 2 mV s<sup>-1</sup> for the materials, prepared using solutions 1-3, showed higher CV area for the material prepared using solution 3 (Fig. 7.15B) due to larger content of MnO<sub>2</sub> in this material. The MnO<sub>2</sub> coated N-AC-MWCNT electrodes showed nearly box shape CVs at scan rates of 5-100 mV s<sup>-1</sup> (Fig. 7.15C). In contrast, previous investigations[52] of MnO<sub>2</sub>-MWCNT composites, prepared by a different method, showed poor capacitance retention for scan rates above 20 mV s<sup>-1</sup>.

The specific capacitances of the electrodes, calculated from the CV data at different scan rates, are compared in Fig. 7.15D. The specific capacitances of MWCNT and N-AC-MWCNT at a scan rate of 2 mV s<sup>-1</sup> were found to be 32.6 F g<sup>-1</sup> (0.68 F cm<sup>-2</sup>) and 104.7 F g<sup>-1</sup> (2.10 F cm<sup>-2</sup>), respectively. The N-AC-MWCNT electrodes showed the capacitance retention of 69.8% at a scan rate of 100 mV s<sup>-1</sup>, whereas the capacitance retention of MWCNT was 52%. The MnO<sub>2</sub> coated N-AC-MWCNT

electrodes, prepared using solutions 1,2 and 3 showed capacitances of  $174.8 \text{ F g}^{-1}$  ( $3.53 \text{ F cm}^{-2}$ ),  $259.3 \text{ F g}^{-1}$ , ( $5.21 \text{ F cm}^{-2}$ ) and  $311.7 \text{ F g}^{-1}$  ( $6.29 \text{ F cm}^{-2}$ ) and capacitance retention of 49.0%, 23.6% and 12.0 % at a scan rate of at  $100 \text{ mV s}^{-1}$ , respectively. The  $\text{MnO}_2$  coated N-AC-MWCNT, prepared using solutions 2 and 3, showed remarkably high capacitances at  $2 \text{ mV s}^{-1}$  for high mass loadings. It is known that the capacitance of  $\text{MnO}_2$  and composite  $\text{MnO}_2$ -CNT electrodes decreases drastically with increasing mass loading[53] due to low conductivity of  $\text{MnO}_2$ . The specific capacitances of  $400\text{-}700 \text{ F g}^{-1}$ , achieved for thin films[54, 55] with mass loadings of  $4\text{-}75 \mu\text{g cm}^{-2}$  are significantly lower than the theoretical capacitance value[56] of  $1370 \text{ F g}^{-1}$  for  $\text{MnO}_2$ . The use of CNT as a conductive additive allows improved capacitance, especially at higher mass loadings. The capacitance of composite  $\text{MnO}_2$ -CNT electrodes[53, 57, 58] with mass loadings of  $0.2\text{-}2 \text{ mg cm}^{-2}$  is typically about  $150\text{-}200 \text{ F g}^{-1}$ . However, significantly higher mass loadings of  $\sim 10 \text{ mg cm}^{-2}$  are necessary for practical applications of  $\text{MnO}_2$ -CNT composites in electrodes of electrochemical supercapacitors[59]. It has been demonstrated that the specific capacitance calculated by the mass normalization cannot provide realistic information about the materials performance, especially at high materials loading [59]. A specific capacitance of  $0.81 \text{ F cm}^{-2}$  was reported[60] for  $\text{MnO}_2$ -CNT electrodes with mass loading of  $11 \text{ mg cm}^{-2}$ . In another investigation[44], the specific capacitance of  $5.9 \text{ F cm}^{-2}$  ( $148 \text{ F g}^{-1}$ ) was achieved for active mass loading of  $40 \text{ mg cm}^{-2}$  using efficient dispersant for  $\text{MnO}_2$  nanoparticles and MWCNT. However, the electrodes showed

poor capacitance retention at high scan rates[44]. The results of MnO<sub>2</sub> coated MWCNT prepared using N-AC-MWCNT, showed that high area normalized capacitance, comparable with the capacitance reported in the previous investigation[44], can be achieved at mass loadings of only 20 mg cm<sup>-2</sup> due to higher mass normalized capacitance of composite materials. Therefore, the electrodes, developed in this investigation are promising for the fabrication of ES devices with significantly reduced mass and enhanced energy density and power density.

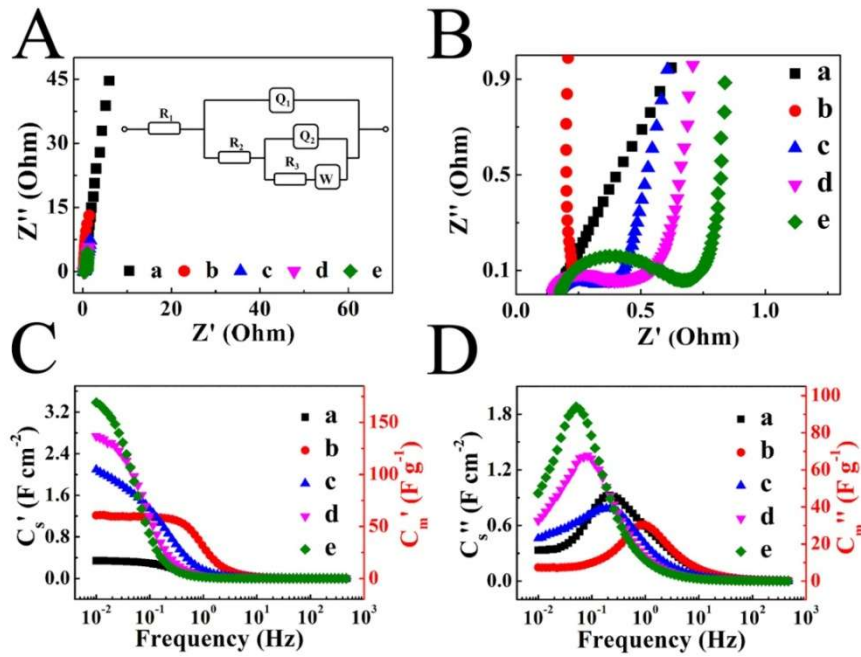


Figure 7.16 (A,B) Nyquist plot of complex impedance, (B) shows high frequency range for (A), inset in (A) shows equivalent circuit, (C)  $C_s'$  and  $C_m'$  and (D)  $C_s''$  and  $C_m''$ , calculated from the impedance data, versus frequency for (a) pristine MWCNT, (b) N-AC-MWCNT and (c-e) MnO<sub>2</sub> coated N-AC-MWCNT, prepared using (c)

solution 1, (d) solution 2 and (e) solution 3. All electrodes have mass loading of 20 mg cm<sup>-2</sup>.

The analysis of the impedance data (Fig. 7.16) indicated relatively low resistance  $R=Z'$  of the electrodes. The slopes of the  $Z''$  versus  $Z'$  curves in the low frequency range were close to 90°, indicating good capacitive behaviour (Fig. 7.16A). In the higher frequency range the semicircles were observed (Fig. 7.16B). The experimental data are in good agreement with the simulation results, which were obtained using the circuit shown in Fig. 7.16A (inset). The circuit includes the R-Q transmission line, solution resistance  $R_1$  and Warburg  $W$  element.  $R_2$  and  $R_3$  represent electrical electrolyte resistance in pores and resistance of active material. The  $Q_1$  and  $Q_2$  elements represent contributions of double layer and pseudocapacitance. The impedance spectroscopy data were used for the calculation of the differential capacitances. The frequency dependencies of the components of complex capacitance, calculated from the impedance data, showed relaxation type[61] dispersions, as indicated by the reduction of  $C'$  with increasing frequency and corresponding maxima in  $C''$  (Fig.7.16C and D). The relaxation frequency gives information on performance of devices at different frequencies. The MWCNT electrodes showed real component of capacitance ( $C'$ ) of 0.34 F cm<sup>-2</sup> at 10 mHz. It was found that  $C'$  decreased rapidly at frequencies above 120 mHz. The N-AC-MWCNT electrodes showed  $C'$  of 1.21 F cm<sup>-2</sup> at 10 mHz. The reduction in  $C'$  was observed at frequencies above 400 mHz. The relaxation frequency, corresponding to the maximum of  $C''$  shifted from 235 mHz for

MWCNT to 858 mHz for N-AC-MWCNT. The results of  $C'$  and  $C''$  measurements indicated higher  $C'$  and improved capacitance retention with increased frequency for N-AC-MWCNT, compared to MWCNT electrodes. The  $\text{MnO}_2$  coated N-AC-MWCNT electrodes, prepared using solutions 1, 2 and 3 showed  $C'$  values of 2.09, 2.74 and 3.38  $\text{F cm}^{-2}$  at 10 mHz and relaxation frequencies of 209, 82 and 51 mHz, respectively. It is suggested that electrical resistance, related to electrolyte diffusion, electrical electrolyte resistance in pores and resistance of active material are major factors, contributing to the time constant of the charging mechanism and relaxation process. The formation of  $\text{MnO}_2$  coating resulted in the increasing resistance, and reduced relaxation frequency. As a result, the relaxation peaks shifted to lower frequencies with increasing amount of deposited  $\text{MnO}_2$ .

The results of impedance spectroscopy provide capacitance behavior at different frequencies, which are important for practical application of capacitors in electronic devices. The relaxation phenomena give limitation of the frequency range, where high capacitance can be achieved. The results of alternating current capacitance measurements are in agreement with the capacitance data, obtained from CVs (Fig. 7.15D), as indicated by higher capacitance of N-AC-MWCNT, compared to MWCNT and capacitance increase with increasing concentration of Mn species in the solutions 1-3 for measurements performed at low alternating current frequencies or low CV scan rates. The highest relaxation frequency of N-AC-MWCNT is in agreement with the best capacitance retention for the same material, obtained from CVs, recorded at

high scan rates. The decrease in relaxation frequency of  $\text{MnO}_2$  coated N-AC-MWCNT with increasing concentration of Mn species in the solutions correlates (Fig. 7.16C) was corresponded to decrease in capacitance retention for the same materials at high scan rates (Fig. 7.15D).

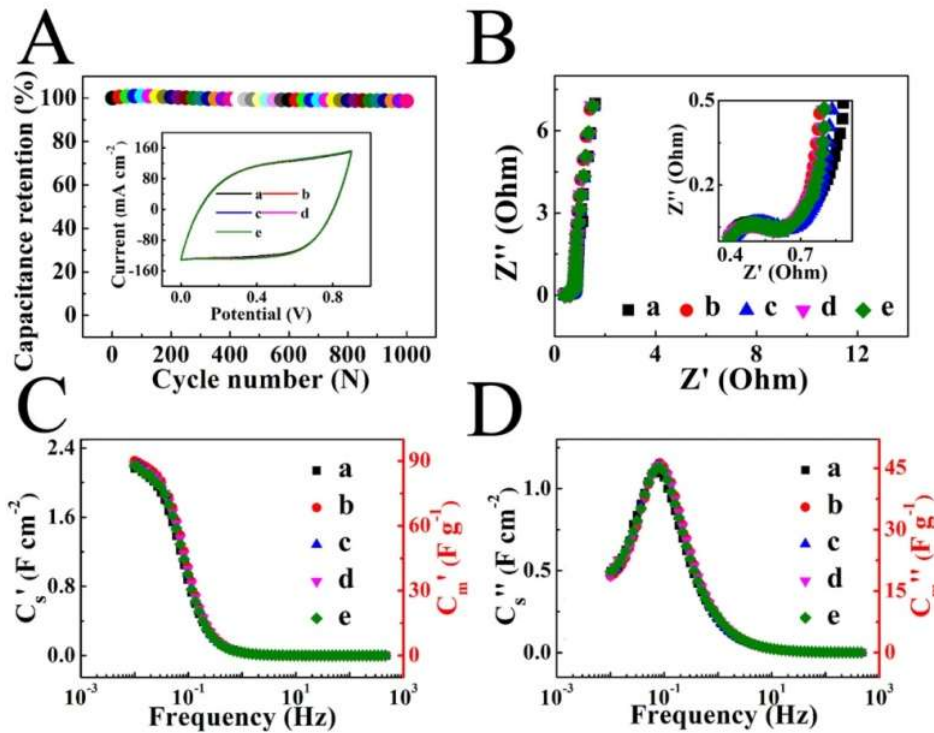


Figure 7.17 (A) Capacitance retention versus cycle number, inset shows corresponding CVs at  $50 \text{ mV s}^{-1}$ , (B) Nyquist plot of complex impedance, inset shows high frequency range, (C)  $C_s'$  and  $C_m'$  and (D)  $C_s''$  and  $C_m''$  versus frequency after (a)1<sup>st</sup>, (b)250<sup>th</sup>, (c) 500<sup>th</sup>, (d)750<sup>th</sup>, (e)1000<sup>th</sup> cycles for  $\text{MnO}_2$  coated N-AC-MWCNT electrodes with mass loading of  $20 \text{ mg cm}^{-2}$ , prepared using solution 2.

The  $\text{MnO}_2$  coated N-AC-MWCNT electrodes, prepared using solution 2 and containing about 41 % of  $\text{MnO}_2$  (Fig. 7.17), were used for further investigation and fabrication of asymmetric cells. As pointed out above, such electrodes showed higher capacitance, compared to the electrodes, prepared from solutions 1 and improved capacitance retention at high scan rates and high frequencies, compared to the electrodes, prepared using solution 3. The  $\text{MnO}_2$  coated N-AC-MWCNT electrodes, prepared using solution 2, showed good cycling stability with 98.7% capacitance retention after 1000 cycles (Fig. 7.17A). The CV shape remained unchanged during cycling (Fig. 7.17A, inset). Electrochemical impedance and alternating current capacitance also remained practically unchanged during cycling (Fig. 7.17B-D).

#### 7.2.4 Capacitive performance of the asymmetric ES cell

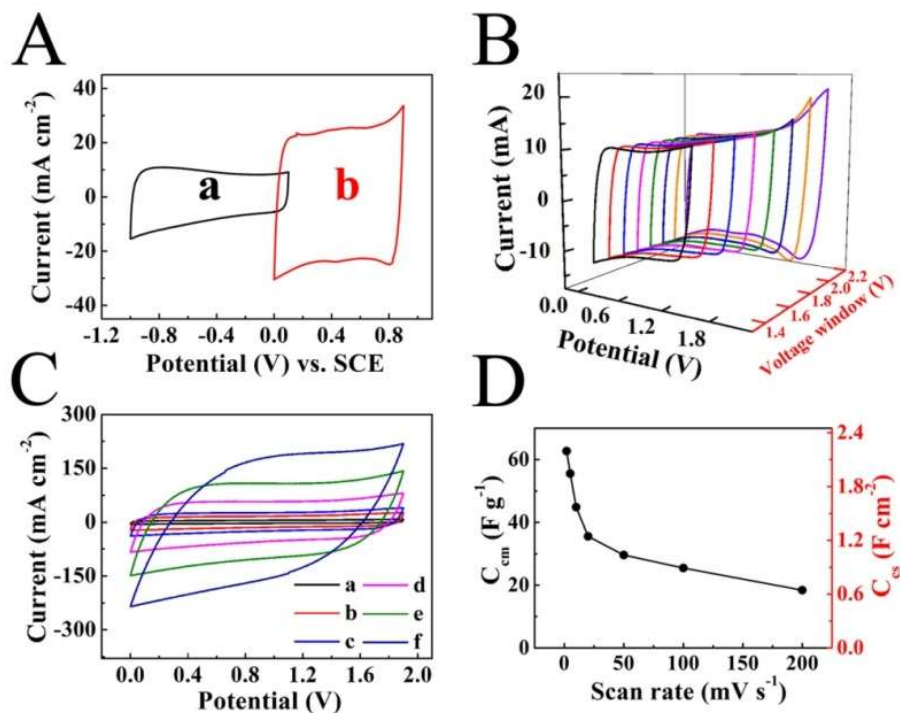


Figure 7.18. (A) CVs at a scan rate of  $5 \text{ mV s}^{-1}$  for (a) N-AC-MWCNT electrode and (b)  $\text{MnO}_2$  coated N-AC-MWCNT electrode, prepared using solution 2. (B) CVs for asymmetric cell in different potential windows at a scan rate of  $5 \text{ mV s}^{-1}$ . (C) CVs for asymmetric cell at scan rates of (a) 2, (b) 10, (c) 20, (d) 50, (e) 100 and (f)  $200 \text{ mV s}^{-1}$ . (D)  $C_{\text{cm}}$  and  $C_{\text{cs}}$  calculated from CVs for asymmetric cell versus scan rate in a voltage window of 1.9 V.

The  $\text{MnO}_2$  coated N-AC-MWCNT positive electrodes were combined with N-AC-MWCNT negative electrodes for the fabrication of ES devices. Fig. 7.18A shows CVs of the N-AC-MWCNT negative electrodes and  $\text{MnO}_2$  coated N-AC-MWCNT positive electrodes of the same mass in different voltage windows. The area of the CV for positive electrode was significantly larger, compared to the area of the CV of the negative electrode due to higher capacitance of the  $\text{MnO}_2$  coated N-AC-MWCNT. In order to achieve comparable capacitances of the individual electrodes, the asymmetric devices were prepared using  $10 \text{ mg cm}^{-2}$   $\text{MnO}_2$  coated N-AC-MWCNT and  $25 \text{ mg cm}^{-2}$  N-AC-MWCNT electrodes. Fig. 7.18B shows CVs for such devices in different voltage windows at a scan rate of  $5 \text{ mV s}^{-1}$ . The CV showed nearly ideal box shapes in voltage windows in the range of 1.4-1.9 V, at larger voltage windows redox peaks appeared (Fig. 7.18B). Therefore, further investigations were performed in a voltage window of 1.9 V. The analysis of CVs at different scan rates (Fig. 7.18C) showed good electrochemical performance with nearly box shapes of CVs at scan rates of 2-100  $\text{mV s}^{-1}$ . The specific capacitances of

asymmetric ES cell were  $2.19 \text{ F cm}^{-2}$  ( $62.7 \text{ F g}^{-1}$ ) and  $0.89 \text{ F cm}^{-2}$  ( $25.4 \text{ F g}^{-1}$ ) at scan rates of 2 and  $100 \text{ mV s}^{-1}$ , respectively (Fig. 7.18D).

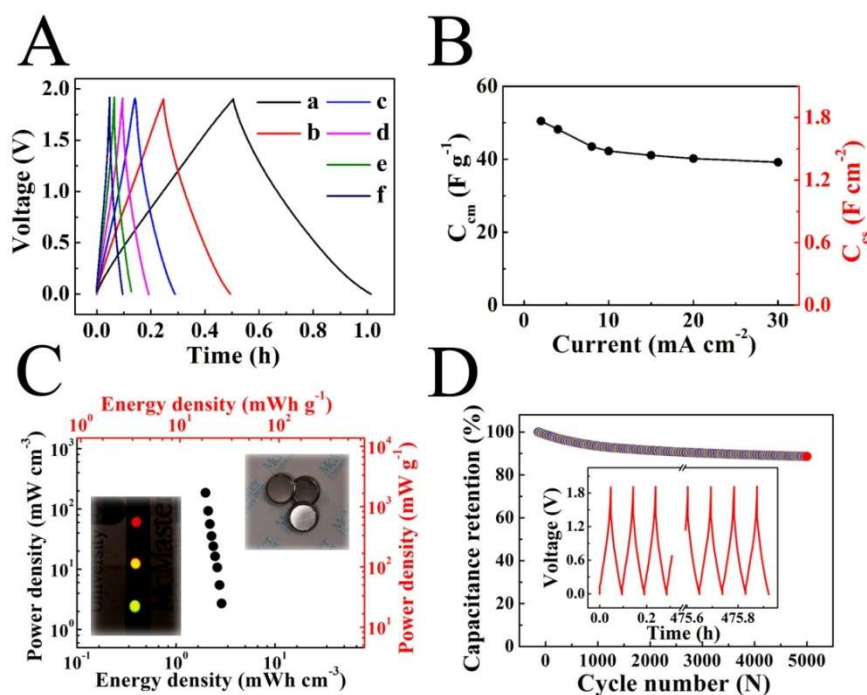


Figure 7.19. (A) Charge-discharge curves in a voltage window of 1.9 V for coin cells at currents of (a) 2, (b) 4, (c) 8, (d) 10, (e) 15 and (f)  $20 \text{ mA cm}^{-2}$ . (B)  $C_{\text{cm}}$  and  $C_{\text{cs}}$  calculated from the discharge curves versus current. (C) Ragone plot for a coin cell, insets show the fabricated coin cells and 20 mA LED bulbs, powered by the coin cells. (D) Capacitance retention of a coin cell versus cycle number, inset shows the initial and final charge-discharge curves in the cycling performance test.

The charge-discharge behavior for the asymmetric cells at different currents is analysed in Fig. 7.19A. The charge-discharge curves were of symmetrical triangular shape, indicating good capacitive behaviour. The specific capacitance of the

asymmetric cell, calculated from the discharge curves (Fig. 7.19B) decreased from  $1.77 \text{ F cm}^{-2}$  ( $50.5 \text{ F g}^{-1}$ ) to  $1.37 \text{ F cm}^{-2}$  ( $39.2 \text{ F g}^{-1}$ ) with increasing current density in the range of  $2\text{-}30 \text{ mA cm}^{-2}$ . The capacitances, calculated from the discharge curves are comparable with the capacitances, calculated from the CV data. Fig. 7.19C shows a Ragone plot for the asymmetric devices. The energy density of  $26.4 \text{ mWh g}^{-1}$  and power density of  $1.7 \text{ W g}^{-1}$  were achieved. Compared with the symmetric devices in the previous investigation, improved energy/power characteristics of the asymmetric devices were attributed to higher voltage window and higher capacitance. The asymmetric cells were used for the powering of LED bulbs with a nominal current of  $20 \text{ mA}$  (Fig. 7.19C, inset). Fig. 7.19D shows cyclic behaviour of the asymmetric device. The capacitance retention was found to be  $93.4$  and  $88.6\%$  after  $1,000$  and  $5,000$  cycles respectively. The decrease in capacitance with increasing cycle number can be attributed to changes in the microstructure of the electrode material during cycling. The corresponding charge-discharge curves (Fig. 7.19D, inset) showed similar triangular shape at the beginning and at the end of  $5,000$  cycling, indicating that the asymmetric cell is stable a voltage window of  $1.9 \text{ V}$ .

### 7.2.5 Conclusion

The  $\text{MnO}_2$  coated N-AC-MWCNT with good capacitive performance was developed as the positive electrode for asymmetric ES device. In this approach, the problem of MWCNT degradation in the reaction with  $\text{KMnO}_4$  has been avoided by the use of

sacrificial N-AC layer. This method offered the advantages of small size of MnO<sub>2</sub> nanoparticles, good electrical contact of MnO<sub>2</sub> and MWCNT and fibrous microstructure of the materials. Testing results showed a high specific capacitance of 6.29 F cm<sup>-2</sup> (311.7 F g<sup>-1</sup>) at high mass loading of 20 mg cm<sup>-2</sup>. The asymmetric devices were fabricated using fibrous electrode materials, which showed capacitance of 2.19 F cm<sup>-2</sup> (62.7 F g<sup>-1</sup>) in a voltage window of 1.9 V in aqueous Na<sub>2</sub>SO<sub>4</sub> electrolyte. The electrodes and asymmetric devices showed good capacitance retention at high charge-discharge rates and good cycling stability.

### 7.3 References

- [1] P. Simon, Y. Gogotsi, Materials for electrochemical capacitors, *Nature Materials*, 7 (2008) 845-854.
- [2] Z. Cao, B. Wei, A perspective: carbon nanotube macro-films for energy storage, *Energy & Environmental Science*, 6 (2013) 3183-3201.
- [3] E. Frackowiak, Q. Abbas, F. Beguin, Carbon/carbon supercapacitors, *Journal of Energy Chemistry*, 22 (2013) 226-240.
- [4] J.J. Vilatela, D. Eder, Nanocarbon composites and hybrids in sustainability: A review, *ChemSusChem*, 5 (2012) 456-478.
- [5] H. Jiang, P.S. Lee, C. Li, 3D carbon based nanostructures for advanced supercapacitors, *Energy & Environmental Science*, 6 (2012) 41-53.
- [6] V.V.N. Obreja, On the performance of supercapacitors with electrodes based on carbon nanotubes and carbon activated material-A review, *Physica E: Low-Dimensional Systems and Nanostructures*, 40 (2008) 2596-2605.
- [7] M. Zhi, C. Xiang, J. Li, M. Li, N. Wu, Nanostructured carbon-metal oxide composite electrodes for supercapacitors: a review, *Nanoscale*, 5 (2013) 72-88.

- [8] W. Gu, M. Sevilla, A. Magasinski, A.B. Fuertes, G. Yushin, Sulfur-containing activated carbons with greatly reduced content of bottle neck pores for double-layer capacitors: a case study for pseudocapacitance detection, *Energy & Environmental Science*, 6 (2013) 2465-2476.
- [9] L.-F. Chen, Z.-H. Huang, H.-W. Liang, W.-T. Yao, Z.-Y. Yu, S.-H. Yu, Flexible all-solid-state high-power supercapacitor fabricated with nitrogen-doped carbon nanofiber electrode material derived from bacterial cellulose, *Energy & Environmental Science*, 6 (2013) 3331-3338.
- [10] L.-F. Chen, X.-D. Zhang, H.-W. Liang, M. Kong, Q.-F. Guan, P. Chen, Z.-Y. Wu, S.-H. Yu, Synthesis of nitrogen-doped porous carbon nanofibers as an efficient electrode material for supercapacitors, *ACS Nano*, 6 (2012) 7092-7102.
- [11] W. Kim, M.Y. Kang, J.B. Joo, N.D. Kim, I.K. Song, P. Kim, J.R. Yoon, J. Yi, Preparation of ordered mesoporous carbon nanopipes with controlled nitrogen species for application in electrical double-layer capacitors, *Journal of Power Sources*, 195 (2010) 2125-2129.
- [12] D.-D. Zhou, W.-Y. Li, X.-L. Dong, Y.-G. Wang, C.-X. Wang, Y.-Y. Xia, A nitrogen-doped ordered mesoporous carbon nanofiber array for supercapacitors, *Journal of Materials Chemistry A*, 1 (2013) 8488-8496.
- [13] D. Hulicova-Jurcakova, M. Seredych, G.Q. Lu, T.J. Bandosz, Combined Effect of Nitrogen and Oxygen Containing Functional Groups of Microporous Activated Carbon on its Electrochemical Performance in Supercapacitors, *Advanced Functional Materials*, 19 (2009) 438-447.
- [14] Y. Song, D. Zhou, Y. Wang, C. Wang, Y. Xia, Preparation of nitrogen-containing mesoporous carbons and their application in supercapacitors, *New J. Chem.*, 37 (2013) 1768-1775.
- [15] L. Wei, M. Sevilla, A.B. Fuertes, R. Mokaya, G. Yushin, Polypyrrole-derived activated carbons for high-performance electrical double-layer capacitors with ionic liquid electrolyte, *Advanced Functional Materials*, 22 (2012) 827-834.
- [16] L. Li, E. Liu, J. Li, Y. Yang, H. Shen, Z. Huang, X. Xiang, W. Li, A doped activated carbon prepared from polyaniline for high performance supercapacitors, *Journal of Power Sources*, 195 (2010) 1516-1521.

- [17] L. Qie, W. Chen, H. Xu, X.-Q. Xiong, Y. Jiang, F. Zou, X. Hu, Y. Xin, Z. Zhang, Y. Huang, Synthesis of functionalized 3D hierarchical porous carbon for high-performance supercapacitor, *Energy Environ. Sci.*, 6 (2013) 2497-2504.
- [18] C. Guo, N. Li, L. Ji, Y. Li, X. Yang, Y. Lu, Y. Tu, N-and O-doped carbonaceous nanotubes from polypyrrole for potential application in high-performance capacitance, *Journal of Power Sources*, 247 (2014) 660-666.
- [19] Z. Wang, L. Qie, L. Yuan, W. Zhang, X. Hu, Y. Huang, Functionalized N-doped interconnected carbon nanofibers as an anode material for sodium-ion storage with excellent performance, *Carbon*, 55 (2013) 328–334.
- [20] L. Qie, W.-M. Chen, Z.-H. Wang, Q.-G. Shao, X. Li, L.-X. Yuan, X.-L. Hu, W.-X. Zhang, Y.-H. Huang, Nitrogen-Doped Porous Carbon Nanofiber Webs as Anodes for Lithium Ion Batteries with a Superhigh Capacity and Rate Capability, *Advanced Materials*, 24 (2012) 2047-2050.
- [21] H.-g. Wang, Z. Wu, F.-l. Meng, D.-l. Ma, X.-l. Huang, L.-m. Wang, X.-b. Zhang, Nitrogen-Doped Porous Carbon Nanosheets as Low-Cost, High-Performance Anode Material for Sodium-Ion Batteries, *ChemSusChem*, 6 (2013) 56-60.
- [22] M. Yang, B. Cheng, H. Song, X. Chen, Preparation and electrochemical performance of polyaniline-based carbon nanotubes as electrode material for supercapacitor, *Electrochimica Acta*, 55 (2010) 7021-7027.
- [23] D. Hulicova-Jurcakova, M. Seredych, G.Q. Lu, T.J. Bandosz, Combined Effect of Nitrogen- and Oxygen- Containing Functional Groups of Microporous Activated Carbon on its Electrochemical Performance in Supercapacitors, *Advanced Functional Materials*, 19 (2009) 438-447.
- [24] T.-H. Wu, C.-T. Hsu, C.-C. Hu, L.J. Hardwick, Important parameters affecting the cell voltage of aqueous electrical double-layer capacitors, *Journal of Power Sources*, 242 (2013) 289-298.
- [25] Y.-K. Hsu, Y.-C. Chen, Y.-G. Lin, L.-C. Chen, K.-H. Chen, High-cell-voltage supercapacitor of carbon nanotube/carbon cloth operating in neutral aqueous solution, *Journal of Materials Chemistry*, 22 (2012) 3383-3387.

- [26] L. Demarconnay, E. Raymundo-Piñero, F. Béguin, A symmetric carbon/carbon supercapacitor operating at 1.6 V by using a neutral aqueous solution, *Electrochemistry Communications*, 12 (2010) 1275-1278.
- [27] Q. Gao, L. Demarconnay, E. Raymundo-Piñero, F. Béguin, Exploring the large voltage range of carbon/carbon supercapacitors in aqueous lithium sulfate electrolyte, *Energy & Environmental Science*, 5 (2012) 9611-9617.
- [28] K. Fic, E. Frackowiak, F. Béguin, Unusual energy enhancement in carbon-based electrochemical capacitors, *Journal of Materials Chemistry*, 22 (2012) 24213-24223.
- [29] K. Shi, I. Zhitomirsky, Influence of current collector on capacitive behavior and cycling stability of Tiron doped polypyrrole electrodes, *Journal of Power Sources*, 240 (2013) 42-49.
- [30] K. Shi, I. Zhitomirsky, Polypyrrole nanofiber-carbon nanotube electrodes for supercapacitors with high mass loading obtained using an organic dye as a co-dispersant, *Journal of Materials Chemistry A*, 1 (2013) 11614-11622.
- [31] L.L. Zhang, Y. Gu, X.S. Zhao, Advanced porous carbon electrodes for electrochemical capacitors, *Journal of Materials Chemistry A*, 1 (2013) 9395-9408.
- [32] L. Wei, G. Yushin, Nanostructured activated carbons from natural precursors for electrical double layer capacitors, *Nano Energy*, 1 (2012) 552-565.
- [33] A.J. Roberts, R.C.T. Slade, Performance loss of aqueous MnO<sub>2</sub>/carbon supercapacitors at elevated temperature: cycling vs. storage, *Journal of Materials Chemistry A*, 1 (2013) 14140-14146.
- [34] S.H. Lee, H. Lee, M.S. Cho, J.-D. Nam, Y. Lee, Morphology and composition control of manganese oxide by the pulse reverse electrodeposition technique for high performance supercapacitors, *Journal of Materials Chemistry A*, 1 (2013) 14606-14611.
- [35] Y. Munaiah, B.G. Sundara Raj, T. Prem Kumar, P. Ragupathy, Facile synthesis of hollow sphere amorphous MnO<sub>2</sub>: the formation mechanism, morphology and effect of a bivalent cation-containing electrolyte on its supercapacitive behavior, *Journal of Materials Chemistry A*, 1 (2013) 4300-4306.
- [36] T. Brousse, P.-L. Taberna, O. Crosnier, R. Dugas, P. Guillemet, Y. Scudeller, Y. Zhou, F.d.r. Favier, D. Belanger, P. Simon, Long-term cycling behavior of asymmetric activated carbon/MnO<sub>2</sub> aqueous electrochemical supercapacitor, *Journal of Power Sources*, 173 (2007) 633-641.

- [37] T. Brousse, M. Toupin, D. Belanger, A Hybrid Activated Carbon-Manganese Dioxide Capacitor using a Mild Aqueous Electrolyte, *Journal of the Electrochemical Society*, 151 (2004) A614-A622.
- [38] J.-H. Lee, T.-Y. Yang, H.-Y. Kang, D.-H. Nam, N.-R. Kim, Y.-Y. Lee, S.-H. Lee, Y.-C. Joo, Designing thermal and electrochemical oxidation processes for  $\delta$ -MnO<sub>2</sub> nanofibers for high-performance electrochemical capacitors, *Journal of Materials Chemistry A*, 2 (2014) 7197-7204.
- [39] S. Chen, W. Xing, J. Duan, X. Hu, S.Z. Qiao, Nanostructured morphology control for efficient supercapacitor electrodes, *Journal of Materials Chemistry A*, 1 (2013) 2941-2954.
- [40] D. Guo, X. Yu, W. Shi, Y. Luo, Q. Li, T. Wang, Facile synthesis of well-ordered manganese oxide nanosheet arrays on carbon cloth for high-performance supercapacitors, *Journal of Materials Chemistry A*, 2 (2014) 8833-8838.
- [41] P. Yang, Y. Li, Z. Lin, Y. Ding, S. Yue, C.P. Wong, X. Cai, S. Tan, W. Mai, Worm-like amorphous MnO<sub>2</sub> nanowires grown on textiles for high-performance flexible supercapacitors, *Journal of Materials Chemistry A*, 2 (2014) 595-599.
- [42] L.-L. Yu, J.-J. Zhu, J.-T. Zhao, Beta-manganese dioxide nanoflowers self-assembled by ultrathin nanoplates with enhanced supercapacitive performance, *Journal of Materials Chemistry A*, 2 (2014) 9353-9360.
- [43] C.-W. Lee, S.-B. Yoon, S.-M. Bak, J. Han, K.C. Roh, K.-B. Kim, Soft templated mesoporous manganese oxide/carbon nanotube composites via interfacial surfactant assembly, *Journal of Materials Chemistry A*, 2 (2014) 3641-3647.
- [44] Y. Wang, Y. Liu, I. Zhitomirsky, Surface modification of MnO<sub>2</sub> and carbon nanotubes using organic dyes for nanotechnology of electrochemical supercapacitors, *Journal of Materials Chemistry A*, 1 (2013) 12519-12526.
- [45] H. Xia, Y. Wang, J. Lin, L. Lu, Hydrothermal synthesis of MnO<sub>2</sub>/CNT nanocomposite with a CNT core/porous MnO<sub>2</sub> sheath hierarchy architecture for supercapacitors, *Nanoscale Research Letters*, 7 (2012) 1-10.
- [46] H. Xia, M. Lai, L. Lu, Nanoflaky MnO<sub>2</sub>/carbon nanotube nanocomposites as anode materials for lithium-ion batteries, *Journal of Materials Chemistry*, 20 (2010) 6896-6902.

- [47] S.-B. Yoon, J.-P. Jegal, K.C. Roh, K.-B. Kim, Electrochemical Impedance Spectroscopic Investigation of Sodium Ion Diffusion in MnO<sub>2</sub> Using a Constant Phase Element Active in Desired Frequency Ranges, *Journal of the Electrochemical Society*, 161 (2014) H207-H213.
- [48] W. Jiang, K. Zhang, L. Wei, D. Yu, J. Wei, Y. Chen, Hybrid ternary rice paper-manganese oxide-carbon nanotube nanocomposites for flexible supercapacitors, *Nanoscale*, 5 (2013) 11108-11117.
- [49] Y. Wang, H. Liu, X. Sun, I. Zhitomirsky, Manganese dioxide-carbon nanotube nanocomposites for electrodes of electrochemical supercapacitors, *Scripta Materialia*, 61 (2009) 1079-1082.
- [50] J. Moon, M. Awano, H. Takagi, Y. Fujishiro, Synthesis of nanocrystalline manganese oxide powders: Influence of hydrogen peroxide on particle characteristics, *Journal of Materials Research*, 14 (1999) 4594-4601.
- [51] G.M. Jacob, I. Zhitomirsky, Microstructure and properties of manganese dioxide films prepared by electrodeposition, *Applied Surface Science*, 254 (2008) 6671-6676.
- [52] J. Li, Q.M. Yang, I. Zhitomirsky, Nickel foam-based manganese dioxide-carbon nanotube composite electrodes for electrochemical supercapacitors, *Journal of Power Sources*, 185 (2008) 1569-1574.
- [53] J. Li, I. Zhitomirsky, Electrophoretic deposition of manganese dioxide-carbon nanotube composites, *Journal of Materials Processing Technology*, 209 (2009) 3452-3459.
- [54] J.N. Broughton, M.J. Brett, Investigation of thin sputtered Mn films for electrochemical capacitors, *Electrochimica Acta*, 49 (2004) 4439-4446.
- [55] S.C. Pang, M.A. Anderson, T.W. Chapman, Novel electrode materials for thin-film ultracapacitors: comparison of electrochemical properties of sol-gel-derived and electrodeposited manganese dioxide, *Journal of the Electrochemical Society*, 147 (2000) 444-450.
- [56] S. Devaraj, N. Munichandraiah, High capacitance of electrodeposited MnO<sub>2</sub> by the effect of a surface-active agent, *Electrochemical and Solid-State Letters*, 8 (2005) A373-A377.
- [57] R. Jiang, T. Huang, Y. Tang, J. Liu, L. Xue, J. Zhuang, A. Yu, Factors influencing MnO<sub>2</sub>/multi-walled carbon nanotubes composite's electrochemical performance as supercapacitor electrode, *Electrochimica Acta*, 54 (2009) 7173-7179.

[58] H. Xia, C. Huo, Electrochemical properties of MnO<sub>2</sub>/CNT nanocomposite in neutral aqueous electrolyte as cathode material for asymmetric supercapacitors, *International Journal of Smart and Nano Materials*, 2 (2011) 283-291.

[59] Y. Gogotsi, P. Simon, True Performance Metrics in Electrochemical Energy Storage, *Science*, 334 (2011) 917-918.

[60] S. Zhang, C. Peng, K.C. Ng, G.Z. Chen, Nanocomposites of manganese oxides and carbon nanotubes for aqueous supercapacitor stacks, *Electrochimica Acta*, 55 (2010) 7447-7453.

[61] K. Shi, I. Zhitomirsky, Fabrication of Polypyrrole-Coated Carbon Nanotubes Using Oxidant-Surfactant Nanocrystals for Supercapacitor Electrodes with High Mass Loading and Enhanced Performance, *ACS Applied Materials & Interfaces*, 5 (2013) 13161-13170.

## **8. Activated carbon based electrodes for capacitive dye removal**

### **8.1 Activated carbon coated MWCNTs for capacitive dye removal**

The progress in capacitive technology generates interests in application of ES for capacitive deionization (CDI) of water[1, 2]. Recent studies showed that the CDI is a robust, energy efficient, and cost effective technology for desalination of water. The progress in the CDI generates innovations of developing ES cells for removal other charged species from aqueous solutions. Of special interest is the possibility of capacitive dye removal (CDR). Organic dyes are widely used for many applications, such as solar cells, photocatalysis, transistors, biological and chemical sensors, lasers, medicine and textile industry[3-6]. In the previous investigation[7], we observed significant mass increase of quartz crystal microbalance resonators in response to an applied electric field in the dilute solution of the cationic dye, methyl blue. The mass gain of the electrode is attributed to the accumulation of the dye molecules at the electric double-layer. It was suggested that such accumulation of the charged dyes can be used for capacitive removal of dyes.

In the following study, we investigated the capacitive behavior of N-doped activated carbon coated multiwalled carbon nanotubes (N-AC-MWCNT) in different dye solutions. The results demonstrated the wide applicability of CDR that can be used for both cationic and anionic dyes. In addition, we found that the energy of CDR could be

stored in the ES cells. Electrode regeneration resulted in energy release that may be further utilized for continued purification, powered neighboring cells or other applications. This method offers the advantage of vastly improved energy utilization.

### 8.1.1 Chemical structure of different dyes



Figure. 8.1 (A) Aqueous solutions of (a) Safranin (SAF), (b) Calcon (CAL), (c) Amaranth (AMA) and chemical structures of (B) SAF, (C) CAL and (D) AMA.

We selected cationic SAF, anionic CAL and AMA dyes for the investigation. SAF and its derivatives are used in the metal electroplating industry[8], medicine[9] and photovoltaic devices[10]. CAL and AMA belong to a large family of azo dyes, which have many applications in the textile and pharmaceutical industry[11-13], and mineral flotation[14]. Fig. 8.1A shows aqueous solutions of the dyes. Fig. 8.1B and C indicate that structures of SAF and CAL have one cationic or anionic charged group, respectively. The structure of AMA is similar to that of CAL(Fig. 8.1D). However,

AMA has three anionic groups. In this investigation, the comparison of the experimental data for AMA and CAL provided an insight into the influence of charge of the molecules on the capacitive behavior.

### 8.1.2 Investigation of capacitive behavior in solution of Safranin and Calcon dyes

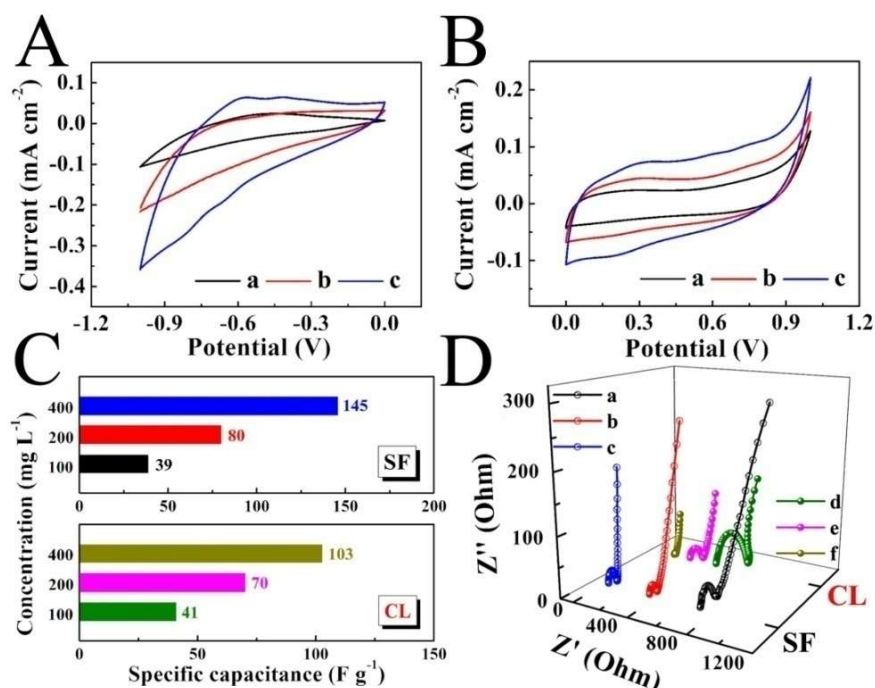


Figure 8.2 (A,B) CVs at a scan rate of  $0.5 \text{ mV s}^{-1}$  for N-AC-MWCNT electrodes in the dye solutions of (A) SAF and (B) CAL with concentrations of (a) 100, (b) 200 and (c)  $400 \text{ mg L}^{-1}$ , (C) specific capacitances, calculated from the CV data, (D) Nyquist plot of complex impedance  $Z^* = Z' - jZ''$  for different solutions: (a) 100, (b) 200 and (c)  $400 \text{ mg L}^{-1}$  SAF and (d) 100, (e) 200 and (f)  $400 \text{ mg L}^{-1}$  CAL.

The micro-structure, surface area and chemical bonds of N-AC-MWCNT were analyzed in section 7.1.1. The results indicated that the use of N-AC-WCNT as an electrode material for CDR offered the advantages of high surface area of activated

carbon and high conductivity of MWCNT. Fig. 8.2 (A,B) shows CVs for N-AC-MWCNT electrodes in SAF and CAL solutions. The area of the CVs increased with increasing dye concentration, indicating the increase in number of adsorbed dye molecules. The capacitances, calculated from the CV data are presented in Fig. 8.2C. The electrodes showed comparable capacitances of 39 and 41 F g<sup>-1</sup> in the solutions of SAF and CAL dyes, respectively, at dye concentration of 100 mg L<sup>-1</sup>. However, the capacitance achieved in SAF solutions at concentrations of 200 and 400 mg L<sup>-1</sup> was higher than the capacitance in CAL solutions of similar concentrations. The capacitances in 400 mg L<sup>-1</sup> solutions of SAF and CAL dyes were found to be 145 and 103 F g<sup>-1</sup>, respectively. The investigations of the electrochemical impedance  $Z^*=Z'-iZ''$  of the N-AC-MWCNT electrodes in SAF and CAL solutions were presented in the Nyquist plot (Fig. 8.2D). The results showed that the increase in dye concentration resulted in decreasing resistance.

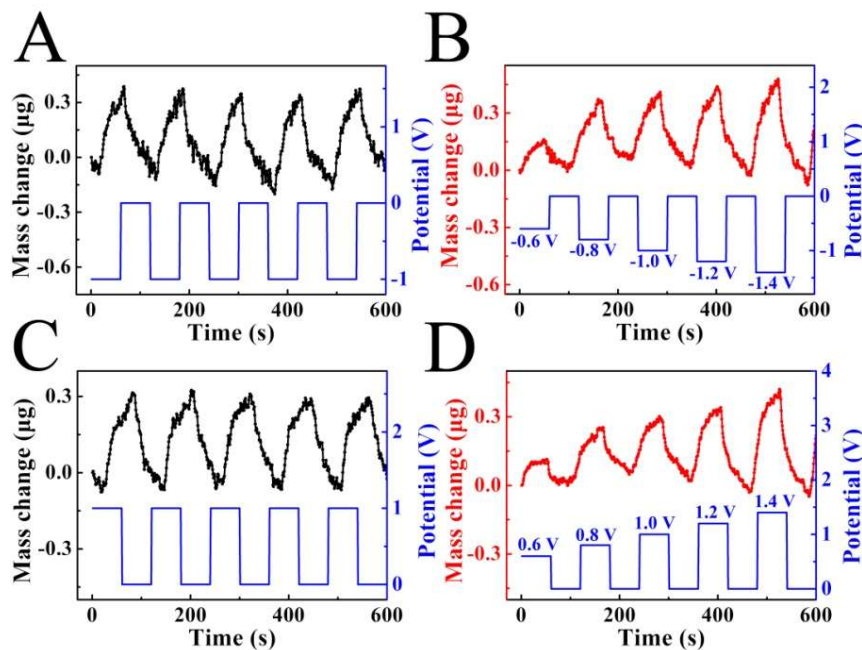


Figure 8.3. QCM data for N-AC-MWCNT coated resonators in 50 mg L<sup>-1</sup> solutions of (A, B) SAF and (C, D) CAL, tested using (A) negative and (C) positive pulses with a constant voltage of 1 V or by applying a series of (B) negative or (D) positive pulses of increasing amplitude in the range of 0.6-1.4 V.

Fundamental studies showed that capacitance of porous carbon materials depends on the size of the electrolyte molecules and pore size of carbon[15-19]. It was found[16] that using ionic liquid electrolytes and activated carbons with controlled pore size, the specific capacitance of 160 F g<sup>-1</sup> can be achieved. This obtained value is much higher than the specific capacitance reported (50-100 F g<sup>-1</sup>) for commercial activated carbons. The size of SAF and CAL dyes is comparable with the size of the ionic liquid molecules[16]. Our results showed that the specific capacitance of N-AC-MWCNT electrodes, achieved in the SAF solutions was comparable with specific capacitance of the carbon materials in ionic liquid electrolytes. It is important to note that the solutions of SAF and CAL dyes contained large cation or anion, respectively, and smaller counter ions. In this case, the capacitive performance is strongly influenced by large ions. The lower capacitance, achieved in the CAL solutions, can be partially attributed to larger mass of the CAL molecules, which can result in lower ion mobility. It is known[17] that charge storage in the electrochemical double-layer is influenced by ion transport. The difference in performance of N-AC-MWCNT electrodes in the solutions of SAF and CAL dyes can also be attributed to electrostatic interactions of N-AC-MWCNT and SAF<sup>+</sup> cations or CAL<sup>-</sup> anions. Recent investigated demonstrated

that cationic and anionic transports in pores depend on point of zero charge of the electrode material[20-23]. The results showed that negatively charged carbon nanotubes promoted cationic transport [21]. It is also important to note that the potential of zero charge could be different from the potential of zero mass change[24], that separates the mass change of the electrode due to adsorption of cations and anions. Other investigations suggested that the interaction within the electrochemical double-layer is influenced by the hydrophobic characteristics of the electrode[25].

The CDR has also been investigated using a QCM method, which is an efficient tool for monitoring the incorporation of ions into the ES electrodes during charge and discharge cycles[24, 26, 27]. Testing results indicated that the application of negative or positive pulses to the N-AC-MWCNT electrodes in SAF or CAL solutions, respectively, resulted in mass gain (Fig. 8.3A and B). It is attributed to incorporation of cationic SAF or anionic CAL species into the electrode. The mass gain versus time curves for the electrodes are typically characterized by several domains, representing complex interactions of ions and porous electrodes[24]. The decrease of the adsorption rate as the voltage increased is explained by the adsorption of counterions, which are expelled from the electrode, leading the formation of an ion exchange zone[28]. The electrode mass decreased during the OFF time. The experiments showed periodic variations in the electrode mass. Such periodic variations, related to dye removal, indicate a possibility of regeneration of the electrode material. The increase in pulse amplitude resulted in increasing mass gain (Fig. 8.3 B,D). This is attributed to the high

electrostatic force resulting from a high voltage. The adsorption mass of SAF and CAL was measured from the maximum of mass variations in QCM curve. The adsorption capacity was calculated using the adsorption mass divided by the mass of active materials of electrode (10  $\mu\text{g}$ ). The data was presented in Table 8.1. It indicated that the rise of applied voltage increased the amount of ions incorporated into the electrodes.

Table 8.1 Capacitive adsorption of SAF and CAL dye solution, measured from Figure 8.3, in the voltage range of 0.6-1.4 V.

| Voltage window (V) | SAF adsorption mass ( $\mu\text{g}$ ) | CAL adsorption mass ( $\mu\text{g}$ ) | SAF adsorption capacity (mg/g) | CAL adsorption capacity (mg/g) |
|--------------------|---------------------------------------|---------------------------------------|--------------------------------|--------------------------------|
| 0.6                | 0.15                                  | 0.10                                  | 15                             | 10                             |
| 0.8                | 0.36                                  | 0.26                                  | 36                             | 26                             |
| 1                  | 0.39                                  | 0.29                                  | 39                             | 29                             |
| 1.2                | 0.44                                  | 0.33                                  | 44                             | 33                             |
| 1.4                | 0.48                                  | 0.41                                  | 48                             | 41                             |

The results of CV and QCM testing paved the way for the fabrication of ES devices that enabled the removal of dyes from aqueous solutions and energy storage in

electrochemical double-layer of N-AC-MWCNT electrodes (Fig. 8.4). We suggested that by applying voltage to the electrodes, dye ions could be drawn to the surface of the electrochemical double-layer and the ES is charged (Fig. 8.4A). Conversely, the ions are released from electrode when discharging the ES (Fig. 8.4B). The deionization and electrode regeneration were accompanied with charge-discharge process.

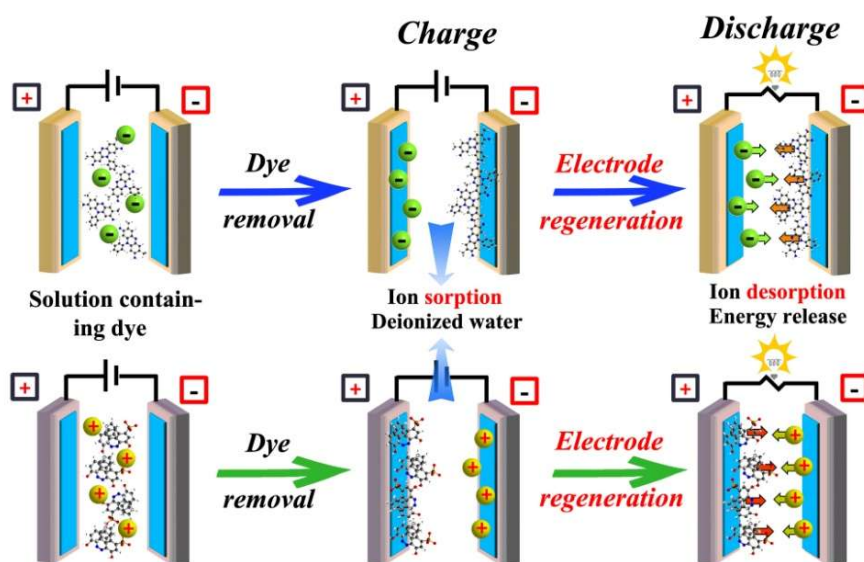


Figure 8.4 Charge and discharge mechanism of symmetric ES fabricated using (A) SAF and (B) CAL dye electrolyte.

The symmetric ES cells were fabricated by two N-AC-MWCNT electrodes and SAF or CAL as electrolyte, separated by a porous polymer membrane. The capacitive performance of the devices was analyzed in different voltage windows (Fig. 8.5A-F). Fig. 8.5(A and D) shows CVs in different voltage windows for the ES devices, containing SAF or CAL electrolytes at a scan rate of  $2 \text{ mV s}^{-1}$ . The increase in the

voltage window above 0.9 V resulted in significant increase in current, attributed to redox reactions. The galvanostatic charge-discharge curves obtained at a current density of  $3 \text{ mA cm}^{-2}$  showed significant voltage drop at the beginning of the discharge for voltage windows above 0.9 V (Fig. 8.5(B and E)). Such voltage drop  $V=IR$  ( $I$ -current) can be attributed to increased electrical resistance  $R$  of the cells. The cell capacitances and Coulombic efficiencies decreased in the potential windows above 0.9 - 1 V (Fig. 8.5(C and F)). Therefore, further investigations were performed in the voltage window of 0.9 V.

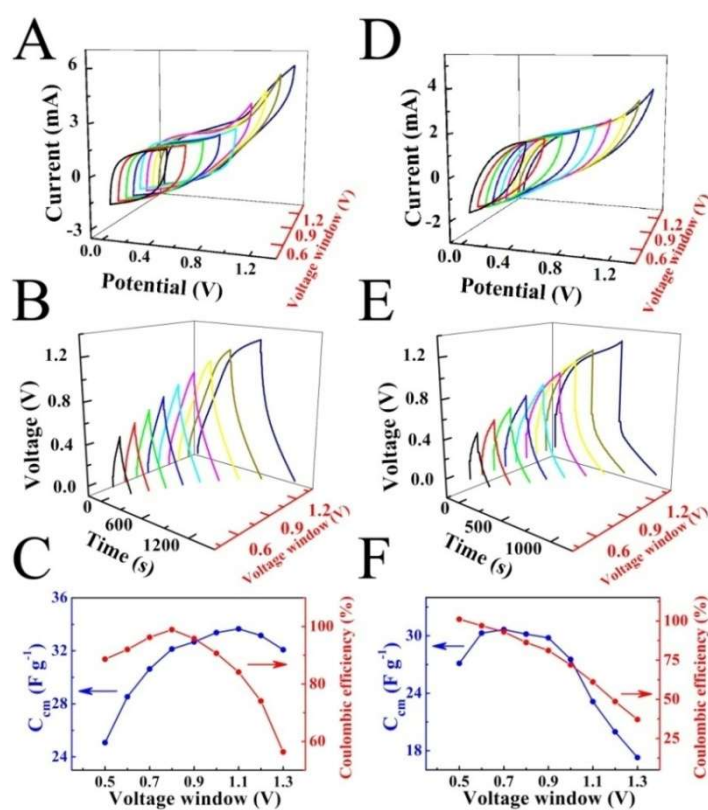


Figure 8.5 Capacitive behavior in different voltage windows (from 0.5 to 1.3 V) for ES cells, containing two N-AC-MWCNT electrodes in  $400 \text{ mg L}^{-1}$  (A, B, C) SAF and

(D, E, F) CAL solutions as electrolytes. (A, D) CVs at a scan rate of  $2 \text{ mV s}^{-1}$ , (B, E) charge-discharge behavior at a current density of  $3 \text{ mA cm}^{-2}$ , (C, F)  $C_{\text{cm}}$  calculated from discharge curves and Columbic efficiency versus the width of the voltage window. The mass loadings of individual electrodes was  $15 \text{ mg cm}^{-2}$ .

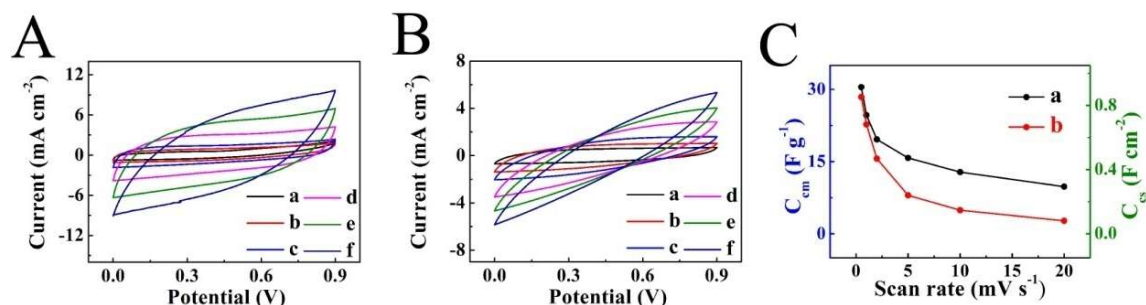


Figure 8.6 CVs in a voltage window of 0.9 V for ES cells prepared using  $400 \text{ mg L}^{-1}$  (A) SAF and (B) CAL electrolytes at scan rates of (a) 0.5, (b) 1, (c) 2, (d) 5, (e) 10 and (f)  $20 \text{ mV s}^{-1}$ . (C)  $C_{\text{cm}}$  and  $C_{\text{cs}}$  calculated from CVs versus scan rate for (a) SAF and (b) CAL electrolytes. The mass loadings of individual electrodes of ES cells is  $15 \text{ mg cm}^{-2}$ .

Fig. 8.6 (A and B) shows CVs of ES cells at different scan rates in the voltage window of 0.9 V. The larger area of the CVs obtained for the cells, containing SAF electrolyte (Fig. 8.6A), compared to the cells, containing CAL electrolyte (Fig. 8.6B), indicated higher capacitance of the SAF cells. The capacitance, calculated from the CV data is plotted versus scan rate in the Fig. 8.6C. The SAF cell showed much higher capacitance compared to the CAL cell, especially at scan rates above  $2 \text{ mV s}^{-1}$ .

Fig. 8.7 (A and B) shows charge-discharge behavior of ES devices, containing two N-AC-MWCNT electrodes and SAF or CAL electrolytes in a voltage window of 0.9 V. The charge-discharge curves showed nearly symmetrical triangular shape, however

voltage drop was observed at the beginning of the discharge curve. This voltage drop  $U=IR$  ( $I$  – current,  $R$  – resistance) was especially evident for the cells, containing CAL electrolyte, due to higher resistance. The devices, based on SAF electrolyte showed higher capacitance and better capacitance retention (Fig. 8.7C) in the current density range of 1-8  $\text{mA cm}^{-2}$ . The energy densities and power densities for the devices were presented in Fig. 8.7D. The devices (Fig. 8.7D, insets), based on SAF and CAL showed maximum energy density of 5.3 and 4.1  $\text{mWh g}^{-1}$  and power density of 525 and 137  $\text{mW g}^{-1}$ , respectively.

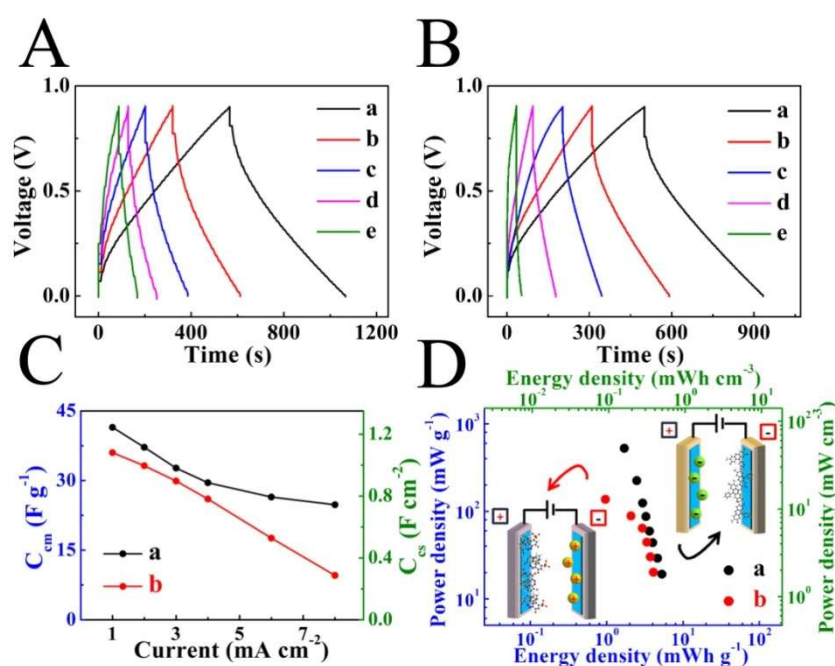


Figure 8.7 (A,B) Charge-discharge behavior of ES cells in (A) SAF and (B) CAL electrolytes at current densities of (a) 2 , (b) 3, (c) 4, (d) 6 and (e) 8  $\text{mA cm}^{-2}$ ; (C)  $C_{\text{cm}}$  and  $C_{\text{cs}}$  calculated from the discharge data versus current density and (D) Ragone plot for ES cells (insets) containing 400  $\text{mg L}^{-1}$  (a) SAF and (b) CAL solutions as

electrolytes. The N-AC-MWCNT mass loadings of individual electrodes of ES cells is  $15 \text{ mg cm}^{-2}$ .

### 6.1.3 Investigation of capacitive behavior in Amaranth solutions

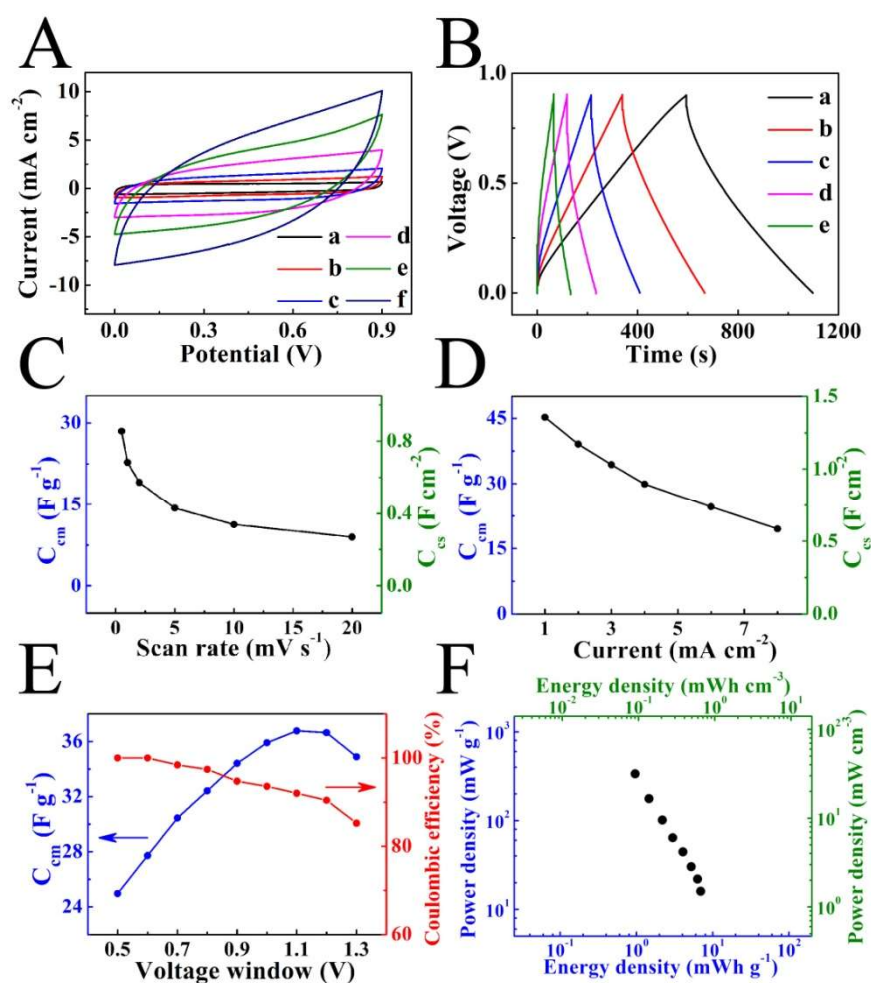


Figure 8.8 (A) CVs at scan rates of (a) 0.5 , (b) 1, (c) 2, (d) 5, (e) 10 and (f) 20  $\text{mV s}^{-1}$  and (B) charge-discharge curves at current densities of (a) 2 , (b) 3, (c) 4, (d) 6 and (e) 8  $\text{mA cm}^{-2}$  in a voltage window of 0.9V, (C)  $C_{\text{cm}}$  and  $C_{\text{cs}}$ , calculated from the CV data versus scan rate, (D)  $C_{\text{cm}}$  and  $C_{\text{cs}}$ , calculated from the discharge data versus current density, (E) Coulombic efficiency and capacitance, calculated from the discharge data

versus the width of the voltage window and (F) Ragone plot for ES cells, containing two N-AC-MWCNT electrodes in 400 mg L<sup>-1</sup> AMA electrolyte.

The SAF and CAL dyes investigated above contain only one charged group per molecule. We suggest that the performance of CDR is influenced by its chemical structure and ratio of charge to mass. As pointed out above, the structure of AMA dye is similar to that of CAL dye, however, the AMA molecule has three charged groups. The higher charge to mass ratio of AMA molecules can be beneficial for their electro-migration during charge and discharge. The ES cells, containing AMA electrolyte, showed improved capacitive behavior, compared to the cells, containing CAL electrolyte of the same concentration. The improved capacitive behavior is indicated by the larger area of CVs and nearly triangular shape of charge-discharge curves with reduced  $V=IR$  drop at the beginning of discharge in the voltage window of 0.9 V (Fig. 8.8 (A and B)). Fig. 8.8 (C and D) show capacitances, calculated from CVs (Fig. 8.8A) and galvanostatic discharge (Fig. 8.8B) data. The AMA cells showed higher capacitance and improved capacitance retention at high charge discharge rates, compared to CAL cells. The capacitance of the AMA cell at a scan rate of 20 V s<sup>-1</sup> was 9.0 F g<sup>-1</sup> (0.27 F cm<sup>-2</sup>), whereas the capacitance of the CAL cell at the same scan rate was only 2.7 F g<sup>-1</sup> (0.08 F cm<sup>-2</sup>). The capacitance of the AMA cell at a discharge current of 8 mA cm<sup>-2</sup> was 19.5 F g<sup>-1</sup> (0.60 F cm<sup>-2</sup>); however, the capacitance of CAL cell at the same discharge current was only 9.60 F g<sup>-1</sup> (0.29 F cm<sup>-2</sup>). The difference can result from higher mobility of the AMA dye, which has higher charge and higher charge to mass

ratio, compared to CAL. The capacitance of the AMA cell, calculated from the discharge data increased with increasing voltage window and showed a maximum at a voltage of 1.1 V (Fig. 8.8E). The Coulombic efficiency (Fig. 8.8E) decreased with increasing voltage window, especially at voltages above 0.9 V. Fig. 8.8F presents a Ragone plot for the cell, containing AMA electrolyte. The cell showed maximum energy density of  $7.0 \text{ mWh g}^{-1}$  and maximum power density of  $337 \text{ mW g}^{-1}$ . The improved energy/power characteristics of the cell, containing AMA electrolyte, are attributed to higher capacitance.

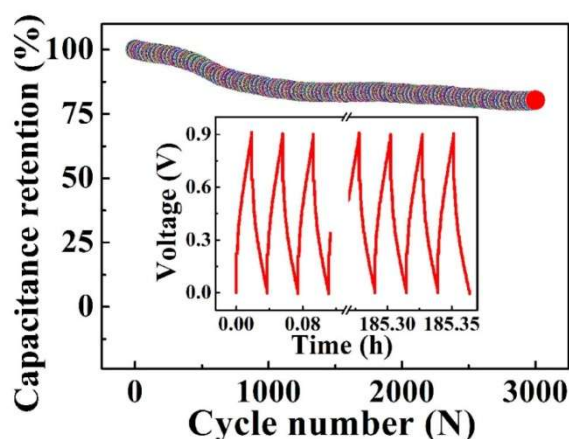


Figure 8.9 Capacitance retention of ES cells, containing two N-AC-MWCNT electrodes in  $400 \text{ mg L}^{-1}$  AMA electrolyte, versus cycle number, inset shows the initial and final charge-discharge curves in the cycling performance test.

The use of CDR offers the advantage of efficient energy utilization, because the dyes, removed from solutions are used for energy storage in the electrochemical double-layer. On the discharge cycle, this energy may be utilized to charge an analogous ES for dye

removal or powering neighbor cells. Turning again to the QCM data, it should be mentioned that the method allows electrode regeneration. The dyes released during the discharge cycle can be used for other applications. This suggestion was supported by the analysis of cyclic stability of the cells. The AMA cells showed 85.3 and 80.4 % capacitance retention after 1000 and 3000 cycles, respectively (Fig. 8.9). It is expected that further advances in the CDR method can be achieved by the development of efficient electrodes with high porosity, and this method will be used for other cationic and anionic dyes.

#### 8.1.4 Conclusions

N-AC-MWCNT electrodes have been investigated for capacitive removal of cationic SAF, anionic CAL and AMA dyes. These electrodes offer a possibility of building ES devices that simultaneously remove dyes and store energy in an electrochemical double-layer. This energy may be further utilized to remove dyes with a similar scheme through discharge of the ES, also fully regenerating the electrode materials for further use. QCM tests showed reversibility of the dye accumulation and removal from the electrodes. ES devices based on the solutions of anionic and cationic dyes as electrolytes showed promising capacitive performance and good cycling stability. The devices, based on anionic AMA dye showed improved capacitive behaviour, compared to electrodes with anionic CAL dye with similar structure due to higher charge of the AMA dye. The CDR offers the advantages of energy saving, reuse of dyes and electrodes and can be utilized for the removal of various cationic and anionic dyes.

## **8.2 Activated carbon nano-fibers for capacitive dye removal**

From the prior investigation, it appears that dye structure has significant influence on the energy storage efficiency. An important task is to investigate different families of organic dyes and analyze the charge storage capability. The possibility of electrode regeneration and cyclic stability are important characteristics of the CDR devices. This is because that some dyes exhibit pH dependent solubility and pH dependent charge. Such dyes can precipitate at electrodes due to the pH increase at the cathode or pH decrease at the anode surface[29-33]. The precipitation is attributed to the electrochemical decomposition of water and other electrochemical electrode reactions in aqueous solutions[29-34]. As a result, these dyes could be removed from solutions by electrodeposition. However, the deposited dyes removed formed continuous films on the surface of cathode or anode, causing the problem of electrode regeneration.

Therefore, development of the CDR technology requires experimental work on analysis of dyes with different chemical structures, due to their diversity and complexity. The goal of following investigation was to investigate CDR method for the removal of dyes, which belong to triphenylmethane and chromotropic acid families. The N-doped activated carbon nano-fibers (N-AC-NF) were prepared by carbonization of PPy nano-fibers, and employed as the active materials for the fabrication of electrodes. Compares with N-AC-MWCNT investigated in the previous work, N-AC-NF offers advantages of simple preparation and low cost. The results for comparison of different dyes provided an insight into the influence of dye structure,

size and charge on capacitive performance, voltage window and power-energy characteristics of ES cells.

### 8.2.1 Chemical structure of different dyes

Fig. 8.10 shows chemical structures of dyes used in this investigation. PV and ECR belong to the triphenylmethane family of anionic dyes (Fig. 8.10A and B). The anionic properties of PV are attributed to  $\text{SO}_3^-$  group, whereas the structure of ECR included one  $\text{SO}_3^-$  group and two  $\text{COO}^-$  anionic groups. The ECR molecule has larger charge to mass ratio, compared to PV. The structure of PV includes a redox-active catechol ligand[35]. CHR, CHRP, CHRN and CHR B (Fig. 8.10C-F) belong to the chromotropic acid family of anionic dyes. The anionic properties of such dyes are attributed to  $\text{SO}_3^-$  groups. The redox properties of CHRP, CHRN and CHR B molecules are attributed to their  $-\text{N}=\text{N}-$  groups[11, 36-38]. Molecular volumes and other characteristics of the CHR dyes were presented in Table 8.2. The 3D molecular structure of the dyes was obtained using Chem3D Ultra 12.0 software after minimization of Molecular Mechanics 2 (MM2) Energy. Molecular size including length, width, and thickness of the dyes were measured. Molecular surface area and volume were determined using Connolly's program[39-41]. In order to express hydrophobicity of the dyes, Log P was adopted[42, 43]. The logP and the polar surface area were calculated using the same software. The results indicated that the size of the molecules increases in the order  $\text{CHR} < \text{CHRP} < \text{CHRN} < \text{CHR B}$ . The CHR

and CHRB have larger charge to mass ratio, compared to that of CHRP and CHRN. Increase of the molecular size resulted in increase of the solvent accessible surface area and molecular surface area. However, the large molecule exhibited higher hydrophobicity. The CHRB exhibited the largest polar surface area ( $307.38 \text{ \AA}^2$ ) attributed to high charge.

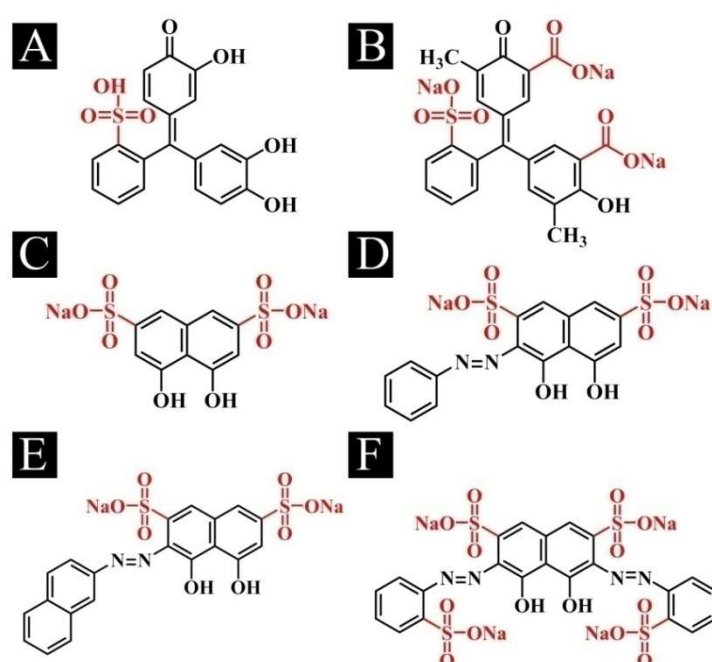
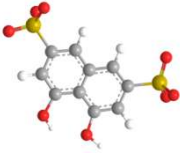
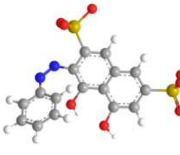


Figure 8.10 Chemical structures of (A) Pyrocatechol Violet (PV), (B) Eriochrome Cyanine R (ECR), (C) Chromotropic Acid Disodium Salt (CHR), (D) 2-(phenylazo) Chromotropic Acid Disodium Salt (CHRP), (E) 2-(1-naphthyl)diazenyl)chromotropic acid disodium salt (CHRN) and (F) 7-Bis(2-sulfophenylazo)chromotropic acid tetrasodium salt (CHRB).

Table 8.2 3D chemical structure and physical-chemical properties of CHR family dyes.

---

| Molecular structure                          |  |  |  |  |
|--|---|---|--|---|
|  | <b>CHR</b>  | <b>CHRP</b>   | <b>CHRN</b>  | <b>CHRb</b>   |
| Molecular weight<br>(g mol <sup>-1</sup> )   | 322.31  | 422.39  | 427.45   | 684.61  |
| Accessible area<br>(Å <sup>2</sup> )         | 462.81  | 589.71  | 651.94   | 760.92  |
| Molecular area<br>(Å <sup>2</sup> )          | 231.47  | 310.25  | 349.42   | 433.65  |
| Polar surface area<br>(Å <sup>2</sup> )      | 149.20  | 173.92  | 211.34   | 307.38  |
| Solvent excluded<br>volume (Å <sup>3</sup> ) | 194.57  | 275.81  | 312.70   | 439.81  |
| log P  | 0.67  | 3.01  | 4.03   | 3.76  |
| Length (Å)                                   | 7.76  | 7.71  | 9.58   | 9.49  |
| Width (Å)                                    | 4.05  | 7.30  | 7.73   | 7.31  |
| Depth (Å)                                    | 2.53  | 4.17  | 5.34   | 4.86  |

---

\*All the properties were calculated for dye ions excluding the influence of counter ions.

### 8.2.2 Characterization of N-doped activated carbon nano-fibers

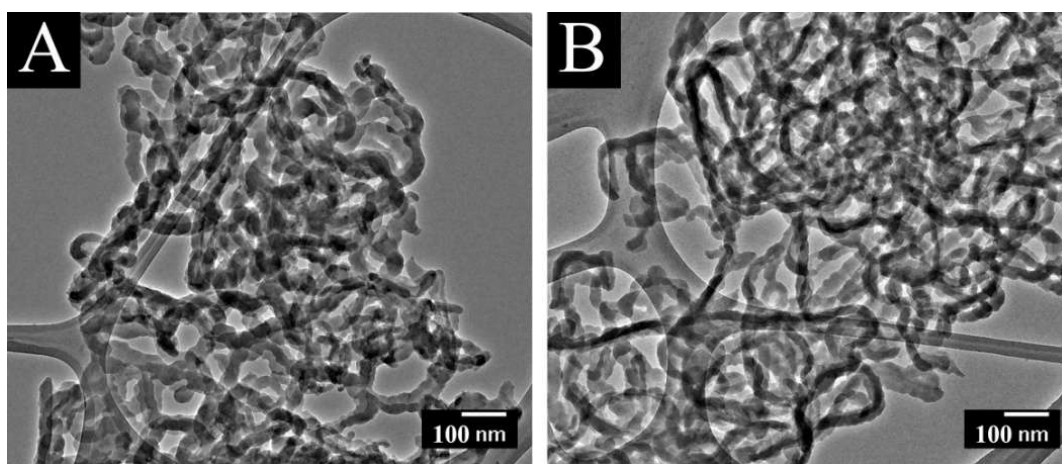


Figure 8.11 TEM images of (A) PPy-NF and (B) N-AC-NF.

Fig. 8.11A shows fibrous microstructure of PPy-NF, prepared by the chemical polymerization method using  $(CTA)_2S_2O_8$ . The N-AC-NF was obtained by carbonization and chemical activation of PPy-NF (section 4.2.3.3). The morphology of obtained materials was shown in Fig. 8.11B. The diameter of the nano-fibers was about 20-25 nm. The  $N_2$  adsorption-desorption isothermal tests were performed to analyze the porosity of fabricated materials (Fig. 8.12A). The N-AC-NF shows  $N_2$  adsorption at low pressure and slightly steep adsorption at the relative pressure of 0.7-1.0, indicating the coexistence of micro-, meso- and macro-pores in N-AC-NF (Fig. 8.12B). The specific surface area, calculated by the Brunauer-Emmett-Teller (BET) model, of PPy-NF and N-AC-NF were 165.8 and 1427.5  $m^2 g^{-1}$ , repetitively.

The high specific area of N-AC-NF nano-architecture can provide a sufficient electrochemical interface for accumulation of ionic dyes. The obtained N-AC-NF was used as the electrode for the ES cells, containing the dyes as electrolytes.

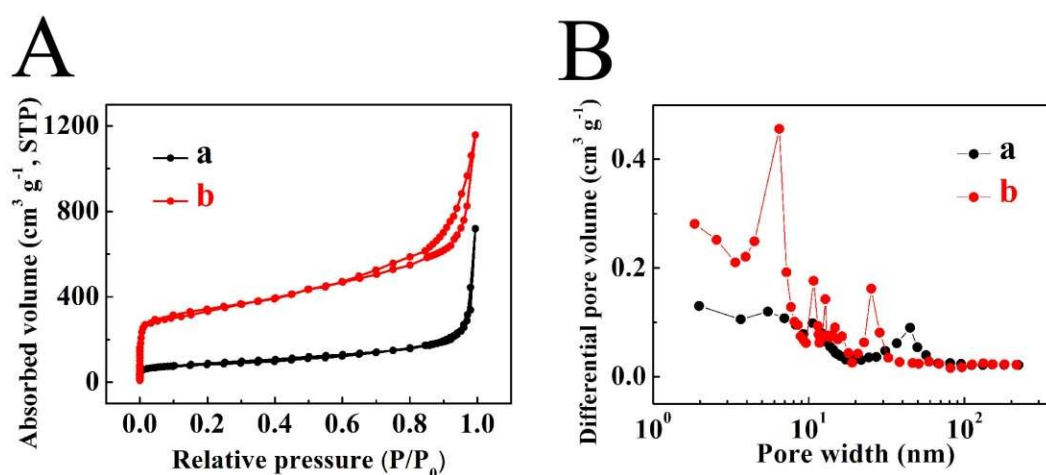


Figure 8.12. (A) Nitrogen adsorption-desorption isotherms at -196 °C and (B) corresponding pore-size distributions calculated with the Barrett-Joyner-Halenda (BJH) method for (a) PPy-NF and (b) N-AC-NF.

### 8.2.3 Optimization of the voltage window for capacitive removal of different dyes

Electrochemical testing of the cells containing N-AC-NF electrodes and different dyes as electrolytes showed capacitive behavior (Fig. 8.13). The CV data for the cells were obtained in different voltage windows. The analysis of the CVs showed a difference in capacitive behavior for the cells, containing dyes from triphenylmethane and chromotropic acid families. The CVs for the cells, containing PV and ECR electrolytes deviated from ideal box shape, especially at cell voltages above 0.6 V. The typical CVs at a scan rate of 2 mV s<sup>-1</sup> in different voltage windows for ECR cells

are shown in Fig. 8.13A. The CVs for cells, containing dyes from the chromotropic acid family were of nearly ideal box shape at a scan rate of  $2 \text{ mV s}^{-1}$ . Fig. 8.13D shows typical CVs for a CHR cell at a scan rate of  $2 \text{ mV s}^{-1}$ . The box shape CVs were observed at voltages 0.3-1.0 V, at higher voltages the CV shapes deviated from the ideal box shape. The capacitances, calculated from the CV data are presented in Fig. 8.13B and E. The capacitance of the ECR cell increased with increasing cell voltage and showed a maximum at 0.6 V. The increase in cell voltage above 0.6 V resulted in decreasing capacitance (Fig. 8.13B). The capacitance of CHR cell decreased with increasing cell voltage, showed a maximum at 1 V and then decreased. The galvanostatic charge-discharge curves for PV and ECR cells deviated from ideal symmetrical triangle shape with increase of cell voltage. Fig. 8.13C presents data for the ECR cell in different voltage windows. The increase in the voltage window above 0.6 V showed significant increase in a voltage drop at the beginning of the discharge (Fig. 8.13C). In contrast, the cells containing dyes from the CHR family showed nearly symmetrical triangular charge-discharge curves at voltages up to 0.9 V, as shown in Fig. 8.13F. At voltages higher than 0.9 V, significant deviation from the triangular shape was observed. Moreover, the increase in voltage above 0.9 V resulted in increasing voltage drop at the beginning of the discharge. On the basis of the analysis of CVs and galvanostatic charge discharge data, the optimized voltage windows of 0.6 V and 0.9 V were selected for the investigation of cells, containing dyes from the triphenylmethane and chromotropic acid families, respectively.

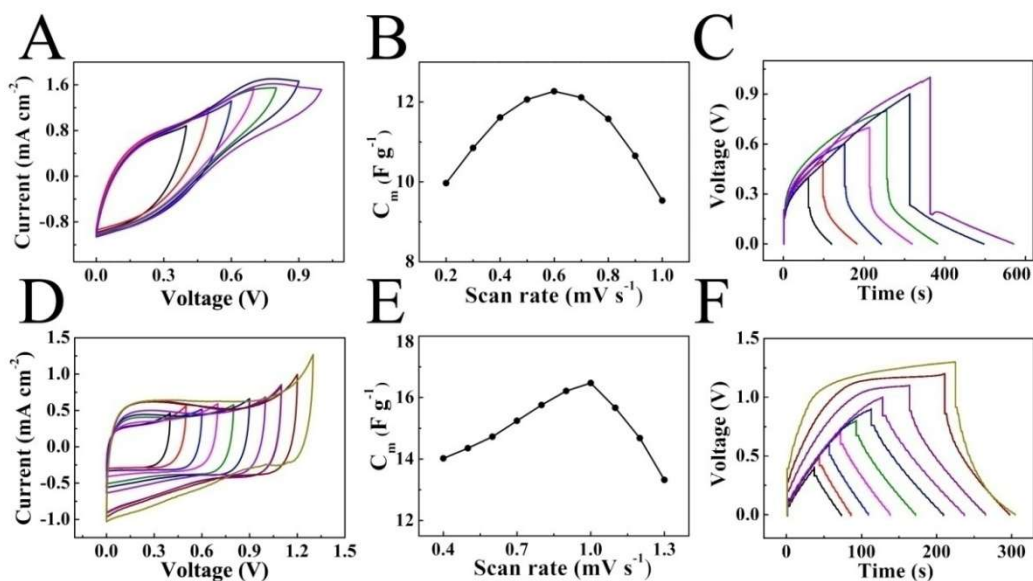


Figure 8.13 Capacitive behavior of cells, containing 500 mg L<sup>-1</sup> (A-C) ECR and (D-F) CHR electrolytes, (A,D) CVs at scan rate of 2 mV s<sup>-1</sup>, (B,E) C<sub>m</sub> calculated from CV data (C,F) constant current charge-discharge data at current densities of (C) 1 and (F) 2 mA cm<sup>-2</sup>.

The accumulation of the dyes in the electrodes during the charging process has been analyzed using a QCM method. Fig. 8.14A shows a schematic of the experimental set-up used for the QCM experiments. The syringe was used to inject the dye solutions to the working electrode, prepared by the N-AC-NF coated quartz crystal. The obtained quartz crystal was put into a sample holder and connected with the QCM tester. The original well-type holder of quartz crystal has been modified, as it was described in the previous investigation[44]. The modification prevented solvent evaporation and allowed to avoid noise, related to the pressure effects[44]. The adsorption of ECR dyes was investigated at a voltage of 0.6 V (Fig. 8.14B), while the

adsorption of CHR dyes was investigated at a voltage of 0.9 V (Fig. 8.14C). The application of the voltage resulted in a mass gain, related to adsorption of the dyes. The mass gain rate decreased with increasing time. The dye removal efficiency measured from QCM was calculated by the maximum mass change divided by the total amount (15  $\mu\text{g}$ ) of the dye injected to the cell. The results indicated that 9.2 mass% ECR and 18.3 mass% CHR were removed in a single charging process. The difference was mainly attributed to lower voltage used in the experiments with ECR dye. The lower mass and lower volume of the CHR (Table 8.2) were also beneficial for the enhanced accumulation of the CHR dyes in the electrode.

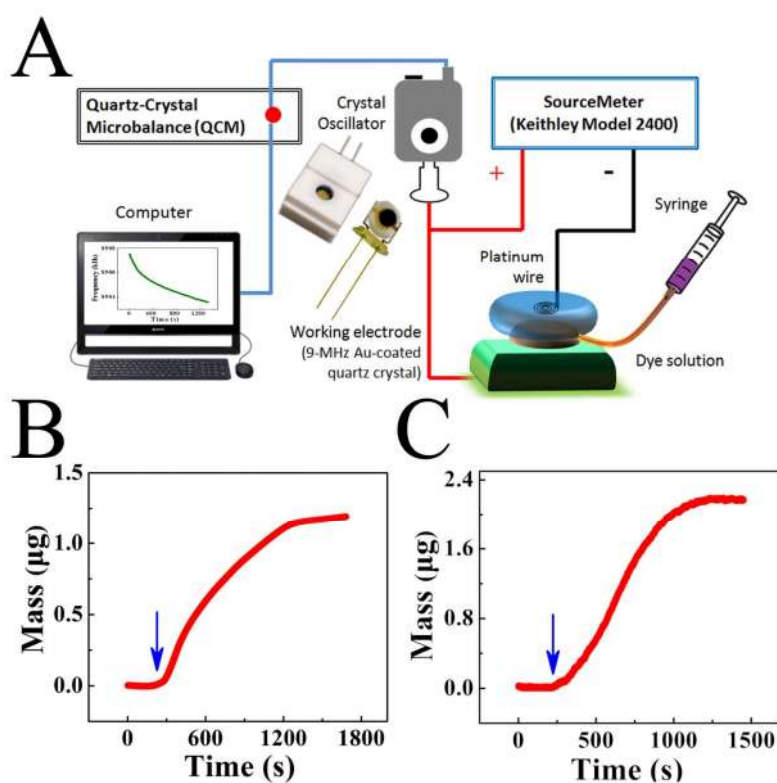


Figure 8.14 (A) Scheme of QCM analysis system for capacitive dye removal, (B,C) mass gain measured by QCM versus time for N-AC-NF coated electrodes in 0.3 mL

of 50 mg L<sup>-1</sup> solutions of (B) ECR at applied voltage of 0.6 V and (C) CHR at applied voltage of 0.9 V. Arrows show the starting points for applying voltage.

### 8.2.4 Capacitive performance of ES cells in triphenylmethane dyes

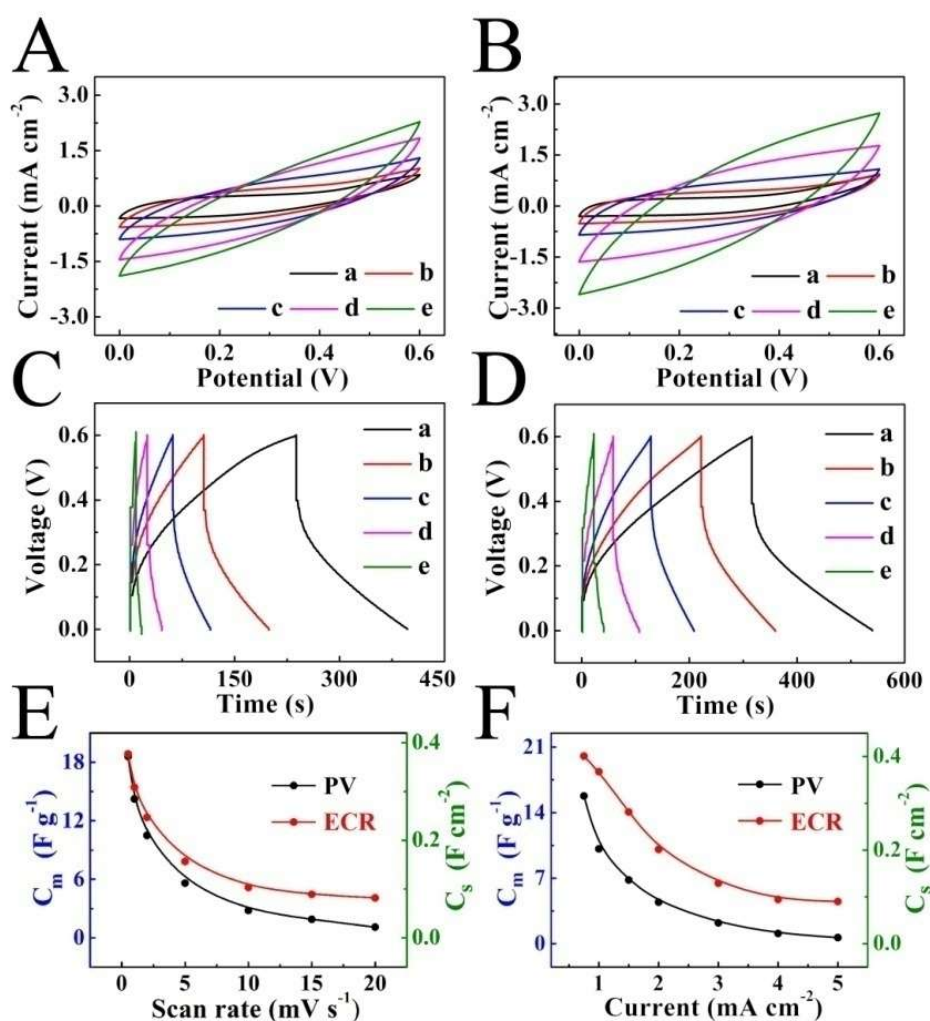


Figure 8.15 (A,B) CVs at scan rates of (a) 0.5, (b) 1, (c) 2, (d) 5 and (e) 10 mV s<sup>-1</sup> and (C,D) charge-discharge data at current densities of (a) 0.75, (b) 1, (c) 1.5, (d) 2 and (e) 3 mA cm<sup>-2</sup> for cells containing 500 mg L<sup>-1</sup> (A,C) PV and (B,D) ECR electrolytes, (E) capacitance calculated from CVs versus scan rate and (F) capacitance calculated from discharge data versus current density .

Fig. 8.15(A-D) compares CVs and galvanostatic charge-discharge data for the cells containing PV and ECR in a voltage window of 0.6 V. The larger area of CVs and longer discharge time for the cells, containing ECR, indicated higher capacitance. The capacitances of the cells, calculated from the CV data and charge-discharge data were presented at different scan rates and discharge currents in Fig. 8.15E and F. The higher capacitance of the ECR cells can be attributed to higher charge to mass ratio of ECR, compared to PV. The higher charge to mass ration can result in higher mobility in an electric field. Testing results did not show significant contribution of the redox-active catechol ligand of PV to the cell capacitance. It is suggested that the charge storage mechanism is mainly attributed to double layer capacitance. The capacitance decreased with increasing scan rate and increasing current density (Fig. 8.15E and F). Such decrease can result from diffusion limitations of the dyes during the charge-discharge process.

The capacitive behavior of the cells was influenced by the electrolyte concentration. Fig. 8.16 show typical data for the cells, containing ECR electrolyte. The increase in the electrolyte concentration resulted in increased CV area, indicating higher capacitance (Fig. 8.16A). The analysis of Nyquist plots of complex impedance (Fig. 8.16B) showed that resistance  $R=Z'$  decreased and the real part of capacitance, derived from the impedance data (Fig. 8.16C), increased with increasing electrolyte concentration. Fig. 8.16D typical charge-discharge curves at a current density of 1.5 mA cm<sup>-2</sup> with different ECR concentrations. The results showed that the increase in

electrolyte concentration resulted in longer discharge times, indicating higher capacitance. The corresponding Ragone plots showed improvement in power density and energy density for the cells with increase in electrolyte concentration (Fig. 8.16E). The investigations of cyclic stability Fig. 8.16F showed that capacitance decreased with increasing cycle number. The capacitance retention of 72 % was observed after 4000 cycles. The Coulombic efficiency was 95 % after 4000 cycles.

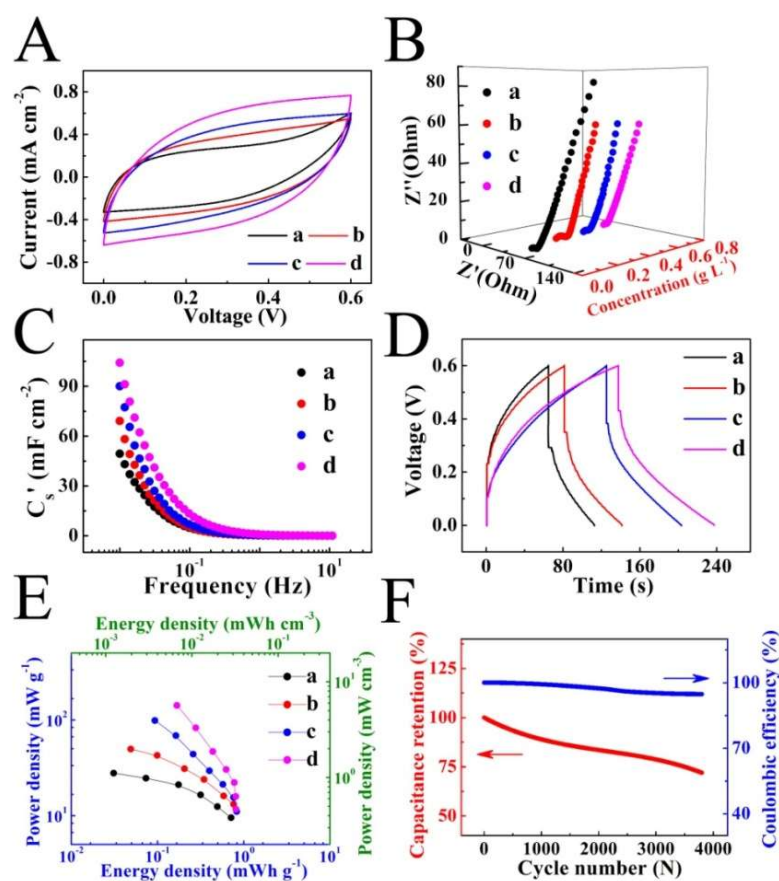


Figure 8.16 Capacitive behavior of cells, containing (a) 100, (b) 300, (c) 500 and (d) 700  $\text{mg L}^{-1}$  ECR electrolyte: (A) CVs at a scan rate of  $2 \text{ mV s}^{-1}$ , (B) Nyquist plots of complex impedance, (C)  $C_s'$  calculated from impedance data, (D) charge-discharge

curves at a current density of  $1.5 \text{ mA cm}^{-2}$  and (E) Ragone plots. (F) Capacitance retention and Coulombic efficiency of cells containing  $500 \text{ mg L}^{-1}$  ECR versus cycle number.

### 8.2.5 Capacitive performance of ES cells in chromotropic dyes

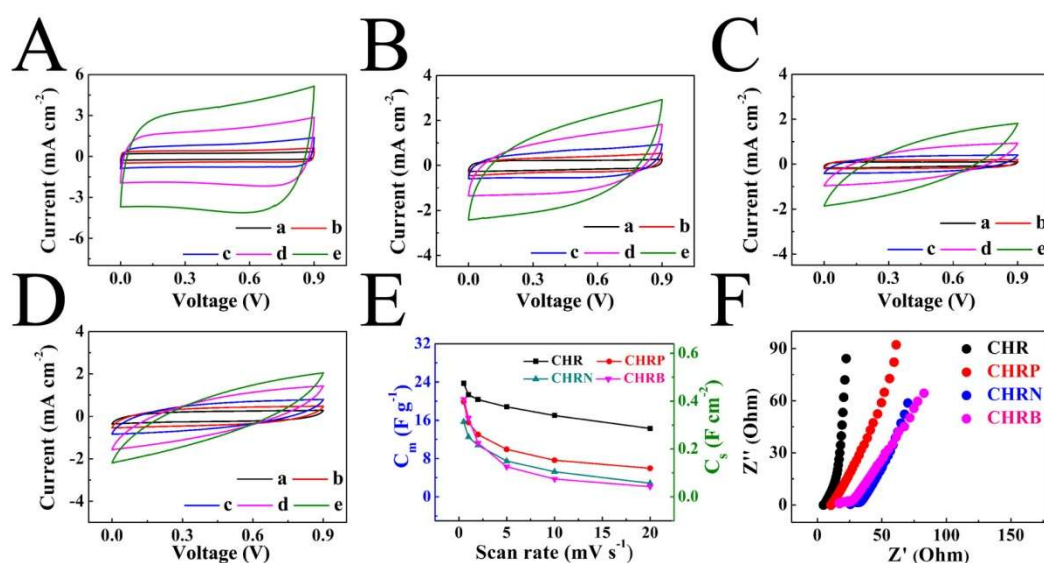


Figure 8.17 (A-D) CVs for cells prepared using  $500 \text{ mg L}^{-1}$  (A) CHR, (B) CHR P, (C) CHR N and (D) CHR B electrolytes at scan rates of (a) 0.5, (b) 1, (c) 2, (d) 5 and (e)  $10 \text{ mV s}^{-1}$ , (E) capacitance calculated from CVs versus scan rate and (F) Nyquist plots of complex impedance.

Fig 8.17 (A-D) compares CVs for cells prepared using  $500 \text{ mg L}^{-1}$  of CHR, CHR P, CHR N and CHR B electrolytes at different scan rates. The cells containing CHR showed larger CV area, compared to other dyes, indicating higher capacitance. Such cells showed nearly box shape CVs. The capacitances were calculated from the CV data at different scan rates and presented in Fig. 8.17E. The CHR based cells showed

higher capacitance compared to other cells, especially at higher scan rates. The impedance data were analyzed at different frequencies and presented in the Nyquist plot (Fig. 8.17F). The lower resistance  $R=Z'$  of the cells, containing CHR electrolyte, can be attributed to lower size and higher charge to mass ratio of the CHR molecules, which resulted in higher mobility and improved CHR electrolyte access to the N-AC-NF electrode material.

The galvanostatic charge-discharge data at different current densities for CHR, CHRP, CHRN and CHRB cells are compared in Fig. 8.18(A-D). The CHR cells showed longer charge-discharge times, indicating higher capacitances, compared to other cells at the same current densities. The CHR cells showed higher capacitances, compared to other cells (Fig. 8.18E). The CHRN cells showed the lowest capacitance, which can be attributed to the lowest charge to mass ratio of CHRN, compared to other molecules. The lower charge to mass ratio can result in lower mobility of the molecules in an electric field. The CHRB cells showed higher capacitances at current densities below  $2 \text{ mA cm}^{-2}$ , compared to CHRP and CHRN cells, due to higher charge to mass ratio of CHRB. However, the capacitance of CHRB cells, decreased significantly with increasing charge-discharge current due to larger size of CHRB. The higher capacitance of the CHR cells, compared to other cells, containing electrolytes from the chromotropic acid family, indicated that capacitive mechanism is mainly related to double layer capacitance, the  $-\text{N}=\text{N}-$  redox groups of CHRP, CHRN, CHRB did not contribute significantly to the capacitances of corresponding

cells. The CHR cells showed capacitance retention of 93% and Coulombic efficiency of 98% after 4000 cycles (Fig. 8.18F). The capacitance retention and Coulombic efficiency of CHR cells in the cycling tests were much higher, compared to ECR cells.

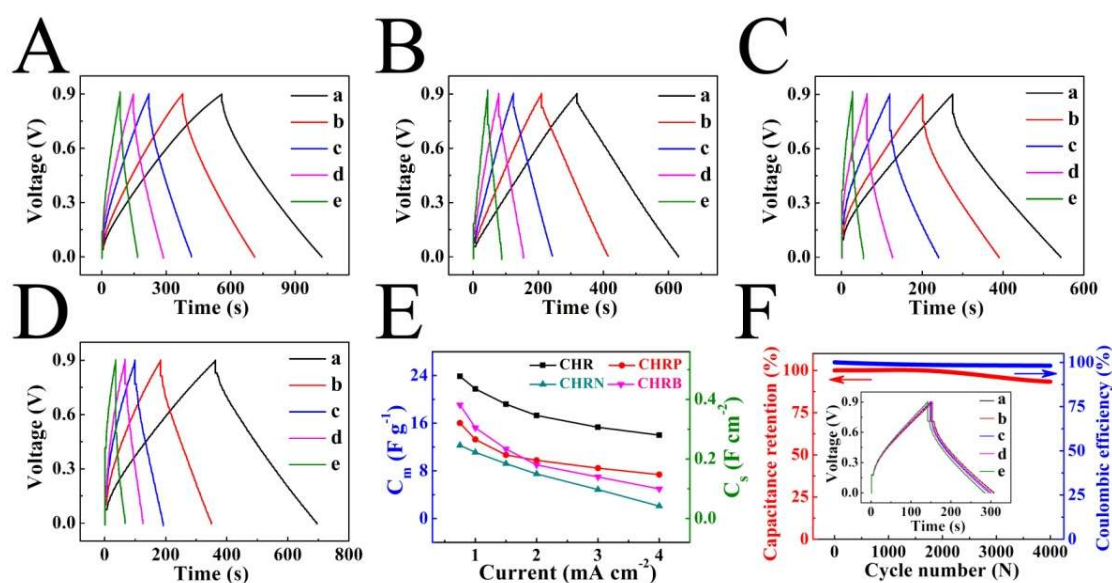


Figure 8.18 (A-D) Charge-discharge curves for cells containing 500 mg L<sup>-1</sup> (A) CHR, (B) CHRP, (C) CHRN and (D) CHRb electrolytes at current densities of (a) 0.75, (b) 1, (c) 1.5, (d) 2 and (e) 3 mA cm<sup>-2</sup>, (E) capacitance calculated from the discharge data versus current density and (F) capacitance retention and Coulombic efficiency for cells containing 500 mg L<sup>-1</sup> CHR versus cycle number.

The higher capacitance and larger voltage window of the cells, containing molecules from the chromotropic acid family, resulted in higher power-energy characteristics, compared to the molecules from the triphenylmethane family (Fig. 8.19). The comparison of the Ragone plots indicated that the highest energy density was

achieved for CHR cells. The PV cells showed lower energy density, compared to other cells. Testing results indicated that the efficiency of the CDR method is influenced by the molecular structure and size of the dyes.

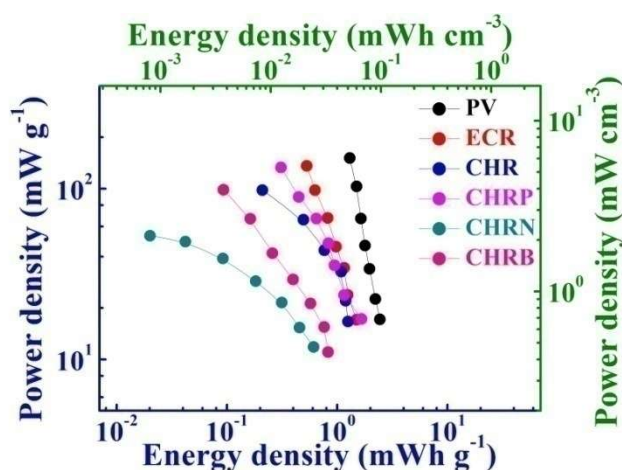


Figure 8.19 Ragone plots for cells, containing different dyes as electrolytes with concentrations of 500 mg L<sup>-1</sup>.

### 8.2.6 Conclusions

N-AC-NF, prepared by carbonization and chemical activation of PPy-NF, was investigated as the electrode material for CDR cells due to its fibrous morphology and high surface area. CDR method can be used for the removal of different dyes from aqueous solution, which belong to the triphenylmethane and chromotropic acid families. The optimal voltage windows were found to be 0.6 and 0.9 V for cells, containing dyes from triphenylmethane and chromotropic acid families, respectively. QCM data indicated that 9.2 mass % ECR and 18.3 mass % CHR were removed in a single charging process. For dyes of the same family, the higher charge to mass ratio

and lower size of the molecules resulted in higher capacitance, lower impedance and higher power-energy characteristics. In addition, the CRD performance of ES cell is influenced the concentration of dye solution. The dyes from the chromotropic family showed higher capacitance, energy density and power density, improved cyclic stability and coulombic efficiency, compared to the dyes from the triphenylmethane family.

### 8.3 References

- [1] S. Porada, R. Zhao, A. van der Wal, V. Presser, P.M. Biesheuvel, Review on the science and technology of water desalination by capacitive deionization, *Progress in Materials Science*, 58 (2013) 1388-1442.
- [2] S. Porada, D. Weingarth, H.V.M. Hamelers, M. Bryjak, V. Presser, P.M. Biesheuvel, Carbon flow electrodes for continuous operation of capacitive deionization and capacitive mixing energy generation, *Journal of Materials Chemistry A*, 2 (2014) 9313-9321.
- [3] K. Singh, S. Arora, Removal of synthetic textile dyes from wastewaters: a critical review on present treatment technologies, *Critical reviews in environmental science and technology*, 41 (2011) 807-878.
- [4] U. Resch-Genger, M. Grabolle, S. Cavaliere-Jaricot, R. Nitschke, T. Nann, Quantum dots versus organic dyes as fluorescent labels, *Nature methods*, 5 (2008) 763-775.
- [5] F. Han, V.S.R. Kambala, M. Srinivasan, D. Rajarathnam, R. Naidu, Tailored titanium dioxide photocatalysts for the degradation of organic dyes in wastewater treatment: a review, *Applied Catalysis A: General*, 359 (2009) 25-40.
- [6] A. Khataee, M.B. Kasiri, Photocatalytic degradation of organic dyes in the presence of nanostructured titanium dioxide: influence of the chemical structure of dyes, *Journal of Molecular Catalysis A: Chemical*, 328 (2010) 8-26.
- [7] K. Shi, M. Ren, I. Zhitomirsky, Activated carbon coated carbon nanotubes for energy storage in supercapacitors and capacitive water purification, *ACS Sustainable Chemistry & Engineering*, 2 (2014) 1289-1298.

- [8] L. Proevska, I. Pojarlieff,  $^1\text{H}$  NMR spectra and structure of safranines. Hindered rotation of the 3-dialkylamino group in 7-azo derivatives, *Dyes and Pigments*, 36 (1998) 177-190.
- [9] C. Ying, H. Xi-Wen, Studies of interaction between Safranin T and double helix DNA by spectral methods, *Spectrochimica Acta, Part A* 54A (1998) 883-892.
- [10] G. Sharma, M. Roy, S. Gupta, Characterization of Safranin O based thin-film sandwich devices by analysing their electrical and photoelectrical behaviour, *Synthetic Metals*, 88 (1997) 57-63.
- [11] R. Jain, N. Sharma, K. Radhapyari, Electrochemical treatment of pharmaceutical azo dye amaranth from waste water, *Journal of Applied Electrochemistry*, 39 (2009) 577-582.
- [12] A. Karunya, C. Rose, C. Valli Nachiyar, Biodegradation of the textile dye Mordant Black 17 (Calcon) by *Moraxella osloensis* isolated from textile effluent-contaminated site, *World Journal of Microbiology and Biotechnology*, 30 (2014) 915-924.
- [13] P. Dachipally, S.B. Jonnalagadda, Kinetics of ozone-initiated oxidation of textile dye, Amaranth in aqueous systems, *Journal of Environmental Science and Health - Part A Toxic/Hazardous Substances and Environmental Engineering*, 46 (2011) 887-897.
- [14] K.A. Matis, G.P. Gallios, Anionic flotation of magnesium carbonates by modifiers, *International Journal of Mineral Processing*, 25 (1989) 261-274.
- [15] H. Wang, A.C. Forse, J.M. Griffin, N.M. Trease, L. Trognko, P.-L. Taberna, P. Simon, C.P. Grey, In Situ NMR Spectroscopy of Supercapacitors: Insight into the Charge Storage Mechanism, *Journal of the American Chemical Society*, 135 (2013) 18968-18980.
- [16] C. Largeot, C. Portet, J. Chmiola, P.-L. Taberna, Y. Gogotsi, P. Simon, Relation between the Ion Size and Pore Size for an Electric Double-Layer Capacitor, *Journal of the American Chemical Society*, 130 (2008) 2730-2731.
- [17] F.W. Richey, B. Dyatkin, Y. Gogotsi, Y.A. Elabd, Ion Dynamics in Porous Carbon Electrodes in Supercapacitors Using in Situ Infrared Spectroelectrochemistry, *Journal of the American Chemical Society*, 135 (2013) 12818-12826.
- [18] H. Wang, T.K.J. Koster, N.M. Trease, J. Segalini, P.-L. Taberna, P. Simon, Y. Gogotsi, C.P. Grey, Real-Time NMR Studies of Electrochemical Double-Layer Capacitors, *Journal of the American Chemical Society*, 133 (2013) 19270-19273.

- [19] P. Simon, Y. Gogotsi, Capacitive Energy Storage in Nanostructured Carbonâ€“Electrolyte Systems, *Accounts of Chemical Research*, 46 (2012) 1094-1103.
- [20] M.D. Levi, G. Salitra, N. Levy, D. Aurbach, J. Maier, Application of a quartz-crystal microbalance to measure ionic fluxes in microporous carbons for energy storage, *Nature Materials*, 8 (2009) 872-875.
- [21] J.N. Barisci, G.G. Wallace, R.H. Baughman, Electrochemical quartz crystal microbalance studies of single-wall carbon nanotubes in aqueous and non-aqueous solutions, *Electrochimica Acta*, 46 (2000) 509-517.
- [22] S. Sigalov, M.D. Levi, G. Salitra, D. Aurbach, J. Maier, EQCM as a unique tool for determination of ionic fluxes in microporous carbons as a function of surface charge distribution, *Electrochemistry Communications*, 12 (2010) 1718-1721.
- [23] N. Levy, M.D. Levi, D. Aurbach, R. Demadrille, A. Pron, Failure and stabilization mechanisms in multiply cycled conducting polymers for energy storage devices, *Journal of Physical Chemistry C*, 114 (2010) 16823-16831.
- [24] M.D. Levi, N. Levy, S. Sigalov, G. Salitra, D. Aurbach, J. Maier, Electrochemical quartz crystal microbalance (EQCM) studies of ions and solvents insertion into highly porous activated carbons, *Journal of the American Chemical Society*, 132 (2010) 13220-13222.
- [25] S. Sigalov, M.D. Levi, G. Salitra, D. Aurbach, A. Janes, E. Lust, I.C. Halalay, Selective adsorption of multivalent ions into TiC-derived nanoporous carbon, *Carbon*, 50 (2012) 3957-3960.
- [26] M.D. Levi, S. Sigalov, G. Salitra, R. Elazari, D. Aurbach, Assessing the solvation numbers of electrolytic ions confined in carbon nanopores under dynamic charging conditions, *The Journal of Physical Chemistry Letters*, 2 (2011) 120-124.
- [27] W.-Y. Tsai, P.-L. Taberna, P. Simon, Electrochemical Quartz Crystal Microbalance (EQCM) Study of Ion Dynamics in Nanoporous Carbons, *Journal of the American Chemical Society*, 136 (2014) 8722-8728.
- [28] M.D. Levi, S. Sigalov, D. Aurbach, L. Daikhin, In Situ Electrochemical Quartz Crystal Admittance Methodology for Tracking Compositional and Mechanical Changes in Porous Carbon Electrodes, *The Journal of Physical Chemistry C*, 117 (2013) 14876-14889.

- [29] M. Ata, Y. Liu, I. Zhitomirsky, A review of new methods of surface chemical modification, dispersion and electrophoretic deposition of metal oxide particles, *RSC Advances*, 4 (2014) 22716-22732.
- [30] M.S. Ata, Y. Sun, X. Li, I. Zhitomirsky, Electrophoretic Deposition of Graphene, Carbon Nanotubes and Composites using Aluminon as Charging and Film Forming Agent, *Colloids Surf., A*, 398 (2012) 9-16.
- [31] Y. Su, I. Zhitomirsky, Electrophoretic deposition of graphene, carbon nanotubes and composite films using methyl violet dye as a dispersing agent, *Colloids and Surfaces A: Physicochemical and Engineering Aspects*, 436 (2013) 97-103.
- [32] Y. Su, I. Zhitomirsky, Electrophoretic Assembly of Organic Molecules and Composites for Electrochemical Supercapacitors, *J. Colloid Interface Sci.*, 392 (2013) 247-255.
- [33] Y. Su, I. Zhitomirsky, Cataphoretic assembly of cationic dyes and deposition of carbon nanotube and graphene films, *Journal of Colloid and Interface Science*, 399 (2013) 46-53.
- [34] I. Zhitomirsky, Cathodic Electrodeposition of Ceramic and Organoceramic Materials. Fundamental Aspects, *Advances in Colloid and Interface Science*, 97 (2002) 277-315.
- [35] Q. Sheng, H. Yu, J. Zheng, Hydrogen peroxide determination by carbon ceramic electrodes modified with pyrocatechol violet, *Electrochimica Acta*, 52 (2007) 7300-7306.
- [36] K. Shi, I. Zhitomirsky, Supercapacitor devices for energy storage and capacitive dye removal from aqueous solutions, *RSC Advances*, 5 (2015) 320-327.
- [37] Y. Su, I. Zhitomirsky, Influence of Dopants on Performance of Polypyrrole Coated Carbon Nanotube Electrodes and Devices, *Journal of The Electrochemical Society*, 162 (2015) A5013-A5019.
- [38] N. Dossi, E. Piccin, G. Bontempelli, E. Carrilho, J. Wang, Rapid analysis of azo- dyes in food by microchip electrophoresis with electrochemical detection, *Electrophoresis*, 28 (2007) 4240-4246.
- [39] M. Connolly, Solvent-accessible surfaces of proteins and nucleic acids, *Science*, 221 (1983) 709-713.
- [40] M.L. Connolly, Computation of molecular volume, *Journal of the American Chemical Society*, 107 (1985) 1118-1124.

[41] M.L. Connolly, The molecular surface package, *Journal of Molecular Graphics*, 11 (1993) 139-141.

[42] C. Hung-Lung, L. Kuo-Hsiung, C. Shih-Yu, C. Ching-Guan, P. San-De, Dye adsorption on biosolid adsorbents and commercially activated carbon, *Dyes and Pigments*, 75 (2007) 52-59.

[43] A.R. Tehrani-Bagha, R.G. Singh, K. Holmberg, Solubilization of two organic dyes by cationic ester-containing gemini surfactants, *Journal of Colloid and Interface Science*, 376 (2012) 112-118.

[44] K.N. Sank, I. Zhitomirsky, L.R. Berry, A.K. Chan, J.L. Brash, Surface modification with an antithrombin-heparin complex for anticoagulation: Studies on a model surface with gold as substrate, *Acta Biomaterialia*, 6 (2010) 2911-2919.

## 9. Conclusions

Chemical and electrochemical polymerizations of PPy were carried out using sulfonic aromatic molecules as anionic dopants. Tiron doped PPy films were obtained by electrochemical polymerization on Ni foil and Ni plaque substrates, respectively. In chemical polymerization,  $(\text{CTA})_2\text{S}_2\text{O}_8$  nano-crystals were used as the multi-functional oxidant to synthesize PPy nano-fibers and PPy coated MWCNT. PPy coated MWCNT allowed to fabricate N-AC-MWCNT with uniform coating, good dispersion and high surface area. The development of  $\text{MnO}_2$  coated N-AC-MWCNT is based on the chemical reaction between  $\text{KMnO}_4$  and N-AC-MWCNT. In this approach, the problem of MWCNT degradation was avoided by using AC as the sacrificial layer. The morphology characterization, structure analysis and electrochemical tests, including the CV, EIS and galvanstatic charge-discharge tests, were employed to investigate the obtained materials as the electrodes for applications in energy storage in supercapacitors and capacitive water purification.

The experimental results indicated that Tiron doped PPy films, prepared by electrochemical polymerization using Ni plaque as the current collectors, showed higher material loading and improved capacitance retention. Compared to Ni foil current collectors, the use of Ni plaques limited PPy swelling during cycling and improved cycling stability of PPy electrode. The capacitive behavior of Tiron doped PPy film was further enhanced by the pulse current polymerization.

Supercapacitive performance of PPy based electrodes was improved using chemical polymerization method. PPy nano-fibers and PPy coated MWCNT were successfully synthesized using  $(\text{CTA})_2\text{S}_2\text{O}_8$ , which obtained from the chemical reaction between cationic surfactant and anionic oxidant. New dispersing agents, such as SAF and MG, were developed for colloidal processing of PPy nano-fibers, MWCNT and graphene composites. Sedimentation testing results, investigation of EPD kinetics and analysis of FTIR and UV-Vis data showed that the dispersants adsorbed on individual materials and provided their electrosteric dispersion. Composite electrodes were obtained by the impregnation of PPy slurry, containing conductive carbon, into a Ni foam as the current collector. High material loading and high active material to current collector ratio were achieved. Good dispersion of PPy nano-fibers, MWCNT and graphene allowed to fabricate composite electrodes with low resistance, good capacitance retention at high charge-discharge rates.

Additionally, activated carbon, prepared by carbonization and chemical activation of PPy, showed good electrochemical performance for supercapacitor applications. Symmetric and asymmetric supercapacitor cells, containing N-AC-MWCNT and aqueous  $\text{Na}_2\text{SO}_4$  electrolyte, were developed with large voltage window, good capacitance retention and good cycling stability. Positive electrode of asymmetric supercapacitor cell was fabricated using  $\text{MnO}_2$  coated N-AC-MWCNT due to its high capacitance. The  $\text{MnO}_2$  coated N-AC-MWCNT showed small size of  $\text{MnO}_2$

nanoparticles, fibrous microstructure of the material and good electrical contact of MnO<sub>2</sub> and MWCNT.

In final, activated carbon electrodes were demonstrated for capacitive removal of various cationic and anionic dyes. Such electrodes were further used for building supercapacitor devices, which simultaneously remove dyes and store energy in an electrical double layer. Electrochemical performance tests indicated that dye concentration, structure, charge and applied voltage influence the electrochemical performance of supercapacitor cells. The higher charge to mass ratio and lower size of the molecules resulted in higher capacitance, lower impedance and higher power-energy characteristics. The dyes from the chromotropic family showed higher capacitance, energy/power density and improved coulombic efficiency, compared to the dyes from the triphenylmethane family.